

Assessment of Cavitation Erosion with a Multiphase Reynolds-Averaged Navier-Stokes Method

Proefschrift

ter verkrijging van de graad van doctor
aan de Technische Universiteit Delft,
op gezag van de Rector Magnificus prof. ir. K.C.A.M. Luyben,
voorzitter van het College voor Promoties,
in het openbaar te verdedigen op dinsdag 5 juni 2012 om 10:00 uur

door Ziru LI

李子如

Master of Engineering in the Design and Manufacture for Ships and Marine
Structures, Wuhan University of Technology, Wuhan, P.R. China
geboren te Xinji, Hebei Province, P.R. China

Dit proefschrift is goedgekeurd door de promotor:

Prof. dr. ir. T.J.C. van Terwisga

Samenstelling promotiecommissie:

Rector Magnificus,	voorzitter
Prof. dr. ir. T.J.C. van Terwisga,	Technische Universiteit Delft, promotor
Prof. dr. ir. H.W.M. Hoeijmakers,	Universiteit Twente
Prof. J. Carlton,	City University, London
Prof. dr. ir. J. Westerweel,	Technische Universiteit Delft
Prof. dr. ir. C. van Rhee,	Technische Universiteit Delft
Dr. ir. M.J.B.M. Pourquie,	Technische Universiteit Delft
Dr. D.Q. Li,	SSPA-Swedish Research Institute, Sweden
Prof. dr. ir. R.H.M. Huijsmans,	Technische Universiteit Delft, reservelid



Keywords: multiphase RANS method, FLUENT, unsteady cavitation, Reboud's correction, cavitation erosion, erosion intensity

Published by: VSSD

Website: <http://www.vssd.nl/hlf>

E-mail: hlf@vssd.nl

ISBN 978-90-6562-300-3

Copyright © 2012 by Z.R. LI

All rights reserved. No part of the material protected by this copyright notice may be reproduced or utilized in any form or by any means, electronic or mechanical, including photocopying, recording or by any information storage and retrieval system, without written permission from the author.

To my family

SUMMARY

Assessment of Cavitation Erosion with a Multiphase Reynolds-Averaged Navier-Stokes Method

By Ziru LI

Cavitation is a common phenomenon that often occurs in the flow over propulsion systems, rudders and other hydraulic machinery. It is essential to predict cavitation and assess cavitation hindrance in an early design stage due to the limitations imposed on the attainable propulsor thrust and efficiency. However, due to the complexities and difficulties involved in a cavitating flow, such as the effects of phase change, compressibility, viscosity and turbulent fluctuations, the prediction of cavitation is a persistent challenge for both researchers and designers. Cavitation erosion is one of the remarkable catastrophic consequences of cavitation. Predicting the cavitation aggressiveness quantitatively and predicting the most probable location of cavitation erosion are complex problems that currently still motivate an important amount of basic and applied research in the fields of hydrodynamics, physics and metallurgy.

This dissertation propose an erosion intensity function for the assessment of the risk of cavitation erosion on the hydrofoil surface by post-processing the results predicted by using a multiphase Reynolds-Averaged Navier-Stokes (RANS) method implemented in FLUENT. The work in this dissertation addresses two main issues: numerical simulations of cavitating flows over hydrofoils and an assessment of the risk of cavitation erosion on the surface of hydrofoils.

Based on existing experimental observations and new numerical simulations, the attention in this dissertation is focused on the behavior of unsteady cavitating flow over hydrofoils, typically characterized by the development of a horse-shoe shaped cloudy cavity and secondary stream-wise cavitating vortices. The erosive cavitation was assumed to be always associated with the collapse of vapor structures in the vicinity of the hydrofoil surface.

Initially a 2D study was conducted of the wetted flow and the steady and unsteady cavitating flows over a NACA0015 and a NACA0018-45 hydrofoil. It was discovered that a realistic dynamic shedding of cavitation is only obtained after attenuating the eddy viscosity in the region with higher vapor fraction.

To further explore the capability of the multiphase RANS method to predict the relevant and critical unsteady cavitation dynamics in the flow over hydrofoils, further investigations were conducted on the same hydrofoils in the 3D domain. The purpose of this study was to get a better understanding of the behavior of unsteady cavitation and the physics that may lead to a high risk of cavitation erosion with regard to the three-dimensionalities. It was also aimed at providing sufficiently good results for the post-processing procedures. It was found that the large-scale structures and the typical unsteady cavitation dynamics predicted by the RANS method implemented in FLUENT were in fair agreement with the observations from experiments. However, the locations of some of the primary structures were found to deviate from the experimental observations. Recommendations to alleviate these discrepancies refer to the improved input and boundary conditions: A more accurate bubble number density as input, improved tunnel wall boundary layer velocity profile and outlet pressure as measured in the experiments.

To find the best criteria for an assessment of the risk of cavitation erosion, current erosion risk assessment models and methodologies that use computational fluid dynamic tools or experimental results as input were reviewed and evaluated. The criteria investigated in this dissertation were based on: instantaneous static pressure p , variation of the local pressure in time $\partial p / \partial t$, variation of the local vapor volume fraction in time $-\partial \alpha / \partial t$, and four time-averaged aggressiveness functions whose integrands are associated with two variables, α (or $-\partial \alpha / \partial t$) and $p - p_v$ (or $\partial p / \partial t$). Ultimately, a new erosion intensity function was proposed based on the mean value of those values of the time derivative of the local pressure that exceeds a certain threshold, and was evaluated for the NACA0015 hydrofoil and NACA0018-45 hydrofoil. A good correlation was found between the locations with the high erosion risk obtained from the computations and the damage area observed from paint tests.

SAMENVATTING

Assessment of Cavitation Erosion with a Multiphase Reynolds-Averaged Navier-Stokes Method

Door Ziru Li

Cavitatie is een gebruikelijk verschijnsel in de stroming over voortstuwingssystemen, roeren en overige hydraulische systemen. Het is noodzakelijk om cavitatie te kunnen voorspellen en de overeenkomstige hinder in een vroeg ontwerpstadium te kunnen bepalen in verband met de beperkingen die hierdoor aan de stuwkracht en het rendement van de voortstuwder gesteld worden. Het bepalen van deze cavitatie hinder is echter een hardnekkige uitdaging, veroorzaakt door de complexiteit van de caviterende stroming en de effecten hierop van fase overgang, samendrukbaarheid, viscositeit en turbulentie. Cavitatie erosie is een opmerkelijk schadelijke bijwerking van cavitatie. Het voorspellen van de agressiviteit van cavitatie erosie en de locatie van de schade zijn complexe problemen die tot op heden een belangrijke mate van fundamenteel en toegepast onderzoek motiveren in de onderzoeksvelden van hydromechanica, fysica en metallurgie.

Deze dissertatie stelt een erosie intensiteits functie voor die gebruikt kan worden in de beoordeling van het risico op cavitatie erosie schade. Deze functie is gebaseerd op de resultaten van een meergefase Reynolds-Averaged Navier-Stokes (RANS) methode zoals geïmplementeerd in FLUENT. Deze studie behandelt twee hoofdzaken: In de eerste plaats wordt de numerieke simulatie van een caviterende stroming over hydrofoils bestudeerd en in de tweede plaats wordt een methode afgeleid voor de schatting van het cavitatie erosie risico op het oppervlak van de hydrofoils.

Gebaseerd op bestaande experimentele observaties en nieuwe numerieke simulaties, wordt in deze studie vooral aandacht gegeven aan het gedrag van instationaire cavitatie in de stroming over hydrofoils, waarbij het cavitatie patroon gedomineerd wordt door de ontwikkeling van een hoefijzervormige wervel en secundaire wervels in stromingsrichting. Erosieve cavitatie wordt verondersteld altijd geassocieerd te zijn met de implosie van

cavitatie structuren in de nabijheid van het hydrofoil oppervlak.

In eerste instantie is een uitgebreide 2D studie uitgevoerd aan zowel de niet-caviterende als ook de caviterende stroming over een NACA0015 en een NACA0018-45 hydrofoil, waarbij voor de caviterende stroming zowel de stationaire als de niet-stationaire omstroming bestudeerd zijn. Hierbij is gevonden dat instationaire afschudding van wolkachtige cavitatie structuren alleen optreedt als de turbulente viscositeit kunstmatig wordt verkleind in de nabijheid van de interface van water en damp.

In een verder onderzoek naar het vermogen van de meergefase RANS methode om relevante en kritische instationaire cavitatie te voorspellen, heeft verder onderzoek zich toegespitst op dezelfde hydrofoils in het 3D domein. Doel van deze studie was om een beter inzicht te verkrijgen in het gedrag van instationaire cavitatie en de fysica die tot hoge risico's kunnen leiden in 3D. Een tweede doel was om voldoende data sets te creëren t.b.v. de postprocessing studie. Hierbij is gevonden dat de grotere cavitatie structuren en de karakteristieke instationaire cavitatie dynamica zoals voorspelt door FLUENT een goede overeenkomst vertoonden met experimentele observaties. Echter, de locatie van deze structuren week af en toe significant af. Er zijn aanbevelingen gedaan om de verschillen tussen simulatie en experiment te verkleinen: Het verbeteren van de input en randvoorwaarden, waarbij een nauwkeuriger bellenspectrum en luchtgehalte bepaald zou moeten worden. Dit resulteert in een nauwkeuriger input van de waterkwaliteit, een betrouwbaar gemeten stromingsprofiel langs de tunnelwand en goed gespecificeerde drukken in het uitstroomvlak.

Teneinde de beste criteria voor de bepaling van het erosie risico te vinden zijn in eerste instantie bestaande cavitatie erosie modellen bestudeerd en geëvalueerd. De criteria die daarna in deze studie onderzocht zijn, zijn: de instantane druk p , de tijdsafgeleide van de druk $\partial p / \partial t$ en de variatie van het locale dampgehalt $-\partial \alpha / \partial t$. Daarnaast zijn vier tijdsgemiddelde intensiteits functies bekeken waarvan de integrand steeds twee van de volgende variabelen bevatte: α (of $-\partial \alpha / \partial t$) en $p - p_v$ (of $\partial p / \partial t$). Deze studie heeft geresulteerd in een nieuwe erosie schade functie die gebaseerd is op het gemiddelde van de tijdsafgeleiden van de druk $\partial p / \partial t$, voor waarden die een bepaalde drempelwaarde overschreden. Deze schadefunctie is ook weer geëvalueerd voor de NACA0015 en de NACA0018-45 hydrofoil waarbij een goede correlatie werd gevonden tussen de locaties met een hoog erosie risico, en de beschadigde zones die verkregen zijn uit een verfproef.

TABLE OF CONTENTS

Summary	V
Samenvatting	VII
Chapter 1: Introduction	1
1.1 Background.....	1
1.2 Objective and Scope	2
1.3 Contents	3
Chapter 2: On the Physics of Cavitation Erosion	7
2.1 Overview.....	7
2.2 Fundamentals of Cavitation	7
2.2.1 What is Cavitation?.....	7
2.2.2 Typical Cavitation Types	8
2.2.3 Effects due to Cavitation.....	11
2.3 Basic Hydrodynamic Mechanisms.....	12
2.4 Physics from Experimental Observations	14
2.4.1 Cloud Cavitation Collapse	15
2.4.2 Cavitating Vortices Collapse.....	17
2.5 Physics From Numerical Simulations	18
2.5.1 Cloud Cavitation Collapse	19
2.5.2 Cavitating Vortices Collapse.....	19
2.6 Hypothesis	20
Chapter 3: Literature Review of Existing Cavitation Erosion Models	21
3.1 Overview.....	21
3.2 Model by Bark et al. (2004a).....	22
3.2.1 Phenomenological Model	22

3.2.2 Guidelines for Observation and Analysis.....	23
3.2.3 Relevance.....	23
3.3 Model by Fortes-Patella et al. (2004).....	24
3.3.1 Energy Approach	25
3.3.2 Relevance.....	26
3.4 Model by Dular et al. (2006).....	26
3.4.1 Cavitation Erosion Process	27
3.4.2 Relevance.....	28
3.5 Model by Kato et al. (1996).....	28
3.5.1 Cavitation Erosion Process	29
3.5.2 Relevance.....	32
3.6 Model by Wang and Brennen (1999).....	32
3.6.1 Collapse Process	32
3.6.2 Relevance.....	35
3.7 Model by Nohmi et al. (2008).....	36
3.7.1 Aggressiveness Indices	36
3.7.2 Relevance.....	37
3.8 Conclusions.....	37

Chapter 4: Modeling Cavitation with a RANS Method 39

4.1 Introduction.....	39
4.2 RANS Equations for Multiphase Flow	40
4.2.1 Continuity Equation (Mass Conservation).....	41
4.2.2 Momentum Equation	41
4.2.3 Reynolds-Averaged Navier-Stokes Equations	42
4.3 Turbulence Models	44
4.3.1 Two Approaches	44
4.3.2 SST $k - \omega$ Turbulence Model (Menter, 1994)	45
4.3.3 Reboud's Correction (Reboud et al., 1998).....	47
4.4 Cavitation Models.....	49
4.4.1 Basic Equations	50
4.4.2 Schnerr and Sauer Model.....	50
4.5 Convergence Issues.....	52
4.5.1 Convergence Criteria	52
4.5.2 Grid Sensitivity.....	54

Chapter 5: Results on 2D Wetted Flow	59
5.1 Overview.....	59
5.2 2D NACA0015 ($A\alpha A = 6^\circ$).....	59
5.2.1 Geometry of the NACA0015 Hydrofoil	60
5.2.2 Case Description.....	60
5.2.3 Results for Different Turbulence Models.....	62
5.2.4 Grid Sensitivity and Convergence Study	65
5.2.5 Comparison with Results from VIRTUE WP4 Workshop	67
5.3 2D NACA0015 ($A\alpha A = 8^\circ$).....	69
5.3.1 Case Description.....	69
5.3.2 Results and Discussion	71
5.4 2D NACA0018-45 ($A\alpha A = 6.5^\circ$).....	72
5.4.1 Geometry of the NACA0018-45 hydrofoil.....	72
5.4.2 Case Description.....	73
5.4.3 Results and Discussion	75
5.5 Conclusions.....	77
Chapter 6: Results on 2D Cavitating Flow	79
6.1 Overview.....	79
6.2 Steady Cavitating Condition.....	80
6.2.1 Case Description.....	80
6.2.2 Input Transient Parameters Study	81
6.2.3 Influence of the Temporal Discretization Scheme	88
6.2.4 Grid Sensitivity.....	90
6.2.5 Conclusions	94
6.3 Unsteady Cavitating Condition.....	94
6.3.1 2D NACA0015 ($A\alpha A = 6^\circ$).....	96
6.3.2 2D NACA0015 ($A\alpha A = 8^\circ$).....	119
6.3.3 2D NACA0018-45 ($A\alpha A = 6.5^\circ$).....	129
6.4 Conclusions.....	138
Chapter 7: Results on 3D Cavitating Flow	141
7.1 Overview.....	141
7.2 Experimental Set-up	141
7.3 3D NACA0015 ($A\alpha A = 8^\circ$)	143

7.3.1 Case Description 143
7.3.2 Wetted Flow Results 144
7.3.3 Results and Discussion on Cavitating Flow 145
7.4 3D NACA0018-45 ($AoA = 6.5^\circ$) 159
7.4.1 Case Description 159
7.4.2 Wetted Flow Results 160
7.4.3 Results and Discussion on Cavitating Flow 161
7.5 Discussion of the Discrepancies 171
7.5.1 Bubble Number Density 171
7.5.2 Location of the Reference Pressure 171
7.5.3 Wall Boundary Layer 173
7.5.4 Reliability of Reboud’s Correction 174
7.5.5 Time Scale 176
7.6 Conclusions..... 176

Chapter 8: Assessment of Risk of Cavitation Erosion 179

8.1 Overview..... 179
8.2 Experimental Results 180
8.2.1 NACA0015 Hydrofoil (Van Rijsbergen and Boorsma, 2011)..... 180
8.2.2 NACA0018-45 Hydrofoil (Van Terwisga, 2009)..... 185
8.3 Rationale Behind The Evaluations 185
8.4 Numerical Results - NACA0015 Hydrofoil..... 186
8.4.1 Instantaneous Pressure 187
8.4.2 Variation of Local Field 188
8.4.3 Time-Averaged Aggressiveness Indices (Nohmi et al., 2008) 195
8.4.4 Discussion and Conclusions 199
8.5 Numerical Results - NACA0018-45 Hydrofoil 201
8.5.1 Instantaneous Pressure 201
8.5.2 Variation of Local Field 204
8.5.3 Time-Averaged Aggressiveness Indices (Nohmi et al., 2008) 210
8.5.4 Conclusions 211
8.6 Bubble Collapse Model 212
8.7 A New Erosion Intensity Function 213
8.7.1 Results on NACA0015 Hydrofoil..... 214
8.7.2 Results on NACA0018-45 Hydrofoil 216
8.7.3 Conclusions 218

8.8 Conclusions.....	218
Chapter 9: Conclusions and Recommendations	221
9.1 Conclusions.....	221
9.2 Recommendations.....	224
Appendix A: A Brief Introduction of Turbulence Models in FLUENT	227
A.1 Overview.....	227
A.2 $k - \varepsilon$ Models	228
A.2.1 Transport Equation for Turbulent Kinetic Energy k	228
A.2.2 Standard $k - \varepsilon$ Model (Launder and Spalding, 1972).....	231
A.2.3 <i>RNG</i> $k - \varepsilon$ Model (Yakhot, V. and Orszag, S.A., 1986).....	233
A.2.4 Realizable $k - \varepsilon$ Model (Shih et al., 1995)	234
A.3 $k - \omega$ Models	235
A.3.1 Standard $k - \omega$ Model (Wilcox, 1998).....	235
A.3.2 <i>SST</i> $k - \omega$ Model (Menter, 1994).....	237
Appendix B: A Brief Introduction of Cavitation Models in FLUENT	241
B.1 Overview.....	241
B.2 The Interface-tracking Approach.....	241
B.3 The Multiphase-flow Approach.....	242
Bibliography	247
List of Figures	255
List of Tables	263
Nomenclature	265
Acknowledgements	271
Curriculum Vitae	273

Chapter 1: INTRODUCTION

1.1 BACKGROUND

Cavitation is the phenomenon of phase change from liquid to vapor at almost constant temperature, caused by the effect of depressurization. Cavitation will occur in regions where the pressure is lower than a certain critical value (often close to the vapor pressure), and vapor cavities will collapse when they travel into regions with a high pressure.

In the late 19th century, an interesting phenomenon drew the attention of maritime engineers and researchers. This phenomenon caused the sailing speed to become lower for an increasing propeller rotation rate beyond a certain critical value. The importance of cavitation was first illustrated by S.W.Barnaby and C.A.Parsons in 1897 when studying the serious loss of propeller thrust and efficiency occurring on HMS Daring. Nowadays, cavitation phenomena have drawn the attention of researchers and developers in a large range of engineering fields. Cavitation plays an important role in the design and operation of propellers, torpedoes and hydrofoils, but also in pump impellers, spillways and hydroturbines in hydropower installations. Cavitation increasingly determines the design of fuel injectors. Cavitation also plays a role in biological and medical applications. These cavitation may cause damage to biological tissue because of its erosive action (e.g. in artificial heart valves) or where it is used in a beneficial way such in kidney stone removal. The avoidance of adverse effects due to cavitation becomes more and more prominent because of an increasing tendency towards high power densities and because of the demand for even higher efficiencies.

Generally, cavitation affects the hydraulic systems and components in undesirable ways. Cavitation erosion is one of the remarkable catastrophic consequences of cavitation phenomena. It may cause fluid contamination, leakage, blockage and undesired operation of the system. It may cause severe material damage leading to increased costly maintenance, and deterioration in performance together with aggravated vibration and noise. Turbines, bearings and pump impellers may need replacement after only a limited number of weeks

in operation or require a regular repair scheme. The assessment of the risk of cavitation erosion in propulsion systems and other hydraulic machinery needs due attention when complex cavitation dynamics are involved.

The prediction of cavitation phenomena and their adverse effects, such as cavitation erosion, in an early design stage imposes strict constraints on the optimization of propulsors and propulsor-aftbody configurations. If cavitation nuisance consisting of hull vibration and cavitation erosion is not predicted adequately, the value of the attainable efficiencies is highly uncertain. The issue of the reliability of cavitation erosion predictions already exists for quite some time. Several ITTC specialist committees on cavitation have addressed this question. It was stated by the 24th ITTC (2005) that “an accurate prediction of cavitation damage at full scale remains a very difficult task although significant progress in modeling the physics has been made. Many types of cavitation have the potential to cause damage, but only those flow conditions for which cavities collapse very near a material surface actually result in damage”. Bark et al. (2004a) observed that cavitation erosion could be generated by different types of cavitation, such as mixed glassy and cloudy root cavities, and propeller blade root cavities with complex dynamic behavior. The prediction of cavitation is, however, a persistent challenge for both researchers and designers due to the extreme complexity and daunting difficulties in experimental studies as well as numerical simulations.

In the last two decades, with powerful computers becoming available and an increasing need for a better understanding of the cavitation erosion process, more general computational fluid dynamics (CFD) approaches have been developed. Nowadays, it becomes possible to develop a practical methodology using contemporary CFD codes to assess the risk of cavitation erosion in an early design stage.

1.2 OBJECTIVE AND SCOPE

This work aims at an assessment of the cavitation erosion risk by using a multiphase RANS method in conjunction with post-processing procedures. Such a procedure is developed from detailed studies on the flow over hydrofoils, using contemporary RANS methods for unsteady flow simulations. The objectives are categorized as follows:

- To explore the capability of RANS methods for multiphase unsteady flow to predict the relevant and critical unsteady cavitation dynamics over the hydrofoils.
- To get a better understanding of the behavior of unsteady cavitation and the

physics that may lead to a high risk of cavitation erosion.

- To review and evaluate the current erosion risk assessment models that use CFD and experimental results as input, and from this to develop an improved methodology for the assessment of the cavitation erosion risk.

Cavitation is a complex vapor-liquid two phase flow including phase change, compressibility and viscous effects. Cavitation erosion is mainly caused by clouds of vapor bubbles collapsing very violently in the vicinity of solid surfaces. The difficulty in the prediction of the risk of cavitation erosion is emphasized with the important role of both large-scale vapor structures and clouds of microscale bubbles. It is suggested that an assessment of the risk of cavitation erosion could be achieved through flow simulations with the RANS method implemented in FLUENT, which is supposed to have the ability to reliably predict the dynamics of the large-scale vapor structures.

This thesis sets out to explore the answers for the questions raised above with the investigation of a NACA0015 hydrofoil at 6° and 8° angle of attack and a NACA0018-45 hydrofoil at 6.5° angle of attack. The computations are conducted with the homogenous multiphase mixture model that is implemented in FLUENT. The validation of the method will be achieved by comparison of results with peer reviewed work for the NACA0015 hydrofoil at 6° angle of attack from the VIRTUE WP4 Workshop (an EU sponsored R&D project), and experimental observations for the NACA0015 hydrofoil at 8° angle of attack and the NACA0018-45 hydrofoil at 6.5° angle of attack (Van Rijsbergen and Boorsma, 2011; Van Terwisga, 2009a). Paint erosion tests for the NACA0015 hydrofoil at 8° angle of attack (Van Rijsbergen and Boorsma, 2011) and the NACA0018-45 hydrofoil at 6.5° angle of attack are also available to evaluate the current assessment methods of cavitation erosion.

1.3 CONTENTS

Chapter 2 of this thesis addresses the physics of cavitation and cavitation erosion. The basic fundamentals of cavitation are briefly introduced. Then the basic hydrodynamic mechanisms that are believed to lead to cavitation erosion are addressed. A study of the different types of cavitation and its erosiveness will give the reader a basic understanding of the most erosive cavitation types. The physics of the unsteady dynamics that potentially lead to cavitation erosion are discussed by utilizing experimental results and results of numerical simulations. A hypothesis is finally formulated for the current study.

Chapter 3 gives a literature review of existing cavitation erosion models that model the characteristic phases in the physical process from cavity macro-structure to microbubble cloud collapse. Six models are evaluated for their suitability to fill the gap between the CFD results and the erosion risk assessment: Bark et al. (2004a), Fortes Patella et al. (2004), Dular et al. (2006), Kato et al. (1996), Wang and Brennen (1999) and Nohmi et al. (2008).

Chapter 4 introduces the numerical methods for cavitation based on a RANS method. The time-dependent Reynolds-Averaged Navier-Stokes (RANS) equations for the homogenous mixture flow are introduced, as well as some classical turbulence models used in FLUENT. The cavitation models accounting for the mass transfer between the liquid and the vapor phases will also be introduced. Finally, the convergence criteria applied in the current study are discussed, as well as the estimation of the errors and uncertainties based on the converged solutions.

The 2D wetted flow over two different NACA hydrofoils is investigated in Chapter 5. The investigation is conducted for a frequently-used 2D NACA0015 hydrofoil at an angle of attack of 6° . Further, two hydrofoils with available experimental data are simulated subsequently: one is again the 2D NACA0015 hydrofoil but at a different angle of attack, namely 8° , and the other is the NACA0018-45 hydrofoil at an angle of attack of 6.5° . Finally, guidelines and conclusions are given for the subsequent simulations of steady and unsteady cavitating flows.

Chapter 6 sets out to explore the answer to whether the RANS method implemented in FLUENT can successfully predict phenomena in the steady and unsteady cavitating flow within a required accuracy in a 2D computational domain. The 2D steady cavitating flow is investigated for a NACA0015 hydrofoil at an angle of attack of 6° ($\sigma = 1.6$). The 2D unsteady cavitating flow is investigated for a NACA0015 hydrofoil at an angle of attack of 6° ($\sigma = 1.0$) and 8° ($\sigma = 2.2$), and a NACA0018-45 hydrofoil at an angle of attack of 6.5° ($\sigma = 0.72$).

Chapter 7 further examines the capability of the RANS method implemented in FLUENT to predict the characteristics of three dimensional unsteady cavitating flows. The investigation will be conducted for the same two hydrofoils, the NACA0015 hydrofoil and the NACA0018-45 hydrofoil, but in a 3D computational domain. The numerical results will be compared with the observations made in the MARIN High Speed Cavitation Tunnel for both hydrofoils.

Chapter 8 explores the best possible criteria for an evaluation of the risk of cavitation erosion for the two hydrofoils considered. The instantaneous pressure, the variation of the local pressure and local vapor volume fraction in time, and the four time-averaged aggressiveness indices proposed by Nohmi et al. (2008) will be evaluated. The feasibility of a quantitative assessment of the risk of erosion by coupling the results from the RANS method to the bubble cloud collapse model of Wang and Brennen (1999) is studied in section 8.6. Finally, a new erosion intensity function is proposed and evaluated.

The conclusions and recommendations for further research are presented in Chapter 9.

Chapter 2: ON THE PHYSICS OF CAVITATION EROSION

2.1 OVERVIEW

This chapter is mainly on the physics of cavitation and cavitation erosion. The basic fundamentals of cavitation are introduced at first. Several basic concepts related to cavitation phenomena and the typical cavitation types will be presented. Then the basic hydrodynamic mechanisms that may generate cavitation erosion are introduced. The physics of the unsteady dynamics that potentially lead to cavitation erosion are discussed from the observations from experimental results and numerical simulations, respectively. Different types of cavitation and its erosiveness that are observed in extensive experiments will give you a first acquaintance of the most erosive cavity types (ITTC, 2005). Finally, a hypothesis is made for the current study.

2.2 FUNDAMENTALS OF CAVITATION

2.2.1 What is Cavitation?

Cavitation is the phenomenon of phase change from liquid to vapor at almost constant temperature, caused by the effect of depressurization. It occurs in regions where the pressure is lower than a certain critical pressure (often related to the vapor pressure). The curve in the P-T plane shown in Figure 2-1 separates the liquid phase and vapor phase: The vertical path at constant temperature represents the cavitation phenomenon, whereas the horizontal path at constant pressure represents the boiling phenomenon.

In most practical industrial cases, the critical pressure for the onset of cavitation is assumed to be approximately the vapor pressure. The vapor pressure at which vaporization occurs depends on the temperature, as shown in Figure 2-1. The cavitation inception can then simply be determined from the condition that the minimum pressure in the domain is lower than or equal to the vapor pressure:

$$p_{\min} \leq p_v \quad (2-1)$$

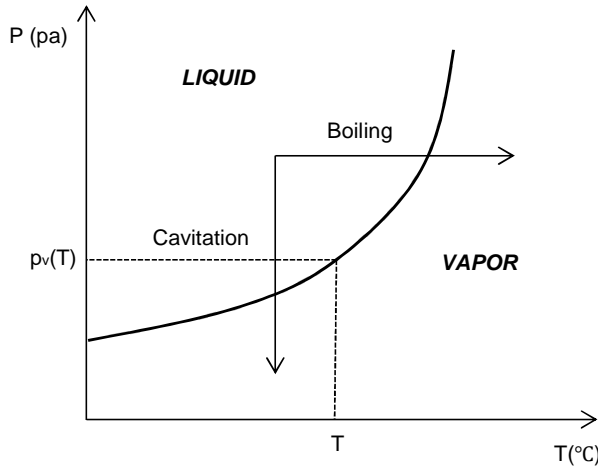


Figure 2-1: Schematic of the phase change from liquid to vapor

An important non-dimensional parameter for cavitating flow is usually denoted by σ , i.e. the cavitation number, and it can be defined as:

$$\sigma = \frac{p_{ref} - p_v}{\frac{1}{2} \rho_l U_{ref}^2} \tag{2-2}$$

where:

- p_{ref} is a reference pressure and p_v is the vapor pressure
- ρ_l is the liquid density
- U_{ref} is a reference velocity in the flow

2.2.2 Typical Cavitation Types

The development of cavitation in the liquid flow can take different patterns. Several typical types of cavitation have been classified according to their physical appearance, such as travelling bubble cavitation, sheet (attached) cavitation, vortex cavitation and cloud cavitation (Young, 1989; Lecoffre, 1999; Franc and Michel, 2004).

Travelling Bubble Cavitation

Cavitation bubbles are initiated from the weak points in the water, which are also called cavitation nuclei. These nuclei are often gas-filled microscopic crevices contained in the liquid, and are too small to be readily obvious. The travelling bubble cavitation develops as more or less isolated bubbles in the region of low pressure resulting from the rapid growth of these microbubble nuclei. These bubbles are carried along by the main flow and collapse

in the region of pressure recovery downstream, as shown in Figure 2-2.

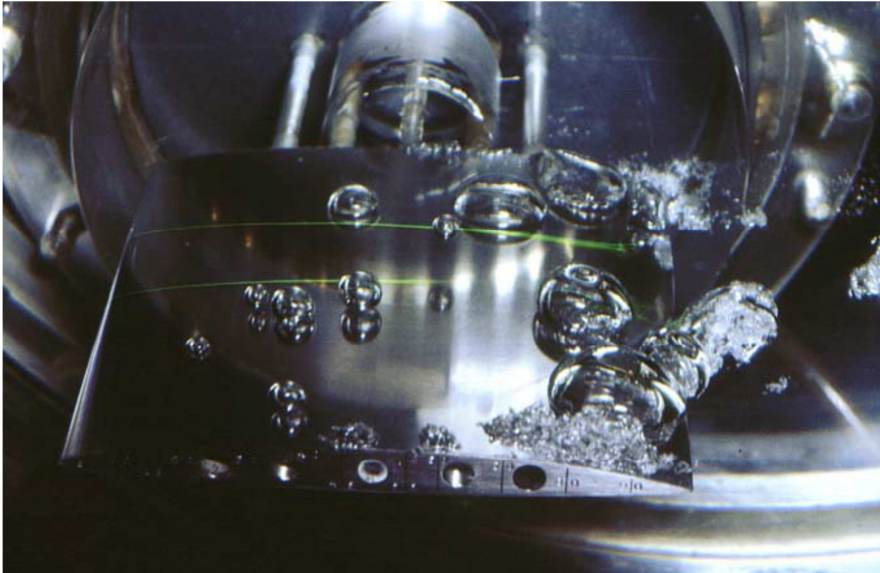


Figure 2-2: Typical visualization of travelling bubble cavitation over a hydrofoil in a cavitation tunnel (Franc, 2006)

Sheet Cavitation

Such cavitation appears in the form of a cavity attached to the leading edge of a body. The sheet cavitation shown in Figure 2-3 is a leading edge partial cavity since it partially covers the suction side of the hydrofoil. Sometimes a sheet cavity can reach the trailing edge of the foil and then fully covers the suction side of the hydrofoil, and then it is called a supercavity.

Vortex Cavitation

This kind of cavitation develops at the vortex core with lower pressure than the vapor pressure. It often can be observed at the blade tips, which is called tip vortex cavitation, and sometimes at the tip of the hub of the propellers, which is called hub vortex cavitation, as shown in Figure 2-4. The tip vortex cavitation is often first observed some distance behind the blade tips (unattached) and becomes attached when the vortex becomes stronger. The hub vortex cavitation is formed from the combined vortices shed by the blade root since the converging boss cap increases the susceptibility to cavitate. Such cavitation may generate damages on either the blades or the rudders, and propeller boss cap fins could alleviate this problem.

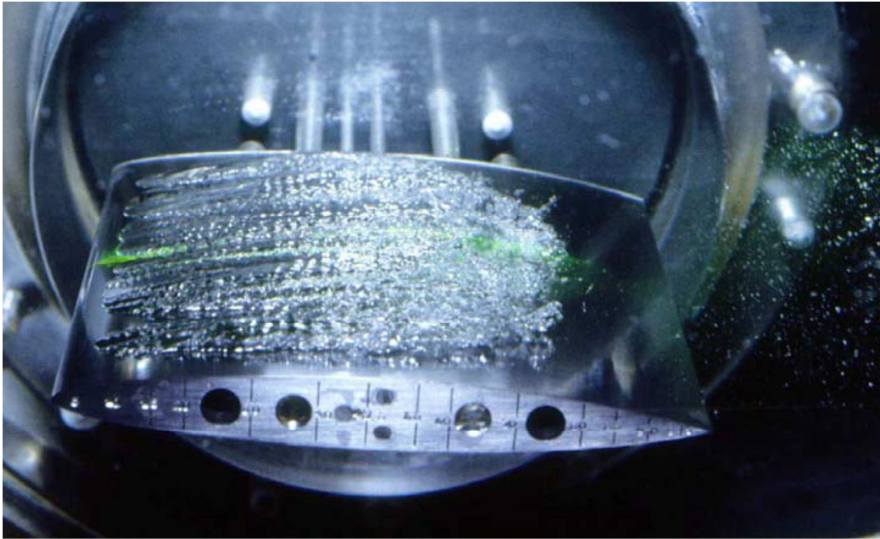


Figure 2-3: Typical visualization of a leading edge sheet cavity over a hydrofoil in a cavitation tunnel (Franc, 2006)

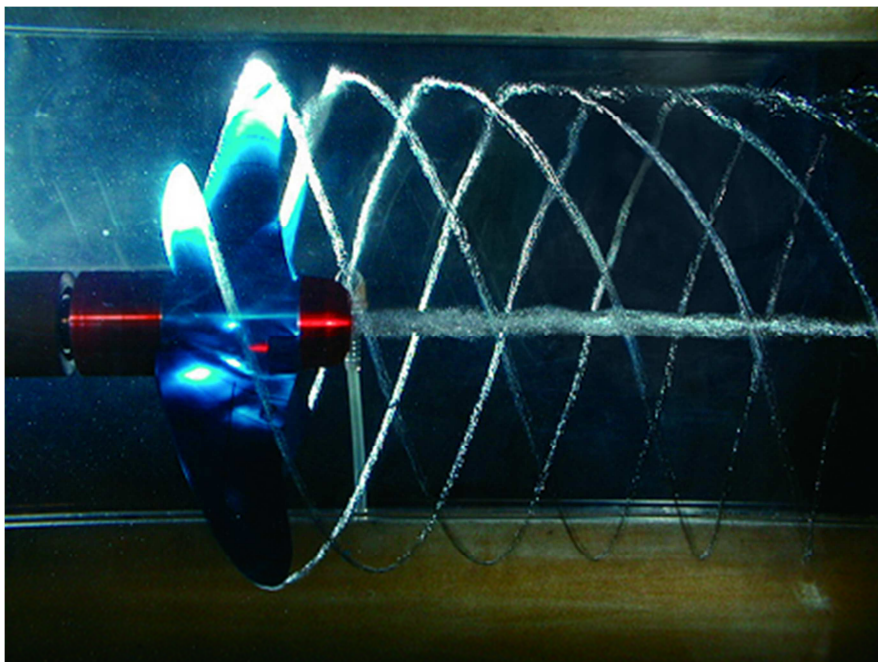


Figure 2-4: Typical visualization of tip and hub vortex cavitation on a propeller (Nakashima Propeller Product Lineups)

Cloud Cavitation

Cloud cavitation is normally observed to be shed from an unsteady partial sheet cavity due

to a re-entrant jet that develops in the closure region and travels towards the leading edge of the body. This kind of cavitation appears as a cloud of many small bubbles or vortices, as shown in Figure 2-5. Such cloud cavitation is carried along by the main flow downstream to the regions of higher pressure, causing a sudden condensation. If condensation, namely collapse, occurs in the vicinity of the body surface, this may give rise to high impacts and finally cause damage on the material surface.

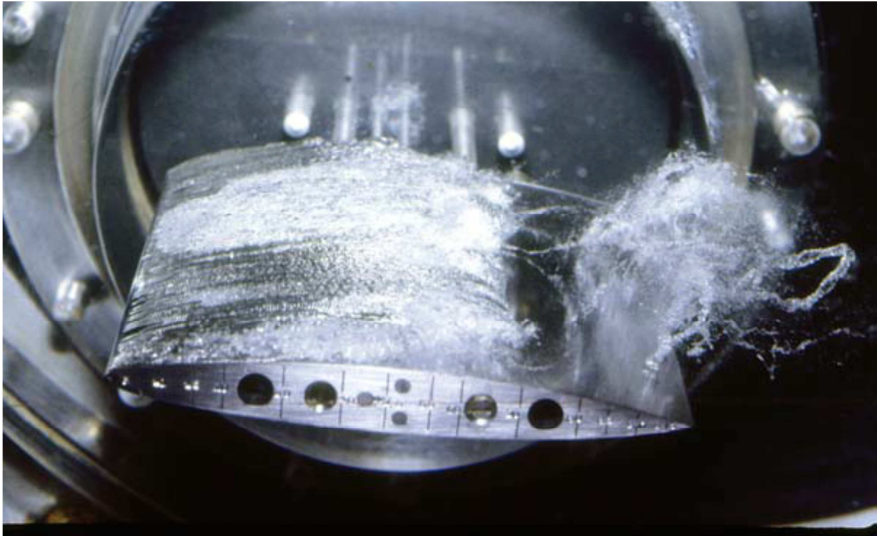


Figure 2-5: Typical visualization of the shed of a cloud cavitation from a partial sheet cavity over a hydrofoil in a cavitation tunnel (Franc, 2006)

2.2.3 Effects due to Cavitation

Generally, cavitation affects the hydraulic systems and components in undesirable ways. The cavitation nuisance that often happens in propulsion systems can be classified as follows:

- Deterioration in performance: It happens when higher loaded applications are involved. Partial cavitation on a propeller blade will not immediately reduce the propeller performance. Both the thrust and torque will be reduced when 20-25% or more of the blade is covered by cavitation (Sampson, 2010).
- Cavitation noise: It may be generated by various types of cavitation. Either sudden collapses of bubble cavitation or vortex cavitation or the periodic fluctuation of the cavity volumes could generate cavitation noise. This problem is important in military applications but is becoming increasingly important for civil shipping.
- Cavitation induced vibrations: The vibrations are often caused by the strong pressure fluctuations due to the dynamical behavior of the cavitation.

- Cavitation erosion: This phenomenon often (but not always) occurs when the cavities collapse in the vicinity of the blade surface. When erosion occurs, other forms of cavitation hindrance are often present too.

Cavitation erosion is one of the striking catastrophic consequences of cavitation phenomena. It may cause severe material damage leading to increased costly maintenance, and deterioration in performance together with aggravated vibration and noise. Turbines, bearing and pump impellers may need replacement after several weeks or require a regular repair. The basic hydrodynamic mechanisms for cavitation erosion will be introduced in the next section.

2.3 BASIC HYDRODYNAMIC MECHANISMS

The notion that the aggressiveness of cavitation could be assessed through a consideration of energy conversion was already acknowledged by Hammitt (1963). He postulated that cavitation damage occurred once the potential energy contained in a shed cavity (E_c) exceeded a certain damage threshold E_s . This threshold would essentially be a function of the material properties of the surface on which the erosive action takes place, and not of the type of cavitation.

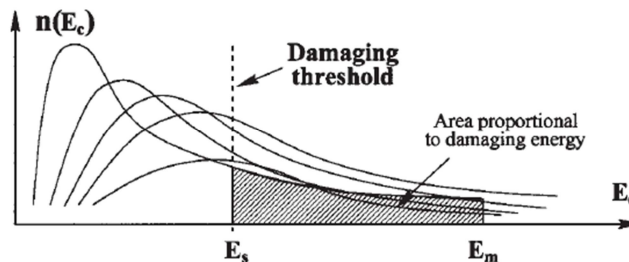


Figure 2-6: Energy spectra and their relation to cavitation erosion (Hammitt, 1963)

From energy considerations, one can see that potential energy contained in a macro cavity is converted into the radiation of acoustic pressure waves, through the conversion of potential energy into kinetic energy during the collapse phase of the macro-scale cavity. This energy cascade was already identified by Fortes-Patella et al. (2004). Thereby, the collapse of cavitation in the vicinity of a surface could cause severe erosion due to the conversion of concentrated kinetic energy into among others acoustic energy in the form of high-amplitude pressure waves.

Bark et al. (2004b) also described the way how cavitation leads to cavitation erosion from energy considerations: “The concentration or focusing as it is called here, of collapse energy density is most obvious for the spherical collapse with its converging flow. Due to this, the kinetic energy density (the kinetic energy per volume of the liquid) will have a maximum at the cavity interface and this maximum will increase as the collapse proceeds. This is clear already from the solution of the Rayleigh-Plesset equation describing this collapse motion. The concept of generalized focusing considers also focusing of energy density for collapses of groups and sequences of cavities.” The accumulated kinetic energy is then converted into acoustic energy in the cavity collapse, associated with the shock waves that are radiated by the final collapse.

Tukker and Kuiper (2004) presented three key factors that determine whether the cavity collapse is sufficiently aggressive to lead to erosion:

- It should occur sufficiently close to the solid surface,
- The velocity of collapse should be sufficiently high, and
- The area over which the collapse occurs is small.

Franc and Michel (2004) also claimed that the energy concentration may be “all characterized by the high values of the impact load they produce, the small area of the impacted surface and the short duration of the impulse”.

Four distinctive hydrodynamic phenomena leading to energy concentration with high erosive potential are reviewed by Franc and Michel (2004) as:

- Collapse and rebound of a spherical bubble: Fujikawa and Akamatsu (1980) showed that “the end of the collapse of a spherical bubble is marked by high values of the internal temperature and pressure, and is followed by the emission of a pressure wave of high intensity.” The pressure amplitude is measured to be of the order of 100 MP, approximately 1000 times atmospheric pressure, and the duration of the shock wave associated with a single bubble collapse is of the order of one microsecond, as shown in Table 2-1.
- Microjet: “A microjet is produced when a bubble collapses under non-symmetrical conditions. If a solid wall is close enough to the solid surface, the microjet is directed towards the wall.” The pressure amplitude is estimated from the pressure rises found in a water hammer associated with a high-speed microjet ($U_j \sim 100$ m/s), to give a value of the order of 150 MPa, close to the measured pressure amplitude for the spherical bubble. The duration of the pressure pulse

related to a 1mm bubble has a very small value, around $0.03 \mu s$.

- **Collective collapse:** Such collective collapse of a cloud cavity is “typically characterized by cascades of implosions. The pressure wave emitted by the collapse and rebound of a particular bubble tends to enhance the collapse velocities of the neighboring bubbles, thus increasing the amplitude of their respective pressure waves.” Multiscale phenomena are involved: the dynamics of the macro-scale cloud and the dynamics of the microscale bubbles. The pressure amplitude and the duration of the collapse of the macroscale cloud are supposed to be considerably increased since a focusing of energy from the peripheral microscale bubbles to the innermost microscale bubbles both in space and time occurs, enhancing the erosive potential.
- **Cavitating vortices:** Cavitating vortices “appear to be responsible for severe erosion in fluid machinery, as described by Oba (1994). Two main features seem to be at the origin of the high erosive potential: the formation of a foamy cloud at the end of the axial collapse in which cascade mechanisms can occur and the rather long duration of the loading time, which is typically several tens of microseconds.”

An overview of the type, amplitude and duration of the four different loading mechanisms is summarized in Table 2-1 (Franc and Michel, 2004). It can then be concluded that the shock wave and the microjet are the basic hydrodynamic mechanisms for the high erosive potential. The most typical feature related to the aggressiveness is the cascade of energy both in space and time either during the collapse of a bubble cloud or the collapse of cavitating vortices. This will be further argued in the following on the observations from experimental results and the numerical simulations.

Table 2-1: Review of impact loadings for different cavity phenomena (Franc and Michel, 2004)

Mechanism	Type of loading	Amplitude (Mpa)	Duration(μs)
Single bubble collapse	pressure wave	100	1
Micro jet (from a 1mm bubble)	impacting jet	150	0.03
Collective bubble cloud collapse	pressure waves	$\gg 100$	$\gg 1$
Cavitating vortices	impacting jet	>100	> 10

2.4 PHYSICS FROM EXPERIMENTAL OBSERVATIONS

The collapse mechanism of cloudy cavities that is normally shed from the partial sheet cavity and cavitating cavities will be discussed in this section with references to existing experiments.

2.4.1 Cloud Cavitation Collapse

A number of experiments on foils and propellers certainly confirm that a crucial phase in the process leading to cavitation erosion is the break-up of the macro sheet cavity into cloudy cavities, which are supposed to consist not only of microbubbles but also of cavitating vortices (Reisman et al., 1998; Foeth et al., 2008; Bark et al., 2004a; Boorsma, 2010).

Reisman et al. (1998) proposed a new view on the local pressure pulses generated by the localized bubbly shock waves propagating within the bubbly cloud cavity, as shown in Figure 2-7. It is suggested by Reisman et al. (1998) that “the formation, focusing and propagation of bubbly shock waves”, due to either local or global vapor structures, “play a critical role in generating the pressure pulses which lead to cavitation noise and damage.”

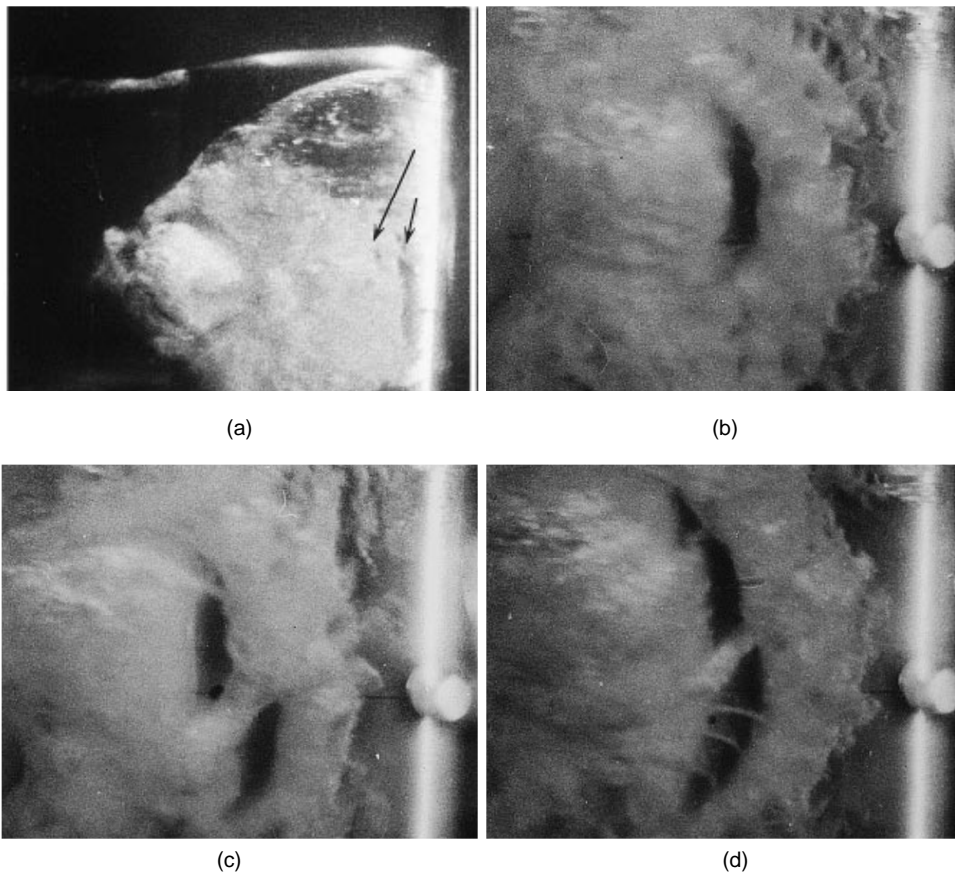


Figure 2-7: Global view, indicated by black arrows seen in (a), and close-up view, seen in (b) (c) and (d) of the local pulse structures in the cavitation on the suction surface of the NACA0021 hydrofoil (flow from right to left) (Reisman et al., 1998)

By studying the images with sufficient resolution as recorded by the high-speed camera during the break-up shedding cycle, Foeth et al. (2008) have shown that cloud cavitation is essentially an organized mixture of cavitating vortices. A detailed view of the shed cloud cavitation is displayed in Figure 2-8, clearly showing the primary span-wise and secondary stream-wise cavitating vortices (indicated by the white arrows). The stream-wise cavitating vortices that generate perturbations near the primary span-wise vortices are stretched around the periphery of these primary vortices which is accompanied by an increase of their vapor cores (Van Terwisga et al., 2009b).

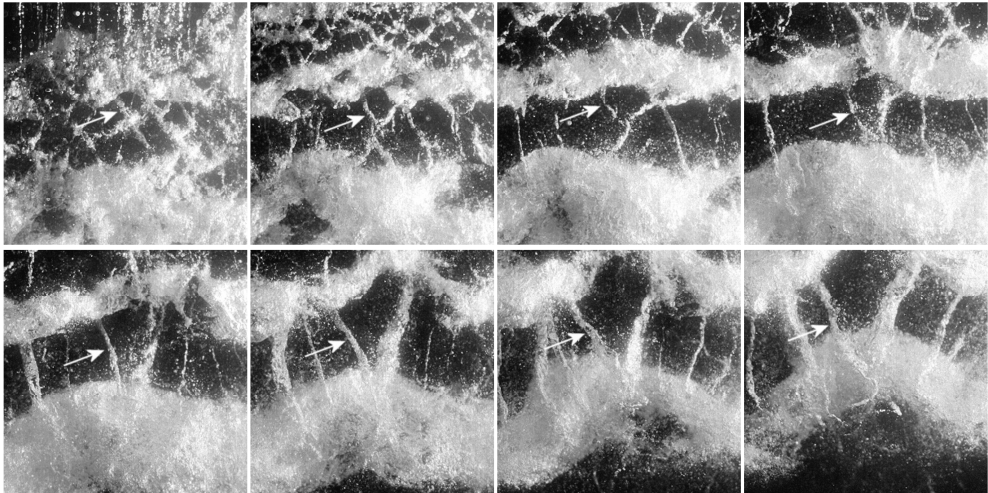


Figure 2-8: Close-up view of the cloudy structures that is shed from the leading edge (flow from top to bottom) over a twisted hydrofoil (Foeth et al., 2008)

The large-scale primary span-wise vapor structures develop into horse-shoe shaped cloudy structures consisting of one cavitating vortex surrounded by many microbubbles (Pereira et al., 1998; Kawanami et al., 2002). The cavity seems to get attracted toward the foil surface possibly by vortex stretching of the legs in the viscous boundary layer over the foil. Next the horse-shoe cavity is split at the head, and the remaining two legs of the horse-shoe cavity focus due to the vorticity concentration and collapse toward the foil surface, potentially causing local cavitation erosion (Kawanami et al., 2002).

It can be concluded from the above experimental observations that it is the cascade of the energy emitted by the collapses of the remaining bubbles associated with the development of the primary span-wise cloud cavitation that leads to the final damage on the solid surface.

2.4.2 Cavitating Vortices Collapse

The typical cavitation erosion due to the collapse of the cavitating vortices is often observed on a rudder/propeller configuration because the rudder is subject to the periodic impact of the propeller tip vortex.

Van Terwisga et al. (2009b) presented that “erosion by cavitating vortices only occurs when they become unstable, and break up into ring vortices around the primary vortex that develop into horseshoe vortices once they get attached to the surface.” A detailed observation of the breaking up of a cavitating vortex is illustrated in Figure 2-9. The aggressiveness of these cavitating vortices collapses was said to be dependent on the potential energy contained in the ring vortex and the effectiveness of focusing of this energy (Van Terwisga et al., 2009b).



Figure 2-9: Visualization of the breaking up tip vortex cavitation (Friesch, 2006)

However, Kuiper (2001) observed that not all cases of rudder erosion are associated with the break-up of the propeller tip vortex, “it seems that a solid cavitating tip vortex core can also erode the rudder”. The propeller tip vortex wraps around the leading edge of the rudder when it hits the rudder, and collapses on the rudder surface to generate high impacts. A

detailed observation of the vortex-rudder interaction on a cruise vessel conducted by Fitzsimmons et al. (2007) is shown in Figure 2-10, revealing the development of the propeller tip vortex that is wrapped around the rudder leading edge (Boorsma and Whitworth, 2011):

- The propeller tip vortex is wrapped around the rudder leading edge, and a secondary cavitating vortex originates above the primary vortex (Figure 2-10-(a));
- The cavitating vortices interact with the rudder flow and then disintegrate on the rudder surface, where erosion can be observed (Figure 2-10-(b)(c));
- The remaining vapor structures further downstream may lead to repeated implosions as the cavity rebounds (Figure 2-10-(d)).

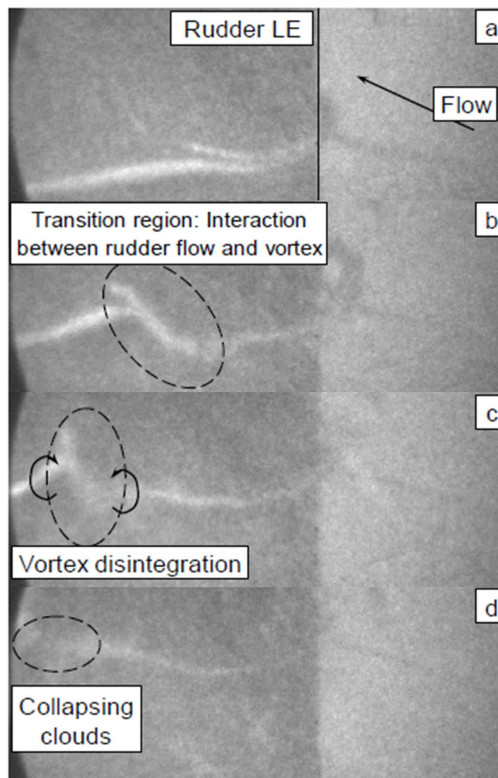


Figure 2-10: Visualization (Fitzsimmons et al., 2007) of the development of the propeller tip vortex on the rudder surface from Boorsma and Whitworth (2011)

2.5 PHYSICS FROM NUMERICAL SIMULATIONS

The multiscale energy cascade involved in the collapse processes, transforming the potential energy contained in large-scale structures into erosive energy contained in clouds

of microbubbles, imposes special difficulties on the numerical simulations of the collapse behavior of the cloudy cavitation and cavitating vortices.

2.5.1 Cloud Cavitation Collapse

Numerous numerical simulations are conducted on hydrofoils or propellers to get a better understanding of the collapse of the cloudy cavity originated from the break-up of the sheet cavity, either through RANS methods limited to only the large-scale resolution or through LES or DES method with higher resolution resolving also small-scale structures.

Schmidt et al. (2007) found that two kinds of collapse were related to the high static pressure peaks during the shedding cycle for the flow over a 3D twist hydrofoil:

- Collapse of a “crescent-shaped” cloudy cavity: Cavitation erosion due to such collapse is generated through a focusing of energy released from the vapor structures contained in this cloud, confirming the observations from experiments (Figure 2-11-Point B).
- Collapse of “leading-edge” vapor structures: Cavitation erosion due to this kind of collapse is possibly associated with the collapses of the secondary cavitating vortices (Figure 2-11-Point A).

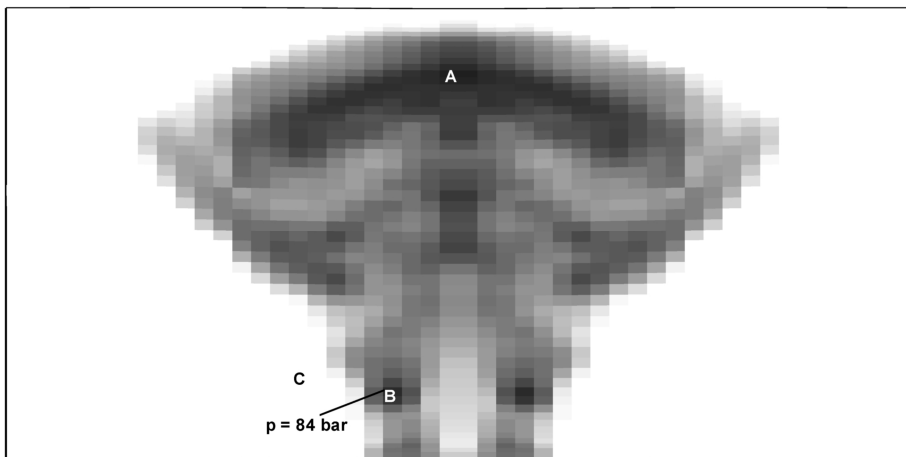


Figure 2-11: Maximum static pressure recorded during cycle 1 for the flow over a 3D twist hydrofoil (Schmidt et al., 2007)

2.5.2 Cavitating Vortices Collapse

Few efforts are devoted to the investigation on the erosion risk by a collapse of the cavitating vortices due to high demands on resolution both in space and in time.

Hasuike et al. (2009) predicted tip vortex cavitation and sheet cavitation on the propeller by a RANS method, which are found to qualitatively agree with the experimental results. He adopted several simple indices (Nohmi et al., 2008), which will be introduced and evaluated later, to predict possible locations that are exposed to high impacts. The results obtained from one of these indices agree well with the model tests, and it is suggested that the rapid shrinking of the propeller tip vortex leads to high impacts around the leading edge at the tip of the propellers.

2.6 HYPOTHESIS

With regard to the objectives of this thesis, our attention is focused on the unsteady cavitating flow over a hydrofoil, which is normally characterized by the collapse of a horse-shoe shaped cloudy cavity and possibly also the collapse of secondary stream-wise cavitating vortices.

Based on the previous observations from existing experimental results and numerical simulations, it is summarized here that erosive cavitation is always associated with the collapse of vapor structures in the vicinity of the solid surface. The focusing of energy that is converted from the potential energy contained in the bubbly cloud into the emitted acoustic power upon collapse is enhanced, due to the synchronized collapse of multiple microbubbles, both in space and in time.

Chapter 3: LITERATURE REVIEW OF EXISTING CAVITATION EROSION MODELS

3.1 OVERVIEW

Cavitation erosion, the removal of material from a solid surface by the erosive action of cavitation, is primarily generated by an accumulation of energy released by collapsing cavities in the vicinity of a solid surface. The erosion may be so aggressive as to result in severe damage on propeller blades, rudders or other appendages, and may also be accompanied by excessive vibrations and a significant loss of performance. Therefore the prediction of cavitation erosion should be an important issue during the early design stage of ship propulsion systems and other hydraulic machinery.

Among all adverse effects of cavitation, the phenomenon of cavitation erosion is very complex since it involves multiple scale hydrodynamic processes combined with the response of a solid material which is exposed to the cavitating flow. Predicting the cavitation aggressiveness quantitatively and predicting the most probable location of cavitation erosion are complex problems that currently still motivate an important amount of basic and applied research in the fields of hydrodynamics, mechanical science and metallurgy. From an industrial point of view concerning both design and maintenance, the evaluation of the erosive power of cavitating flows and the prediction of the material damage remains a major concern to manufacturers and users.

A wide range of studies that deal with problems ranging from bubble dynamics to material testing have been made all aiming toward a deeper understanding of these phenomena. Recently, there were many attempts to predict the magnitude of cavitation erosion, with the aid of visual observation and CFD tools. Although much is known about the individual bubble dynamics and material reaction, no reliable theoretical prediction methods for cavitation erosion, which involve all relevant physics of cavitation erosion, have so far successfully been made. It is still a big challenge to numerically predict the risk of cavitation erosion without the support of model tests.

In this chapter, a brief review is given of six cavitation erosion models that in some way model the characteristic phases in the physical process: From the cavity macro-structure to the microbubble cloud collapse. These cavitation models are evaluated with respect to their suitability to assess the risk of cavitation erosion by using the results from a RANS method.

The following six cavitation erosion models will be discussed here:

- Bark et al. (2004a)
- Fortes Patella et al. (2004)
- Dular et al. (2006)
- Kato et al. (1996)
- Wang and Brennen (1999)
- Nohmi et al. (2008)

3.2 MODEL BY BARK ET AL. (2004A)

The main aim of the work within the European Project EROCAV was to develop a practical tool for the assessment of the risk of erosion on ship propellers and rudders in an early design stage. The observation handbook (Bark et al., 2004a) gives a good insight into the complete hydrodynamic process from the early and global development of the erosive cavity to the focused cavity collapse and possible rebound.

The model is built on the notion that erosion is primarily the result of an accumulation of energy transferring from macro scale cavities to collapsing cavities close to a solid surface. The core of the model consists of a number of definitions. A conceptual model is constituted to sharpen the visual interpretation of observations of cavitation process by high-speed video, and a systematic nomenclature is proposed to describe and classify the cavitation behavior with respect to focusing and the generation of erosion.

3.2.1 Phenomenological Description

The small cavities that result from the focusing cavity are assumed to cause the pitting in the material. They may be considered approximately spherical at the start of the collapse, but later, if close enough to the body surface, develop a high speed microjet hitting the solid. This jet, as well as the local pressure wave generated during the collapse, can contribute to the deformation and fatigue of the solid material. It is assumed that either the microjet or the pressure wave alone can be the dominating mechanism, depending on actual conditions. “The most violent collapse of the cavities is associated with the collective collapse of cloud cavitation. This collective behavior consists of a cascading energy transfer from the

collapse of the peripheral bubbles to the innermost bubbles whereby the collapse energy is focused into a small volume” (Bark et al., 2004a).

Following the idea of an energy cascade model, following a phenomenological description of the successive procedures of the erosive process is proposed as follows:

- The creation of a transient, usually travelling, cavity from the global cavity on a propeller blade or similar.
- The main focusing collapse. This is the early collapse motion of the transient cavity that can be observed by the selected recording technique.
- The micro focusing collapse. This is the last part of the collapse, not resolved in detail by high-speed recordings.
- The rebound.

3.2.2 Guidelines for Observation and Analysis

Bark et al. (2004a) provide guidelines to assess the erosiveness from visual observations. They first search for violent rebounds and estimate its violence. They then advise to attempt to backtrack the cavity to its origin. Alternatively they suggest to directly detect focusing cavities from the global cavity structure. An assessment of the vapor content should be made, where Bark et al. define the quality of a cavity in terms of “glassy”, “cloudy” or “mixed”. The first qualification refers to a close to 100% vapor fraction cavity, the latter two to significantly smaller vapor fractions. Information on the focusing efficiency can also be obtained from:

- The amount of disintegration
- The acceleration of the collapse motion
- The shape and symmetry of the collapse motion
- The cyclic behavior of the focusing in relation to forced oscillations, e.g. through the propeller shaft rate.

All the listed points concern mainly the focusing cavity from its early development toward the rebound, the latter event being used as an indicator of a violent collapse. No detailed observation of the micro focusing process is requested, which is identified as a topic for further investigation.

3.2.3 Relevance

The proposed erosion assessment model can easily be applied on rather large-scale cavities, at a scale which can be predicted by contemporary RANS methods. However, in cases

where the erosive cavities are small in size and form part of a complex cavity behavior, application of this model becomes more difficult. It is noted by the authors that in an experimental assessment, the time and costs needed to make useful high-speed video recordings are more limiting than the visual analysis itself. In addition, due to scale effects or lack of experience, it may also happen that the risk of erosion is over-estimated or underestimated. A combination of the visual method and paint tests is therefore recommended by the authors, possibly supplemented also by noise measurements in the high frequency range.

3.3 MODEL BY FORTES-PATELLA ET AL. (2004)

Fortes-Patella et al. (2004) proposed a physical scenario to describe the mechanism of cavitation erosion (see Figure 3-1). Similar to the model by Bark et al. (2004a), this cavitation erosion model is based on the concept of the energy cascade, in which the potential power related to the macro cavities is converted into acoustic power produced by collapsing clouds of microbubbles. It is thereby suggested that pressure waves emitted during the collapses of vapor structures are the main source contributing to the cavitation erosion. The emission of the pressure wave can be generated by spherical bubble or vortex collapses as well as by microjet formation. The emitted pressure waves interact with neighboring solid surfaces, leading to material damage. The development of macro cavities, which was taken as input in this model, can either be observed from experiments or calculated using various CFD multiphase methods. Finally, the volume damage rate can be calculated as output from this model.

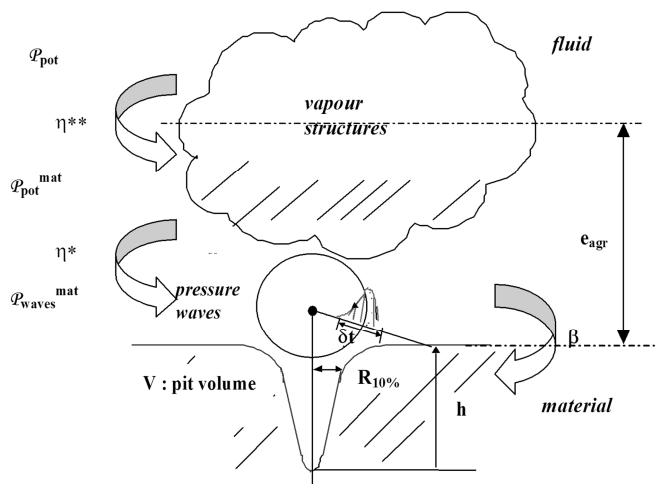


Figure 3-1: Scheme of the physical scenario based on an energy balance

3.3.1 Energy Approach

This model shows us how to evaluate the energy transfer between the cavitating flow and the material which is damaged. It is based on the following phases:

- The collapses of the vapor structures of the cavitating flow
- The emission and the propagation of the pressure wave during the collapse of vapor structures of the cavitating flow (Challier et al., 2000)
- The interaction between the pressure waves and the neighboring solid surface (Fortes-Patella et al., 2001)
- The damage of the material exposed to the pressure wave impacts (Fortes-Patella and Reboud, 1998)

Instantaneous Potential Power

The instantaneous potential power of the cavitating flow can be derived from a consideration of the macroscopic cavity structure. It is defined by:

$$P_{pot} = \Delta p \left(\frac{dV_v}{dt} \right) \quad (5-1)$$

where $\Delta p = p_\infty - p_v$, p_∞ is the surrounding pressure, p_v is the vapor pressure and V_v is the volume of the vapor structures at given time t .

Flow Aggressiveness Potential Power

The flow aggressiveness potential power, derived from the potential power that relates to the erosive aggressiveness before the occurrence of collapse, was given by:

$$P_{pot}^{mat} = \eta^{**} P_{pot} \quad (5-2)$$

where the energy transfer efficiency η^{**} is a function of the hydrodynamic characteristics (U_{ref} and σ) of the main flow and the distance between the collapse center and the material surface. The quantity U_{ref} is the reference velocity of the flow, and σ is the cavitation number. This Flow aggressiveness power is influenced by the type, unsteadiness and geometry of the cavitating flow, such as the angle of attack and the shape of the leading edge for a hydrofoil.

It is noted here however, that according to the definition of the potential power P_{pot} , information about the development of cavitation, which can be related to the flow hydrodynamics and the type and geometry of the cavitating flow is already accounted for. Consequently, the most relevant influence factor appears to be the distance between the collapse center and the material surface.

Pressure Wave Power

The pressure wave power applied to the material during the vapor bubble collapse is defined by:

$$P_{waves}^{mat} = \eta^* P_{pot}^{mat} \quad (5-3)$$

where the efficiency η^* is suggested to be determined by the collapses of spherical bubbles of vapor and gas. It depends mainly on the change in the surrounding pressure p_∞ relative to the pressure at the first generation of cavitation for which the potential power is determined, and the air content in the flow.

Volume Damage Rate

The volume damage rate V_d was measured by a 3D laser profilometer and was related to the flow aggressiveness, referred to as $P_{pot}^{mat} / \Delta S$, by the formula:

$$V_d = \frac{\eta^* P_{pot}^{mat}}{\beta^* \Delta S} = \frac{P_{waves}^{mat}}{\beta^* \Delta S} \quad (5-4)$$

where ΔS is the analyzed sample surface, and β^* is a mechanical transfer function depending strongly on the characteristics of the material.

3.3.2 Relevance

An advantage of this model is that it follows the description of the physical energy transfer processes. The reliability of this model depends directly on the assessment of the two efficiencies involved in the energy conversion. However, details on the determination of these efficiencies have not been found in the open literature. The applicability of this model for interpretation of CFD results depends therefore on the reliability of the assessment of these energy transfer ratios. The effectiveness of the focusing process should be represented by these transfer ratios.

3.4 MODEL BY DULAR ET AL. (2006)

Dular et al. (2006) suggested a model for the cavitation erosion process based on the damage caused when a bubble collapses in the vicinity of a solid surface. These single bubbles are supposed to be excited by the shock wave that is emitted from the collapse of a cavitation cloud. The cavitation erosion model is based on partly theoretical, partly empirical considerations, which are derived from knowledge that was gained during earlier studies of different authors. An obvious correlation between the cavitation structures and

cavitation erosion was found through experimental investigations and statistical calculations. Perhaps the most important assumption in the assessment of erosion risk is that the value of the standard deviation of gray level for each position correlates with the magnitude and distribution of damage caused by the cavitation erosion.

3.4.1 Cavitation Erosion Process

The cavitation erosion process is broken down into four different phases, ultimately leading to pit formation (see Figure 3-2):

- Collapse of the cavitation cloud causes a shock wave that radiates into the fluid.
- The magnitude of the shock wave is attenuated as it travels toward the solid surface.
- Single bubbles present near the solid surface begin to oscillate and a microjet phenomenon will occur if the bubble is close enough to the wall.
- The damage (single pit) is caused by a high velocity liquid jet impacting the solid surface.

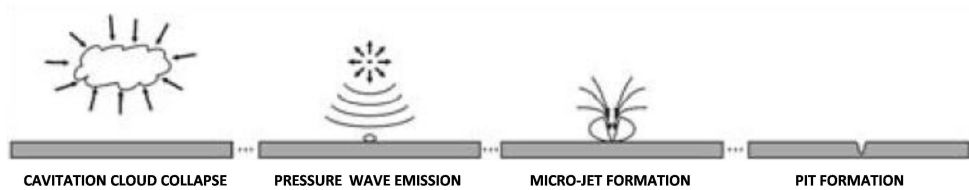


Figure 3-2: Cavitation erosion model by Dular et al. (2006)

The power and consequently the magnitude of the emitted pressure wave are closely related to the velocity of the change of the vapor cloud volume (velocity of cavitation cloud collapse) and to the surrounding pressure. This power term corresponds to the instantaneous potential power P_{pot} defined in the model by Fortes-Patella et al. (2004). It can be written as the following relation:

$$P_{wave} = \Delta p \left(\frac{dV_v}{dt} \right) \quad (5-5)$$

where Δp is the pressure difference between the surrounding pressure p_{sur} and the vapor pressure p_v , and dV_v / dt is the change of the vapor cloud volume in time t .

From acoustical theory, it follows that the amplitude of the emitted pressure wave is proportional to the square root of the acoustic power ($p_{emit} \propto \sqrt{P_{wave}}$). Dular et al. consider the pressure difference Δp in the potential power to remain approximately constant during

the process, so that the distribution of the mean change in cavitation cloud volume on the hydrofoil reveals the mean distribution of amplitude of the pressure wave that is emitted by the cavitation cloud collapse.

A hypothesis that the standard deviation of the gray level is related to the dynamics of cavitation was made on the basis of previous studies by Dular et al. Based on this hypothesis, they substitute the instantaneous change of the cavitation cloud volume by the standard deviation of the gray level in the experimental observations, which is then related to the power of the emitted pressure wave. “Standard deviation can be used in this manner since it is a function of the change of the gray level in the image, which is a function of the cavitation cloud volume: $gray\ level = f(V_v) \Rightarrow s \propto dV_v / dt$.”

3.4.2 Relevance

It is interesting to note that the physical process assumed to be responsible for cavitation erosion by Dular et al. is the reverse of the physical process hypothesized in Chapter 2, where in the latter one initial implosion synchronizes the implosion of a bubble cloud.

Another comment on this model is that the erosion aggressiveness is based on the notion that the damage is caused by the impingement of the microjet associated with the implosion of the individual bubbles, whereas in the hypothesized model (see section 2.6), it is argued that the acoustic power that is released from this mechanism is significantly smaller than the acoustic power released from the synchronized bubble cloud collapse.

A third comment refers to the use of the standard deviation of pixels as a measure for the time rate of change of the vapor volume. Based on digital post-processing of high speed video observations, it is our experience that high standard deviations in the gray value at one position do not necessarily refer to the time rate of change of the cavity volume, but may also refer to e.g. the size of the bubbles contained in a transient cavity.

3.5 MODEL BY KATO ET AL. (1996)

A scenario for quantitative prediction of cavitation erosion was proposed by Kato et al. (1996). The prediction follows six phases of cavity development, where it is assumed that the shock wave caused by the collapse of bubbles separated from the sheet cavity is the primary mechanism for erosion. The following characteristic parameters in the process are assessed:

- Stage 1: Cavity type and extent
- Stage 2: Cavity generation rate
- Stage 3: Number and size distribution of cavity bubbles
- Stage 4: Characteristics of collapsing bubbles
- Stage 5: Impact force/pressure distribution on solid wall due to cavity bubble collapse
- Stage 6: Amount of erosion caused by successive impact forces

In this paper, the research is focused on the stages 2 to 5. It is pointed out that the key value during the whole process is the estimation of impact force distribution or pressure spectrum on a solid surface caused by cavitation bubble collapse. These quantities can be measured and correlated directly with the pit distribution or be estimated through fluid dynamic analysis. The examined case is conducted on a partially cavitating hydrofoil, and it is supposed to be applied as a method of predicting cavitation erosion without a model test.

3.5.1 Cavitation Erosion Process

Cavity Generation Rate

The cavity generation rate was derived from measurement of the air flow rate of a ventilated cavity, with the assumption that the flow rate necessary to maintain a certain length of the cavity should be same as for a vapor cavity and a ventilated cavity (Brennen, 1969; Billet and Weir, 1975). An empirical formula is derived to calculate the non-dimensional flow rate:

$$C_{Qc} = \frac{Q}{U_{\infty} BC} = \frac{1.82 \times 10^{-6}}{1.14 \times 10^{-4} + (\sigma / (AoA - AoA_0))^5} \quad (3-1)$$

where:

- Q is ventilated flow rate (m^3 / s)
- U_{∞} is the main flow velocity
- B and C are the breadth and chord length of the examined foil
- σ is the cavitation number
- AoA is the angle of attack, and AoA_0 is the zero lift angle

It is assumed that the equation (3-1) is generally valid for a cavitating foil and could be used to estimate the cavity generation rate. It is also discussed in the paper that the behavior of ventilated cavitation is surprisingly similar to that of natural cavitation including the shedding of cloud cavitation.

Number and Size Distribution of Cavity Bubbles

It is difficult to measure the number and size distribution of cavity bubbles, as their size changes rapidly. However, the number and size distributions of cavity bubbles can be estimated from a measurement of the air bubble distribution downstream of the cavity collapse region, because the air bubbles downstream are “remains” of the cavity bubbles and their distribution should thus be similar, as shown in Figure 3-3. Diffusion of the gas into the liquid is supposed to be negligible because of the short time scale.

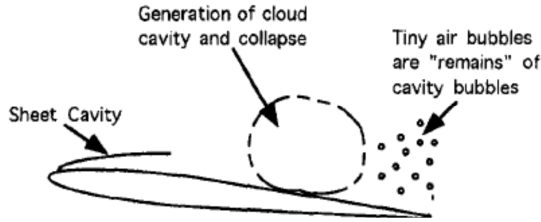


Figure 3-3: Generation and collapse of cloud cavity (Kato et al., 1996)

The number density of cavitation bubbles are given as:

$$\left. \begin{aligned} N &= KR^{-4.36}, & R &\geq R_0 \\ N &= KR_0^{-4.36} = const., & R &< R_0 \end{aligned} \right\} \quad (3-2)$$

and K is a constant which can be derived by substituting the above equation (3-2) into the relation, which indicating the cavity generation rate equal to the total flow rate of cavity bubbles, as follows:

$$C_{qc} = \frac{Q}{U_{\infty}BC} = \frac{1}{U_{\infty}BC} (U_{\infty}Bh_b \int_0^{\infty} \frac{4}{3} \pi R^3 NdR) \quad (3-3)$$

where h_b is the bubble layer thickness, and can be estimated from the images of cloud cavity. Then the accumulative distribution of cavity bubbles I_R is then obtained by integrating equation(3-2), and can be written as:

$$I_R = \int NdR \quad (3-4)$$

Characteristics of Collapsing Bubbles

It is assumed that the shock wave caused by bubble collapse is the major mechanism to produce impact on the solid surface. A single spherical bubble, with an initial bubble radius R_0 , is examined in viscous compressible fluid. The maximum pressure p_{max} is achieved when the bubble size becomes minimum R_{min} at the final stage of collapse (Tomita and Shima, 1977). The following approximate equations can be used to estimate the maximum

pressure p_{\max} and minimum bubble radius R_{\min} :

$$\frac{p_{\max}}{p_{\infty}} = 0.345 \left(\frac{p_0}{p_{\infty}} \right)^{-1.8} \quad (3-5)$$

$$\frac{R_{\min}}{R_0} = 1.502 \left(\frac{p_0}{p_{\infty}} \right)^{0.7} \quad (3-6)$$

where:

- p_0 is the initial gas pressure inside the bubble
- p_{\max} and p_{∞} are the maximum pressure and the pressure at far field
- R_{\min} and R_0 are the minimum and initial bubble radius

Impact Force/Pressure Distribution on Solid Surface

The impact pressures on the foil surface are then estimated based on a model for an isolated implosion of a single bubble in an infinite space. An approximate equation for the impact pressure on solid wall can be written as:

$$p_h = p_{\max} R_{\min} / h \quad (3-7)$$

where h is the distance between the bubble center and the solid surface. This model neglects interference effects that occur in bubble clouds (see e.g. Reisman et al., 1998). Furthermore, it neglects diffraction effects from the nearby wall.

By combining the cavity generation rate and the number and size of the bubbles, the impact force/pressure spectrum on the solid surface can be estimated. First, the cavity collapsing region and the ambient pressure for collapse is estimated. Next, the bubble collapsing rate at a certain position on the solid surface should be estimated with the spatial distribution of bubbles, which is assumed to be Gaussian. It is however very time consuming to calculate the impact forces and pressure caused by each collapsing bubble. Therefore, it is assumed that only the bubbles in the effective layer can cause impact forces and pressures high enough to damage the solid surface. The trajectory of the bubbles then can be represented by a reference trajectory, see Figure 3-4.

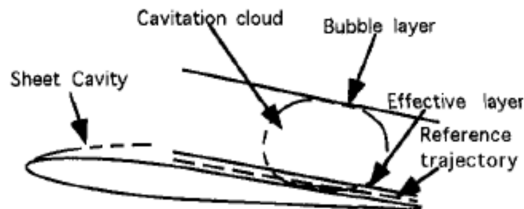


Figure 3-4: Bubble layer, effective layer, and reference trajectory

Then, three reference length scales are introduced: bubble layer thickness (h_b), effective layer thickness (h_e) and reference trajectory (h_r). The effective layer thickness h_e is assumed to be one-tenth of the bubble layer thickness and the reference trajectory is supposed to follow the center of the effective layer, i.e. $h_e = h_b / 10$; $h_r = h_e / 2$. The accumulative collapsing rate on the pickup then can be estimated as:

$$I_{pR} = I_R U_\infty h_e \phi \quad (3-8)$$

where ϕ is the probability of a bubble collapsing on a pickup.

3.5.2 Relevance

This model allows for a quantitative prediction of cavitation erosion without using a model test. However, it involves several parameters which were assumed or neglected without confirmation, such as the initial gas pressure inside a bubble, the spatial distribution of collapsing bubbles, the change of ambient pressure around collapsing bubbles, and the interaction of bubbles as well as that between bubbles and the solid wall. Although the model by Kato et al. (1996) is an interesting attempt to capture the process from cavity shedding up to and including the generation of shock waves, the neglects and simplified empirical relations, often derived from model experiments on only one configuration, make the applicability of this model for propellers and rudders highly questionable. This is acknowledged by the authors, who state that “further experimental as well as theoretical verifications of the assumed values (and relations) are essential for the development of the proposed method”. Furthermore, the described mechanism lacks the important role a vortical flow in the focusing of the energy. The reference trajectory for the shed cavities defined in this model seems to differ from the development of shed vortices into horseshoe vortices, as hypothesized in the foregoing section 2.6.

3.6 MODEL BY WANG AND BRENNEN (1999)

Wang and Brennen proposed a bubble cloud model to simulate the nonlinear growth and collapse of a cloud cluster of bubbles (1999). It is assumed that this model can make up the shortcoming of the RANS method which is only capable of observing the large scale dynamics, and look into microscale details of the collapse of the cloud cavity.

3.6.1 Collapse Process

It uses the fully nonlinear continuum mixture equations coupled with the Rayleigh-Plesset

equation for the interaction of the bubbles with the flow. This model considers a spherical bubble cloud surrounded by an unbounded pure liquid (see Figure 3-5), and it is hypothesized that the population of bubbles per unit volume of liquid η is piecewise uniform initially and remains constant and piecewise uniform within the cloud.

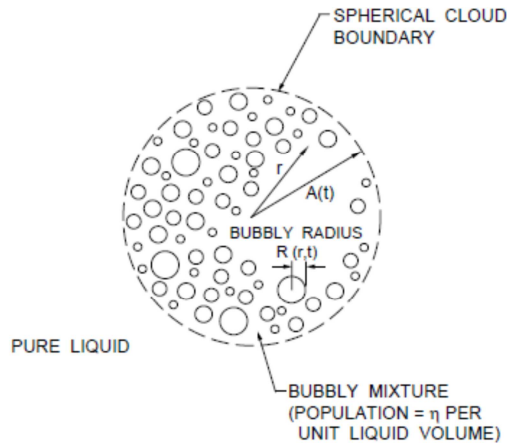


Figure 3-5: Schematic of a spherical bubble cloud (Wang and Brennen, 1999)

Bubble Dynamics

The non-dimensional forms of the continuity and momentum equations for the spherical bubbly flow are:

$$\frac{1}{r^2} \frac{\partial(r^2 u)}{\partial r} = \frac{12\pi\eta R^2}{3 + 4\pi\eta R^3} \frac{DR}{Dt}; r \leq A(t) \quad (3-9)$$

$$\frac{Du}{Dt} = -\frac{1}{6}(3 + 4\pi\eta R^3) \frac{\partial C_p}{\partial r}; r \leq A(t) \quad (3-10)$$

and

$$\eta = \frac{\alpha / (1 - \alpha)}{\frac{4}{3} \pi R^3} \quad (3-11)$$

$$C_p(r, t) = \frac{p(r, t) - p_0}{\frac{1}{2} \rho_l U_{ref}^2} \quad (3-12)$$

where:

- r is the radial coordinate from the center of the cloud
- u is the radial velocity of the mixture, and U_{ref} is the reference velocity
- η is the bubble population per unit liquid volume and α is the vapor volume fraction

- R is the bubble radius, and A is the radius of the bubble cloud
- C_p is the pressure coefficient, $p(r, t)$ is the mixture pressure and p_0 is the initial equilibrium pressure

The non-dimensional form of the Rayleigh-Plesset equation, which relates the local mixture pressure to the bubble dynamics, is:

$$R \frac{D^2 R}{Dt^2} + \frac{3}{2} \left(\frac{DR}{Dt} \right)^2 + \frac{4}{\text{Re}} \frac{1}{R} \frac{DR}{Dt} = \frac{\sigma}{2} (R^{-3\kappa} - 1) + \frac{2}{\text{We}} (R^{-3\kappa} - R^{-1}) - \frac{1}{2} C_p \quad (3-13)$$

and:

$$\sigma = \frac{p_0 - p_v}{\frac{1}{2} \rho_l U_{ref}^2} \quad (3-14)$$

where:

- R is the bubble radius, developed with time t , and R_0 is the initial bubble radius
- σ is the cavitation number, ρ_l is the liquid density, and U_{ref} is the reference velocity
- κ is the polytropic index for the non-condensable gas inside the bubble
- Re is the Reynolds number, defined as $\text{Re} = \rho_l U_{ref} R_0 / \mu_E$, where μ_E is the effective viscosity
- We is the Weber number, defined as $\text{We} = \rho_l U_{ref}^2 R_0 / \gamma$, where γ is the surface tension

Pressure Perturbation

To solve the unknowns in equations (3-9), (3-10) and (3-13), appropriate initial and boundary conditions are demanded. The number and size of the initial bubble cloud at a specific instance are extracted from the RANS results as the input, which is also taken as an important item in the model by Kato et al. (1996), related to section 3.5.1. The time-dependent boundary condition at the surface cloud can be written as:

$$C_p(A(t), t) = C_{p_\infty}(t) + \frac{2}{A(t)} \frac{d[A^2(t)u(A(t), t)]}{dt} - u^2(A(t), t) \quad (3-15)$$

and:

$$C_{p_\infty}(t) = (p_\infty - p_0) / \frac{1}{2} \rho_l U_{ref}^2 \quad (3-16)$$

where:

- A is the radius of the bubble cloud
- ρ_l is the liquid density, and U_{ref} is the reference velocity

- p_∞ and p_0 are the pressure at infinity and initial pressure at undisturbed condition
- $C_{p_\infty}(t)$ is the pressure coefficient at infinity, and can be retrieved from the RANS results.

Acoustic Pressure

Subsequently, the radiated acoustic pressure in the far field can be calculated by the volumetric acceleration of the cloud. The normalized far-field acoustic pressure $p_a(t)$ is calculated as:

$$p_a(t) = \frac{2R_0}{D} \left[A^2(t) \frac{d^2 A(t)}{dt^2} + 2A(t) \left(\frac{dA(t)}{dt} \right)^2 \right] \quad (3-17)$$

where:

- R_0 is the initial bubble radius
- D is the length scale
- A is the radius of the bubble cloud

3.6.2 Relevance

This model is similar to the model by Kato et al. (1996), which also considers the impulsive force occurring during the violent collapse of a cloud cavity filled with microbubbles. However, the bubble collapse behavior is calculated by the Rayleigh-Plesset equations rather than by an estimation equation based on the spatial distribution of bubbles, see equation (3-3). This model looks promising as a postprocessor for a quantitative relation between the numerical results by the unsteady RANS method and the risk of cavitation erosion.

At first, due attention should be paid to choose the appropriate results from the RANS method as input for the bubble cloud model. These input parameters should be carefully translated to provide a quasi-equivalent bubble cloud. Then, a pressure perturbation $C_{p_\infty}(t=0)$, corresponding to the pressure field at the selected specific instant from the RANS results, is to be imposed on the pure liquid at infinity. The response of the cloud to this pressure perturbation is taken for the details of the bubble dynamics within the cloudy bubble cluster during its collapse. The surrounding pressure will however vary in some way because the assumed bubble cloud travels downstream during its collapse. This change of the ambient pressure is neglected in view of the very short time period for which this model is developed.

3.7 MODEL BY NOHMI ET AL. (2008)

Nohmi et al. (2008) proposed a formula to numerically predict the time-averaged local cavitation aggressiveness by using only the flow field results without looking into the microscale collapse details.

3.7.1 Aggressiveness Indices

Important Hypotheses

It is assumed that only the bubbles that possibly cause damage are taken into account which is held responsible for the cavitation aggressiveness. The formula is based on three hypotheses:

- The bubbles in the vicinity of the solid surface are more dangerous than bubbles further away from the surface.
- The bubbles that are exposed to a pressure rise will implode and could be dangerous.
- The erosion risk will be increased when a larger number of bubbles implode at the same time, and the vapor void fraction α is simply selected as an indicator of the number of bubbles.

Examples of the Aggressiveness Indices

The formula that indicates the instantaneous local cavitation aggressiveness is then written in the following general form:

$$\left(-\frac{\partial^{N1}\alpha}{\partial t^{N1}} \right)^{N2} \left(-\frac{\partial^{N3}(p-p_v)}{\partial t^{N3}} \right)^{N4} \quad (3-18)$$

and:

$$\alpha > 0; \frac{\partial\alpha}{\partial t} < 0; p > p_v \quad (3-19)$$

where $N1$, $N2$, $N3$ and $N4$ are zero or natural numbers which still have to be chosen.

By applying the two factors in equation (3-18) with different exponents, different formulas are obtained. Four examples of time-averaged local cavitation aggressiveness functions are thus introduced by Nohmi et al. (2008) as follows:

$$Index_1 = \frac{1}{T_c} \int_0^{T_c} \alpha \max\left[\frac{\partial p}{\partial t}, 0\right] dt \quad (3-20)$$

$$Index_2 = \frac{1}{T_c} \int_0^{T_c} \alpha \max[(p - p_v), 0] dt \quad (3-21)$$

$$Index_3 = \frac{1}{T_c} \int_0^{T_c} \max\left[-\frac{\partial \alpha}{\partial t}, 0\right] \max[(p - p_v), 0] dt \quad (3-22)$$

$$Index_4 = \frac{1}{T_c} \int_0^{T_c} \max\left[-\frac{\partial \alpha}{\partial t}, 0\right] dt \quad (3-23)$$

where T_c is the period of one time cycle for the case of unsteady dynamic shedding. It is assumed that the time averaged values can be qualitatively related to the local erosion rate.

3.7.2 Relevance

These formulas proposed by Nohmi et al. (2008) can be readily obtained with the help of CFD tools, and they are assumed to be qualitatively related to the local erosion rate. However, except for the integrand in equation (3-22), which is in accordance with the instantaneous potential power P_{pot} defined in the model by Fortes-Patella et al. (2004), the physical meaning of the other three functions is not clarified. The authors suggested that the formulas could be modified to a practical design tool for detecting the high risk areas of erosion. It was suggested that for a quantitative prediction of erosion rate, it is also required to measure proportionality coefficient and perhaps some additional exponents to the formula depending on the characteristics of a particular solid material.

The weak point of these damage functions is that they lack a physical background. This lack is emphasized by the time averaging that is involved, for a process which appears to be governed by extreme events of a much shorter duration than one shedding cycle, which is the time interval currently used as the integration period.

3.8 CONCLUSIONS

Based on the experiments and observations published in open literature (see section 2.4 and section 2.5), it is hypothesized that cavitation erosion is based on the conversion of potential energy contained in the cavity into emitted acoustic power upon the collapse. The focusing of this energy in space and in time is mainly caused by either spherical bubble cloud or vortex collapse in the vicinity of the solid surface.

The models by Bark et al. (2004a) and Fortes-Patella et al. (2004) are based on energy

transfer considerations, and show good correspondence to the hypothesized mechanism in section 2.6. The focusing efficiency in the model by Bark et al. (2004a) is difficult to obtain by only the RANS methods, and a combination of visual observations and paint tests is therefore recommended by the authors, possibly supplemented by noise measurements in the high frequency range. Likewise, the energy transfer ratios in the model by Fortes-Patella et al. (2004) are suggested to be of an empirical nature, but a method for a reliable determination of these efficiencies is lacking in the open literature.

The model by Dular et al. (2006) is based on the notion that the damage is caused by a high velocity liquid jet associated with a bubble implosion, and is not in agreement with the hypothesized mechanism for cavitation erosion from our work.

The models by Kato et al. (1996) and Wang and Brennen (1999) assume that the risk of cavitation erosion is related to the violent collapse of a cloud cavity, and focus on the details of the collapse processes. Unlike the empirical relations adopted by Kato et al., the latter model by Wang and Brennen adopts the Rayleigh-Plesset equation to describe the dynamics of the cloudy cluster of bubbles. The capability of the model by Wang and Brennen to close the gap between the output of the multiphase RANS method and the prediction of the risk of cavitation erosion will be assessed in Chapter 8.

The model by Nohmi et al. (2008) is easy to be used in a post-processing phase to RANS results, but careful consideration of the integrands in the equations is required. The effectiveness of these formulas for the prediction of cavitation erosion is evaluated through comparisons with experimental results in Chapter 8.

It is concluded that the relatively promising mathematical models for the prediction of cavitation erosion risk in connection to RANS results are due to Wang and Brennen (1999) and Nohmi et al. (2008), although the physical background of the latter is not clearly described. The work by Bark et al. (2004a) and Fortes Patella et al. (2004) is useful for a physical understanding of the cavitation erosion process.

Chapter 4: MODELING CAVITATION

WITH A RANS METHOD

4.1 INTRODUCTION

A cavitating flow is a complicated multiphase flow involving effects of phase change, compressibility, viscosity and turbulent fluctuations. It is a challenge to build a general-purpose method suitable for a wide range of practical applications in maritime engineering. Due to the complex mechanisms that govern the unsteady cavitation dynamics, such as the formation of the re-entrant jet and the generation and collapse of a cloudy cavity, phenomena with a wide range of length and time scales that are affected significantly by turbulence are involved. To solve the turbulent flows, the following methodologies are applied: Direct Numerical Simulation (DNS), in which all turbulent scales can be simulated by directly solving the Navier-Stokes equations on a sufficiently fine grid; Large Eddy Simulation (LES), in which spatially filtered Navier-Stokes equations are solved, and effects due to eddies smaller than order of mesh size magnitude are modeled; and Reynolds-Averaged Navier-Stokes (RANS) Method, in which time-averaged Navier-Stokes equations are solved for a statistically steady flow whereas ensemble-averaged Navier-Stokes equations are solved for a transient flow, and effects due to turbulence of all scales are modeled.

In FLUENT (ANSYS 12.0) and other commercially available CFD tools, DNS is not affordable due to its prohibitive cost in computation time. Though LES is available in FLUENT and is computationally less expensive than DNS, very fine and carefully structured meshes must be used, also demanding extensive computational resources and preparation time refer to objective and scope of the current study. Therefore, the more practical RANS method is utilized here and its capabilities to capture steady and unsteady cavitation phenomena are studied. Attention is focused on the mean flow quantities and the larger cavitation structures as well as turbulence effects on these flow phenomena.

In modeling cavitation with a RANS method, three important assumptions are made:

- The cavitating flow is taken as a mixture of liquid and vapor, and the mass transfer

between the liquid and vapor phase is modeled by the cavitation models.

- The influence of the vapor/liquid mixture compressibility on the turbulence structures can be accounted for by reducing the mixture turbulent viscosity in regions with higher compressibility (Coutier-Delgosha et al., 2003a).
- Heat transfer is ignored, i.e. the flow is taken as isothermal.

The time-dependent Reynolds-Averaged Navier-Stokes (RANS) equations for the homogenous mixture flow are introduced in section 4.2. Some classical turbulence models we used are introduced in section 4.3. The cavitation models accounting for the mass transfer between the liquid and the vapor phases are introduced in section 4.4. Finally, the convergence criteria applied in the current study are discussed, as well as the estimation of the errors and uncertainties based on the converged solutions.

4.2 RANS EQUATIONS FOR MULTIPHASE FLOW

There are two general approaches for the numerical simulation of multiphase flows (ANSYS, 2009), and both approaches use Reynolds-Averaged Navier-Stokes (RANS) equations for the Eulerian phases:

- Euler-Lagrange Approach: This approach treats the fluid phase as a continuum by solving the Navier-Stokes equations, while solves the dispersed phase by tracking a large number of particles, bubbles or droplets through the calculated flow field, also known as DEM (Discrete Element Method). The dispersed phase can exchange momentum, mass and energy with the fluid phase.
- Euler-Euler Approach: In this approach, the different phases are treated mathematically similar as each other. A concept of phasic volume fraction is introduced and these volume fractions are assumed to be continuous functions of space and time, and their sum is equal to one.

In the Euler-Lagrange approach, each particle is tracked individually, the size distribution of the particles can be captured but demands very high computational efforts (Syamlal et al., 2006). Moreover, due to the basic underlying assumption that the dispersed second phase occupies a low volume fraction, the Euler-Lagrange approach is inappropriate for the modeling of flows in which the volume fraction of the second phase cannot be neglected.

Euler-Euler methods have the least number of equations (RANS) to be solved, but the constitutive equations can be stiff, which leads to small time steps and long CPU times.

There are three Euler-Euler multiphase models available in FLUENT (ANSYS 12.0): the volume of fluid (VOF) model, in which a surface-tracking technique is applied to track the volume fraction of each phase which is assumed not interpenetrating; the mixture model, in which the phases are allowed to be interpenetrating; and the Eulerian model, in which the conservation equations are solved for each phase.

Considering the nature of cavitating flows, the Euler-Euler approach is more appropriate to do the numerical calculation of the liquid/vapor two-phase flow. The mixture model is eventually chosen to describe the dispersed phases by solving the mixture continuity and momentum equation. The cavitating flow is thereby simplified to be regarded as a homogeneous mixture with liquid and vapor in the current study.

4.2.1 Continuity Equation (Mass Conservation)

The mass conservation equation for the mixture is derived from the physical principle of mass conservation, which states that the rate of change of mass in an arbitrary material volume V equals the flow through the boundary of volume V , which can be written as:

$$\frac{d}{dt} \iiint_V \rho_m dV = - \iint_S \rho_m \bar{u} \cdot \bar{n} dS \quad (4-1)$$

where ρ_m is the mixture density and \bar{u} is the velocity of the phases, which are assumed to move at the same velocity.

Then by using the divergence theorem the following continuity equation can be obtained:

$$\frac{\partial}{\partial t} (\rho_m) + \frac{\partial}{\partial x_i} (\rho_m u_i) = 0 \quad (4-2)$$

and the relationship between the mixture density ρ_m and the vapor volume fraction α is defined as:

$$\rho_m = \alpha \rho_v + (1 - \alpha) \rho_l \quad (4-3)$$

where the subscripts m , v and l denote the mixture, vapor and liquid phase, respectively.

4.2.2 Momentum Equation

According to Newton's second law, the rate of change of momentum is equal to the sum of the forces on the fluid element, i.e. $m\bar{a} = \bar{F}$. There are two types of forces, which can be categorized as:

- Body forces, which act directly on the volumetric mass, such as gravity force and centrifugal force.
- Surface forces, which act directly on the surface, such as pressure force and

viscous force.

In a similar way as for the continuity equation, the differential momentum equations for the mixture can be written as:

$$\frac{\partial}{\partial t}(\rho_m u_i) + \frac{\partial}{\partial x_j}(\rho_m u_i u_j) = -\frac{\partial p}{\partial x_i} + \frac{\partial \tau_{ij}}{\partial x_j} + f_i \quad (4-4)$$

where:

- p is the pressure
- f_i denotes the body force term, generally thought to be related to the gravitational field, and is ignored in the current study
- τ_{ij} denotes the viscous stress tensor. Based on the assumption of Stokes in 1845, this term for a Newtonian fluid can be expressed as

$$\tau_{ij} = \mu_m \left[\left(\frac{\partial u_i}{\partial x_j} + \frac{\partial u_j}{\partial x_i} \right) - \frac{2}{3} \delta_{ij} \frac{\partial u_k}{\partial x_k} \right] \quad (4-5)$$

where:

- μ_m denotes the viscosity of the mixture: $\mu_m = \alpha \mu_v + (1 - \alpha) \mu_l$
- δ_{ij} denotes the Kronecker symbol, where $\delta_{ij} = 1$ if $i = j$ and $\delta_{ij} = 0$ otherwise
- Stokes hypothesis is used to express the so-called second viscosity coefficient as

$$-\frac{2}{3} \mu_m$$

The above equations (4-2) and (4-4) constitute the general Navier-Stokes equations for isothermal homogeneous mixture flows.

4.2.3 Reynolds-Averaged Navier-Stokes Equations

When the effect of turbulence on the mean flow properties is investigated, every variable can be replaced by the sum of a mean and a fluctuating component. This decomposition of the flow properties is the so-called Reynolds decomposition.

In a statistically steady flow, an arbitrary quantity can be written as the sum of the mean component independent of time and a time-dependent fluctuating component:

$$\phi(x_i, t) = \bar{\phi}(x_i) + \phi'(x_i, t) \quad (4-6)$$

where:

- x_i denotes any arbitrary coordinates, and t denotes the time

- $\phi(x_i, t)$ denotes an arbitrary quantity varying in space and time
- $\bar{\phi}(x_i)$ denotes the mean component, which is a time-averaged value over a period of T , and is defined as:

$$\bar{\phi}(x_i) = \frac{1}{T} \int_0^T \phi(x_i, t) dt \quad (4-7)$$

- $\phi'(x_i, t)$ denotes the fluctuation about the mean of the arbitrary quantity

When the transient flow is investigated, both components are not only a function of the spatial coordinates but also a function of time:

$$\phi(x_i, t) = \bar{\phi}(x_i, t) + \phi'(x_i, t) \quad (4-8)$$

and ensemble averaging is used, also known as Reynolds averaging:

$$\bar{\phi}(x_i, t) = \lim_{N \rightarrow \infty} \frac{1}{N} \sum_{n=1}^N \phi(x_i, t) \quad (4-9)$$

where N is the number of members of the ensemble which must be large enough to eliminate the effects of the fluctuations by assuming that the time scale of the unsteadiness is much larger than the turbulent time scales. The two averaging schemes (Ferziger and Peric, 2002) are schematized in Figure 4-1.

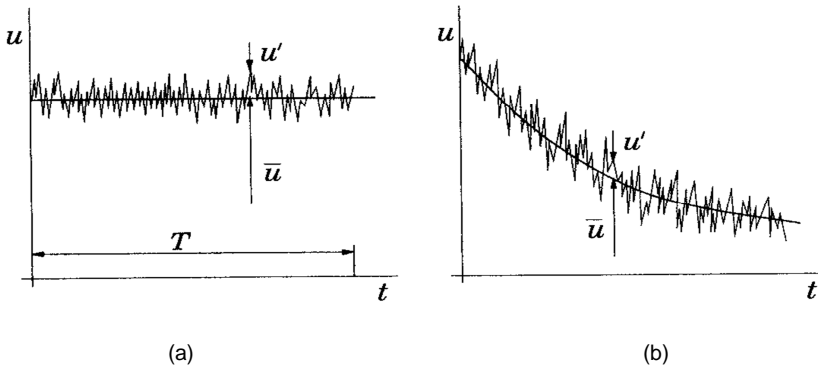


Figure 4-1: (a) Time averaging for a statistically steady flow and (b) ensemble averaging in case of a transient flow

In view of the fact that the averaging value of the fluctuating component equals zero, the averaged continuity and momentum equations for mixture flows can be written as:

$$\frac{\partial \rho_m}{\partial t} + \frac{\partial (\rho_m \bar{u}_i)}{\partial x_i} = 0 \quad (4-10)$$

$$\frac{\partial}{\partial t}(\rho_m \bar{u}_i) + \frac{\partial}{\partial x_j}(\rho_m \bar{u}_i \bar{u}_j + \rho_m \overline{u'_i u'_j}) = -\frac{\partial \bar{p}}{\partial x_i} + \frac{\partial \bar{\tau}_{ij}}{\partial x_j} \quad (4-11)$$

where $\bar{\tau}_{ij}$ is the mean viscous stress tensor:

$$\bar{\tau}_{ij} = \mu_m \left[\left(\frac{\partial \bar{u}_i}{\partial x_j} + \frac{\partial \bar{u}_j}{\partial x_i} \right) - \frac{2}{3} \delta_{ij} \frac{\partial \bar{u}_k}{\partial x_k} \right] \quad (4-12)$$

The extra terms $\rho_m \overline{u'_i u'_j}$ in equation (4-11) are called the Reynolds stresses and represent the correlation between fluctuating variables due to the effects of turbulence. Equations (4-10) and (4-11) are known as the Reynolds-Averaged Navier-Stokes (RANS) equations, which cannot be solved without further relations due to the additional unknown Reynolds stresses. Therefore, turbulence models are required to solve the turbulent flow with the RANS equations.

4.3 TURBULENCE MODELS

Experience has learned as that turbulence models play a key role in the numerical simulation of cavitating flows. Especially the unsteady dynamics, such as the break-up of the sheet cavity and the vortex shedding, depend strongly on the characteristics of the turbulence models.

4.3.1 Two Approaches

By adopting the methodology based on the RANS Equations, two approaches are usually followed for the Reynolds stresses: Eddy Viscosity Models and Reynolds Stress Transport Models.

In FLUENT (ANSYS 12.0), the Spalart-Allmaras Model, $k - \varepsilon$ models and $k - \omega$ models use the Eddy Viscosity Approach, following Boussinesq's eddy-viscosity hypothesis to relate the Reynolds stresses to the mean flow as:

$$-\rho_m \overline{u'_i u'_j} = \mu_t \left(\frac{\partial \bar{u}_i}{\partial x_j} + \frac{\partial \bar{u}_j}{\partial x_i} \right) - \frac{2}{3} \delta_{ij} \left(\mu_t \frac{\partial \bar{u}_k}{\partial x_k} + \rho_m k \right) \quad (4-13)$$

where k is the turbulent kinetic energy, which can be written as:

$$k = \frac{1}{2} \overline{u'_i u'_i} = \frac{1}{2} (\overline{u'_x u'_x} + \overline{u'_y u'_y} + \overline{u'_z u'_z}) \quad (4-14)$$

Although the eddy-viscosity hypothesis is not strictly valid due to the isotropic eddy-viscosity assumption, it requires relatively modest computational resources and efforts and has also proven to be capable of providing acceptable results for many flows.

The Reynolds Stress Model (RSM) follows an alternative approach and solves transport equations for each Reynolds stress component and an equation for the dissipation rate ε . Although this model has a greater potential to give accurate predictions, challenges are added due to the difficulties presented in the modeling of diffusion terms, pressure-strain interaction terms and the dissipation-rate. Thereby large additional computational costs are involved due to the large number of equations that need to be solved.

It is suggested by FLUENT that models based on the Boussinesq's hypothesis perform very well for many flow problems, and that the additional computational expense of the RSM is often not justified. Elaborate studies on the flow over a 2D NACA0015 foil by many experts in the VIRTUE WP4 Workshop have indicated that the two-equation turbulence models based on the Eddy Viscosity Approach, i.e. $k - \varepsilon$ models and $k - \omega$ models, are widely used and validated. The available two-equation turbulence models in FLUENT (ANSYS 12.0) are listed in Table 4-1, and a brief introduction of these models is provided in Appendix A. Among these models, the *SST* $k - \omega$ model is highlighted due to its prominent feature of being capable of flows with an adverse pressure gradient, transonic shock waves, and flows over airfoils (ANSYS, 2009). This model is selected for the calculations in the current study and will be introduced in the following.

Table 4-1: Available two-equation turbulence models in FLUENT (ANSYS 12.0)

k- ε model	Standard k- ε model
	RNG k- ε model
	Realizable k- ε model
k- ω model	Standard k- ω model
	SST k- ω model

4.3.2 *SST* $k - \omega$ Turbulence Model (Menter, 1994)

The velocity distribution near a wall can be plotted using non-dimensional variables, as shown in the Figure 4-2, with an increasing distance from the wall we have the viscous sublayer and the log-law layer, where u^+ and y^+ are two non-dimensional quantities:

$$u^+ = U_\infty / u_\tau; \quad y^+ = \rho_l u_\tau y / \mu \quad (4-15)$$

where:

- U_∞ is the mean flow velocity
- u_τ is the velocity scale: $u_\tau = \sqrt{\tau_\omega / \rho_l}$, where τ_ω is the wall shear stress
- y is the distance to the wall
- ρ_l is fluid density and μ is the dynamic viscosity

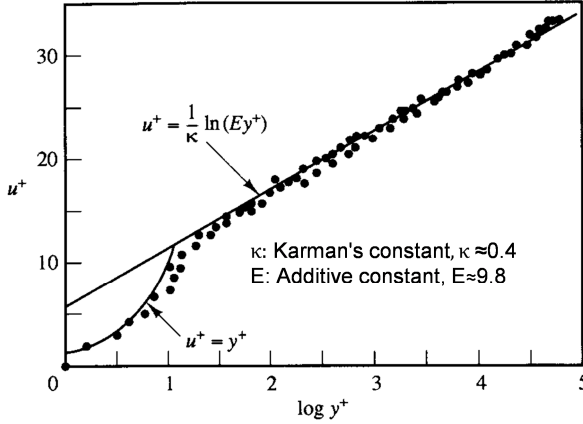


Figure 4-2: Velocity distribution near a solid wall (Versteeg and Malalasekera, 2007)

The *SST* $k - \omega$ turbulence model was proposed by Menter (1994), and is a blending between the standard $k - \omega$ model in the near-wall region and the standard $k - \varepsilon$ model in the far field. To achieve this, the standard $k - \varepsilon$ model is transformed into a $k - \omega$ formulation, and is blended with the standard $k - \omega$ model by a blending function F_1 . The blending function F_1 is designed to be equal to 1.0 in the sublayer and log-law layer (near-wall region), and to gradually switch to zero in the outer wake region and in the free shear layers (far field).

If we use ϕ_1, ϕ_2 and ϕ to represent the terms in the standard $k - \omega$ model, standard $k - \varepsilon$ model (see Appendix A) and *SST* $k - \omega$ model respectively, then the relation between them can be written as:

$$\phi = F_1 \phi_1 + (1 - F_1) \phi_2 \quad (4-16)$$

And the following transport equations for the turbulent kinetic energy k and its specific dissipation rate ω can be obtained:

$$\frac{\partial}{\partial t}(\rho k) + \frac{\partial}{\partial x_j}(\rho k \bar{u}_j) = \frac{\partial}{\partial x_j} \left[\left(\mu + \frac{\mu_t}{\sigma_k} \right) \frac{\partial k}{\partial x_j} \right] + G_k - Y_k + S_k \quad (4-17)$$

$$\frac{\partial}{\partial t}(\rho \omega) + \frac{\partial}{\partial x_j}(\rho \omega \bar{u}_j) = \frac{\partial}{\partial x_j} \left[\left(\mu + \frac{\mu_t}{\sigma_\omega} \right) \frac{\partial \omega}{\partial x_j} \right] + G_\omega - Y_\omega + D_\omega + S_\omega \quad (4-18)$$

where:

- σ_k and σ_ω are the turbulent Prandtl numbers for k and ω , respectively
- G_k and G_ω represent the generation of k and ω , respectively
- Y_k and Y_ω represent the dissipation of k and ω due to turbulence
- S_k and S_ω are the source terms for k and ω , respectively
- D_ω represents the cross-diffusion term due to the transformation of the standard $k - \varepsilon$ model into equations based on k and ω , respectively

The acronym ‘‘SST’’ stands for shear-stress transport because of the definition of the turbulent viscosity μ_t which is modified to account for the transport of the turbulent shear-stress. The turbulent viscosity μ_t is defined as (ANSYS, 2009):

$$\mu_t = \frac{\rho k}{\omega} \frac{1}{\max\left[\frac{1}{\alpha^*}, \frac{SF_2}{a_1 \omega}\right]} \quad (4-19)$$

where:

- k is the turbulent kinetic energy, defined as $k = \frac{1}{2} \overline{u'_i u'_i}$
- ω is the specific dissipation rate, defined as the ratio of the dissipation rate ε and k : $\omega = \varepsilon / k$
- $S \equiv \sqrt{2S_{ij}S_{ij}}$ is the strain rate magnitude, where $S_{ij} = \frac{1}{2} \left(\frac{\partial \bar{u}_i}{\partial x_j} + \frac{\partial \bar{u}_j}{\partial x_i} \right)$
- α^* is a coefficient which damps the turbulent viscosity μ_t representing a low-Reynolds-number correction, where $\alpha^* = \alpha_\infty^* = 1$ in a high-Reynolds-number flow
- a_1 is the model constant equaling 0.31
- F_2 is a function that is 1.0 for boundary-layer flows and zero for free shear layers and is meant to obtain improved results for the adverse pressure gradient boundary layer

4.3.3 Reboud’s Correction (Reboud et al., 1998)

The two-equation turbulence models are originally developed for single-phase flows. In cavitating flows, the two-phase fluid is taken as a mixture of an incompressible liquid and vapor cavities. This implies that large and steep density variations occur in the low-pressure regions resulting in strong pressure gradients and local compressibility-like effects (Sorguven and Schnerr, 2003). It is suggested that the standard two-equation turbulence models tend to overestimate the turbulent viscosity μ_t in the region of transition between the vapor and liquid phase, and damp the unsteadiness of the cavitating regime (Sorguven and

Schnerr, 2003; Li et al., 2009).

Reboud et al. (1998) proposed a simple modification of the $k-\varepsilon$ turbulence model by artificially reducing the turbulent viscosity μ_t in order to take into account the suggested two-phase flow effects on the turbulent structures. The turbulent viscosity μ_t is originally calculated by $\mu_t = f(\rho)C_\mu k^2 / \varepsilon$. For the general case of incompressible single-phase flows, the function $f(\rho)$ simplifies to ρ and remains constant. However, for two-phase mixture flows, the density function $f(\rho)$ is modified as follows:

$$f(\rho) = \rho_v + \frac{(\rho_m - \rho_v)^n}{(\rho_l - \rho_v)^{n-1}}; \quad n \gg 1 \tag{4-20}$$

where the mixture density ρ_m is obtained from equation (4-3). The density function $f(\rho)$ will be equal to ρ_v and ρ_l in the regions with pure vapor and water, but decreases rapidly in regions with a mixture of liquid and vapor. Coutier-Delgosha et al. (2003a, b) suggested that this modification accounts for effects of compressibility in the vapor/liquid mixture on the turbulent structures.

It was also concluded at the SMP 2011(Hoekstra et al., 2011) that all RANS codes failed to produce cavity shedding when they calculated the flow over the Delft Twist 11 Foil until they applied Reboud’s corrections. Some other RANS codes do find cavity shedding, however, for other hydrofoils, such as the 2D NACA0015 hydrofoil, which was an objective of study in the VIRTUE WP4 Workshop (Oprea, 2009; Hoekstra and Vaz, 2009). In the current study, the Reboud’s correction is applied to the SST $k-\omega$ turbulence model to better simulate the unsteady cavitation dynamics. The constant density ρ in equation (4-19) is replaced by the density function $f(\rho)$ calculated from (4-20). With the recommended exponent value of $n = 10$, the density function $f(\rho)$ in the region with higher vapor volume fraction α is reduced as shown in Figure 4-3.

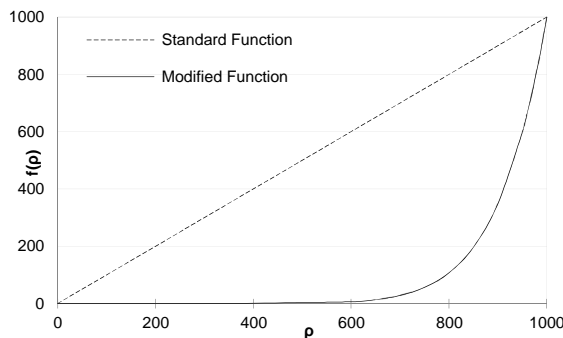


Figure 4-3: Modification of the density function in the turbulent viscosity ($n = 10$)

4.4 CAVITATION MODELS

It is a challenge to predict the cavitating flows, especially the unsteady dynamics of the cavities. In general, the current numerical cavitation models can be roughly divided in two main categories (Kawamura and Sakoda, 2003; Frikha et al., 2008; Liu et al., 2008):

- **The Interface-tracking Approach:** This is based on the free surface flow hypothesis. The cavity region is assumed to have a constant pressure equal to the vapor pressure of the corresponding liquid at the cavity interface. The computations are performed only for the liquid phase, and the cavity shape is iterated until the vapor pressure is achieved at the cavity boundary (Bouziad, 2006; Koop, 2008; Frikha et al., 2008).
- **The Multiphase-flow Approach:** This is based on the concept of phase averaging. The cavitating flow can be taken as a homogenous mixture of liquid and vapor (sometimes non-condensable gas is considered as the third phase). The mass and momentum transfer between the two phases can be modeled by two methods: the barotropic state law or the void fraction transport equation model (Frikha et al., 2008; Morgut et al., 2011).

There are three cavitation models available in FLUENT (ANSYS 12.0): the Singhal et al. model, the Zwart-Gerber-Belamri Model and the Schnerr and Sauer Model. All of these models are developed based on the following assumptions:

- There is no slip between the vapor and liquid phases, so that identical velocities are expected in both phases.
- Mass transfer only occurs between the liquid and vapor phases. When the local pressure is lower than a certain value, the local liquid will evaporate resulting in mass transfer from the liquid phase to the vapor phase; whereas the condensation process will result in mass transfer from the vapor phase to the liquid phase.
- The cavitation models are based on the Rayleigh-Plesset equation for spherical bubbles, neglecting the bubble-bubble interaction.

A brief introduction of the current cavitation models will be given in Appendix B. In this section, only the derivation of the Schnerr and Sauer model is introduced in detail since most of the published results adopt this model to calculate the unsteady cavitating flows over a hydrofoil (Hoekstra and Vaz, 2008, 2009; Li et al., 2009; Oprea, 2009a).

4.4.1 Basic Equations

The general vapor conservation equation can be written as:

$$\frac{\partial}{\partial t}(\rho_v \alpha) + \frac{\partial}{\partial x_j}(\rho_v \alpha u_{v,j}) = S_e - S_c \quad (4-21)$$

where:

- ρ_v is the vapor density
- α is the vapor volume fraction
- u_v means the vapor phase velocity
- S_e and S_c represent the mass transfer source terms due to the evaporation (growth) and condensation (collapse) of the vapor bubbles

The bubble dynamics, evaporation (growth) and condensation (collapse), are governed by the Rayleigh-Plesset equation:

$$R_B \frac{D^2 R_B}{Dt^2} + \frac{3}{2} \left(\frac{DR_B}{Dt} \right)^2 = \frac{p_B - p}{\rho_l} - \frac{4\nu_l}{R_B} \frac{DR_B}{Dt} - \frac{2\gamma}{\rho_l R_B} \quad (4-22)$$

where:

- R_B denotes the bubble radius
- ρ_l and ν_l are the density and kinematic viscosity of the liquid, respectively
- γ is the liquid surface tension
- p_B and p represent the bubble surface pressure and local far-field pressure, respectively

It is assumed that the influence of the surface tension, viscosity and inertia effects (second derivative term) can be ignored due to the pressure difference $p_B - p$ being large. Therefore, the Rayleigh-Plesset equation can be simplified as:

$$\frac{DR_B}{Dt} = \sqrt{\frac{2}{3} \frac{p_B - p}{\rho_l}} \quad (4-23)$$

4.4.2 Schnerr and Sauer Model

It is assumed by Schnerr and Sauer (2001) that the vapor structure is filled with lots of tiny spherical bubbles which are governed by the simplified Rayleigh-Plesset equation (4-23).

The vapor volume fraction α can then be calculated by the expression:

$$\alpha = \frac{n_b \frac{4}{3} \pi R_B^3}{1 + n_b \frac{4}{3} \pi R_B^3} \quad (4-24)$$

where R_B is the bubble radius and n_b is the number of tiny spherical bubbles per volume of liquid which is the only pre-specified value in this model.

It should be noted that the local far-field pressure p is the ambient pressure in the computational cell center and the bubble surface pressure p_B in equation (4-23) is the pressure at the bubble surface which is assumed to be equal to the saturation vapor pressure $p_v(T)$, which is only a function of temperature.

With the formula $\rho_m = \alpha\rho_v + (1-\alpha)\rho_l$, the derivative of the mixture density can be related to the change of the vapor volume fraction as:

$$\frac{D\rho_m}{Dt} = -(\rho_l - \rho_v) \frac{D\alpha}{Dt} \quad (4-25)$$

Using the definition of the substantial derivative, we obtain the continuity equation as:

$$\frac{\partial \rho_m}{\partial t} + \frac{\partial(\rho_m \bar{u}_i)}{\partial x_i} = \frac{D\rho_m}{Dt} + \rho_m \frac{\partial \bar{u}_i}{\partial x_i} = 0 \quad (4-26)$$

Combining equations (4-25) and (4-26), the mass transfer source terms can be written in the form of:

$$\frac{\partial}{\partial t}(\rho_v \alpha) + \frac{\partial}{\partial x_j}(\rho_v \alpha u_{v,j}) = \rho_v \frac{D\alpha}{Dt} + \alpha \rho_v \frac{\partial \bar{u}_j}{\partial x_j} = \frac{\rho_v \rho_l}{\rho_m} \frac{D\alpha}{Dt} = S \quad (4-27)$$

The derivative of the vapor volume fraction can be derived from the equation (4-24) as follows:

$$\frac{D\alpha}{Dt} = \frac{4\pi n_b R_B^2}{(1 + \frac{4}{3}\pi n_b R_B^3)^2} \frac{DR_B}{Dt} = \frac{3}{R_B} \alpha(1-\alpha) \frac{DR_B}{Dt} \quad (4-28)$$

Therefore, the expression of the mass transfer rate S can be finally related to the bubble radius by substituting equation (4-23) and (4-28) into equation (4-27):

$$S = \frac{\rho_v \rho_l}{\rho_m} \frac{3\alpha(1-\alpha)}{R_B} \sqrt{\frac{2}{3} \frac{p_v - p}{\rho_l}} \quad (4-29)$$

The two source terms in the transport equation (4-21) representing the evaporation and condensation processes can then be expressed as:

$$\text{Evaporation:} \quad S_e = \frac{\rho_v \rho_l}{\rho_m} \frac{3\alpha(1-\alpha)}{R_B} \sqrt{\frac{2}{3} \frac{p_v - p}{\rho_l}}, \quad p_v \geq p \quad (4-30)$$

and

$$\text{Condensation:} \quad S_c = \frac{\rho_v \rho_l}{\rho_m} \frac{3\alpha(1-\alpha)}{R_B} \sqrt{\frac{2}{3} \frac{p - p_v}{\rho_l}}, \quad p_v \leq p \quad (4-31)$$

4.5 CONVERGENCE ISSUES

4.5.1 Convergence Criteria

Convergence in the numerical process is an important issue because of the iterative nature of the solution procedures. It is crucial to know when to stop the iteration process to hit the right balance between computational accuracy and computational efficiency. Excessive iteration will consume unnecessary computational power, whereas an insufficiently converged iteration process can lead to insufficient accuracy. In FLUENT (ANSYS 12.0), convergence criteria can be set to monitor the residuals, statistics, force values, surface and volume integrals (ANSYS, 2009).

Residuals

The first convergence criterion in the current study is addressed to the residuals. Only the definition of residuals for the pressure-based solver that is applied for the current study is introduced here, whereas the definition for the density-based solver can be found in the help documents (ANSYS, 2009).

In FLUENT (ANSYS 12.0), residuals are reported for each of the continuity equation and each of the conservation equations for velocities and other variables appearing in additional models, such as turbulence models and cavitation model. The residuals by the pressure-based solver are defined as the imbalance of these conservation equations summed

over all the computational cells.

It can be obtained as follows. Taking an arbitrary scalar quantity ϕ as an example, the discretized conservation equation for variable ϕ in cell P can be written simply as:

$$a_P \phi_P = \sum_{nb} a_{nb} \phi_{nb} + b \quad (4-32)$$

where a_P is the center coefficient resulting from the discretization for a control volume designated cell P , and a_{nb} is the influence coefficients for the neighboring cells. ϕ_P and ϕ_{nb} represent the values for a generic variable at the center of cell P and its neighboring cells, respectively. b is the contribution of the source term.

The equation (4-32) can also be written in the form:

$$\sum_{nb} a_{nb} \phi_{nb} + b - a_P \phi_P = 0 \quad (4-33)$$

For any iteration, the left-hand side of equation (4-33) will not be exactly equal to the zero vectors. The deviation from the zero vectors is taken as an indicator of how far the solution is away from achieving convergence.

In the pressure-based solver, a scaled overall imbalance in the governing equations is used for monitoring the iteration convergence error, which is written as the sum of the absolute value of the left-hand side of equation (4-33) over all computational cells divided by the sum of $a_P \phi_P$ over all computational cells (kind of a weighted L_1 norm):

$$R^\phi = \frac{\sum_{cells P} \left| \sum_{nb} a_{nb} \phi_{nb} + b - a_P \phi_P \right|}{\sum_{cells P} a_P \phi_P} \quad (4-34)$$

A specific value of 0.001, which is the default value in FLUENT (ANSYS 12.0), indicates that a reduction of three orders of magnitude has been achieved for the corresponding residuals if the criterion is met. However, it is not the absolute indicator of convergence. Essentially, a converged solution means that this quantity is no longer changing with successive iterations, e.g. the residuals flatten in the plot of residual values vs. iterations. However, the residuals are still decreasing is not the issue, it is more important to check a relevant quantity is still with a declining or oscillatory tendency. In practical numerical simulations, the reports of forces, mass balance or other integrated quantities are often used as an additional way to judge the convergence.

Lift and Drag

For steady flows, the behavior of the lift and drag coefficients are often taken as alternative convergence indicators. When the solution is converged, the lift and drag coefficients should be constant and do not change with further iterations.

Mass Transfer Rate

For transient flows, it is suggested that the residuals should reduce by around three orders of magnitude within one time step to ensure accurate resolution of transient behavior (ANSYS, 2009). Apart from this, it is better to check the behavior of the mass transfer rate during one time step to ascertain that a constant mass transfer is achieved.

Hoekstra and Vaz (2009) have proposed that the convergence in a cavitating flow can be checked by observing the balance between the change of the total vapor volume and the volume integral of the source term:

$$\frac{d}{dt} \int \alpha dV = \int \frac{S}{\rho_v} dV \quad (4-35)$$

where the integrals are taken over the whole computational domain, α is the vapor fraction, ρ_v is the vapor density and S represents the source term. Since we are considering here the vapor production (or destruction) rate, the integral value should vanish when steady flow is achieved.

4.5.2 Grid Sensitivity

Grid convergence studies require a minimum of $m = 3$ solutions to check the convergence behavior and to estimate errors and uncertainties. A number of $m = 2$ solutions is inadequate, and it can indicate sensitivity but not convergence. In the current study, the convergence studies are conducted on three systematically and substantially refined grids by varying the k^{th} input parameter Δx_k , while keeping all other parameters constant. The solutions for both wetted flow (non-cavitating flow) and steady cavitating flow over the NACA0015 hydrofoil at 6° angle of attack are examined.

Convergence Conditions

It is suggested by the 22nd ITTC workshop (1999) that the convergence ratio R_k can be used to determine the convergence condition, which is defined as:

$$R_k = \varepsilon_{k_{23}} / \varepsilon_{k_{12}} \quad (4-36)$$

$$\mathcal{E}_{k_{12}} = S_{k_1} - S_{k_2}; \quad \mathcal{E}_{k_{23}} = S_{k_2} - S_{k_3} \quad (4-37)$$

where:

- S_{k_1} , S_{k_2} and S_{k_3} are the solutions obtained with coarse, medium and fine grid, respectively
- $\mathcal{E}_{k_{12}}$ and $\mathcal{E}_{k_{23}}$ are the solution changes for coarse-medium and medium-fine solutions

Four convergence conditions are defined (ITTC, 1999&2002; Stern, 2007):

- Monotonic convergence: $0 < R_k < 1$
- Oscillatory convergence: $-1 < R_k < 0$
- Monotonic divergence: $R_k > 1$
- Oscillatory divergence: $R_k < -1$

For the divergence conditions, i.e. $R_k > 1$ or $R_k < -1$, errors and uncertainties cannot be estimated. For the oscillatory convergence condition, i.e. $-1 < R_k < 0$, uncertainties can be estimated by error bounds based on oscillation maxima S_U and minima S_L , i.e. $U_k = (S_U - S_L) / 2$. Error estimates δ_k^* and uncertainties U_k for the monotonic convergence, i.e. $0 < R_k < 1$, are evaluated by the generalized Richardson Extrapolation Technique, which is introduced subsequently. The error estimate δ_k^* represents an estimate of both sign and magnitude of the difference between a simulation value and the truth (i.e. error δ_k), whereas the uncertainty U_k is an estimate of magnitude of the error δ_k .

Richardson Extrapolation Technique

Based on the assumption that the error terms are in the form of a power series expansion, the error estimate $\delta_{k_m}^*$ for the k^{th} parameter and m^{th} solution can be written as:

$$\delta_{k_m}^* = \sum_{i=1}^n (\Delta x_{k_m})^{p_k^{(i)}} g_k^{(i)} \quad (4-38)$$

where:

- n represents the number of terms retained in the power series, and can be calculated by $n = (m - 1) / 2$, where m is the number of solutions
- Δx_{k_m} is the k^{th} input parameter related to the grid size for the m^{th} solution
- $p_k^{(i)}$ is the order of accuracy corresponding to the i^{th} item in the expansion

- $g_k^{(i)} = f\left(\frac{\partial^i S}{\partial x_k^i}\right)$ is referred to as “grid” function which is a function of continuous derivatives of the solution S (Stern et al., 1999)

Usually the error is estimated for the finest grid, i.e. $\delta_k^* = \delta_{k_3}^*$ corresponding to the solution on the finest grid S_{k_3} . For three solutions ($m = 3, n = 1$), the numerical error and order of accuracy p_k can be calculated as:

$$\delta_k^* = \delta_{RE_k}^* = \frac{\mathcal{E}_{k_{23}}}{r_k^{p_k} - 1} \quad (4-39)$$

$$p_k = \frac{\ln(\mathcal{E}_{k_{12}} / \mathcal{E}_{k_{23}})}{\ln(r_k)} \quad (4-40)$$

where:

- $\mathcal{E}_{k_{23}}$ is the solution change for medium-fine solutions
- r_k is the factor by which the grid density was increased, which is equal to the cell size ratio between the two grids, i.e. $r_k = h_{k_2} / h_{k_3}$

According to the verification conducted by Stern et al. (ITTC, 1999), the equation (4-39) is in the correct form, but the order of accuracy is poorly estimated except in the asymptotic range. Therefore, two approaches are recommended by the 23rd ITTC (2002) to improve the estimation of the numerical error and uncertainties: Correction Factor Approach and Factor of Safety Approach.

- Correction Factor Approach

The effects of higher-order terms are accounted for by including a correction factor C_k , $C_k = (r_k^{p_k} - 1) / (r_k^{p_{kest}} - 1)$, where p_{kest} is an estimate for the limiting order of accuracy of the first term as the spacing size tends to zero and the asymptotic range is reached so that $C_k \rightarrow 1$. For $C_k \approx 1$, the error estimate δ_k^* and uncertainty U_k can be estimated as:

$$\delta_k^* = C_k \delta_{RE_k}^* = \frac{\mathcal{E}_{k_{23}}}{r_k^{p_{kest}} - 1}; \quad U_k = |(1 - C_k) \delta_{RE_k}^*| \quad (4-41)$$

When solutions are far from the asymptotic range, $C_k < 1$ or $C_k > 1$, only the magnitude of error is estimated through the uncertainty U_k :

$$U_k = \left| C_k \delta_{RE_k}^* \right| + \left| (1 - C_k) \delta_{RE_k}^* \right| \quad (4-42)$$

- Factor of Safety Approach

The uncertainties are obtained by multiplying with a factor of safety F_s to bound simulation error:

$$U_k = F_s \left| \delta_{RE_k}^* \right| \quad (4-43)$$

where $\delta_{RE_k}^*$ is based on the single-term estimate given by equation (4-39), and F_s is recommended to be taken equal to 1.25 for careful grid convergence studies using solutions on three or more grids, whereas it equals to 3.0 when only two grids are used. The order of accuracy is obtained from the theoretical value p_{th} (ITTC, 2002).

For the transient calculations, the influence of the temporal input parameters, including time step size Δt and iteration numbers per time step I_N , on the accuracy of the solution will be examined in this thesis.

Chapter 5: RESULTS ON

2D WETTED FLOW

5.1 OVERVIEW

The wetted, i.e. non-cavitating, flow over two different NACA hydrofoils in 2D is investigated in this chapter. First, the investigation is conducted on a frequently-used 2D NACA0015 hydrofoil at 6° angle of attack, which has been recommended by the VIRTUE WP4 Workshop as a standard test case to investigate the adequacy of numerical modeling of cavitating flows (Hoekstra and Vaz, 2008; Oprea, 2009a; Li et al., 2009). An assessment of the capabilities to predict the integrated quantities is carried out for several turbulence models embedded in FLUENT (ANSYS 12.0). Three grids of different density are used to study grid dependency. Another two hydrofoils with available experimental data are considered subsequently: one is the 2D NACA0015 hydrofoil with the same geometry definition as the first case but at a different angle of attack, namely 8° , and the other is the 2D NACA0018-45 hydrofoil at 6.5° angle of attack. The results from FLUENT for these hydrofoils are also compared to the results from XFOIL¹. Finally, guidelines and conclusions are given for numerical simulations of steady and unsteady cavitating flows.

5.2 2D NACA0015 ($AoA = 6^\circ$)

A 2D NACA0015 hydrofoil at an angle of attack of 6° ($AoA = 6^\circ$) is firstly investigated with different turbulence models and different grid densities. The results predicted by FLUENT are compared with the results from XFOIL and published numerical simulation results on the same geometry related to the VIRTUE WP4 Workshop (Hoekstra and Vaz, 2008; Oprea, 2009a; Li et al., 2009).

¹ XFOIL uses a panel method to predict the potential flow, and accounts for viscous effects by coupling with an integral boundary layer method. This method is the de-facto standard in aeronautical engineering for the High-Reynolds numbers flow over airfoils. It should be noted that XFOIL assumes the flow domain boundaries are infinitely far from the airfoil, while the current test cases calculated by FLUENT are within a limited domain.

5.2.1 Geometry of the NACA0015 Hydrofoil

For the well-known four-digit series NACA foils, the first and second number specify the maximum camber m in percentage of the chord and its position in tenths of the chord, respectively. The last two numbers specify the maximum thickness of the foil in percentage of the chord. The thickness distribution y_t above (+) and below (-) the mean line is defined as:

$$\pm \frac{y_t}{C} = \frac{t}{0.2} \left(0.2969 \sqrt{\frac{x}{C}} - 0.1260 \frac{x}{C} - 0.3516 \left(\frac{x}{C} \right)^2 + 0.2843 \left(\frac{x}{C} \right)^3 - 0.1015 \left(\frac{x}{C} \right)^4 \right) \quad (5-1)$$

where:

- $x \in [0, C]$, C represents the length of the chord
- t corresponds to the last two numbers in the NACA number, representing the maximum thickness of the foil as portion of the chord

Thus, the NACA0015 hydrofoil has a maximum thickness of 15%, i.e. $t = 0.15$, with a zero camber, i.e. it is a symmetric geometry, as illustrated in Figure 5-1.

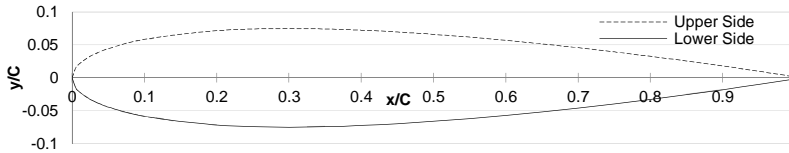


Figure 5-1: Geometry of the NACA0015 hydrofoil with a unit chord length

5.2.2 Case Description

The studied NACA0015 hydrofoil has a chord length of $C = 200mm$ and the foil is rotated over 6° around the center of gravity at $x/C = 0.3086$. The size of the rectangular computational domain is $1400 \times 570mm$, extending 2 chord lengths ahead of the leading edge and 4 chord lengths behind the trailing edge, as presented in Figure 5-2.

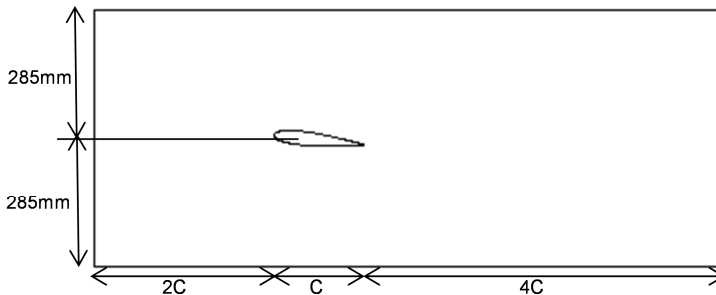


Figure 5-2: Computational domain for a NACA0015 hydrofoil at 6° angle of attack

Grid Topology

The NACA0015 hydrofoil coordinates calculated by equation (5-1) has a gap at the trailing edge of the foil, though only 0.1575% of the chord. The common way is to truncate it with a small thickness or use a rounded trailing edge. Either way allows for an O-grid mesh topology rather than a C-grid mesh topology (normally for the sharp trailing edge).

In the current study, the rounded method is used to close the trailing edge. The grid sensitivity and grid convergence are investigated on three grids with different densities but with similar multiblock topology: an O-grid around the foil embedded in an H-grid, resulting in a total of 12 blocks. The features of the three grids are listed in Table 5-1. The full image of the coarsest grid *G1* with 234 edges along the foil is presented in Figure 5-3, and an enlargement of the O-grid around the foil is also presented to give more details.

Table 5-1: Grid Features of a NACA0015 hydrofoil at 6° angle of attack

Grid	# Cells	#edges on foil	Level	Y+max
G1	27,808	234	Coarse	0.3747
G2	62,568	351	Medium	0.2432
G3	111,232	468	Fine	0.1797

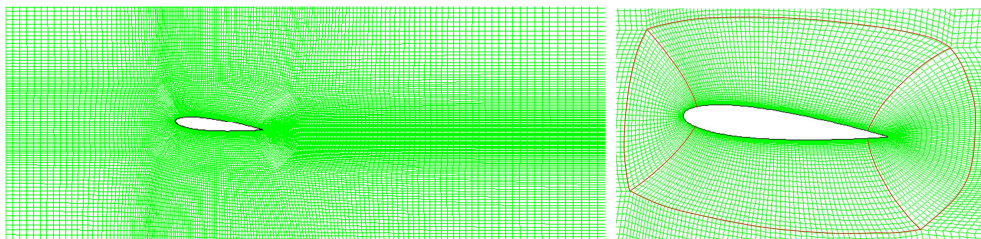


Figure 5-3: The coarse grid *G1* for a NACA0015 hydrofoil at 6° angle of attack: (a) Overall view; (b) Enlargement view of the O-grid around the foil

Computational Set-up

A velocity inlet condition is applied at the upstream inflow, and a pressure outlet condition is used at the outlet boundary. The boundary layer thickness is small compared to the computational domain, therefore the top and bottom walls are taken as slip walls, as is done for most of the published numerical simulation results for the same geometry. The physical properties of the two phases, liquid and vapor, are taken at a temperature of 24°C. The detailed initial and boundary conditions and the corresponding flow properties are listed in Table 5-2.

Table 5-2: Boundary conditions and flow properties for a NACA0015 hydrofoil (AoA=6°)

Boundary Conditions	NACA0015 (AoA=6°)
Velocity Inlet (m/s)	V=6
Pressure Outlet(kPa)	80
Turbulent Intensity (%)	1
Turbulent Viscosity Ratio	10
Foil	No-slip Wall
Tunnel Walls (Top & Bottom)	Slip Wall
Flow Properties (T=24°C)	Liquid
Density (kg/m ³)	998
Dynamic Viscosity(kg/ms)	0.0011

For the wetted flow, a pressure-based steady solution scheme is adopted, and the coupling schemes and spatial discretization methods of the convection terms in the equations are listed in Table 5-3. The definitions of these schemes can be found in the help documents of FLUENT (ANSYS, 2009).

Table 5-3: The chosen solver and discretization schemes for a NACA0015 hydrofoil (AoA=6°)

Terms	Methods
Pressure-Velocity Coupling	Coupled
Gradient	Green-Gauss Cell Based
Discretization for Pressure	PRESTO!
Discretization for Momentum	QUICK
Discretization for K	QUICK
Discretization for ω	QUICK

5.2.3 Results for Different Turbulence Models

The calculations are conducted on the coarse grid *G1* with seven different turbulence models that are implemented in FLUENT (ANSYS 12.0):

- Spalart-Allmaras (S-A)
- $k - \varepsilon$ models: Standard (SKE), RNG (RNGKE) and Realizable (RKE)
- $k - \omega$ models: Standard (SKW) and SST (SSTKW)
- Reynolds Stress Model (RSM)

The specification method of the turbulence parameters at the boundary is chosen as Turbulent Intensity and Viscosity Ratio. Only the latter parameter is demanded for the Spalart-Allmaras model. The values used are set at 1% for the turbulent intensity, and 10 for the viscosity ratio.

The convergence criteria for the residuals of all equations are set at a value of 10^{-8} . It is found that some of the residuals cannot reach this pre-set convergence criteria, especially

for the equations associated with several turbulence models, such as the *RNG* $k - \varepsilon$ model, Realizable $k - \varepsilon$ model and Reynolds Stress Model, whereas a higher but still very small value of at least 10^{-5} can be reached. In these three instances, the drag and lift coefficients did not converge to an asymptotic value but kept showing a small oscillation, which was of the order of 10^{-7} when using *RNG* $k - \varepsilon$ model. Among the models, the one-equation Spalart-Allmaras model takes the least time to converge due to the small number of partial differential equations to be solved. The *SST* $k - \omega$ model is the most economic model of the two-equation models in terms of the computational effort and accuracy.

Pressure Distribution

The pressure distributions along the NACA0015 hydrofoil at 6° angle of attack of and a zoom in of the distributions near the leading edge at the suction side are shown in Figure 5-4, including the results from XFOIL. The Reynolds number is the same for both FLUENT and XFOIL as $Re = 1.09 \times 10^6$. It should be noted that free transition is specified in XFOIL, whereas fully turbulent flow is assumed for standard $k - \varepsilon$ model.

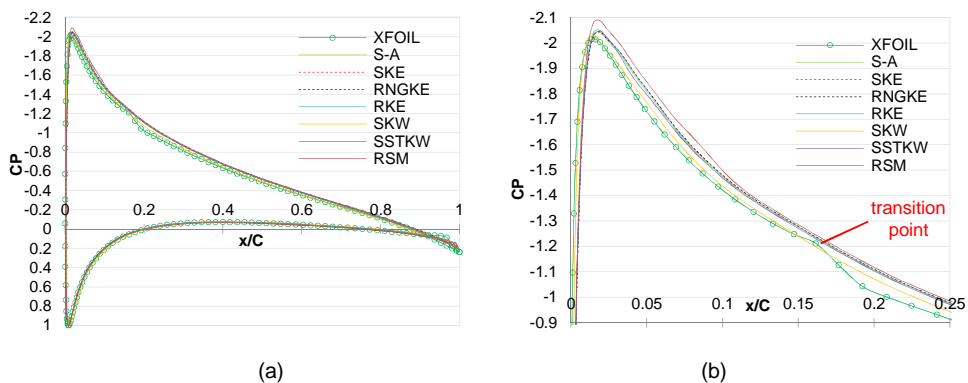


Figure 5-4: (a) The pressure distribution along a NACA0015 hydrofoil at 6° angle of attack for the coarse grid G1 ($Re = 1.09 \times 10^6$); and (b) an enlargement of the pressure distribution at the upper side near leading edge

The pressure distributions of different turbulence models match each other well on the lower side, while on the upper side, discrepancies between XFOIL and FLUENT are observed near the leading edge. It can be observed that the results predicted by XFOIL clearly show that the transition point on the upper side is around $0.167x/C$, which are not observed from the results by FLUENT ($k - \varepsilon$ models, $k - \omega$ models, RSM etc.).

Turbulent Viscosity

The contours of the turbulent viscosity around the hydrofoil and further downstream that calculated by different turbulence models are compared in Figure 5-5. Except for the

standard $k - \epsilon$ model, other two-equation turbulence models predict a similar distribution pattern of the turbulent viscosity but with different maximum value. The Reynolds Stress Model (RSM) predicts a similar maximum turbulent viscosity as $SST k - \omega$ model.

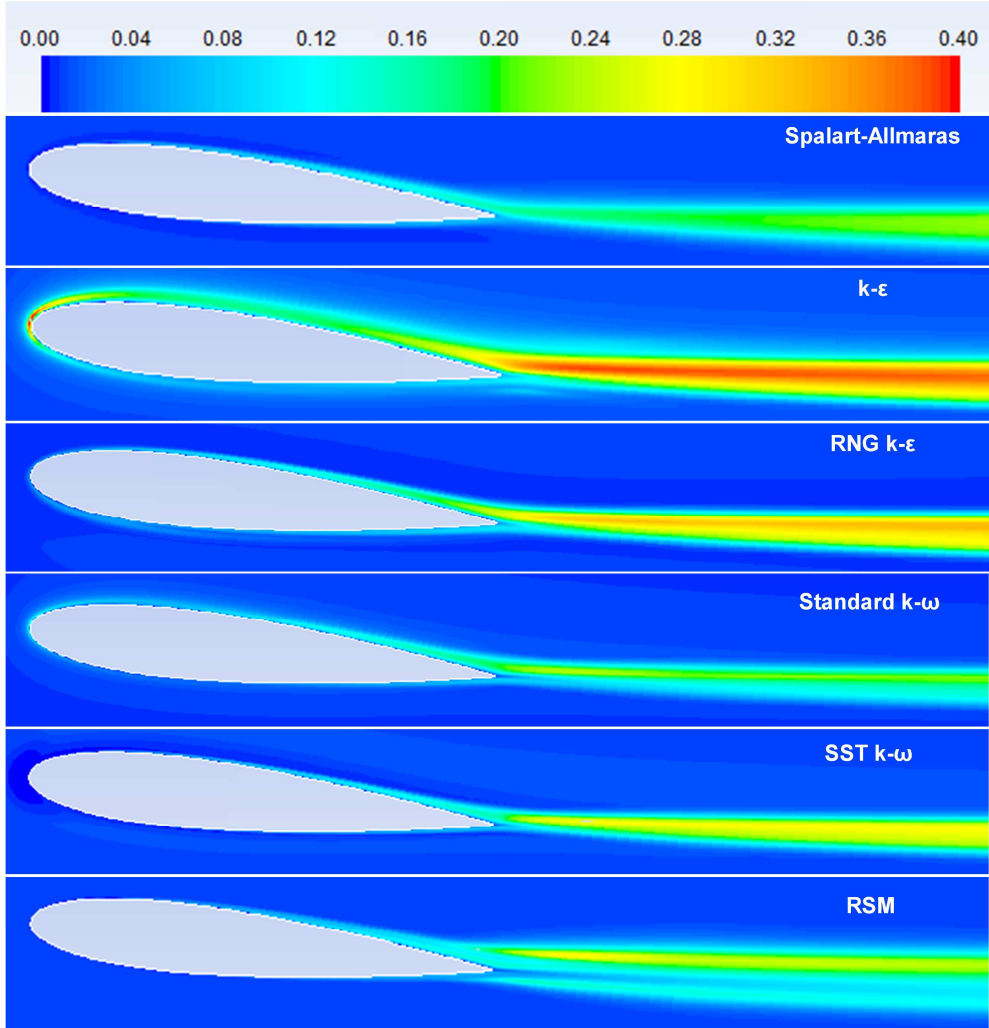


Figure 5-5: Contours of the turbulent viscosity predicted by different turbulence models for a NACA0015 hydrofoil at 6° angle of attack ($Re = 1.09 \times 10^6$)

Lift and Drag

The lift and drag coefficients, normalized with the mean value of all turbulence models, are plotted in histogram form, see Figure 5-6. It should be noted that the suffix V and P stand for the force attributable to viscous and pressure effects, respectively. It can be observed that:

- The lift coefficient is not sensitive to the turbulence models, but the drag coefficient does differ for different turbulence models.
- The lift due to viscous effects is very small for each turbulence model, while the drag due to viscous effects is more than 50% for all turbulence models and same for the results predicted by XFOIL.
- XFOIL gives the lowest values of lift and drag. The lower values computed by XFOIL than FLUENT are due to the infinite domain adopted for XFOIL on the contrary to a limited domain adopted for FLUENT (Li and Van Terwisga, 2011). This effect will be examined later on the NACA18-45 hydrofoil.

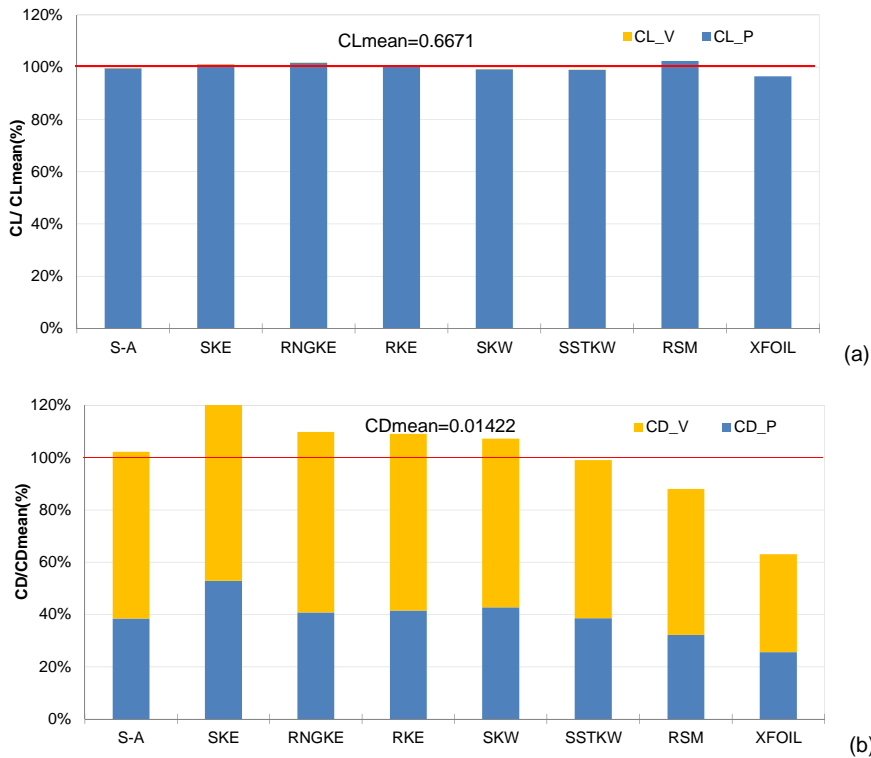


Figure 5-6: The histogram of normalized (a) lift and (b) drag coefficient obtained for different turbulence models employing coarse grid G1 (NACA0015 hydrofoil, AoA= 6°, Re = 1.09×10⁶), including the comparison with results predicted by XFOIL

In view of the computational effort and the numerical accuracy, the SST $k-\omega$ model is selected for the following investigations for both steady and unsteady cavitating flows.

5.2.4 Grid Sensitivity and Convergence Study

Three geometrically similar grids that have been refined substantially are investigated to

study the grid sensitivity with the *SST k – ω* turbulence model. The grid features are already given in Table 5-1. The errors and uncertainties will eventually be evaluated on the fine grid *G3*. The turbulent parameters at the boundary are set to the same value as specified in the previous section, i.e. 1% of turbulent intensity and a viscosity ratio of 10. The convergence criteria for the residuals of all equations are again set to 10^{-8} . After close examination, it can be observed that the impact of grid resolution on the pressure distribution is not significant, as illustrated in Figure 5-7. The pressure distributions for different grids are almost identical on the lower side. However, there are some discrepancies on the upper side, and the results predicted by the fine grid *G3* and medium grid *G2* are within plotting accuracy. It can be concluded that a better resolution can be obtained when finer grid adopted. This improve resolution has potential to predict a sudden change in pressure gradient, indicating transition.

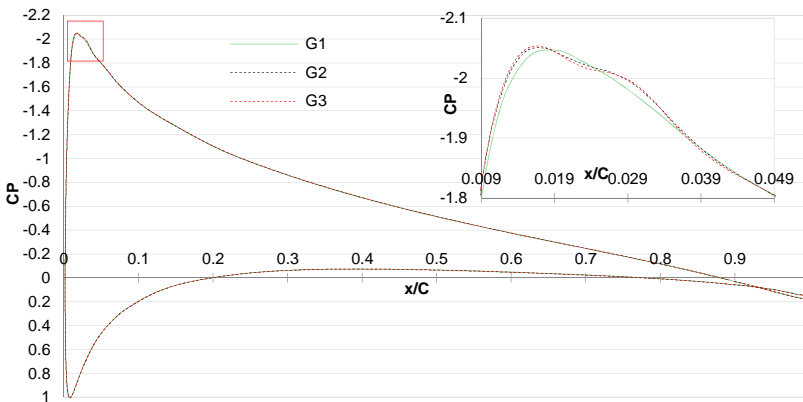


Figure 5-7: Pressure distribution along a NACA0015 hydrofoil at 6° angle of attack for different grid densities with *SST k – ω* turbulence model: G1 (Coarse), G2 (Medium), G3 (Fine) ($Re = 1.09 \times 10^6$)

Flow characteristics calculated by the three grids are compared in Table 5-4, including the maximum values of y^+ representing the typical grid features near the hydrofoil surface. Moreover, the convergence ratios calculated by equation (4-32) are also listed in Table 5-4.

Table 5-4: Flow characteristics comparison by different grids

Grids	CL_P	CL_V	CL	CD_P	CD_V	CD	CPmin	Y+max
G1	0.659883	0.000069	0.659952	0.005470	0.008612	0.014082	-2.046643	0.374698
G2	0.662328	0.000045	0.662373	0.005405	0.008830	0.014235	-2.049812	0.243248
G3	0.662282	0.000041	0.662322	0.005409	0.008925	0.014333	-2.053287	0.179728
Rk	-0.018810	0.198663	-0.020930	-0.060020	0.433637	0.642741	----	----

The forces due to pressure show an oscillatory convergence behavior ($-1 < R_k < 0$), whereas the viscous parts show monotonic convergence ($0 < R_k < 1$). On the whole, the drag coefficient satisfies the monotonic convergence condition, however, the lift coefficient is in the range of oscillatory convergence. Therefore, the error estimation based on drag coefficients can adopt the Richardson Extrapolation Method, which gives a value in the order of 10^{-5} by taking the order p as the theoretical accuracy order, i.e. $p = 2$. A safer estimation of the uncertainty is within an order of 10^{-4} . It can be concluded from above investigations that the pressure distribution and the predicted flow characteristics are not sensitive to the grid resolution.

5.2.5 Comparison with Results from VIRTUE WP4 Workshop

The case selected for the second VIRTUE WP4 Workshop (e.g. Hoekstra and Vaz, 2008; Oprea, 2009a; Li et al., 2009) is a NACA0015 hydrofoil at 6° angle of attack, identical to the test case adopted here. The main objective of this workshop was to compare the numerical results of all participants for the same configuration for both non-cavitating and cavitating conditions. A brief summary of the participants and the methods they adopted, made by an anonymous contributor from Chalmers University (2008), is shown in Table 5-5. It should be noted that the meshes they used were generated by themselves.

Table 5-5: Participants and their adopted methods in the VIRTUE WP4 Workshop

Orgnization/Code	Formulation	Turbulence Modeling	Phase Modeling
ARL/Uncle-M (WR)	Compr-DES/WR	k-eps	VoF+Kunz
ARL/Uncle-M (WM)	Compr-DES/WM	k-eps with wall function	
Twente	Compr-Euler	-----	Equilibrium
MU/CATUM	Compr-Euler	-----	Equilibrium
TKK/Inflow	Compr-RANS	k-eps	Merkle
Principia/EOLE	Pesudo Compr-RANS	k-eps with wall function	VoF+KMT1
HSVA/Comet	Incompr-RANS	RNG k-eps	VoF+Sauer
HSVA/FreSCo	Incompr-RANS	k-omega	VoF+Sauer&Kunz
MARIN/FreSCo	Incompr-RANS	SST k-omega	VoF+Sauer
Wartsila/Star-CD	Incompr-RANS	RNG k-eps	VoF+Sauer
Chalmers/OF	Incompr-LES	ILES	VoF+Sauer

The mean value of the lift and drag coefficients are reported as:

$$C_{Lmean} \approx 0.65 \pm 5\%; \quad C_{Dmean} \approx 0.014 \pm 14\% \quad (5-2)$$

On a percentage basis, the differences between the results predicted by FLUENT using three grids adopting the *SST k- ω* model and the above reported mean values are listed in Table 5-6. All current results are within the reported error bandwidth from this workshop. It is also observed that the coarse grid *G1* already does a reasonable job in the prediction of the integral quantities.

Table 5-6: Difference between the results predicted by FLUENT and the reported mean values from VIRTUE WP4 Workshop

Grids	CL	±%	CD	±%
G1	0.659952	153%	0.014082	0.59%
G2	0.662373	190%	0.014235	1.68%
G3	0.662322	190%	0.014333	2.38%

The results predicted by FLUENT in the current study and FreSCo from the Maritime Research Institute Netherlands (Hoekstra and Vaz, 2008) are compared in Figure 5-8 for the same grids in different densities. The differences in the lift and drag coefficients and the minimum pressure coefficients of these two CFD tools for the three grids are plotted in a histogram. The same conclusion is drawn by Hoekstra as that there is little influence of the grid densities on the integral quantities, like lift and drag. From the three plots in Figure 5-8, large differences are not observed between the results of the two CFD tools for the wetted flow over the NACA0015 hydrofoil at 6° angle of attack.

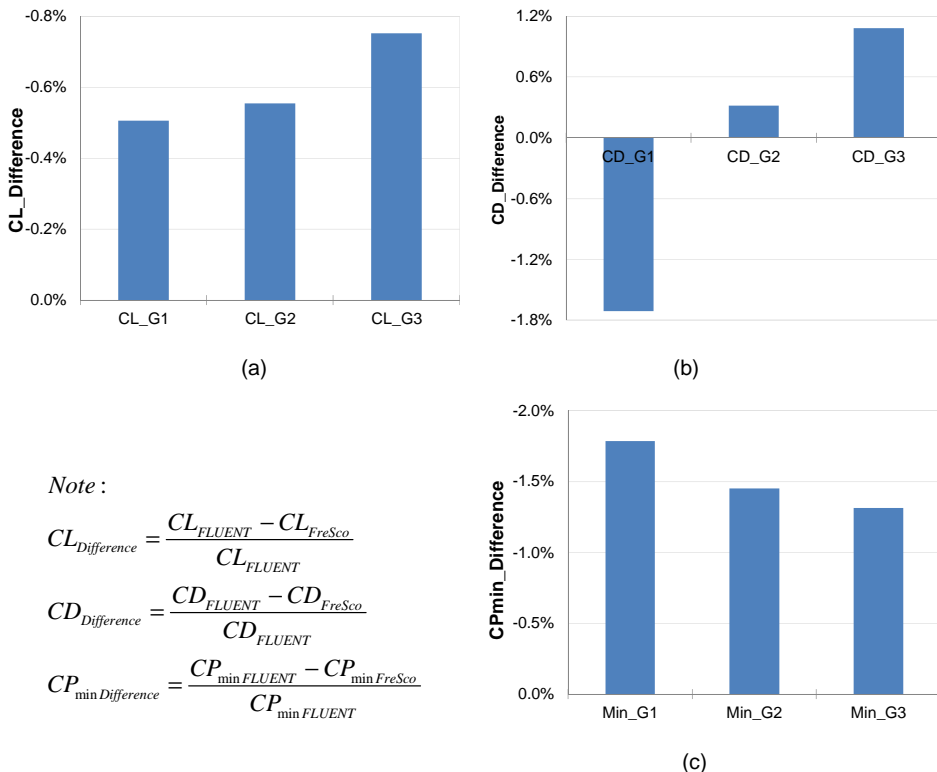


Figure 5-8: Comparisons between the (a) lift, (b) drag and (c) the minimum pressure coefficients predicted by FLUENT and FreSCo for three grids (NACA0015 hydrofoil, AoA= 6° , Re = 1.09×10⁶)

5.3 2D NACA0015 ($AoA = 8^\circ$)

The second case to be studied is the flow over a NACA0015 hydrofoil at an increased angle of attack of 8° . This will provide additional preliminary experience on calculating more complex 2D and 3D cavitating flows where experimental data has been provided by the CRS Erosion II Project (Boorsma, 2010; Van Rijsbergen and Boorsma, 2011).

5.3.1 Case Description

The studied case is the flow over a NACA0015 hydrofoil defined by equation (5-1) with a chord length $C = 60\text{mm}$, rotated over 8° around the mid-chord at $x/C = 0.5$. The size of the rectangular computational domain is $570 \times 80\text{mm}$, extending 3 chord lengths ahead of the leading edge and 5.5 chord lengths behind the trailing edge, as presented in Figure 5-9.

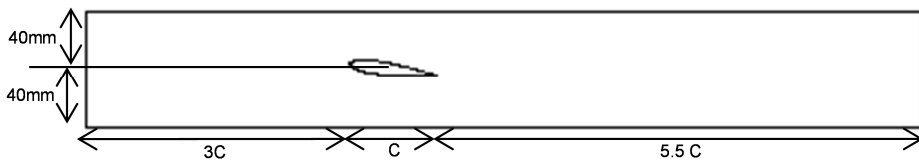


Figure 5-9: Computational domain for a NACA0015 hydrofoil at 8° angle of attack

Grid Topology

A similar multiblock topology is adopted as for computations at the lower angle of attack (6°), consisting of an O-grid around the foil embedded in an H-grid (12 blocks). An enlargement of the grid around the foil is presented in Figure 5-10 to give more details.

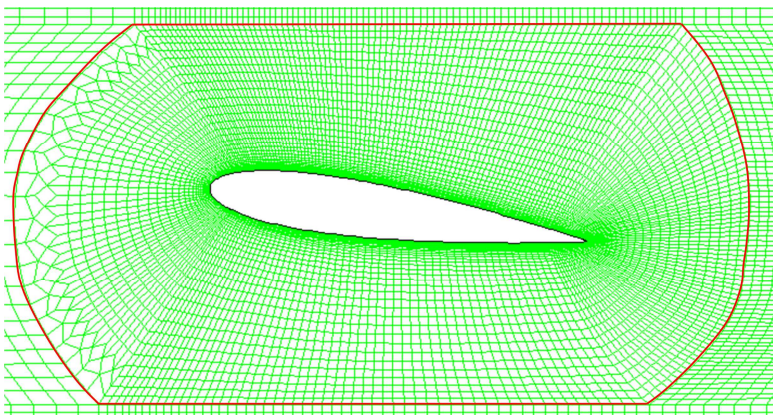


Figure 5-10: Enlarged view of the O-grid around a NACA0015 foil at 8° angle of attack

A coarse grid *G1* with 264 edges on the foil is used to calculate the wetted (non-cavitating) flow. The solution on a locally refined grid *G2*, obtained by utilizing the embedded command “adapt” in FLUENT (ANSYS 12.0), has also been calculated to assess the uncertainties of the original coarse grid. The properties of these two grids are listed in Table 5-7.

Table 5-7: Characteristics of the grids for NACA0015 at 8° angle of attack

Grid	# Cells	#edges on foil	Level	Y+max
G1	29,585	264	Coarse	0.3744
G2	118,340	528	Fine	0.1889

Computational Set-up

Similar initial and boundary conditions are adopted as the case of the NACA0015 hydrofoil at 6° angle of attack. The physical properties of the two phases, liquid and vapor, are taken at a temperature of 16.3°C. The detailed initial and boundary conditions and the flow properties are listed in Table 5-8. For the wetted flow, the pressure-based steady solution scheme is adopted again, and the same coupling schemes and spatial discretization methods of the convection terms in the equations are chosen as for the case of NACA0015 hydrofoil at 6° angle of attack, see Table 5-9. The definitions of these schemes can be found in the help documents of FLUENT (ANSYS, 2009).

Table 5-8: Boundary conditions and flow properties for a NACA0015 hydrofoil (AoA=8°)

Boundary Conditions	NACA0015 (AoA=8°)
Velocity Inlet (m/s)	V=17.71
Pressure Outlet(kPa)	800
Turbulent Intensity (%)	1
Turbulent Viscosity Ratio	10
Foil	No-slip Wall
Tunnel Walls (Top & Bottom)	Slip Wall
Flow Properties (T=16.3°C)	Liquid
Density (kg/m ³)	998.85
Dynamic Viscosity(kg/ms)	0.0011

Table 5-9: The chosen solver and discretization schemes for a NACA0015 hydrofoil (AoA=8°)

Terms	Methods
Pressure-Velocity Coupling	Coupled
Gradient	Green-Gauss Cell Based
Discretization for Pressure	PRESTO!
Discretization for Momentum	QUICK
Discretization for K	QUICK
Discretization for omega	QUICK

5.3.2 Results and Discussion

The calculation is mainly conducted with the *SST* $k - \omega$ turbulence model. The turbulence parameters at the boundary are set to be 1% for the turbulence intensity, and 10 for the viscosity ratio. The convergence criteria for the residuals of all equations are set to be 10^{-8} .

The pressure distributions predicted by XFOIL and FLUENT on two grids with different grid densities are plotted in Figure 5-11. A lower absolute value of the minimum pressure coefficient and lower lift and drag coefficients are obtained by XFOIL than FLUENT due to the limited domain adopted in FLUENT (Li and Van Terwisga, 2011). This effect will be examined in the next section on the NACA0018-45 hydrofoil. A comparison of the contours of the x-velocity between the two grids is shown in Figure 5-12. The x-velocities predicted on the two grids have a similar distribution in the whole domain with approximately 0.01% difference for the maximum value.

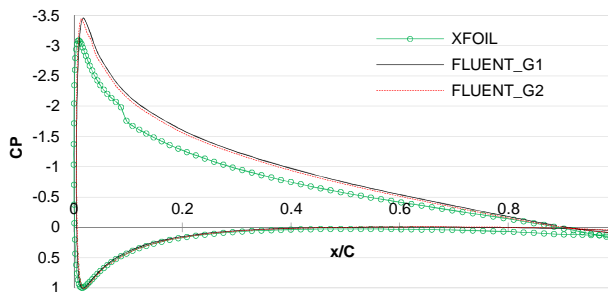


Figure 5-11: Pressure distributions by XFOIL and FLUENT on two grids with different densities for a NACA0015 hydrofoil at 8° angle of attack ($Re = 9.65 \times 10^5$)

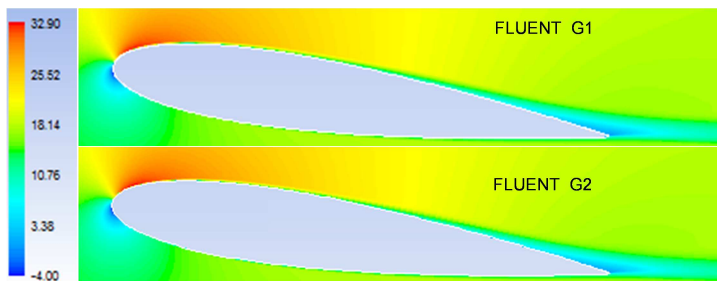


Figure 5-12: Contours of the x-velocity predicted by FLUENT on the two grids for a NACA0015 hydrofoil at 8° angle of attack ($Re = 9.65 \times 10^5$)

The values of the flow characteristics, such as the lift and drag coefficients, and also the minimum pressure coefficients for the three flow structures are displayed in the Table 5-10.

The deviations between these results are also calculated in order to investigate the influence of the grid refinement. Deviation (1) and Deviation (2) represent the difference between the results obtained by XFOIL and FLUENT on grids $G1$ and $G2$, respectively, and the Relative Deviation represents the difference between the two grids.

Table 5-10: Flow characteristics and error estimation for NACA0015 hydrofoil at 8° angle of attack

Properties	XFOIL	FLUENT_G1	Deviation(1)	FLUENT_G2	Deviation(2)	RelativeDeviation
CL	0.908700	1.035674	12.26%	1.025102	11.36%	-1.03%
CD	0.011950	0.018053	33.84%	0.018918	36.83%	4.57%
Cpmin	-3.087800	-3.459842	10.75%	-3.442630	10.34%	-0.50%

It can be observed that the absolute relative deviations between the results predicted by the two grids are within 5%. It is indicated that the grid refinement does not show significant influence on the prediction of the wetted flow.

5.4 2D NACA0018-45 ($AoA = 6.5^\circ$)

An interesting case for which experimental data is available is the NACA0018-45 hydrofoil at 6.5° angle of attack. The parameter setting is based on the set-up in the experiments conducted by Van der Hout (Van der Hout, 2008; Van Terwisga, 2009a).

5.4.1 Geometry of the NACA0018-45 hydrofoil

This hydrofoil section is slightly different from the NACA0018 hydrofoil because it has been modified. The original four-digit NACA0018 hydrofoil has a similar geometry as the NACA0015 hydrofoil but with a different maximum thickness, i.e. $t_{\max} = 0.18$. The two last numbers “45” indicate a modification of the standard foil.

The first number refers to the roundedness of the nose, where a value of 0 represents a sharp leading edge, while a value of 6 represents the same leading edge radius as the original hydrofoil. The leading edge radius is calculated as:

$$r_{LE} = \frac{1.1019}{36} \left[\frac{t_{\max}}{C} I_{Le} \right]^2 \quad (5-3)$$

where:

- I_{Le} is the index indicating the modification of the nose radius, that is, the first number behind the dash
- t_{\max} / C is the ratio between the maximum thickness and the chord of the hydrofoil

The second number defines the location of the maximum thickness in tenths of the chord length. It should be noted that the default location of the maximum thickness for all four digit hydrofoils is 30% downstream from the leading edge. Therefore, the number 5 means that the maximum thickness has been moved aft towards the middle of the chord.

The thickness distribution y_t above (+) and below (-) the mean line for the modified series has different expressions ahead and aft of the maximum thickness:

$$\begin{aligned} \pm y_t &= a_0 \sqrt{x/C} + a_1(x/C) + a_2(x/C)^2 + a_3(x/C)^3 && \text{ahead of } t_{\max} \\ \pm y_t &= d_0 + d_1(1-x/C) + d_2(1-x/C)^2 + d_3(1-x/C)^3 && \text{aft of } t_{\max} \end{aligned} \quad (5-4)$$

where x is the coordinate along the length of the hydrofoil and $x \in [0, C]$, and C is the chord length of the hydrofoil. According to the value of the maximum thickness and leading edge radius, the constants in Equation (5-4) are specified as follows:

$$\begin{aligned} a_0 &= 0.1781; & a_1 &= -0.0425; & a_2 &= -0.0095; & a_3 &= -0.0985 \\ d_0 &= 0.0019; & d_1 &= 0.4185; & d_2 &= -0.6167; & d_3 &= 0.2642 \end{aligned} \quad (5-5)$$

The thickness distribution for three types of hydrofoils, NACA0015, NACA0018, and NACA0018-45, are compared in Figure 5-13.

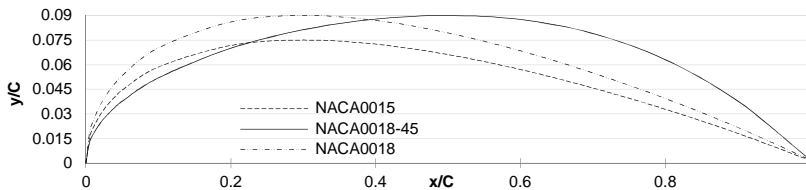


Figure 5-13: Geometry of the NACA0015, NACA0018 and NACA0018-45 foils with unit chord length

It is noteworthy to observe that the gradient of the thickness distribution for NACA0018-45 hydrofoil is much steeper towards the trailing edge than in the case for the standard thickness distribution, leading to a steeper adverse pressure gradient and a greater risk of flow separation.

5.4.2 Case Description

The investigation will be conducted on the NACA0018-45 hydrofoil with a chord length of $C = 60\text{mm}$ rotated over 6.5° around the center $x/C = 0.5$. The size of the rectangular computational domain is $420 \times 80\text{mm}$, extending 2 chord lengths ahead of the leading edge and 4 chord lengths aft of the trailing edge, and the height of the domain corresponds to the

dimension of the cavitation tunnel. With a similar topology as the NACA0015 hydrofoil at 6° angle of attack, the grid to be investigated is also an O-H multiblock grid with 309 edges on the foil, as shown in Figure 5-14.

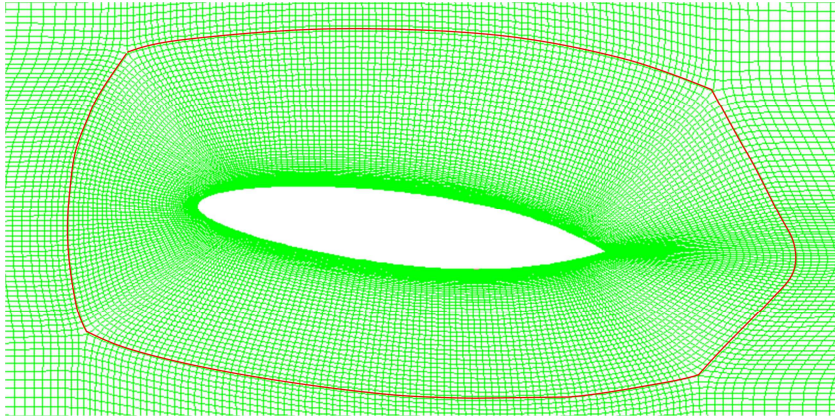


Figure 5-14: Enlarged view of the O-grid around a NACA0018-45 foil at 6.5° angle of attack

A velocity inlet condition is applied at the upstream inflow with a uniform velocity of 24.2 m/s. A pressure outlet condition is used at the outlet boundary with a uniform pressure of 1000 kPa. The physical properties of the two phases, liquid and vapor, are taken at the temperature of $23^\circ C$. The detailed initial and boundary conditions and the flow properties are listed in Figure 5-11.

Table 5-11: Boundary conditions and flow properties for a NACA0018-45 hydrofoil ($AoA=6.5^\circ$)

Boundary Conditions	NACA0018-45 ($AoA=6.5^\circ$)
Velocity Inlet (m/s)	$V=24.2$
Pressure Outlet(kPa)	1000
Turbulent Intensity (%)	1
Turbulent Viscosity Ratio	10
Foil	No-slip Wall
Tunnel Walls (Top & Bottom)	Slip Wall
Flow Properties ($T=23^\circ C$)	Liquid
Density (kg/m ³)	997.5
Dynamic Viscosity(kg/ms)	0.00093

For the wetted flow, the pressure-based steady solution scheme is adopted again, and the coupling schemes and spatial discretization methods of the convection terms in the equations are chosen identical to those of the previous cases, as listed in Table 5-12. The definitions of these schemes can be found in the help documents of FLUENT (ANSYS, 2009).

Table 5-12: The chosen solver and discretization schemes for a NACA0018-45 hydrofoil (AoA= 6.5°)

Terms	Methods
Pressure-Velocity Coupling	Coupled
Gradient	Green-Gauss Cell Based
Discretization for Pressure	PRESTO!
Discretization for Momentum	QUICK
Discretization for K	QUICK
Discretization for omega	QUICK

5.4.3 Results and Discussion

With regard to the computational efforts, the current investigation only focuses on the results predicted by the *SST k- ω* turbulence model. The turbulence parameters at the boundary are set to be 1% of the turbulent intensity, with a viscosity ratio equal to 10. The convergence criteria for the residuals of all equations are set at 10^{-8} .

The pressure distribution along the NACA0018-45 hydrofoil has a much steeper adverse pressure gradient than that on the NACA0015 hydrofoil, as presented in Figure 5-15. From the contours of x-velocities shown in Figure 5-16, a larger separation zone can be observed near the trailing edge for the NACA0018-45 hydrofoil as compared to the NACA0015 hydrofoil. This steeper pressure gradient also implies that more intense dynamics can be expected when the flow turns into an unsteady cavitating flow.

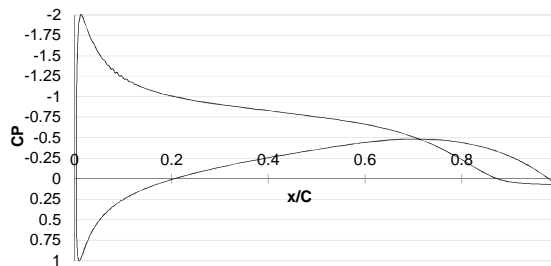


Figure 5-15: Pressure distribution along a NACA0018-45 hydrofoil at 6.5° angle of attack

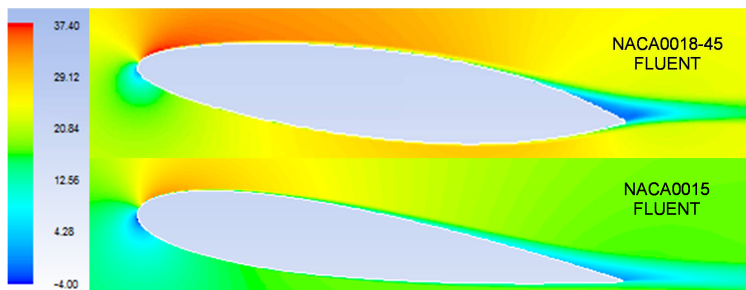


Figure 5-16: Contours of x-velocity of the NACA0015 hydrofoil at 6° angle of attack and NACA0018-45 hydrofoil at 6.5° angle of attack, clearly showing the difference in the size of separation zone

The XFOIL results at $Re = 1.56 \times 10^6$ for the NACA0018-45 hydrofoil at 6.5° angle of attack are used to give a comparison with the flow characteristics predicted by FLUENT. The steeper adverse pressure gradient is also obtained by XFOIL, however, predicts a lower absolute value of minimum pressure coefficient, $C_{p_{min}}$, and also lower lift and drag coefficients. It also appears that the flow separation is retarded. It was assumed that the differences between the results predicted by FLUENT and XFOIL are due to the wall effect caused by the bounded domain within only $66\%C$ distance from the foil surface to the tunnel walls. Therefore, another grid with the same cells around the foil but with a large domain is generated to investigate the effect of the wall. The pressure distributions predicted by FLUENT with a bounded and a large domain are compared with the results predicted by XFOIL (equivalent to an unbounded domain), as shown in Figure 5-17. It shows that the minimum pressure coefficient and the flow separation zone predicted by FLUENT with the large domain are much closer to the results predicted by XFOIL.

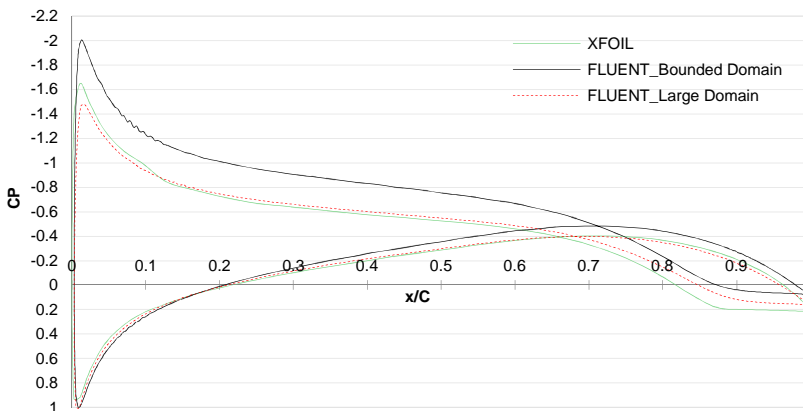


Figure 5-17: Pressure distribution along a NACA0018-45 hydrofoil at 6.5° angle of attack as computed by FLUENT and XFOIL ($Re = 1.56 \times 10^6$)

The values of the lift and drag and the minimum pressure coefficient of the NACA0018-45 hydrofoil predicted by XFOIL and FLUENT with different computational domains are listed in Table 5-13. Deviation (1) and Deviation (2) reveal the errors between results predicted by XFOIL and FLUENT with bounded domain and large domain separately. The abbreviation BD means bounded domain, and LD means large domain. It is observed that comparable flow characteristics are obtained if the calculation domain is large, which reduced the tunnel wall effect. It is then concluded that there is a significant influence on the prediction of the flow characteristics over the hydrofoil when the flow is confined.

Table 5-13: Flow characteristics for NACA0018-45 hydrofoil predicted by XFOIL and FLUENT

	XFOIL	FLUENT_BD	Deviation(1)	FLUENT_LD	Deviation(2)
CL	0.3454	0.5181	50.00%	0.36735	6.35%
CD	0.01369	0.018348	34.02%	0.017765	29.77%
Cpmin	-1.6487	-2.0033252	21.51%	-1.4730593	-10.65%

5.5 CONCLUSIONS

In this chapter three cases have been investigated to explore the capability of the RANS method implemented in FLUENT to predict the wetted flow over hydrofoils. These cases are the NACA0015 hydrofoils at 6° and 8° angle of attack and the NACA0018-45 hydrofoil at 6.5° angle of attack. The results match the published numerical simulation results, even for the coarse grid. However, it should be noted that the maximum $y+$ value on the foil surface for all grids used in the three cases considered are smaller than 1.0, indicating a relatively fine mesh near the hydrofoil surface for all grids employed.

The following conclusions are drawn from these results:

- The RANS method implemented in FLUENT, using the current numerical settings, can produce good correspondence of results for the unbounded domains with results obtained by XFOIL.
- Among the two-equation turbulence models, the *SST* $k - \omega$ turbulence model is the preferred one in terms of the computational effort required and accuracy attained.
- The pressure distributions along the foil and the integral flow characteristics are grid independent, provided that appropriate $y+$ values are attained along the foil. A maximum value for $y+$ along the hydrofoil smaller than 1.0 indicates a fine enough mesh near the hydrofoil surface.
- The size of the computational domain in the direction normal to the main flow direction will significantly affect the flow characteristics, and a bounded domain will give a delayed flow separation.

Chapter 6: RESULTS ON 2DCAVITATING FLOW

6.1 OVERVIEW

This chapter sets out to seek an answer to the question whether the RANS method implemented in FLUENT can successfully predict steady and unsteady cavitating phenomena within certain accuracy. Similar as for the investigation on the 2D wetted flows, thorough studies are conducted on the cavitating flows over the 2D NACA0015 hydrofoils with angle of attack of 6° and 8° , and also the 2D NACA0018-45 hydrofoil with an angle of attack of 6.5° .

To inspect the capability of the RANS method implemented in FLUENT to describe steady cavitating flows over hydrofoils, a thorough study is performed on the 2D NACA0015 hydrofoil with an angle of attack of 6° in section 6.2. The cavitation regime to be examined corresponds to a cavitation number of $\sigma = 1.6$, identical to one of the studied cases in the VIRTUE WP4 Workshop. An overview that includes all test cases in the investigation of the steady cavitating phenomena is shown in Table 6-1.

Table 6-1: Matrix of the tested cases related to the investigation of steady cavitating phenomena

Type	Geometry	Turbulence Model	Cavitation Model	Grid	Time Step Size Δt (s)	Temporal Discretization	Iteration Numbers Per Time Step (In)
Steady Cavitating Flow	NACA0015 (AoA=6)	Standard SST K-w model	Schnerr-Sauer Model (Nb=1e+13)	G1(Coarse) 27,808 cells	5.00E-04	1st-order implicit	100
					2.00E-04	1st-order implicit	60
					1.00E-04	2nd-order implicit	60
				G2(Medium) 62,568 cells	2.00E-04	1st-order implicit	60
						1st-order implicit	
					G3(Fine) 111,232 cells	2.00E-04	1st-order implicit
1st-order implicit							

In section 6.3, the capability of the RANS method implemented in FLUENT to predict unsteady cavitation dynamics is explored through the calculations of the cavitating flow around 2D hydrofoils. Specific cavitation regimes characterized by different cavitation numbers have been studied. For the NACA0015 hydrofoil with an angle of attack of 6° , the examination is carried out for a cavitation number of $\sigma = 1.0$, which is another case

studied in the VIRTUE WP4 Workshop. As to the other two hydrofoils, the cavitation regimes are selected with regard to the available experimental data. Therefore, the cavitation number of $\sigma = 2.2$ is chosen for the 2D NACA0015 hydrofoil with an angle of attack of 8° , and $\sigma = 0.72$ is chosen for the 2D NACA0018-45 hydrofoil with an angle of attack of 6.5° . To give a clear overview of the various cases that are involved in the investigation of the unsteady cavitating phenomena over different hydrofoils, a matrix is shown in Table 6-2.

Table 6-2: Matrix of the tested cases related to the investigation of unsteady cavitating phenomena

Type	Geometry	Grid	Turbulence Model	Cavitation Model		Time Step Size Δt (s)	Temporal Discretization	Iteration Numbers Per Time Step (In)
Unsteady Cavitating Flow	NACA0015 (AoA=6)	G1 (Coarse) 27,808 cells	Standard SST K-w model	Schnerr-Sauer Model (Nb=1e+13)		5.00E-04	1st-order implicit	20
						100		
			Modified SST K-w model	Schnerr-Sauer Model (Nb=1e+13)		2.00E-04	1st-order implicit	20
						50		
		G3 (Fine) 111,232 cells	Standard SST K-w model	Schnerr-Sauer Model (Nb=1e+13)		5.00E-04	1st-order implicit	20
						100		
	Modified SST K-w model	Schnerr-Sauer Model (Nb=1e+13)		2.00E-04	1st-order implicit	20		
				50				
	NACA0015 (AoA=8)	G1 29,585 cells	Standard SST K-w model	Schnerr-Sauer Model	Nb=1e+13	2.50E-05	1st-order implicit	50
					Nb=1e+08			50
			Modified SST K-w model		Nb=1e+10	2.50E-05	1st-order implicit	50
					Nb=1e+13			50
Modified SST K-w model			Nb=1e+15		50			
NACA 0018-45 (AoA=6.5)	G1 52,485 cells	Standard SST K-w model	Schnerr-Sauer Model (Nb=1e+13)		1.00E-05	1st-order implicit	40	
		Modified SST K-w model			1.00E-05		40	

6.2 STEADY CAVITATING CONDITION

6.2.1 Case Description

The investigation of the steady cavitation phenomena over hydrofoils is mainly conducted on the NACA0015 hydrofoil at 6° angle of attack with three substantially and systematically refined grids. The grids are referred to as G1 representing a coarse grid with 27,808 cells, G2 representing a medium grid with 62,568 cells and G3 representing a fine grid with 111,232 cells, where the features have already been illustrated in section 5.2.2. The maximum height of the cells adjacent to the foil is such that $y^+ < 1$ for all three grids.

In the condition defined by a cavitation number of $\sigma = 1.6$, the flow is expected to show a

stable sheet cavitation developing from the leading edge and extending to approximately 20% of the chord length (Oprea, 2009a; Hoekstra and Vaz, 2008). Based on the convergence criteria in Chapter 4, the numerical results are thoroughly explored to obtain the guidelines for the choice of appropriate transient input parameters: time step size, Δt , and iteration numbers per time step, I_N . Subsequently, the temporal discretization schemes and the sensitivity of the grid densities will be investigated.

A velocity-inlet condition is applied to the upstream flow with the vapor fraction equal to zero. On the outlet boundary, a pressure-outlet boundary condition is used. The specified pressure at the outlet can be derived from the cavitation number under consideration. The physical properties of the two-phases, liquid and vapor, are taken at a temperature of 24°C . The detailed initial and boundary conditions and the flow properties are listed in Table 6-3.

Table 6-3: Boundary conditions and flow properties for a NACA0015 hydrofoil ($AoA=6^\circ$)

Boundary Conditions	NACA0015 ($AoA=6^\circ$)	
Mean Velocity Inlet (m/s)	V=6	
Pressure Outlet (kPa)	317	
Turbulent Intensity (%)	1	
Turbulent Viscosity Ratio	10	
Foil	No-slip Wall	
Tunnel Walls (Top & Bottom)	Slip Wall	
Flow Properties ($T=24^\circ\text{C}$)	Vapor	Liquid
Density (kg/m ³)	0.023	998
Dynamic Viscosity (kg/ms)	9.95E-06	0.0011
Vapor Pressure (kPa)	2.97	

The simulations are carried out by using the pressure-based transient solver, and a fully coupled solver is selected to solve the pressure and momentum equations. The pressure is discretized using the PRESTO! scheme, and the convection terms of the momentum equations are discretized by the QUICK scheme which is also used for the terms in turbulence equations and vapor volume fraction equation (ANSYS, 2009).

6.2.2 Input Transient Parameters Study

The current investigation is conducted with a transient solver. The time step size, Δt , and iteration numbers per time step, I_N , need to be chosen appropriately to achieve a balance between the numerical accuracy and computational efforts. The investigation of the influence of the time step size, Δt , and iteration numbers per time step, I_N , on the numerical convergence is conducted on the coarse grid G1 with the standard $SST\ k - \omega$ turbulence model and the Schnerr-Sauer cavitation model with bubble number density of $1e+13$.

Time Step Size

The time step size for the transient solver could be estimated by the following methodologies:

- **Courant Number Methodology:** The flow is allowed to travel over an estimated characteristic length of the cells over the hydrofoil during each time step. The time step size based on this methodology can be written as:

$$\Delta t = \Delta x \cdot Courant / U_{ref} \quad (6-1)$$

where *Courant* is the courant number which is supposed to be one or less, Δx represents a characteristic length scale, which could be estimated from the spatial structures as a certain percent of the chord length, and U_{ref} is the reference velocity of the main flow.

- **Bubble Collapse Time Scale:** Three characteristic time scales related to the bubble dynamics described by the Rayleigh-Plesset equation are presented by Franc and Michel (2004), and they are the pressure time, the viscous time and the surface tension time. Among these three time scales, the pressure time is analogous to the Rayleigh time for the bubble collapse, and is estimated to give the smallest value. There this pressure time scale is considered as one of the estimation method of the time step size. It is defined as:

$$\tau_p = R_0 \sqrt{\frac{\rho}{p_{ref} - p_v}} \quad (6-2)$$

where R_0 is the initial radius, representing the length scale, ρ is the density, and $p_{ref} - p_v$ is the characteristic pressure difference between the reference pressure and vapor pressure.

- **Turbulent Time Scales:** One of the main properties of a turbulent flow is its multiscale aspect. The largest turbulent time scale can be estimated from the time for the flow travelling through the boundary layer thickness, and the smallest turbulent time scale, also named as Kolmogorov time scale, is defined as:

$$\tau_\eta = \left(\frac{\nu}{\varepsilon} \right)^{\frac{1}{2}} \quad (6-3)$$

where ν is the kinematic viscosity, representing the ratio between the dynamic viscosity μ and the density ρ , and ε represents the average rate of energy dissipation per unit volume.

Among the three methodologies, the Courant Number Methodology is chosen for the estimation of the time step size, because it is capable of revealing the resolution in the

spatio-temporal relationship. The other two methodologies seem to consider about only one specific aspect of the physics involved in the simulation of cavitating flow.

To start the computations, the characteristic length scale in equation (6-1) is estimated by using the discretized cell numbers on the foil: $\Delta x \approx 0.012C$, where C is the chord length, equaling to 0.2m in the current case. Three time step sizes are respectively selected as $5 \times 10^{-4} s$, $2 \times 10^{-4} s$ and $1 \times 10^{-4} s$, as shown in Table 6-4.

Table 6-4: Properties of the selected time step size

Δt (s)	$\Delta x/C$	C (m)	U (m/s)	Courant Number
5.00E-04	0.012	0.2	6	1.25
2.00E-04	0.012	0.2	6	0.50
1.00E-04	0.012	0.2	6	0.25

Iteration Numbers per Time Step

The convergence criterion for the residual of each equation is set to be a sufficiently small value of 10^{-8} . The definition of the residual of each equation has been introduced in section 4.5.1, which was the scaled overall imbalance in the governing equations (related to equation (4-33)). A thorough study on the required iteration numbers per time step starts from a quasi-converged solution obtained with a time step size of $\Delta t = 5 \times 10^{-4} s$ and the default 20 iterations per time step ($I_N = 20$). The lift and drag coefficients are approaching constant values, as well as the total volume of vapor, as represented in Figure 6-1.

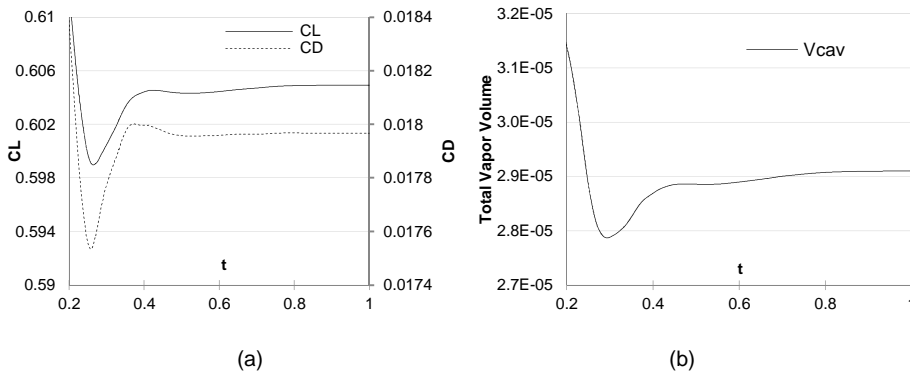


Figure 6-1: The time history of (a) lift, drag coefficients ; and (b) the total volume of vapor for the flow over a NACA0015 hydrofoil at 6° angle of attack at $\sigma = 1.6$ with time step size of $\Delta t = 5 \times 10^{-4} s$

With three different time step sizes, $5 \times 10^{-4} s$, $2 \times 10^{-4} s$ and $1 \times 10^{-4} s$, the convergence histories of the residual of each equation and the volume integral of the mass transfer rate during two successive time steps are investigated to examine whether the default 20 iterations in FLUENT (ANSYS 12.0) are sufficient, as illustrated in Figure 6-2.

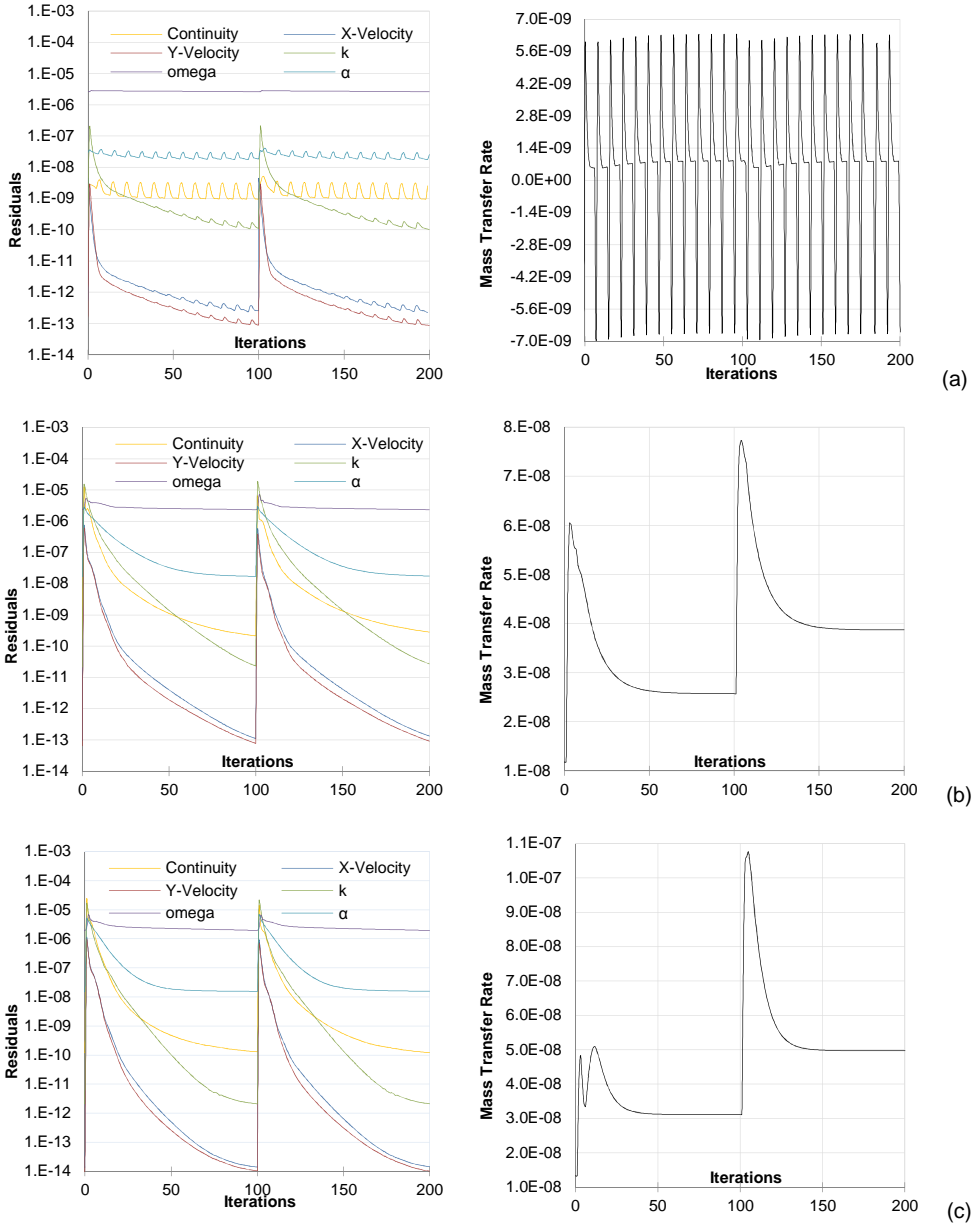


Figure 6-2: The convergence histories of the residuals and the mass transfer rate during two successive time steps for the flow over a NACA0015 hydrofoil at 6° angle of attack at $\sigma = 1.6$ with time step size of (a) $5 \times 10^{-4} s$, (b) $2 \times 10^{-4} s$ and (c) $1 \times 10^{-4} s$

The choice of the iteration number during each time step is based on the assumption that dynamic equilibrium occurs in each time step. Therefore, the first criterion is addressed to the adequately small residuals for all governing equations. It should be noted that the

residual of α is calculated based on the transport equation for vapor volume fraction α , related to equation (4-21) & (4-27), representing the imbalance of the following equation:

$$\frac{\rho_v \rho_l}{\rho_m} \frac{D\alpha}{Dt} = S \quad (6-4)$$

where:

- ρ_v , ρ_l and ρ_m are the density of vapor, liquid and mixture, respectively
- α is the vapor volume fraction
- S is the mass transfer rate, i.e. the net mass source term

In Figure 6-2, the right plots represent the volume integral of the mass transfer rate S at the interface of vapor/liquid, which should arrive at an invariant quantity as an indication of the number of iterations performed during each time step. In summary, the choice of the proper iteration number per time step is made dependent on the convergence of the volume integral of mass transfer rate between the interface and adequately small residuals.

It is observed that the convergence history of the mass transfer rate shows a fluctuating behavior for the time-step of $\Delta t = 5 \times 10^{-4} s$ but within a very small magnitude, whereas the mass transfer rate got converged during each time step when the smaller time step sizes $\Delta t = 2 \times 10^{-4} s$ and $\Delta t = 1 \times 10^{-4} s$ are adopted. It is thus found that about 60 iterations per time step are demanded for the time step size of $\Delta t = 2 \times 10^{-4} s$ and 45 iterations for $\Delta t = 1 \times 10^{-4} s$.

Results and Discussions

In order to investigate the influence of the time step size, Δt , and iteration numbers per time step, I_N , the calculations are conducted on three time step sizes with the suggested sufficient iteration number:

- Coarse grid G1, $\Delta t = 5 \times 10^{-4} s$ and $I_N = 100$
- Coarse grid G1, $\Delta t = 2 \times 10^{-4} s$ and $I_N = 60$
- Coarse grid G1, $\Delta t = 1 \times 10^{-4} s$ and $I_N = 45$

In a totally steady flow, there is no net change in the total vapor volume and the integral of the source term should vanish (Hoekstra and Vaz, 2009), that is to say:

$$\frac{d}{dt} \int \alpha dV = \int \frac{S}{\rho_v} dV = 0 \quad (6-5)$$

It is indicated that the fully converged solution should satisfy the above equation. Apart from the criterion of the supposed vanished volume integral of the source term, the flow

characteristics, such as lift and drag, are also supposed to be stable when the solution becomes converged. It is assumed that in each time step there is no dynamic equilibrium occurs. The lift and drag coefficients finally reach stable values after hundreds of time steps, as listed in Table 6-5. Simultaneously, the volume integral of the mass transfer rate reaches a very small value in the order of 10^{-9} for all three time step sizes. The “Deviation” terms in the table represent the relative differences between the solutions, and are defined as:

$$\epsilon_a = \frac{|\phi_h - \phi_{ah}|}{\phi_h} \tag{6-6}$$

where a is a ratio between the two time step size, and ϕ_h and ϕ_{ah} are the solutions for smaller time step size and larger time step size, respectively.

Table 6-5: Flow characteristics comparison with different time step size

Δt (s)	CL	CD	Vcav
5.00E-04	0.6049	0.0180	2.9105E-05
2.00E-04	0.6047	0.0180	2.9104E-05
Deviation1(%)	0.033%	0.463%	0.001%
1.00E-04	0.6042	0.0182	2.9050E-05
Deviation2(%)	0.091%	0.720%	0.188%

It can be observed that the deviation between the solutions by $\Delta t = 5 \times 10^{-4} s$ and $\Delta t = 2 \times 10^{-4} s$ are smaller than the deviation between the solutions by $\Delta t = 2 \times 10^{-4} s$ and $\Delta t = 1 \times 10^{-4} s$. However, all of these deviations are very small, and the maximum value is 0.72% .

A steady sheet cavity is obtained with a small reversed flow which fills with a mixture of liquid and vapor. Similar distributions of the pressure coefficient and the vapor volume fraction along the NACA0015 hydrofoil with an angle of attack of 6° at $\sigma = 1.6$ can be observed for three different time step sizes, as shown in Figure 6-3.

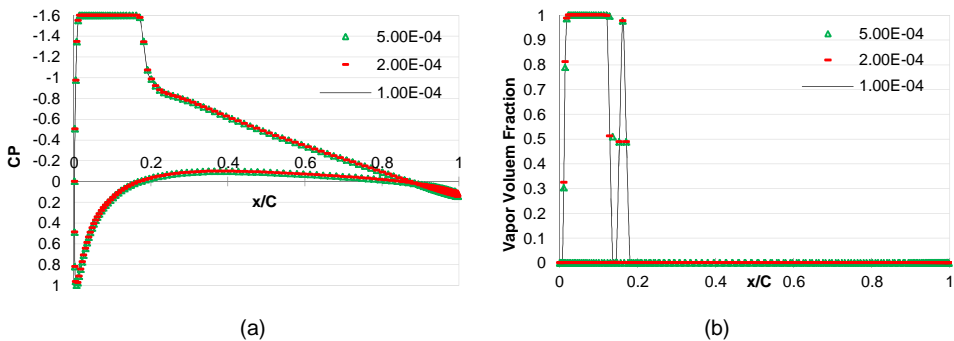


Figure 6-3: The distributions of (a) pressure coefficients and (b) vapor volume fraction along a NACA0015 hydrofoil with an angle of attack of 6° at $\sigma = 1.6$ for different time step size

From the plot of the vapor volume fraction distribution over the hydrofoil (Figure 6-3 (b)), it can be observed that there is a sudden change from around 14% chord length to 20% chord length, indicating a mixture of liquid and vapor appears over this region.

The contours of the vapor volume fraction and the velocity vectors are compared in Figure 6-4. The enlargement of the vector plot shows that there is a reversed flow appearing at the rear region of the sheet cavity. It can also be observed that a mixture with fluid and vapor appears at the same location, extending from around 14% chord length to 20% chord length from the leading edge.

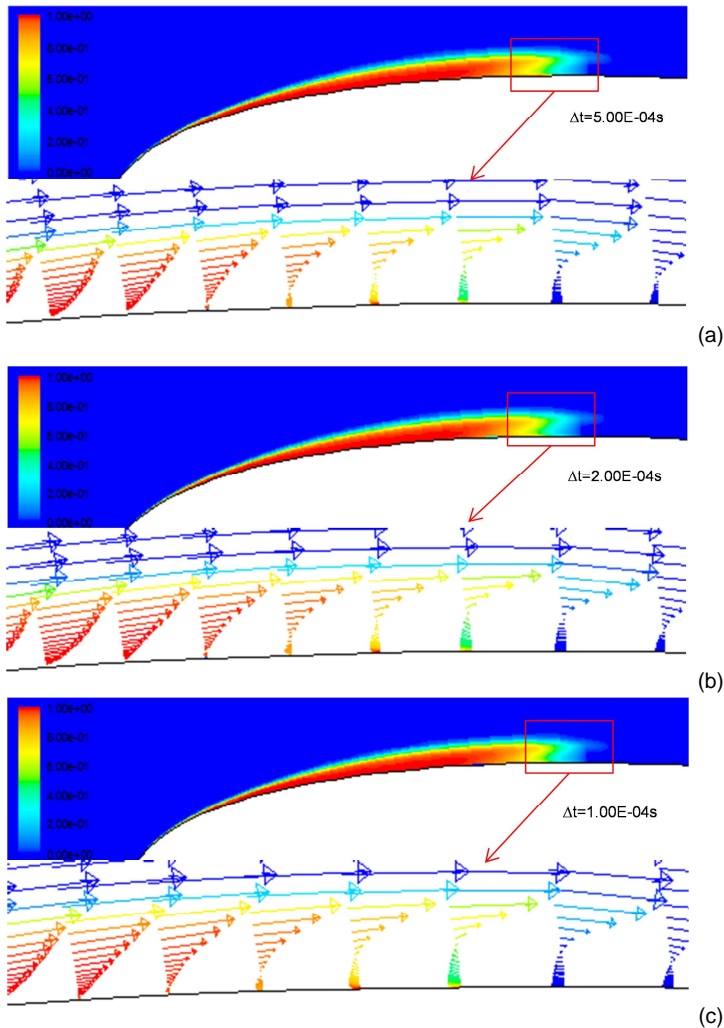


Figure 6-4: The contours of the vapor volume fraction and the vectors of the velocity for a NACA0015 hydrofoil with an angle of attack of 6° at $\sigma = 1.6$ for different time step sizes of (a) $\Delta t = 5 \times 10^{-4} s$, (b) $\Delta t = 2 \times 10^{-4} s$ and (c) $\Delta t = 1 \times 10^{-4} s$ (Flow from left to right)

It can be concluded that the time step size does not influence the predicted results significantly under a steady cavitating condition. The time step size of $\Delta t = 2 \times 10^{-4} s$ seems a good balance between the computational effort and the numerical accuracy. A guideline for the selection of the time step size could be addressed to the equation (6-1) with a courant number at most in a value of one.

6.2.3 Influence of the Temporal Discretization Scheme

For transient flows, the equations are discretized in both space and time. Temporal discretization involves the integration of every term in the differential equations over a time step Δt . Two schemes are available under the pressure-based transient solver in FLUENT (ANSYS 12.0): first-order implicit and second-order implicit (ANSYS, 2009).

Definition of the Temporal Discretization Scheme

Take the time evolution of an arbitrary variable ϕ as an example, the time evolution can then be expressed in a generic formulation:

$$\frac{\partial \phi}{\partial t} = F(\phi) \quad (6-7)$$

where the function $F(\phi)$ incorporates any spatial discretization.

Then the first-order implicit temporal discretization is given by:

$$\frac{\phi^{n+1} - \phi^n}{\Delta t} = F(\phi^{n+1}) \quad (6-8)$$

The second-order implicit temporal discretization is given by:

$$\frac{3\phi^{n+1} - 4\phi^n + \phi^{n-1}}{2\Delta t} = F(\phi^{n+1}) \quad (6-9)$$

where:

- ϕ is an arbitrary variable to be studied
- ϕ^n is the value at the current time t
- ϕ^{n+1} and ϕ^{n-1} are the values at the next time, $t + \Delta t$, and the previous time, $t - \Delta t$, respectively

This is referred to as implicit integration since ϕ^{n+1} in a given cell is related to ϕ^{n+1} in the neighboring cell through $F(\phi^{n+1})$, and the implicit equation will be solved iteratively at each time before moving to the next time step.

Results and Discussions

By examining the time histories of the residuals of each equation and the volume integral of mass transfer rate during each time step ($\Delta t = 2 \times 10^{-4} s$), convergence will be achieved after 60 iterations per time step with the second-order implicit temporal discretization scheme, see Figure 6-5.

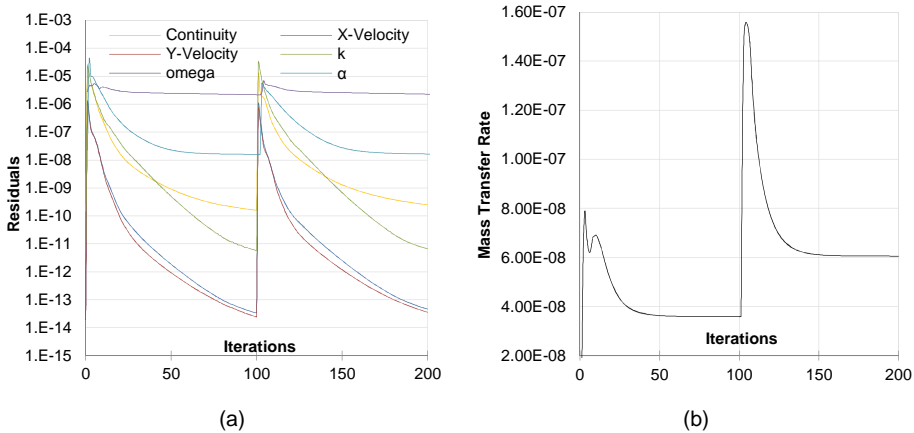


Figure 6-5: The time histories of the (a) residuals and (b) mass transfer rate during two successive time steps with second-order implicit temporal discretization scheme for the flow over a NACA0015 hydrofoil at 6° angle of attack at $\sigma = 1.6$ with time step size of $\Delta t = 2 \times 10^{-4} s$ for the coarse grid G1

The lift, drag coefficients and the total vapor volume calculated with different order of temporal discretization scheme are compared in Table 6-6. The deviation between the lift coefficients obtained with these two schemes is very small, with an absolute value of 0.06%. The maximum absolute deviation among the drag coefficients and the total vapor volume is even within 0.4% .

Table 6-6: Flow characteristics comparison with different temporal discretization schemes

TemporalDiscretization	CL	CD	Vcav
1st-order implicit	0.6047	0.0180	2.9104E-05
2nd-order implicit	0.6044	0.0181	2.9050E-05
Deviation(%)	-0.06%	0.37%	-0.19%

For different orders of the temporal discretization schemes, the distributions of the pressure coefficient and the vapor volume fraction along the NACA0015 hydrofoil at $\sigma = 1.6$ are shown in Figure 6-6. The profiles in each plot are graphically indistinguishable. The length of the cavity predicted by the second-order implicit temporal discretization scheme takes up around 20% chord length of the foil, which is the same as the results predicted by the

first-order implicit. Similarly, the reversed flow filled with a mixture of fluid and vapor can be observed at the same location, $14\%C \sim 20\%C$, for both orders of temporal discretization schemes.

It can then be concluded that the order of the temporal discretization scheme does not play a primary role on the integral quantities. Considering the more complex formulation involved in the second-order implicit temporal discretization scheme, the first-order implicit scheme will be adopted in the following simulations to balance the computational efforts and the numerical accuracy.

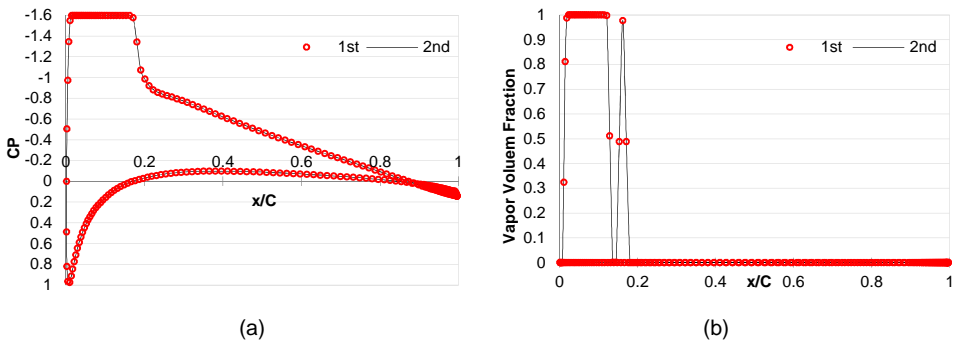


Figure 6-6: The distributions of (a) pressure coefficients and (b) vapor volume fraction along a NACA0015 foil at 6° angle of attack at $\sigma = 1.6$ for different orders of temporal discretization scheme

6.2.4 Grid Sensitivity

The sensitivity of the grid densities is examined on three geometrically similar grids with a substantially refinement level. The time step sizes are adopted as $\Delta t = 2 \times 10^{-4} s$ with a courant number of one or smaller for each grid, as shown in Table 6-7.

Table 6-7: Properties of the grids related to the time step size

Grid	Level	Δt (s)	$\Delta x/C$	Courant Number
G1	Coarse	0.0002	0.012	0.5
G2	Medium	0.0002	0.08	0.75
G3	Fine	0.0002	0.006	1

The appropriate iteration numbers per time step I_N for the two refiner grids are investigated by checking both of the time histories of residuals and volume integral of mass transfer rate between the phase interface, as shown in Figure 6-7 and Figure 6-8. It reveals that 60 iterations per time step satisfy the convergence criteria for the medium grid G2, whereas 100 iterations per time step are demanded for the fine grid G3.

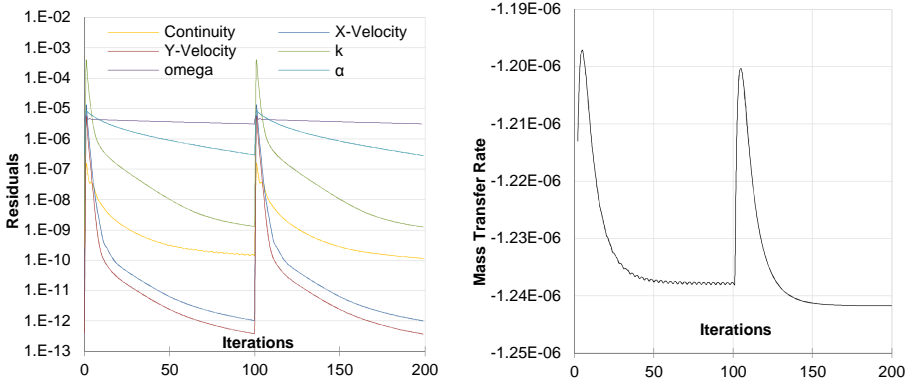


Figure 6-7: Time histories of the residuals and mass transfer rate during two successive time steps for a NACA0015 hydrofoil at 6° angle of attack at $\sigma = 1.6$ for the medium grid G_2

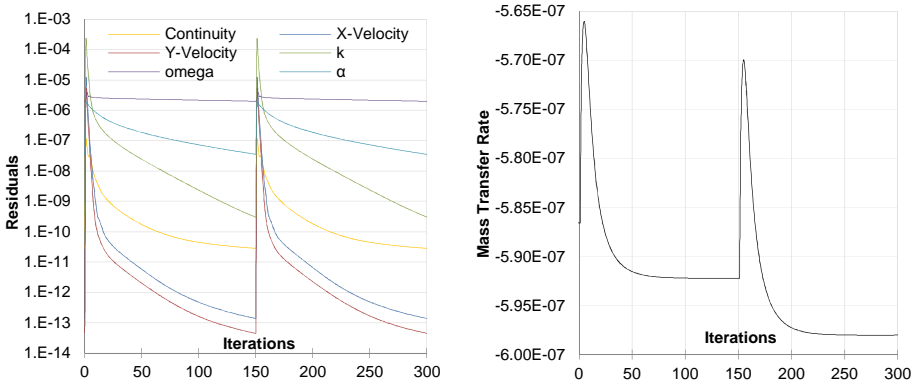


Figure 6-8: Time histories of the residuals and mass transfer rate during two successive time steps for a NACA0015 hydrofoil at 6° angle of attack at $\sigma = 1.6$ for the fine grid G_3

The lift and drag coefficients and their respective contributions by pressure and viscous stresses predicted by the three grids are listed in Table 6-8, where R_k is the convergence ratio, an important indicator for the convergence condition, as defined in section 4.5.2. The numerical error is estimated for the fine grid G_3 , referred to the equation (4-37). Based on the information given in the Table 5-1, the cell size ratio equals 1.5, i.e. $r_k = 1.5$.

Table 6-8: Flow characteristics comparison with different grid densities

Grid	CL_P	CL_V	CL	CD_P	CD_V	CD
G1	0.6050	-0.0002	0.6047	0.0120	0.0061	0.0180
G2	0.6103	-0.0003	0.6100	0.0118	0.0062	0.0181
G3	0.6124	-0.0003	0.6122	0.0117	0.0064	0.0181
Rk	0.41	0.60	0.41	0.99	0.78	-0.09

For the lift coefficient, monotonic convergence is achieved ($0 < R_k < 1$), and the numerical error δ_k^* can be estimated by the Richardson Extrapolation Technique (see equation (4-37) and (4-38)), which gives $|\delta_k^*| \sim o(10^{-3})$. The uncertainty U_k can be estimated by adopting the factor of safety approach, i.e. $U_k = 1.25|\delta_k^*|$, also giving $U_k \sim o(10^{-3})$. For the drag coefficient, oscillatory convergence is achieved ($-1 < R_k < 0$), and the uncertainty U_k can be estimated by the bounding errors between the maximum and minimum solutions, i.e. $U_k = (S_{\max} - S_{\min}) / 2$, giving $U_k \sim o(10^{-5})$.

The distributions of the pressure coefficient and the vapor volume fraction along the NACA0015 hydrofoil for the three grids are illustrated in Figure 6-9. It can be observed that the distributions of the pressure coefficient only show differences at the suction side around 20% C (C =chord length) from the leading edge. The larger cavity region is obtained for the fine grid $G3$. This is also confirmed by the plot of the vapor volume fraction distribution. The differences between the distributions of the vapor volume fraction that are in Figure 6-9 are very small. The length of the cavity predicted by the fine grid $G3$ is however 1.5% C longer than what is obtained by the medium grid $G2$.

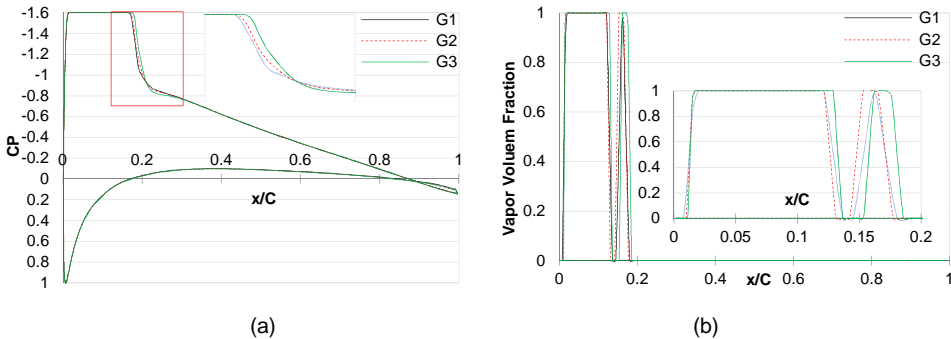


Figure 6-9: The distribution of (a) pressure coefficient and (b) vapor volume fraction along the NACA0015 hydrofoil for three grids with at 6° angle of attack at $\sigma = 1.6$ with time step size of $\Delta t = 2 \times 10^{-4} s$

More details can be observed at the rear of the sheet cavity for the fine grid $G3$, see Figure 6-10, where the red color indicates pure vapor and blue color indicates pure liquid. Additionally, the turbulent kinetic energy (k) for three grids are respectively illustrated in Figure 6-11. It is seen here that no significant difference can be observed, indicating that the turbulent kinetic energy is not significantly influenced by the grid. It can be concluded that the integral forces and the turbulent kinetic energy are grid independent based on current grid resolution. However, the length and the total volume of the sheet cavity show some discrepancies in the closure region. The clearly observed clearer reverse flow on the fine grid $G3$ indicates that more resolution can be obtained with the finer grid.

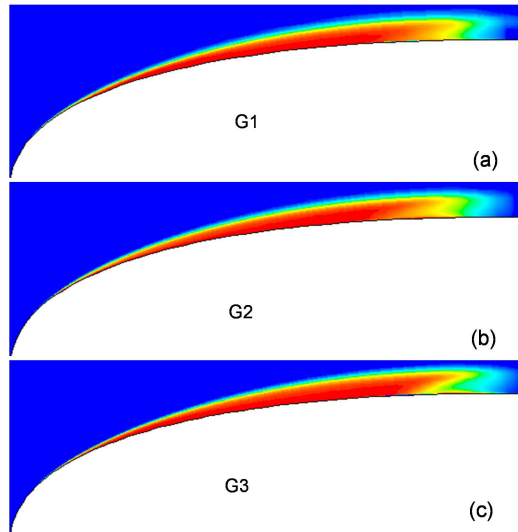


Figure 6-10: Contours of vapor volume fraction for a NACA0015 hydrofoil at 6° angle of attack at $\sigma = 1.6$ with $\Delta t = 2 \times 10^{-4} s$ for (a) coarse grid $G1$, (b) medium grid $G2$ and (c) fine grid $G3$ (Flow from left to right)

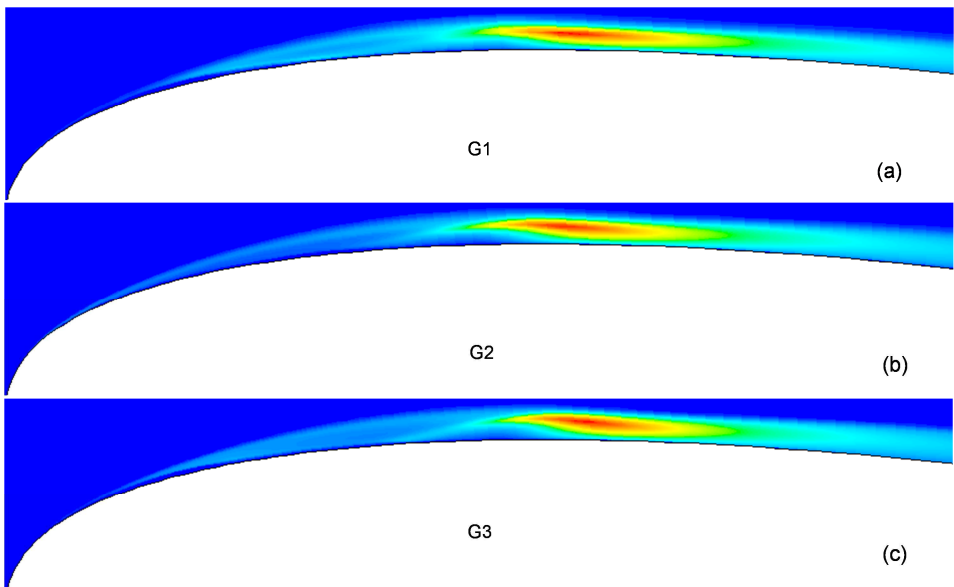


Figure 6-11: Contours of turbulent kinetic energy for a NACA0015 hydrofoil at 6° angle of attack at $\sigma = 1.6$ with $\Delta t = 2 \times 10^{-4} s$ for (a) coarse grid $G1$, (b) medium grid $G2$ and (c) fine grid $G3$ (Flow from left to right)

6.2.5 Conclusions

Some important conclusions drawn from the investigation of the steady cavitating flow over the NACA0015 hydrofoil at 6° angle of attack are summarized as follows:

- The time step size does not influence the predicted results significantly when the courant number in the estimation equation (6-1) has a value of the order of one or even smaller. Therefore, it can be used as a guideline for the appropriate time step size for a given grid.
- The order of the temporal discretization scheme does not play a primary role on the integral quantities under the steady cavitating condition. The first-order implicit scheme will be adopted in the following simulations to balance the computational efforts and the numerical accuracy.
- The integral forces and the turbulent kinetic energy are grid independent when using the current grid resolution. However, the length and the total volume of the sheet cavity show some grid dependencies in the closure region. The observed clearer reverse flow on the fine grid $G3$ indicates that more resolution of the cavity structures at the closure of the main cavity can be obtained with the finer grid.

6.3 UNSTEADY CAVITATING CONDITION

In unsteady cavitating flows over hydrofoils, it has been observed in experiments that the rear part of the sheet cavity, which develops from the leading edge, sheds off and develops into a cloud consisting of tiny bubbles and vortices.

A schematic regular break-off cycle and a sequence of High Speed Video frames are shown in Figure 6-12. The phenomena are described by De Lange and De Bruin (1998): “

- Following a previous break-off, a sheet cavity starts to grow (Figure 6-12(a-1)).
- At a certain length the growth will cease and a strong re-entrant jet is formed at the closure of the cavity (Figure 6-12(a-2)).
- This jet is directed towards the leading edge. The velocity of the (front of the) jet is of the same order of magnitude as the free stream velocity (Figure 6-12(a-3)).
- The re-entrant jet reaches the cavity near the leading edge and impinges on the cavity interface (Figure 6-12(a-4)).
- The rear part of the sheet cavitation then breaks off and transforms into a bubble cloud which is more or less cylindrical in span-wise direction (Figure 6-12(a-5)).
- The front part of the original cavity is reduced to a tiny sheet cavity, which will

grow again and the cycle starts all over. The cloud will be transported in downstream direction (Figure 6-12(a-6)).”

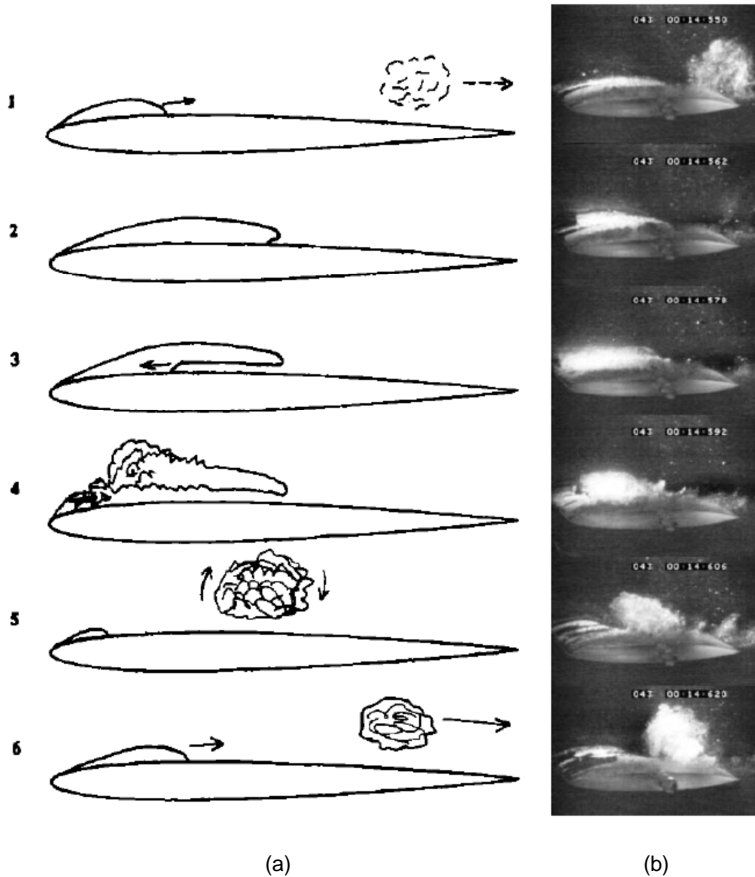


Figure 6-12: The break-off cycle: (a) Schematic view and (b) High Speed Video (HSV) observations (De Lange and De Bruin, 1998) (Flow from left to right)

In the case of a 3D cavitating flow around NACA0015 hydrofoil with tunnel sidewalls, a U-shaped cloud cavity can be observed both experimentally and numerically rather than the cylindrical shape (Saito et al., 2007). A similar phenomenon, called a horseshoe structure, has also been seen on an ALE (Asymmetric Leading Edge) hydrofoil by Dular et al. (2005). It should be noted that early shedding of small-scale vapor structures may also occur at other chord positions rather than at the leading edge. The small-scale instabilities which develop on the cavity interface and upper boundary of the re-entrant jet make that the thin vapor layer between the cavity interface and the re-entrant jet can break at many different points. The vapor structure of the sheet cavity is then broken into small vortex cavities

instead of one distinct large-scale cloud as shown in Figure 6-12.

A characteristic phenomenon associated with the sheet cavitation is its break-up behavior, leading to the shedding of patches of cavitation. However, it is found that the shedding phenomenon is not always found from a multiphase CFD code. Reboud et al. (1998) were amongst the first to conclude this and proposed a procedure to attenuate the eddy viscosity at the vapor-liquid interface to remedy this problem. Also with the RANS method implemented in FLUENT, the break-up of the sheet cavity and the corresponding periodic shedding of the cloud cavity at the trailing edge of the sheet can only be predicted by an artificial reduction of the turbulence viscosity in the regions of higher vapor volume fraction (Li et al., 2009). It should however be noted that the modification of the turbulence model based on the idea of Reboud et al. (1998) is not a prerequisite for shedding for all commercial CFD tools, as demonstrated for FreSCo (Hoekstra and Vaz, 2008) and Star-CD (Oprea, 2009a).

In this section, the capability of the RANS method implemented in FLUENT (ANSYS 12.0) to capture unsteady dynamics will be investigated for a NACA0015 hydrofoil at 6° angle of attack, and a comparison with the various numerical results supplied by VIRTUE WP4 Workshop will be made subsequently. Then the investigation will be conducted on a NACA0015 hydrofoil at 8° angle of attack to compare with the experimental observations conducted by Boorsma (2010). Finally, a NACA0018-45 hydrofoil at 6.5° angle of attack is examined where more intense dynamics are expected due to the higher adverse pressure gradient induced by this specific geometry, and experimental data are also available for this hydrofoil (Van Terwisga, 2009a).

6.3.1 2D NACA0015 ($AoA = 6^\circ$)

A specific cavitation regime with cavitation number at $\sigma = 1.0$ is investigated to examine the unsteady dynamics on the NACA0015 hydrofoil with an angle of attack at 6° . A study of the effect of the modification of the turbulence model on the unsteady dynamics, referred to section 4.3.3, will be conducted on the coarse grid *G1* at first.

The test case will be conducted on two different time step sizes, $\Delta t = 5 \times 10^{-4} s$ and $\Delta t = 2 \times 10^{-4} s$, to assess the influence of the sensitivity of time-step. The former one is the one adopted in some published papers that did simulations on the same geometry in the same cavitation regime $\sigma = 1.0$ (Hoekstra and Vaz, 2009; Li et al., 2009). The latter

time-step corresponds to the suggested value for the same geometry at the steady cavitating condition, which is estimated by equation (6-1) with a courant number of 0.5. Besides that, the grid sensitivities will be investigated to check whether it would affect the break-up phenomena.

A velocity-inlet condition is applied at the upstream boundary with the vapor fraction equal to zero. A pressure-outlet boundary condition is used at the outlet boundary. The physical properties of the two-phases, liquid and vapor, are taken at a temperature of $24^{\circ}C$, the same as the temperature in the previous case for the same geometry at steady cavitating condition. The detailed initial and boundary conditions and the flow properties are listed in Table 6-9.

Table 6-9: Boundary conditions and flow properties for a NACA0015 hydrofoil ($AoA=6^{\circ}$)

Boundary Conditions	NACA0015 ($AoA=6^{\circ}$)	
Velocity Inlet (m/s)	V=6	
Pressure Outlet(kPa)	20.9	
Tubulent Intensity (%)	1	
Tubulent Viscosity Ratio	10	
Foil	No-slip Wall	
Tunnel Walls (Top & Bottom)	Slip Wall	
Flow Properties (T=24°C)	Vapor	Liquid
Density (kg/m ³)	0.023	998
Dynamic Viscosity(kg/ms)	9.95E-06	0.0011
Vapor Pressure (kPa)	2.97	

The simulations are carried out by using the pressure-based transient solver, and a fully coupled solver is selected to solve the pressure and momentum equations. The pressure is discretized using the PRESTO! scheme, and the convection terms in the momentum equations are discretized by the QUICK scheme, which is also used for the turbulence equations and vapor volume fraction equation (ANSYS, 2009). The temporal discretization uses the first-order implicit scheme.

Results for the Standard SST $k - \omega$ Turbulence Model

In line with the analysis carried out for the steady cavitating condition, an investigation on the temporal parameters, time step size Δt and iteration number per time step I_N , will be conducted on the coarse grid G1.

As can be seen from the plots of the residuals for each equation and the volume integral of the mass transfer rate, convergence can only be achieved with 100 iterations per time step for $\Delta t = 5 \times 10^{-4} s$ and 50 iterations for $\Delta t = 2 \times 10^{-4} s$, see Figure 6-13.

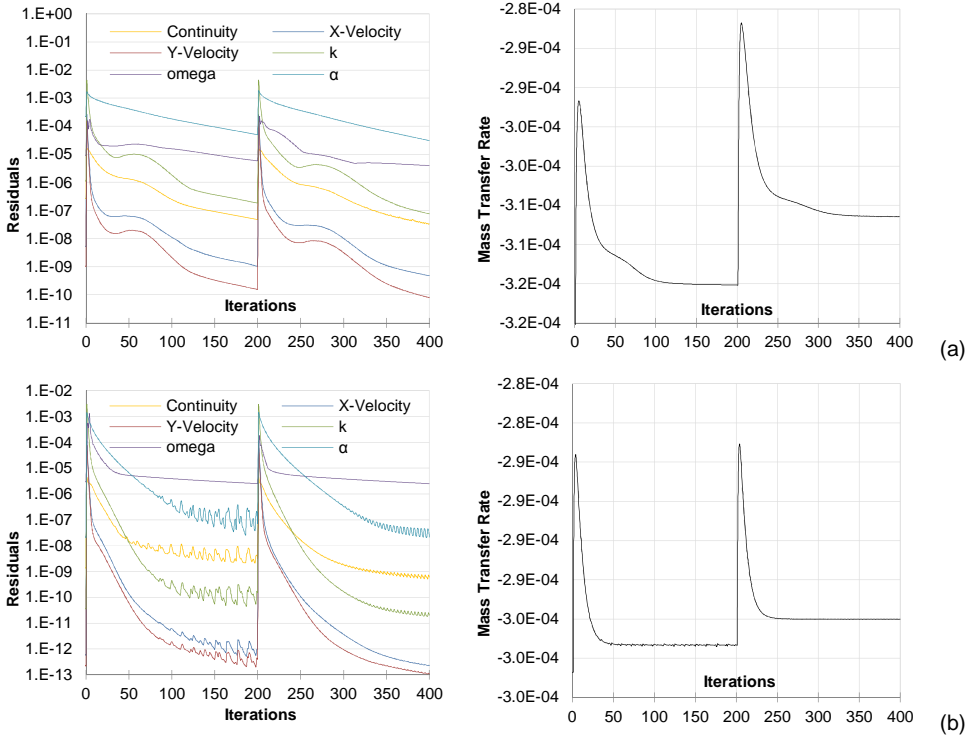


Figure 6-13: The time histories of the residuals and mass transfer rate during two successive time steps with (a) $\Delta t = 5 \times 10^{-4} s$; and (b) $\Delta t = 2 \times 10^{-4} s$ for a NACA0015 hydrofoil at 6° angle of attack at $\sigma = 1.0$ on coarse grid $G1$

For a time step size of $\Delta t = 5 \times 10^{-4} s$, the time histories of the total vapor volume predicted using the suggested iteration numbers per time step for convergence are compared with the default 20 iterations in Figure 6-14. The two profiles are slightly different in magnitude, but have a similar first harmonic frequency, 4.33 Hz for 100 iterations and 4.76 Hz for the 20 iterations, see Figure 6-15.

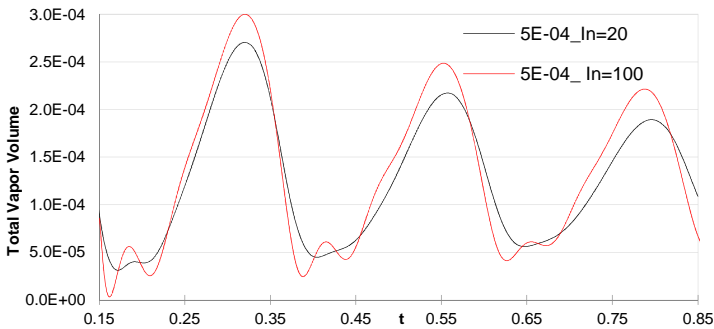


Figure 6-14: Time histories of the total vapor volume obtained by different I_N with $\Delta t = 5 \times 10^{-4} s$

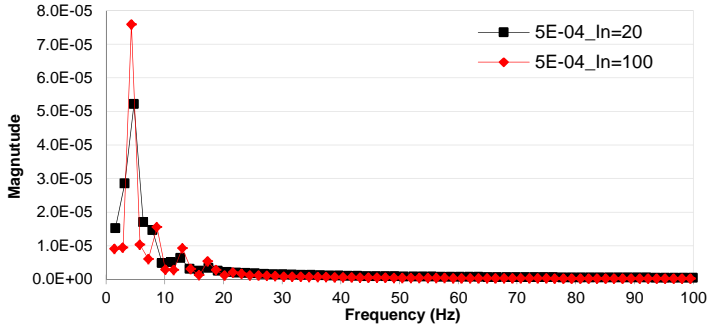


Figure 6-15: Spectral analysis of the time history of the total vapor volume shown in Figure 6-14

For a time step size of $\Delta t = 2 \times 10^{-4} s$, a comparison of the time histories of the total vapor volume predicted by different iteration numbers I_N per time step are shown in Figure 6-16. The differences between the two profiles are very small, and a same frequency of 4.37 Hz can be obtained from a FFT analysis, see Figure 6-17.

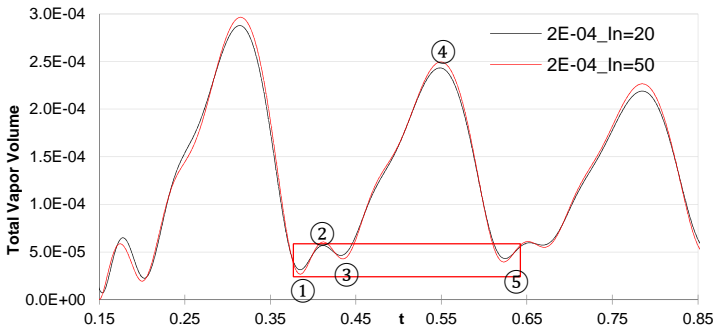


Figure 6-16: Time histories of the total vapor volume obtained by different I_N with $\Delta t = 2 \times 10^{-4} s$

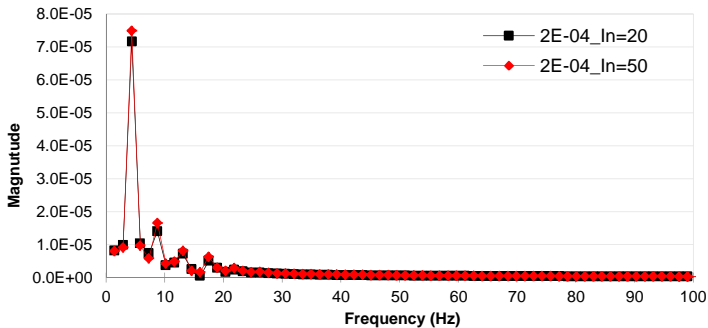


Figure 6-17: The spectral analysis of convergence histories of the total vapor volume (Figure 6-16)

A comparison of the results predicted by the different time step size with their suggested iteration number per time step is shown in Figure 6-18. The two plots match each other,

indicating that the unusual discrepancy of the results predicted using 20 iterations (default value in FLUENT) per time step would be fixed by using a sufficient number of iteration per time step. It is noted that the required number of iterations is time step dependent.

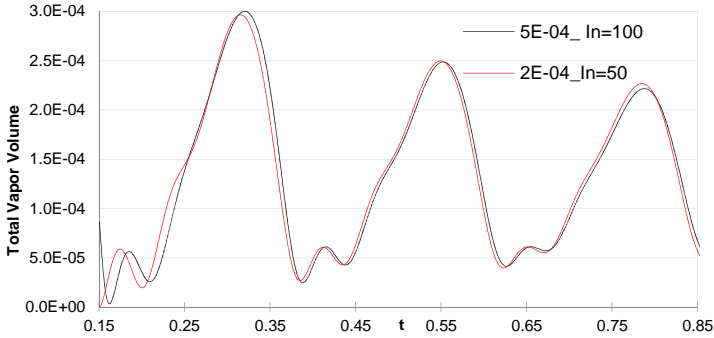


Figure 6-18: Time histories of the total vapor volume obtained by 100 iterations per time step with time step size $\Delta t = 5 \times 10^{-4} s$ and 50 iterations per time step with $\Delta t = 2 \times 10^{-4} s$

It can be also observed that it is not sensitive to the iteration number I_N per time step when we use the time step size $\Delta t = 2 \times 10^{-4} s$. On the contrary, for the time step size $\Delta t = 5 \times 10^{-4} s$, there is a big discrepancy between the results predicted by the default 20 iterations per time step and the required iteration number for convergence, $I_N = 100$.

By checking the convergence history of the volume integral of the mass transfer rate during one time step (related to Figure 6-13), the relative deviations between the sufficiently converged value and the value obtained from the default 20 iterations are investigated further, where this relative deviation is normalized with the converged value, see Table 6-10.

Table 6-10: Relative deviations between the sufficiently converged value and the value obtained from the default 20 iterations

Time Step Size	Mass Transfer Rate		Deviation
	In=20	Converged	
$\Delta t=5E-04s$	-2.9607E-04	-3.0571E-04	3.15E-02
$\Delta t=2E-04s$	-2.9321E-04	-2.9497E-04	5.94E-03

The relative deviation for the time step size $\Delta t = 5 \times 10^{-4} s$ is around five times higher than the deviation for $\Delta t = 2 \times 10^{-4} s$. It indicates that the sensitivity of the solutions to the iteration numbers I_N per time step is monitored by the convergence behavior of the volume integral of the mass transfer rate. An incomplete calculation for each time step may lead to

inaccurate predictions, especially when the volume integral of the mass transfer rate gets converged slowly.

For all of the calculations, the basic phenomena are similar. Only a back-and-forth oscillating sheet cavity is obtained without any unsteady shedding dynamics. Five typical instants during one cycle (red framed period in Figure 6-16) of the contours of vapor fraction predicted by the required iteration number per time step, $I_N = 50$, are shown in Figure 6-19. However, according to the results from the VIRTUE WP4 Workshop, a number of other RANS codes find an unsteady cyclic shedding on the NACA0015 hydrofoil with an angle of attack of 6° at $\sigma = 1.0$ (Hoekstra and Vaz, 2008; Oprea, 2009a; Li et al., 2009).

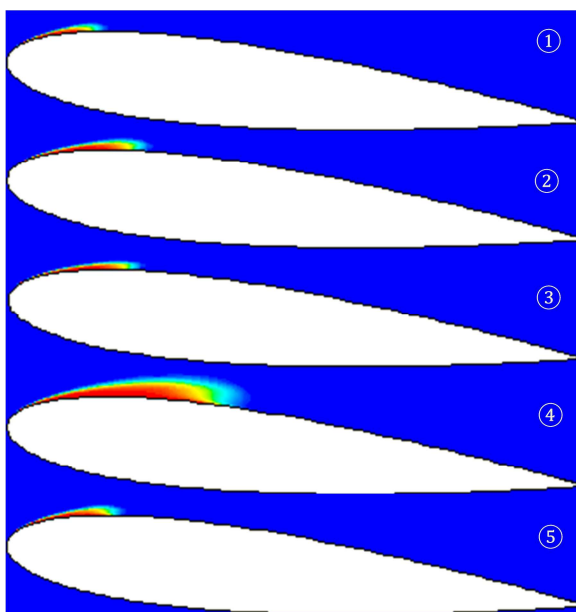


Figure 6-19: Contours of vapor fraction during one cycle for a NACA0015 hydrofoil at 6° angle of attack at $\sigma = 1.0$ with the standard *SST* $k - \omega$ model on the coarse grid *G1* (Flow from left to right)

The expected unsteady cyclic shedding is still not obtained after a thorough study of the possible factors that may retard the break-up dynamics, such as the grid sensitivity, higher order temporal discretization scheme, bubble number density (input parameter in the cavitation model). This suggests a lack of compliance with physics for the prediction of the turbulent quantities of the standard *SST* $k - \omega$ turbulence model, which led us to a further investigation of the modified *SST* $k - \omega$ turbulence model following the idea of Reboud et al. (1998).

Results for the Modified SST $k - \omega$ Turbulence Model (Reboud et al., 1998)

It was suggested in the literature that the expected unsteady dynamic shedding on the hydrofoils would not be triggered unless one applies Reboud's modification for the eddy viscosity in the region of the vapor-liquid interface (Sorguven, 1998; Li et al., 2009). We now turn to the application of Reboud's correction.

The effect of the time step size and the iteration numbers per time step I_N on the unsteady shedding dynamics (e.g. shedding frequency) will be investigated on the test cases with two time step sizes: $\Delta t = 5 \times 10^{-4} s$ and $\Delta t = 2 \times 10^{-4} s$, and with different iteration numbers per time step I_N , as summarized below:

- $\Delta t = 5 \times 10^{-4} s$ with $I_N = 20$
- $\Delta t = 5 \times 10^{-4} s$ with $I_N = 100$
- $\Delta t = 2 \times 10^{-4} s$ with $I_N = 20$
- $\Delta t = 2 \times 10^{-4} s$ with $I_N = 50$

Based on the idea of Reboud et al. (1998) to modify the standard $k - \varepsilon$ turbulence model, the standard SST $k - \omega$ model is modified by applying an artificial reduction of the turbulence viscosity in the regions of higher vapor volume fraction. It is found that the modified SST $k - \omega$ turbulence model can indeed predict the break-up of the sheet cavity and also the periodic shedding of the cloud cavity at the trailing edge of the sheet. Though the basic unsteady shedding phenomena can be captured in all of the four cases, the predicted shedding frequencies differ from each other.

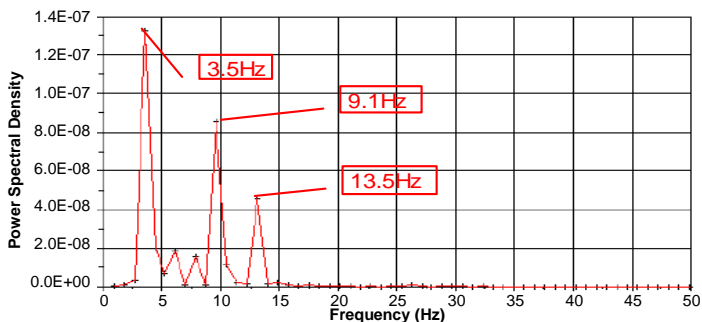
The FFT analysis is conducted on the time histories of the total vapor volume for the case adopting $\Delta t = 5 \times 10^{-4} s$ with $I_N = 20$ in the first instance. The periodic shedding of the cloud cavity at the trailing edge after break-up of the sheet cavity occurs with a first harmonic frequency of $f \approx 3.42 Hz$, which is almost equal to the first main frequency $f \approx 3.5 Hz$ reported by Li et al. (2009), as shown in Figure 6-20. This is in significant disagreement with the frequency of $f \approx 24 Hz$ reported by Koop (2008).

Koop (2008) also presented some of the published frequencies on the same geometry, NACA0015 hydrofoil at 8° of angle of attack. An experimentally observed frequency of $f \approx 16 Hz$ found by Keller and Arndt (1999) was referred by Schnerr et al. (2006) and Li et al. (2009). Some of the published numerically obtained frequencies are summarized in Table 6-11, and neither of them is as low as what is observed above, i.e. $f \approx 3.42 Hz$.

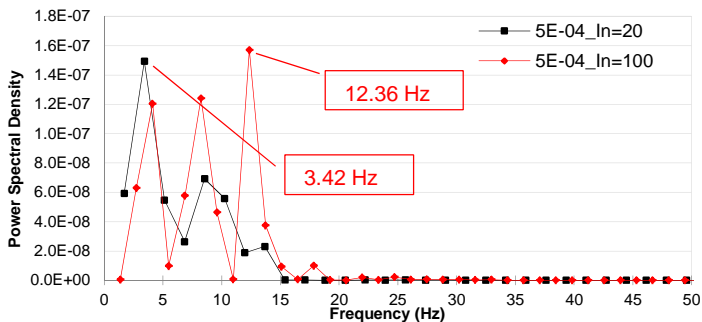
Table 6-11: Summary of the numerically obtained frequencies

Author	Frequency (Hz)
Sauer (2000)	≈11
Schnerr et al (2006)	≈11.18 (Incompressible)
	≈9 (Compressible)
Koop (2008)	≈24
Oprea (2009a)	≈14
Hoekstra and Vaz (2008)	≈15.4

By increasing the default 20 iterations per time step to the number of 100 iterations during each time step of $\Delta t = 5 \times 10^{-4} s$, a larger main shedding frequency of $f \approx 12.36 Hz$ is obtained, see Figure 6-20. It should be noted that the FFT analysis for the cases adopting $\Delta t = 5 \times 10^{-4} s$ is based on the total vapor volume over ten cycles that already eliminate the start-up effect.



(a)



(b)

Figure 6-20: Shedding frequencies based on FFT analysis of the integrated vapor volume predicted by (a) Li et al.(2009); and (b) the current approach with $\Delta t = 5 \times 10^{-4} s$ and two different iteration number per time step for a NACA0015 hydrofoil at 6° angle of attack

For the instances with time step of $\Delta t = 2 \times 10^{-4} s$, the default 20 iterations per time step predicts a first harmonic frequency of $f \approx 5.41 Hz$, whereas for the case with $I_N = 50$, a main natural frequency of $f \approx 11 Hz$ is obtained, as shown in Figure 6-21. The two charts respectively display the shedding frequencies based on spectral analysis of the integrated

vapor volume and lift coefficients for $\Delta t = 2 \times 10^{-4} s$ with different iteration numbers per time step. It should be noted that the FFT analysis for the cases adopting $\Delta t = 2 \times 10^{-4} s$ is based on the total vapor volume over eight cycles that already eliminate the start-up effect.

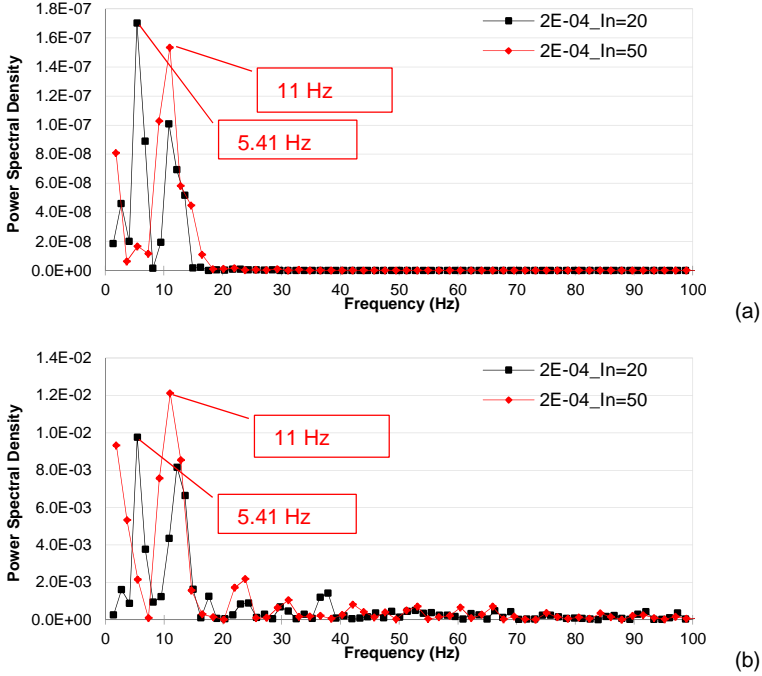


Figure 6-21: Shedding frequencies based on FFT analysis of the (a) integrated vapor volume; and (b) lift coefficient, for $\Delta t = 2 \times 10^{-4} s$ with different I_N for a NACA0015 hydrofoil at 6° angle of attack

By studying the time history of the total vapor volume (Figure 6-22), it is observed that the unsteady behavior of the cavity is not exactly periodic, but show an irregular pattern. The corresponding shedding dynamics is therefore not repeatable.

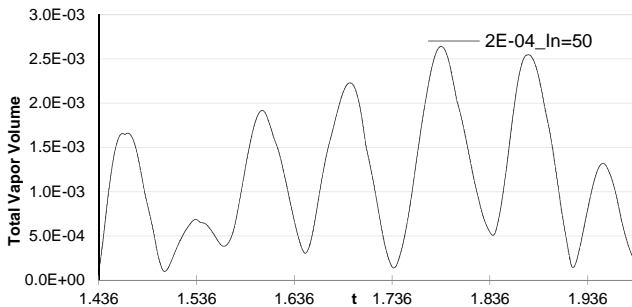


Figure 6-22: Time history of the integrated vapor volume by $\Delta t = 2 \times 10^{-4} s$ with $I_N = 50$ for a NACA0015 hydrofoil at 6° angle of attack

A typical cycle is selected to show the essential features of the unsteady shedding dynamics predicted by the modified *SST* $k - \omega$ turbulence model with $\Delta t = 2 \times 10^{-4}$ and $I_N = 50$. Twelve instants that describe the characteristic unsteady dynamics are shown in Figure 6-23, and they can be illustrated as follows:

- A sheet cavity is growing from the leading edge after the last cavity pinch-off, and a cloud cavity from the last shedding is visible downstream (Figure 6-23-①);
- The sheet cavity continues growing. The cloud cavity is convected with the main flow and starts to collapse downstream. A new cavity develops at the trailing edge (Figure 6-23-②);
- The sheet cavity ceases growing at a certain length, and both the cloud cavity and the newly developed cavity at the trailing edge of the hydrofoil are almost completely collapsed. The rear part of the sheet cavity shows a triangle shape and tends to shed off cavities (Figure 6-23-③④);
- A vortical vapor structure is shed off from the main sheet cavity, travels along with the main flow and collapses downstream of the sheet cavity. The front part of the sheet cavity decreases, and subsequently tends to shed off small vapor structures again (Figure 6-23-⑤⑥);
- A second shedding of smaller scale structures (already visible in Figure 6-23-⑥) than the first shedding occurs around the mid-chord, and the two shed vapor structures merge into a mixture with a relatively lower vapor fraction than the upstream sheet cavity (Figure 6-23-⑦);
- The leading edge sheet cavity continues to decrease and simultaneously sheds even smaller vapor structure (Figure 6-23-⑧⑨);
- The sheet cavity near the leading edge completely collapses and this causes a sudden increase of the vapor fraction of the downstream merged mixture (Figure 6-23-⑩);
- The third shed tiny vapor structure travels along with the main flow and collapses downstream, causing several vapor structures to develop near the leading edge. Simultaneously, the mixture that is located near the trailing edge of the hydrofoil collapses, causing several vapor structures to develop from around 60% chord length, just in front of the mixture (Figure 6-23- ⑪);
- These vortical vapor structures are convected with the flow and tend to merge into the larger vapor structures near the trailing edge of the foil. A tiny sheet cavity from the leading edge grows again, and a new cycle starts (Figure 6-23-⑫).

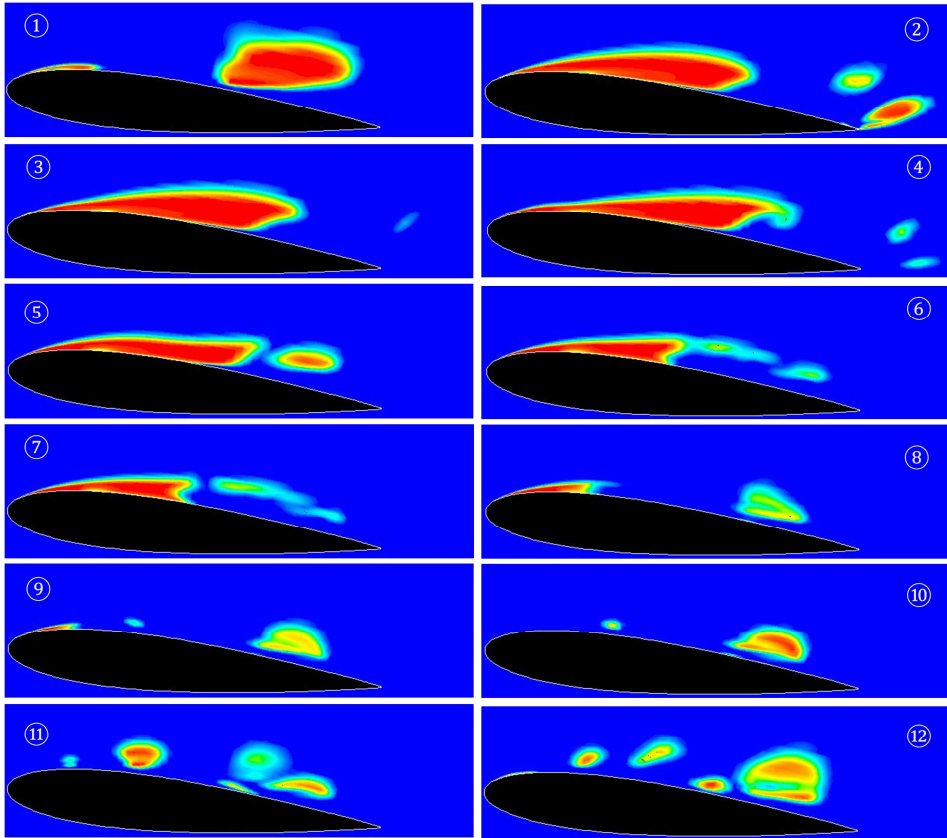


Figure 6-23: Contours of the vapor volume fraction during one typical cycle for a NACA0015 hydrofoil at angle of attack of 6° with the modified *SST* $k-\omega$ model on coarse grid *G1* (red color indicates pure vapor, whereas blue color indicates pure liquid) (Flow from left to right)

In Figure 6-24, the corresponding twelve instants within the selected shedding cycle in Figure 6-23 are marked on the time histories of the total vapor volume, and the lift and drag coefficients. It can be observed that the typical unsteady dynamics occurs simultaneously with a sudden leap both in the lift and drag coefficients. From the plot of the time history of the total vapor volume (Figure 6-24-(a)), it can be observed that the increase of the total vapor volume at the initial period can be related to the growth of the main sheet cavity near the leading edge, though the downstream cloud cavity is collapsing. The decrease can be mostly related to a decreasing length and thickness of the main sheet cavity and the collapses of the downstream vapor structures. The sudden leap in both lift and drag are always accompanied with the shed dynamics or collapse behavior.

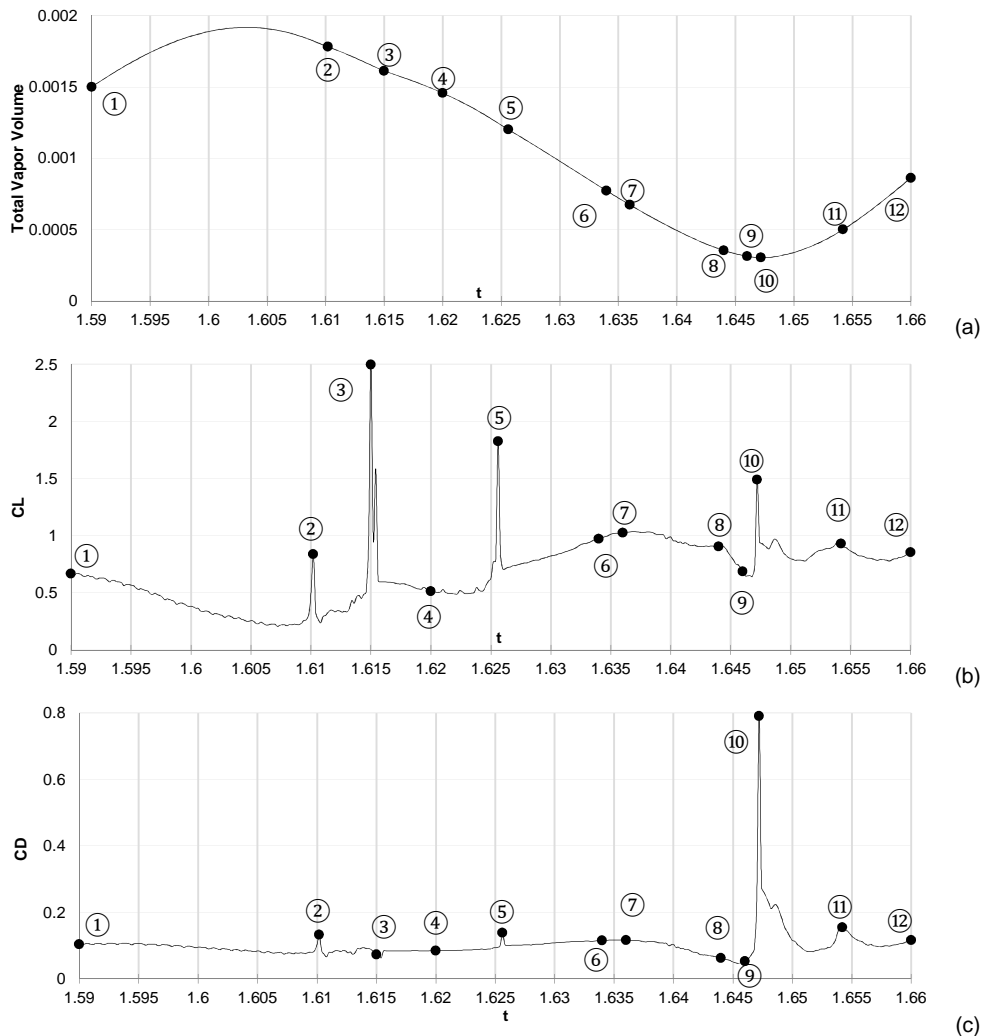


Figure 6-24: Time histories of the (a) total vapor volume; (b) lift; and (c) drag coefficients within a selected shedding cycle for a NACA0015 hydrofoil at 6° angle of attack, and the twelve instants shown in Figure 6-23 are indicated with number

At the instant ⑩, the total vapor volume reduces to the local minimum value, and the drag coefficient shows a significant leap, simultaneously with a sudden leap of the lift coefficient. Another instant that should be noted is ③, the lift coefficient increases suddenly to a high value, whereas the drag coefficient shows a sudden decrease. At the same time, the downstream large-scale vapor structures collapse into tiny volumes, and then develop again. It is also shown that only the first shedding of the largest vapor structure (instant ⑤), among the three shed structures, and induces a sudden leap in both lift and drag. The other two sheddings of relative smaller vapor structures, instants ⑦-⑨, do not induce a

significant change of the lift and drag, possibly due to the weaker interaction between the thinner sheet cavity and smaller sheddings.

Three important conclusions can be made based on above investigations:

- Unsteady dynamic shedding can be obtained when the modified *SST k - ω* turbulence model is adopted, showing break-up of the main sheet cavity and shedding of cloud cavity.
- The selection of a proper iteration number per time step should be emphasized when the unsteady cavitation phenomena are involved, because an incomplete calculation for each time step would predict too low a shedding frequency.
- For different time step sizes, the simulations predict slightly different shedding frequencies but a similar order of magnitude of the total vapor volume when the modified *SST k - ω* turbulence model is adopted.

Grid Sensitivity

To investigate the influence of the grid density on the unsteady dynamics, the test cases are conducted on the fine grid G_3 with standard and modified *SST k - ω* turbulence model respectively. The time step size is chosen as $\Delta t = 2 \times 10^{-4} s$, corresponding to a courant number equal to one (referred to equation (6-1)).

The time histories of the residuals and the mass transfer rate during two successive time steps are shown in Figure 6-25. The number of iterations per time step is set at $I_N = 100$ to do the following computations with the fine grid G_3 . It can be seen from Figure 6-25, a number of iterations of $I_N = 100$ shows convergence during each time step.

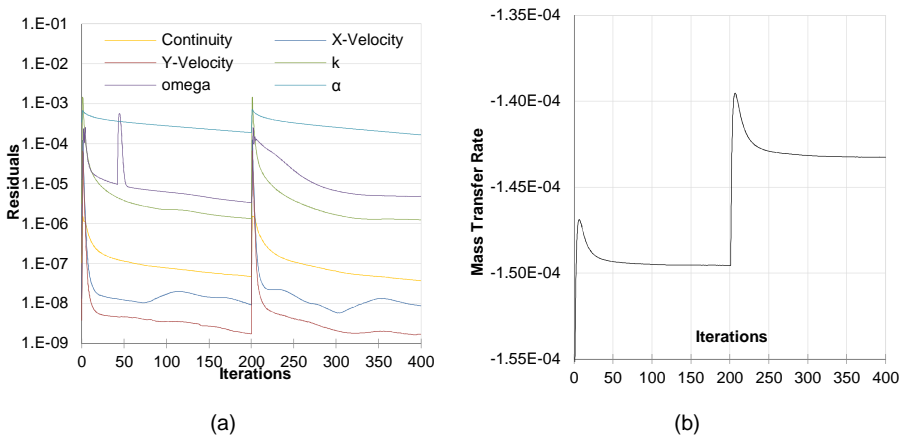


Figure 6-25: The time histories of (a) the residuals and (b) mass transfer rate during two successive time steps with $\Delta t = 2 \times 10^{-4} s$ for a NACA0015 hydrofoil at 6° angle of attack at $\sigma = 1.0$ on fine grid G_3

The time histories of the total vapor volume and lift coefficients that are predicted by the coarse grid *G1* and fine grid *G3* are compared in Figure 6-26. It is found that the integral fluid quantities, such as the total vapor volume, and the lift and drag coefficients, show a similar behavior in frequency but with a different magnitude when the standard *SST k - ω* turbulence model is adopted. A rough calculation of the difference between the results for the two grids is conducted for the averaged value over an arbitrary cycle. It is found that the deviations between the two grids are around 11.1% for the averaged total vapor volume and 1.8% for the averaged lift coefficient.

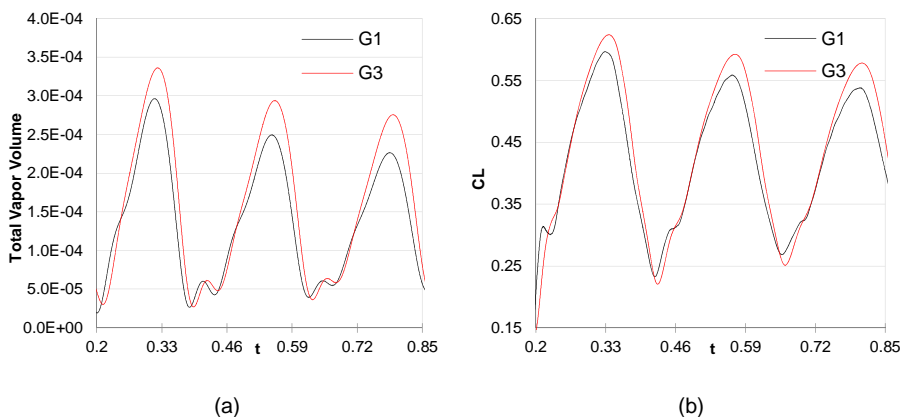


Figure 6-26: Time histories of (a) the integrated vapor volume; and (b) lift coefficient, predicted by coarse grid *G1* and fine grid *G3* for a NACA0015 hydrofoil at 6° angle of attack

The unsteady dynamic behavior of break-up of sheet cavitation is only obtained after attenuating the eddy viscosity in the region with higher vapor fraction (Reboud et al., 1998). Several cycles of the time history of the total vapor volume predicted by both grids are compared in Figure 6-27. It should be noted that the initial time is set to be zero, already eliminating the start-up effect.

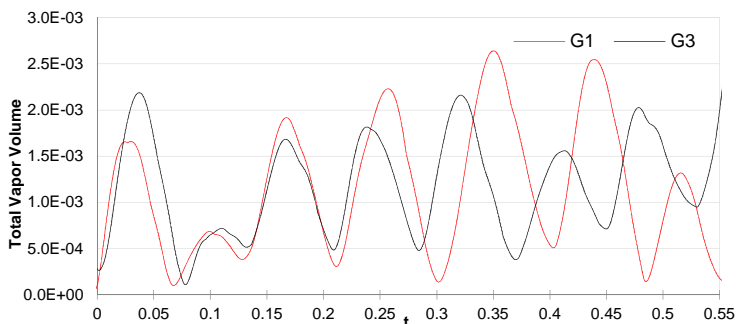


Figure 6-27: The time history of the total vapor volume predicted by coarse grid *G1* and fine grid *G3* for a NACA0015 hydrofoil at 6° angle of attack

Though there are discrepancies between the results predicted by both grids, the mean magnitude of the integrated vapor volume is around the same order. The shedding frequency predicted by the fine grid $G3$ with the time step size of $\Delta t = 2 \times 10^{-4}$ is $f \approx 11.4 \text{ Hz}$, a bit higher than the frequency predicted by the coarse grid $G1$, which is $f \approx 11.0 \text{ Hz}$. The FFT analysis is based on the total vapor volume over eight cycles that already eliminate the start-up effect.

The contours of the vapor volume fraction produced by the fine grid are illustrated to examine the sensitivity to grid densities, as shown in Figure 6-28. Similar as to the analysis on the results for coarse grid $G1$, twelve instants are selected to describe the characteristic unsteady dynamics.

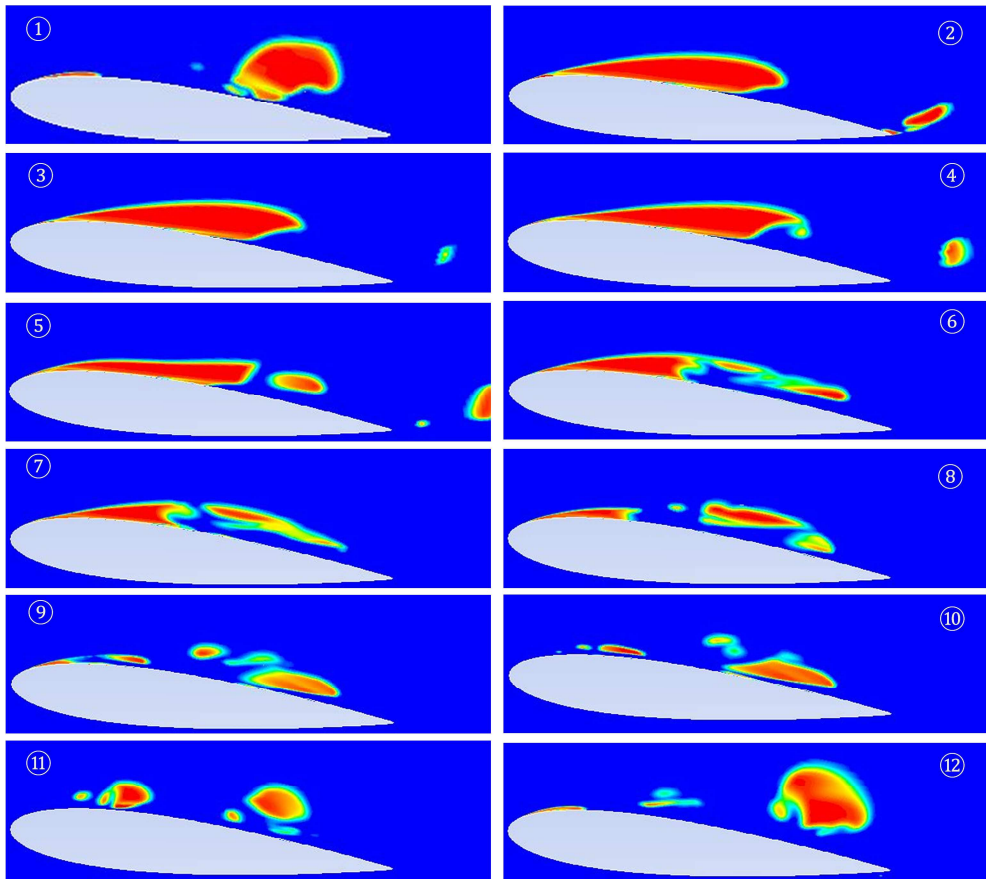


Figure 6-28: Contours of the vapor volume fraction during one typical cycle for a NACA0015 hydrofoil at angle of attack of 6° with the modified $SST\ k - \omega$ model on fine grid $G3$ (Red color indicates pure vapor, whereas blue color indicates pure liquid) (Flow from left to right)

The twelve instants representing the typical unsteady dynamics are marked on the time histories of the total vapor volume, lift and drag coefficients within the selected cycle, as shown in Figure 6-29.

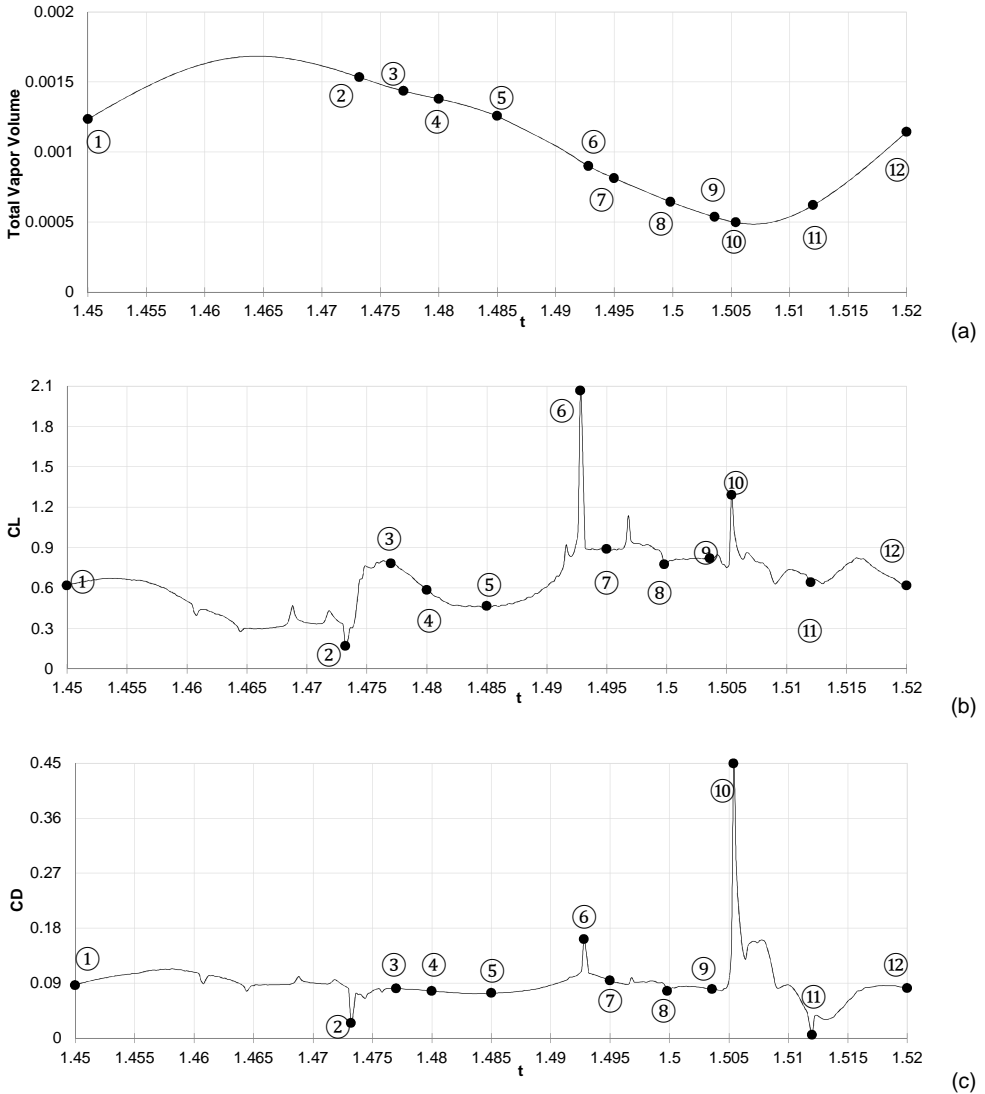


Figure 6-29: Time histories of the (a) total vapor volume; (b) lift; and (c) drag coefficients within a selected shedding cycle in accordance with the instants in Figure 6-28

It can be observed that similar basic unsteady dynamics are captured by both grids, such as the collapse of the large-scale structures together with the development of the main sheet

cavity at the leading edge (instants ①-②), the three times shedding off of vapor structures (instants ④-⑨), and the tendency of the small vapor structures to merge into the large one. The wavy shape of the upper liquid-vapor surface is same as what is observed with the coarse grid.

Several relations between the dynamics and the integral flow characteristics are similar to what is observed for the coarse grid *G1*. The following conclusions can be drawn:

- The increase of total vapor volume can be related to the growth of the main sheet cavity at the leading edge, whereas, the decrease can be related to the shortening of the sheet cavity length, accompanied with the collapse of the downstream cavities.
- When the total vapor volume reduces into a local minimum value, a major increase of the drag coincides with a sudden jump in lift (instant ⑩).

And the discrepancies between the two grids can be summarized as follows:

- In the case of the coarse grid, the large-scale cavity and the cavities developed from the trailing edge collapse almost at the same time, as shown at the instant ③ in Figure 6-23, corresponding to the pronounced sudden jump in lift and drag. However, in the case of the fine grid, the large-scale cavity collapses at the instant ②, and the cavities developed from the trailing edge collapse into a small volume and then develop again. Therefore, the sudden jump is observed at instant ② rather than instant ③.
- During the three sheddings of vapor structures, the large peak both in lift and drag is observed when the second shedding is going to occur (instant ⑥), whereas for the coarse grid, it is observed at the instant when the first shedding is completed (instant ⑤). The vapor structures downstream of the trailing edge at the instant ⑤, which is not present in the case of the coarse grid, may retard the sudden change of the forces.

Though the refinement in grid appears to predict more details, the essential unsteady dynamics can already be captured by adopting the coarse grid *G1* in the current topology and resolution. If we focus on the properties of the large-scale structures, such as their volume, location and collapse time, the results predicted by both grids are consistent. It can be concluded that the current approach of RANS method is capable of predicting the large-scale unsteady dynamics even with the coarse grid *G1*, which is in an O-H topology with appropriate discretization around the nose and trail of the foil.

Discussions on the Reboud's Correction

It should be noted that a physical justification for Reboud's correction of the turbulence model is lacking. For the same case conducted on a NACA0015 hydrofoil with an angle of attack of 6° , Reboud's correction is not a prerequisite for all commercial CFD tools. Star-CD (Oprea, 2009a) and FreSCo (Hoekstra and Vaz, 2008) are reported to show dynamic shedding of sheet cavitation on a 2D foil. However, for the case conducted on the Delft Twist-11 Hydrofoil (Hoekstra et al., 2011), only steady or at most a breathing behavior was observed by all the participants applying a RANS method in the workshop SMP2011 (Abdel-Maksoud, 2011), where unsteady dynamics is actually observed in the experiments.

In Figure 6-30, contours of stream function around the hydrofoil when no eddy viscosity attenuation is adopted (Reboud's correction switched off) are illustrated on the left, and the corresponding sequences of the cavity image are shown on the right. It can be observed that there is always a flow separation bubble near the closure region of the leading edge sheet cavity, indicating that a reversed flow occurs in these regions.

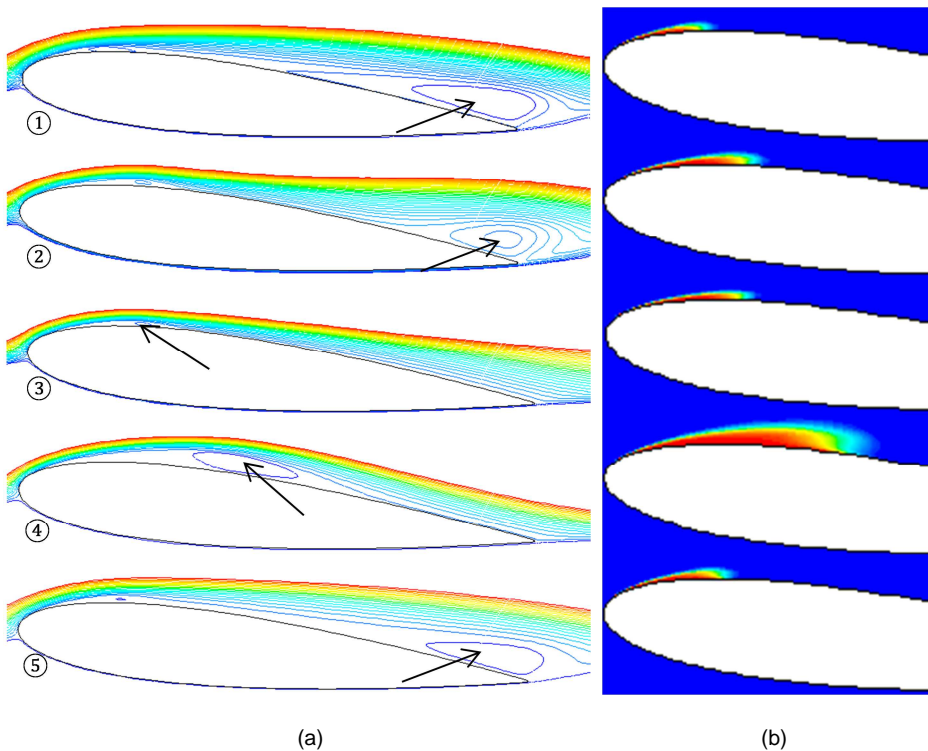


Figure 6-30: Contours of (a) stream function; and (b) vapor volume fraction, for the NACA0015 hydrofoil with standard *SST* $k - \omega$ turbulence model (Flow from left to right)

To get more details, the velocity vectors magnitude colored by the vapor volume fraction in these swirling zones are examined and shown in Figure 6-31, where the vectors in red color represent the pure liquid flow directions and the blue color represents the pure vapor.

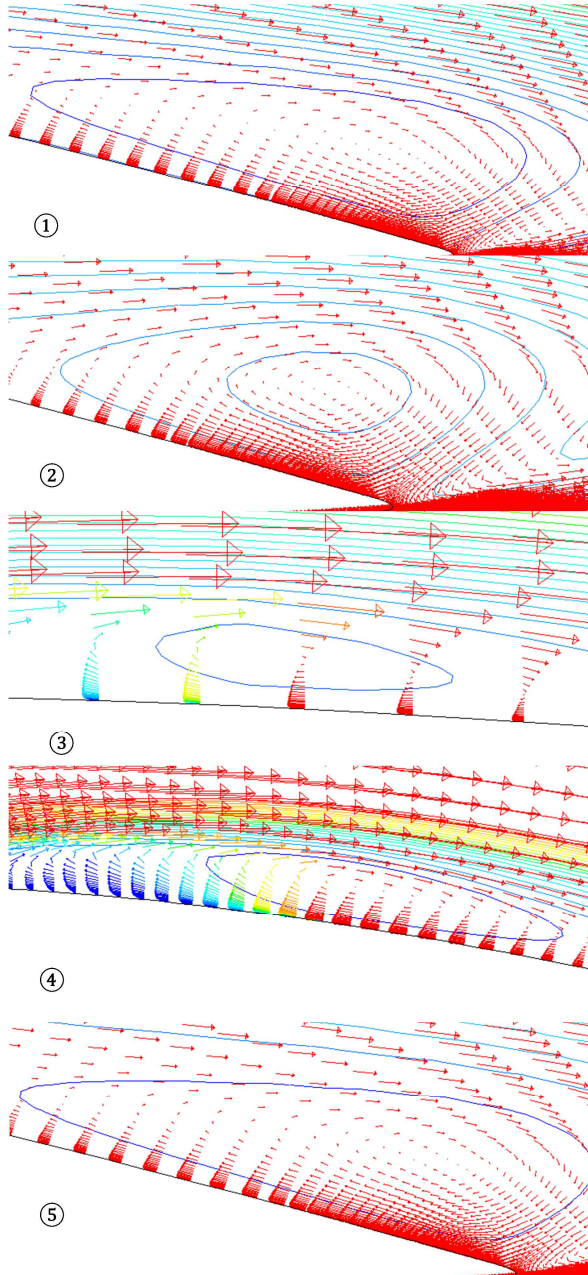


Figure 6-31: Velocity vectors in the color of vapor volume fraction showing the overlap between the separation bubbles and the cavity (Red color: the pure liquid; Blue color: the pure vapor)

By looking into the details around the circle that is located near the leading edge of the hydrofoil, it is found that the separation bubble is partially overlapping with the closure region of the sheet cavity. The five instants in Figure 6-31 are in accordance with the instants in Figure 6-30 but with more details for specific regions (as indicated by black arrows in Figure 6-30):

- For the instants ①②&⑤, a recirculating liquid flow occurs in the separation bubbles near the trailing edge.
- A reversed liquid flow travels along the hydrofoil towards the leading edge, at the same time, the vapor inside the cavity and the mixture of the liquid and vapor at the tail of the cavity also move towards the leading edge, as shown in Figure 6-31-③④.

However, these recirculating flow patterns do not trigger any unsteady shedding before they travel downstream of the hydrofoil. The turbulent viscosity distributions for the *SST k - ω* turbulence model with and without Reboud's correction are examined along four lines at different locations, as shown in Figure 6-32.

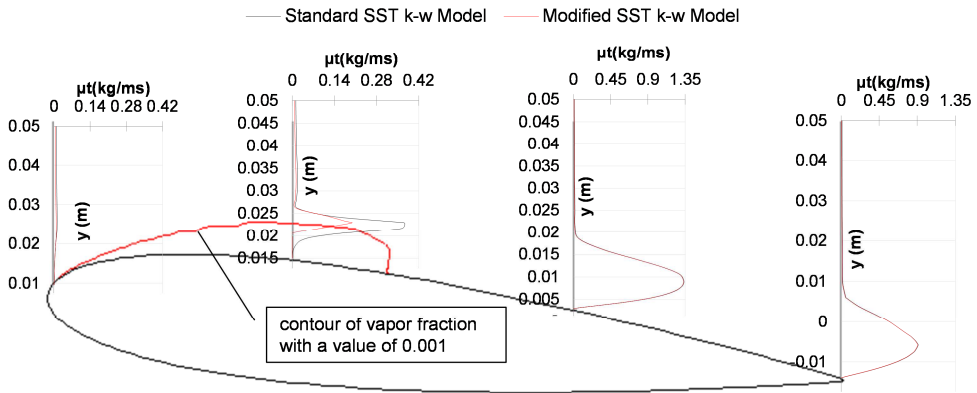


Figure 6-32: The comparison of the turbulent viscosity distribution for the *SST k - ω* turbulence model with and without Reboud's correction along four lines at different locations over the hydrofoil

It can be observed that at the regions where the vapor volume fraction is higher, the eddy viscosity is indeed reduced when the Reboud's correction is applied. However, at the regions where the vapor volume fraction is small or zero, there is no significant change for the turbulent viscosity.

With the standard *SST k - ω* turbulence model, the unsteady cavitation phenomena cannot

be observed even when the cavitation number reduces to a much lower value like $\sigma = 0.7$. Other two-equation turbulence models also could not predict the expected break-off and cloud shedding. It seems that the unsteadiness is dampened by an excessive eddy viscosity generated by the current turbulence model. With Reboud's correction, the eddy viscosity will be reduced, so that the turbulence model will become less dissipative and hence avoids a too big damping effect on the unsteadiness in the flow. It can then be concluded that Reboud's correction on the eddy viscosity in the region with higher vapor fraction is an important trigger to obtain unsteady shedding in FLUENT for some flows.

The Re-entrant Jet Mechanism

De Lange and De Bruin (1998) mentioned that the cause of the break-off is the formation of a re-entrant jet and the subsequent impingement of the jet on the front cavity interface. Franc (2001) stated that the re-entrant jet is the source of the cloud cavitation instability. Yakusihiji (2001) showed that the thickness of the re-entrant jet is an important factor to the cut-off phenomena of the leading edge sheet cavity. However, Hoekstra (2011) states that the widely accepted cut-off mechanism where the re-entrant jet pushes the interface forward until it reaches the front end of the cavity and then cuts the cavity into two parts is a visual illusion because the motion of the cavity-liquid interface is not necessarily the same as the motion of the fluid particles.

To get a better understanding of the break-off mechanism, a further study will be conducted on the flow details predicted by adopting the fine grid *G3* with the modified *SST k- ω* turbulence model. Our focus will be on the characteristic shedding behavior that is shown between instant ③ and ⑨ in Figure 6-28.

Velocity vectors during the period when the first vapor structure is shed off from the tail of the sheet cavity (instant ③ to ⑤ in Figure 6-28) are illustrated in Figure 6-33. A rotational motion of a liquid vortex in a clockwise direction is observed at the tail of the sheet cavity at instant ③, and this vortex continually absorbs energy from the surrounding flow, consequently affecting the closure region of the sheet cavity. Subsequently, the flow around the center of this vortex is evaporated into vapor when the pressure at the center drops below the vapor pressure. This new developed vapor structure grows bigger and bigger, simultaneously a rotational motion is observed inside the sheet cavity at the closure region of the sheet cavity, but in a counter-clockwise direction (as indicated by the black arrow in image (d) and (e) in Figure 6-33). The vapor structure is not pinched off from the sheet cavity but comes into existence at the tail of the sheet cavity.

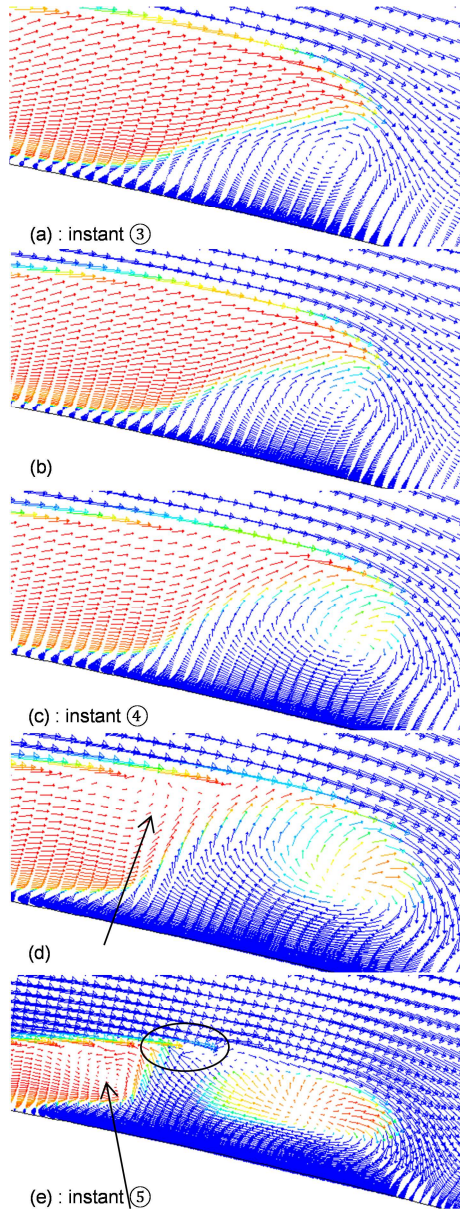


Figure 6-33: Typical sequences of the velocity vectors colored by the vapor fraction at the tail of the sheet cavity during instant ③ to ⑤ in Figure 6-28 (Red color represents pure vapor, whereas blue color represents pure liquid)

Analogous to the investigation of the first shedding, velocity vectors corresponding to the subsequent two sheddings (instant ⑥ to ⑨) are plotted in Figure 6-34. The statement by Hoekstra that “the reversed flow is not necessarily merely a liquid flow and that phase changes may well occur in the recirculation zone” is confirmed by looking into the images

as follows. In the recirculation zone, three kinds of fluids can be observed, pure liquid, pure vapor as well as the mixture of liquid and vapor.

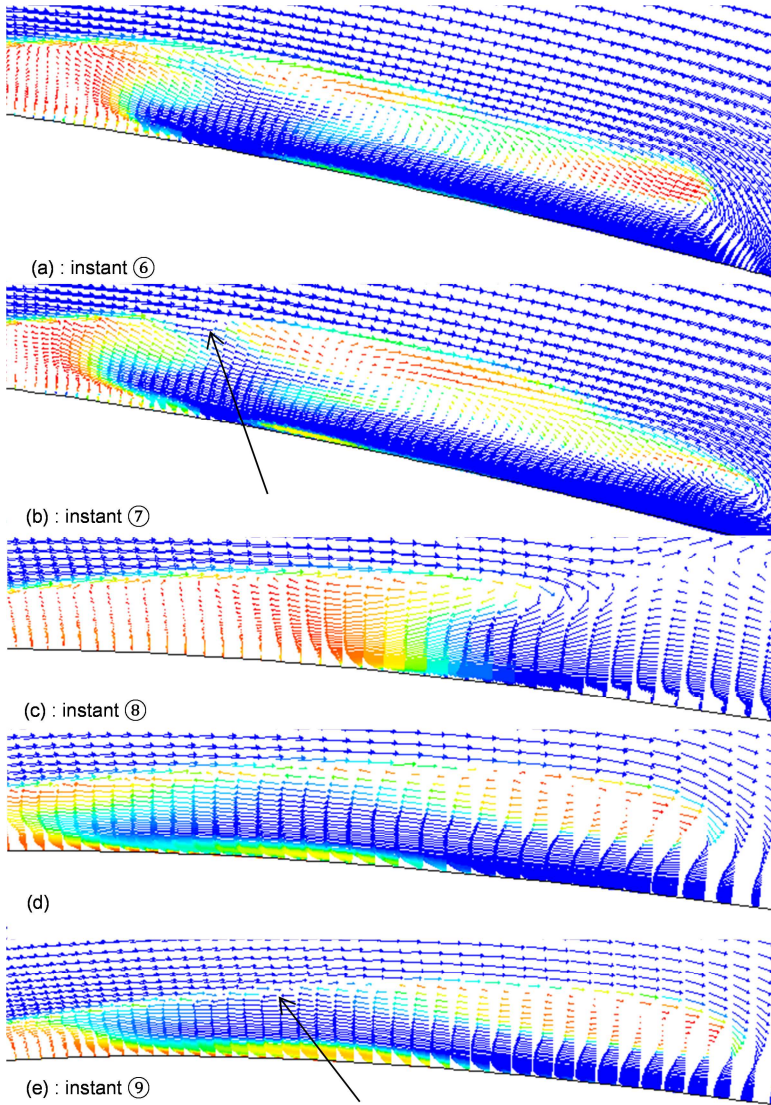


Figure 6-34: Sequences of the velocity vectors colored by the vapor fraction corresponding to the period from instants ⑥ to ⑨ in Figure 6-28 (Red color represents pure vapor, whereas blue color represents pure liquid)

During these two sheddings, it seems that the break-off can be explained by the re-entrant jet mechanism. The black arrows (in the images (b) and (e)) point to the location where the reversed liquid flow touches the upper liquid/vapor interface, revealing that the liquid flow

indeed penetrates into the sheet cavity thereby cutting off vapor structures. In this sense, this liquid flow can be taken as a “re-entrant jet”. Nevertheless, it is not the main objective to perceive every detail of the unsteady cavitation phenomena, but to focus on the capability to capture the large-scale cavity dynamics by the RANS method implemented in FLUENT.

Conclusions

Several important conclusions can be drawn from the investigations of unsteady cavitation phenomena on a NACA0015 hydrofoil at 6° angle of attack:

- Rebound’s correction on the eddy viscosity in the region with higher vapor fraction is an important trigger to obtain unsteady shedding in FLUENT for some flows.
- The sensitivity of the solutions to the iteration numbers per time step is monitored by its convergence behavior in each time step. The selection of a proper iteration number per time step should be a point of attention when unsteady cavitation phenomena are involved, because an incomplete calculation for each time step would predict too low a shedding frequency.
- The current approach of RANS method is capable of predicting the large-scale unsteady dynamics even with the coarse grid $G1$, which is in an O-H topology with appropriate discretization around the nose and tail of the foil.
- Except for the generally accepted “re-entrant jet” break-off mechanism, the rotational motion inside and at the tail of the sheet cavity are also important factors that may contribute to the break-off of the sheet cavity, as shown in Figure 6-33.
- The sudden peak in both lift and drag can be attributed to unsteady phenomena, such as the cavity sheddings and collapses.

6.3.2 2D NACA0015 ($AoA = 8^\circ$)

The second test geometry is the NACA0015 hydrofoil with an angle of attack of 8° . The adopted mesh is the coarse grid with 264 edges on the foil, which is equal to the grid used in the non-cavitating condition. The unsteady dynamics is then investigated on a specific cavitation regime for a cavitation number of $\sigma = 2.2$, where the results can qualitatively be compared to the experimental data provided by Boorsma (2010). The time step size is selected using the equation(6-1) with a courant number around 0.75, giving a value of $2.5 \times 10^{-5} s$.

A velocity-inlet condition is applied at the upstream boundary with the vapor fraction equal

to zero. A pressure-outlet boundary condition is used at the outlet boundary. The physical properties of the two-phases, liquid and vapor, are taken at a temperature of $16.3^{\circ}C$. The detailed initial and boundary conditions and the flow properties (taken at a temperature of $16.3^{\circ}C$) are listed in Table 6-12.

Table 6-12: Boundary conditions and flow properties for a NACA0015 hydrofoil ($AoA=8^{\circ}$)

Boundary Conditions		NACA0015 ($AoA=8^{\circ}$)	
Velocity Inlet (m/s)	V=17.71		
Pressure Outlet(kPa)	346.466		
Turbulent Intensity (%)	1		
Turbulent Viscosity Ratio	10		
Foil	No-slip Wall		
Tunnel Walls (Top & Bottom)	No-slip Wall		
Flow Properties (T=16.3°C)		Vapor	Liquid
Density (kg/m ³)	0.01389	998.85	
Dynamic Viscosity(kg/ms)	9.63E-06	0.0011	
Vapor Pressure (kPa)	1854		

The simulation is carried out by using a pressure-based transient solver, and a fully coupled solver is selected to solve the pressure and momentum equations. The pressure is discretized using the PRESTO! scheme, and the convection terms of the momentum equations are discretized by the QUICK scheme which is also done for the turbulence equations and vapor volume fraction equation (ANSYS, 2009). The temporal discretization uses the first-order implicit scheme.

Results and Discussion

The residuals of each equation and the volume integral of the mass transfer rate are plotted in Figure 6-35, and it is found that 50 iterations are needed to get a converged solution for each time step.

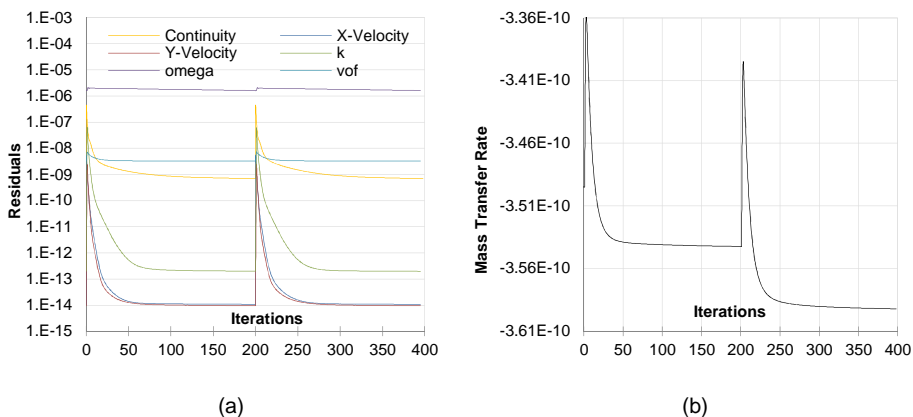


Figure 6-35: The time histories of (a) the residuals and (b) mass transfer rate during two successive time steps with $\Delta t = 2.5 \times 10^{-5} s$ for the NACA0015 hydrofoil at 8° angle of attack at $\sigma = 2.2$

With the standard *SST k – ω* turbulence model, only a steady sheet cavity is observed with a length of 12% of the chord, see Figure 6-36. When the modified *SST k – ω* turbulence model is applied, the typical unsteady dynamics, such as the break-up of the sheet cavity and the shedding of cloud cavities, can be observed. The time history of the total vapor volume after subtracting the start-up phase is shown in Figure 6-37. The cavity that breaks up from the sheet is shed at a high frequency, however with a cyclic variation of the magnitude of the total vapor volume at a lower frequency. From a spectral analysis, two main frequencies are obtained as 31.1 Hz and 279.7 Hz respectively (see Figure 6-38).

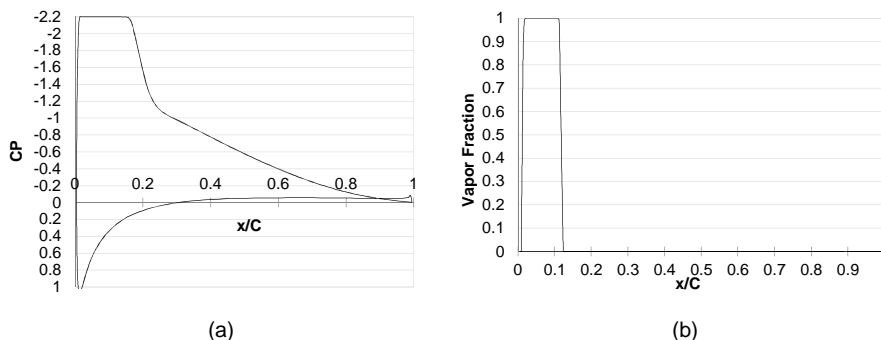


Figure 6-36: The (a) pressure distribution; and (b) vapor fraction distribution over the NACA0015 hydrofoil at 8° angle of attack with the standard *SST k – ω* turbulence model at $\sigma = 2.2$

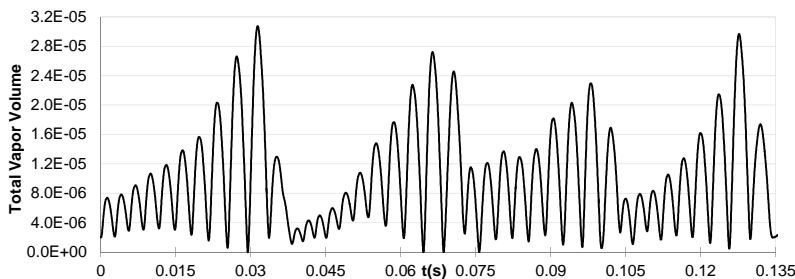


Figure 6-37: Time history of total vapor volume over a NACA0015 hydrofoil at 8° angle of attack with the modified *SST k – ω* turbulence model at $\sigma = 2.2$

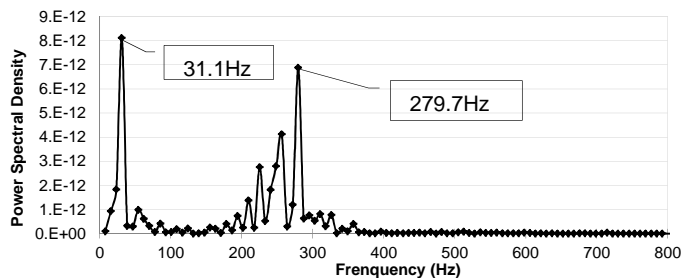


Figure 6-38: Shedding frequencies based on FFT analysis of the time history of the total vapor volume over a NACA0015 hydrofoil at 8° angle of attack with the modified *SST k – ω* turbulence model at $\sigma = 2.2$ (as shown in Figure 6-37)

The unsteady dynamics of two particular sheddings are compared in Figure 6-39, corresponding to oscillations with a minimum and a maximum magnitude of the total vapor volume amplitude within one cycle at the lower frequency ($f \approx 31.1Hz$). The observed essential features for these two cycles are similar to each other, and can be characterized as follows:

- A sheet cavity is growing from the leading edge after the last cavity pinch-off (Figure 6-39 (a) (b)- ①);
- The growth of the sheet cavity ceases at a certain length, simultaneously the downstream cloud cavity collapses near the trailing edge, and a re-entrant jet forms subsequently (Figure 6-39(a) (b)- ②);
- The re-entrant jet moves upstream towards to the leading and then breaks up the sheet cavity (Figure 6-39(a) (b)- ③④);

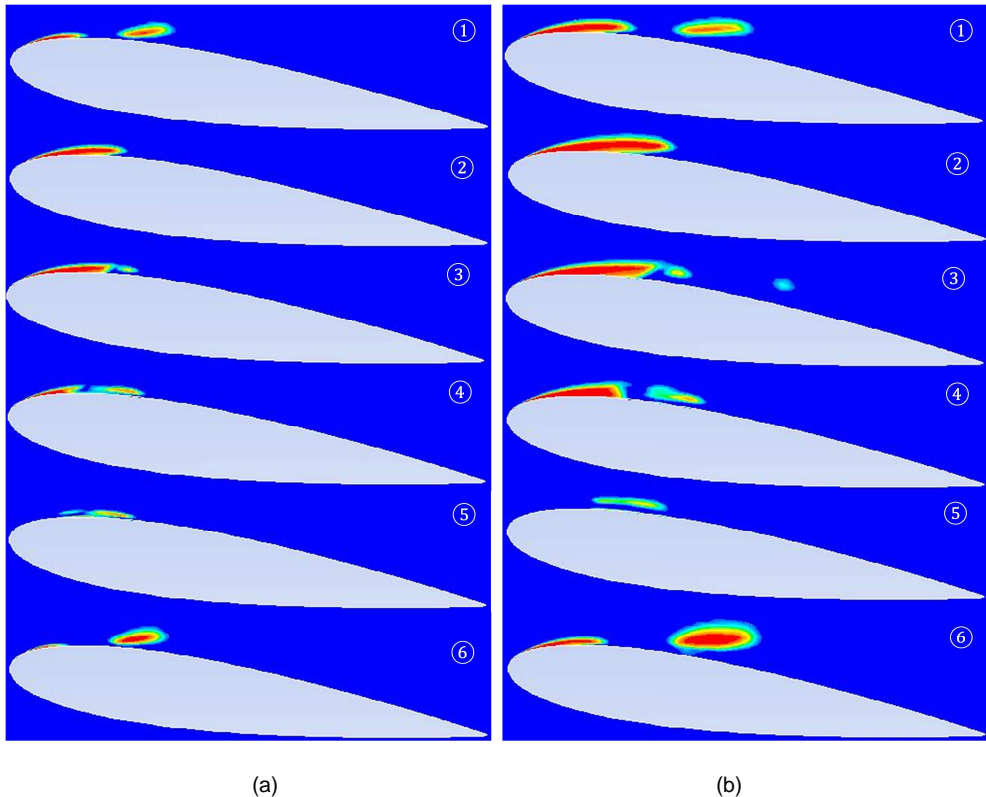


Figure 6-39: Two shedding cycles showing the contours of the vapor volume fraction corresponding to the oscillations with (a) minimum; and (b) maximum magnitude of the total vapor volume amplitude over a NACA0015 foil at 8° angle of attack with the modified *SST* $k - \omega$ turbulence model at $\sigma = 2.2$ (Red color indicates pure vapor, whereas blue color indicates pure liquid) (Flow from left to right)

- The upstream part of the sheet cavity subsequently decreases to a very tiny volume, whereas the downstream part rolls up and transforms into a bubbly cloud (Figure 6-39(a) (b)- ⑤);
- Finally, the cloud cavity is lifted from the foil surface and travels downstream, at the same time a tiny sheet cavity from the leading edge grows again, and a new cycle starts (Figure 6-39(a) (b)- ⑥).

The synchronized lift and drag coefficients of the specific six instants of the oscillation with maximum magnitude of the total vapor volume, as depicted in Figure 6-39 (b), are plotted in Figure 6-40. It can be observed that the sudden peak both in the lift and drag coefficients can be correlated to the collapse (instant ②) or shed (instant④). The sudden peak observed at the instant ⑤ could be related to the disappeared sheet cavity at the leading edge.

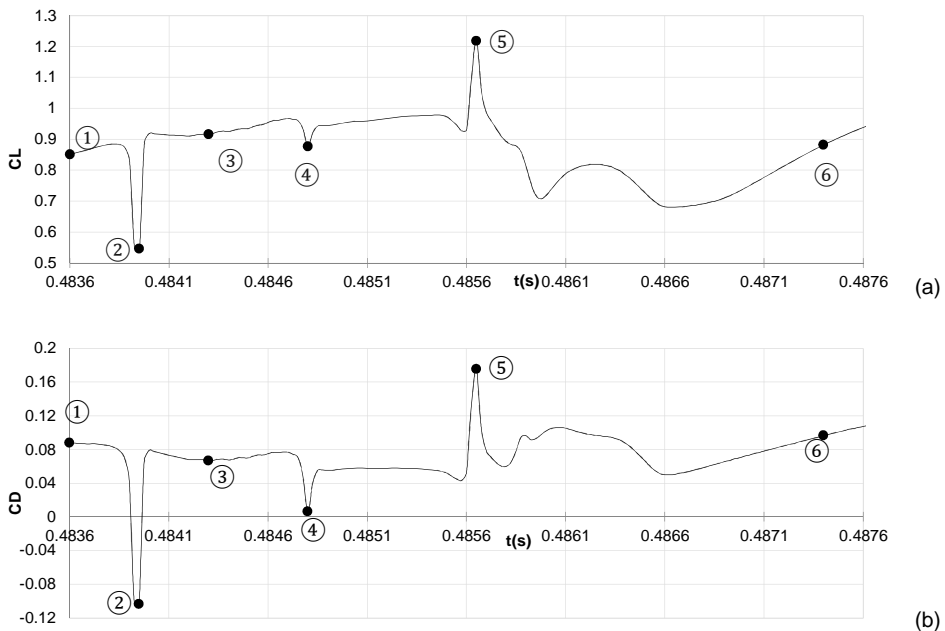


Figure 6-40: Time histories of the (a) lift; and (b) drag coefficients within a specific shedding cycle in accordance with the instants in Figure 6-39 (b)

Comparison with Experimental Results

The cavitation tests on a NACA0015 foil are performed by Lloyd's Register in cooperation with MARIN within the framework of a Cooperative Research Ships (CRS) project on Cavitation Erosion (Boorsma, 2010). A NACA0015 foil with a chord of 60 mm and a width

of 40 mm was placed in MARIN’s high speed tunnel of a height of 80 mm. High-resolution pictures observed by the high-speed camera for the test case S02M10 are compared with the results from the simulation discussed above. The test conditions of this case are listed in Table 6-13, closely resembling the conditions for the simulation with FLUENT.

Table 6-13: Test conditions for S02M10

	S02M 10
AoA (deg)	8
T(°C)	16.3
V(m/s)	17.71
σv	2.2
Re	9.70E+05

From the recorded images shown in the report by Boorsma (2010), it can be observed that the characteristic shedding phenomena show a good qualitative match with the simulation results but with a different cavity length and volume. Six characteristic frames recorded by the high-speed camera are shown in Figure 6-41 (both top and side view), and are compared with the predicted simulation results by FLUENT.

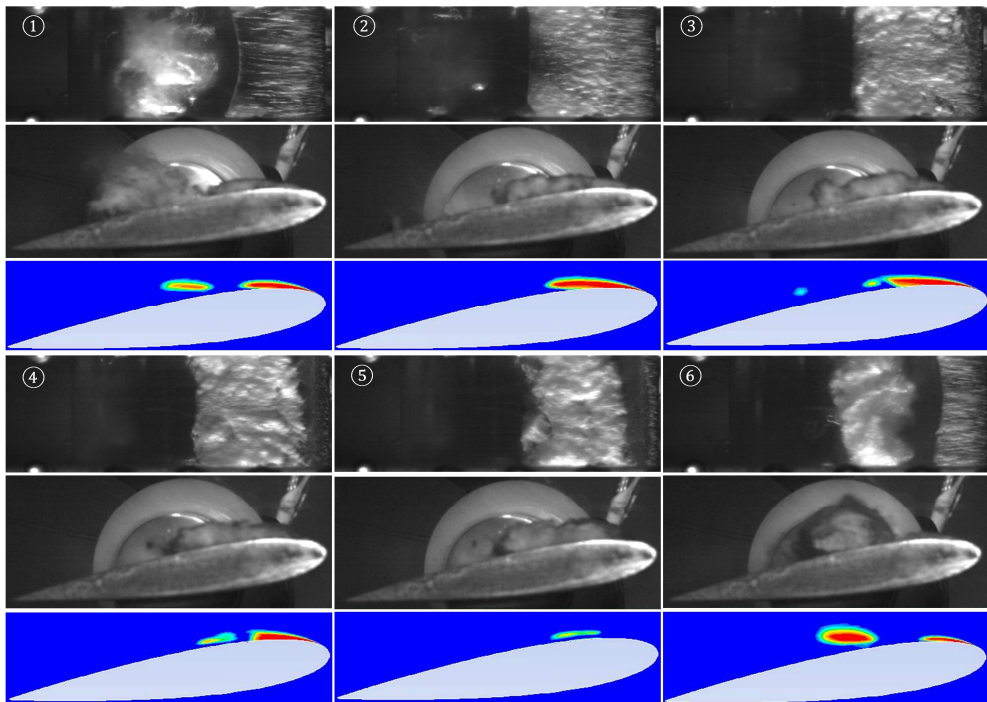


Figure 6-41: Characteristic frames during a cycle recorded by high-speed camera in top view and side view respectively, compared with the contours of vapor volume fraction corresponding to the six instants in Figure 6-39 (Red color indicates pure vapor, blue color indicates pure liquid) (Flow from right to left)

It is hypothesized that the quantitative discrepancies may result from the bubble number density preset which is given as input in the Schnerr-Sauer cavitation model. This bubble density is defined as the number of spherical bubbles per volume of fluid. Liu et al. (1993) presented an experimental sensitivity study on the effect of the nuclei density spectrum. Although the nuclei density spectrum in the test facility used by Boorsma (2010) has not been measured, this spectrum is likely to be different from the input density spectrum used in our numerical cavitation model.

In the Schnerr-Sauer cavitation model, the bubble number density is related to the vapor volume fraction in the following formula:

$$\alpha = \frac{\frac{4}{3} \pi n_b R_B^3}{1 + \frac{4}{3} \pi n_b R_B^3} \tag{6-10}$$

If we assume that the whole domain can initially be characterized with a vapor volume fraction approaching zero, a series of values for the averaged initial bubble radius can be obtained for different bubble number densities n_b . The experimental bubble spectra obtained by Waniewski et al. (2001) for the distribution downstream of a two-dimensional hydraulic jump and Zima et al. (2009) for the inlet flow upstream of the hydrofoils in a cavitation tunnel are included to make a comparison with the theoretical values calculated by equation (6-10), as shown in Figure 6-42.

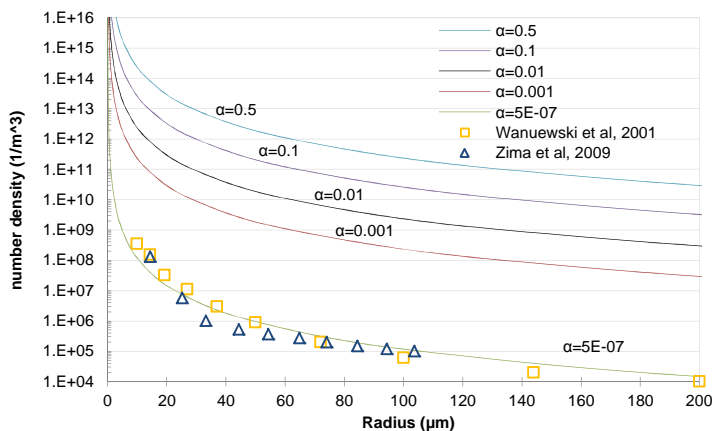


Figure 6-42: Comparison of measured bubble spectra and theoretical values calculated by equation (6-10)

In FLUENT, the default bubble number density is in the order of $1e+13$, and it can be observed from the theoretical plots that the bubbles have a radius within a bandwidth of $[0\mu m \sim 10\mu m]$ when the vapor volume is lower than 0.01. However, the bubble radius could be larger than $200\mu m$ when smaller bubble number densities are adopted. It is not easy to choose the proper input value of the bubble number density due to the unknown spectrum for the current test facility in MARIN’s high speed tunnel. Nevertheless, it is important to be aware of the influence of the bubble number density on the predicted cavitation phenomena by RANS method implemented in FLUENT. Thereby, a sensitivity study of the bubble number density is conducted in the next section.

Sensitivity Study for the Bubble Number Density

In this section, the unsteady cavitation phenomena for three different input of the bubble number density in the numerical cavitation model will be explored for a specific cavitation regime with a cavitation number of $\sigma = 2.2$ over the NACA0015 hydrofoil at 8° angle of attack. All of the results to be analyzed are calculated under identical conditions except for adopting different bubble number densities, $n_b = 1e+08, 1e+10$ and $1e+15$, respectively.

The basic unsteady dynamics captured by all input bubble number densities are similar to each other: the cavity that breaks up from the sheet is shed at a high frequency, however with a cyclic variation of the magnitude of the total vapor volume amplitude at a lower frequency. It is noted that the maximum magnitude of the total vapor volume and the two main shedding frequencies show differences for the different input values of n_b , as shown in Table 6-14.

Table 6-14: Comparison of results predicted by different input of bubble number density

Bubble Number Density	Maximum Total Vapor Volume(m^3)	SheddingFrequency (Hz)	
		f (low)	f (high)
Nb=1e+15	3.00E-05	31.1	279.7
Nb=1e+13	3.00E-05	31.1	279.7
Nb=1e+10	4.00E-05	36.6	201.5
Nb=1e+08	5.00E-05	40.0	159.8

It can be observed that the results predicted by the higher input bubble number density $n_b = 1e+15$ show a good match with the results by the default input value: $n_b = 1e+13$. However, for smaller input values of n_b , a higher maximum magnitude of the total vapor volume and a higher main low frequency are obtained, whereas a smaller main high frequency is obtained.

Looking at the contours of the vapor volume fraction, no big differences are observed by adopting the bubble number density $n_b = 1e + 15$, whereas a larger extent of the cavity can be obtained when a smaller bubble number density $n_b = 1e + 08$ is used, as shown in Figure 6-43.

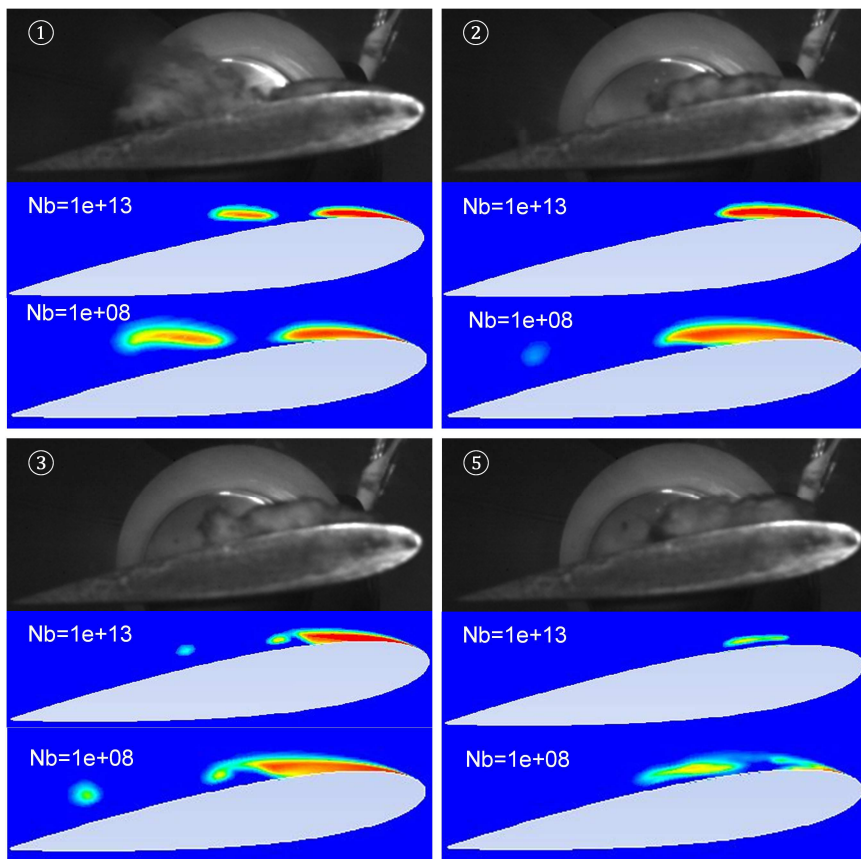


Figure 6-43: Comparison of the side views of the images recorded by the high speed camera and the contours of vapor volume fraction predicted by $n_b = 1e + 13$ and $n_b = 1e + 08$ corresponding to the instants shown in Figure 6-41 (Flow from right to left)

Smoother lift and drag are observed on the hydrofoil when smaller bubble number density $n_b = 1e + 08$ is used. The unsteady dynamics does not trigger any significant peak in the lift and drag, as shown in Figure 6-44. This phenomenon is in agreement with the Sauer's observation (2000) that the peaks in the lift and drag become smaller for smaller bubble number density n_b . He correlated this phenomenon to the over-fluctuations due to the source strength, which is supposed to be proportional to bubble number density n_b . The smaller bubble number density generates fewer over-fluctuations, therefore resulting in

smaller changes in the lift and drag as time proceeds.

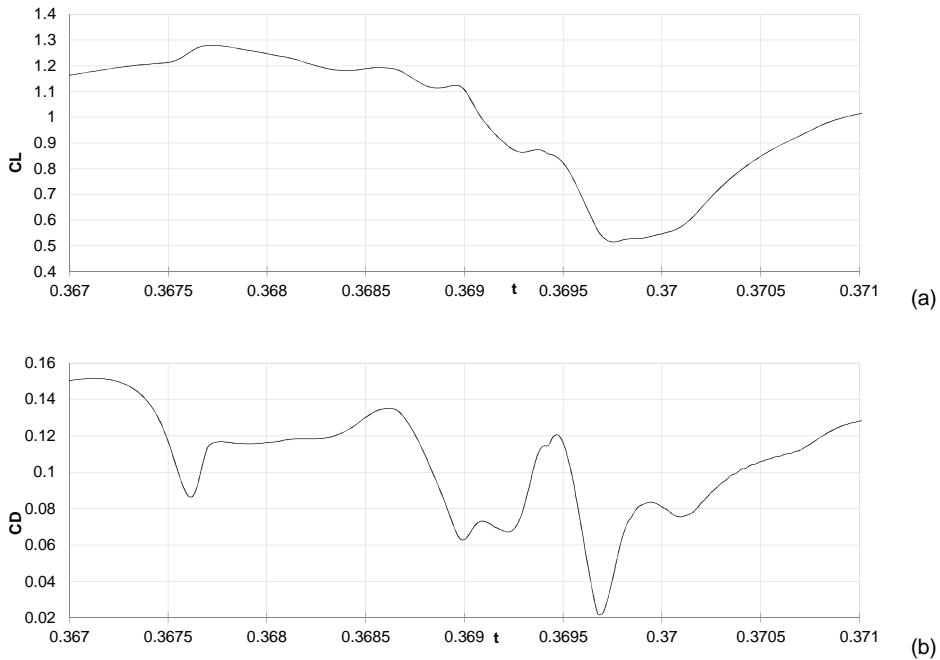


Figure 6-44: Time histories of the (a) lift; and (b) drag coefficients within a specific shedding cycle, predicted by bubble number density of $n_b = 1e+08$

Conclusions

The following conclusions can be drawn from the investigations of the unsteady cavitation phenomena on the NACA0015 hydrofoil at 8° angle of attack:

- The necessity of Reboud's correction on the eddy viscosity in the region with higher vapor fraction to obtain unsteady shedding in FLUENT is confirmed again.
- The unsteady cavitation phenomena for the NACA0015 hydrofoil at 8° angle of attack are more regular than those events observed on the NACA0015 hydrofoil at 6° angle of attack.
- The unsteady phenomena, such as the cavity sheddings and collapses, do not always trigger high peaks in lift and drag in some simulations (depending on the bubble number density n_b).
- The numerical prediction of unsteady cavitation by the RANS method implemented in FLUENT qualitatively matches the experimental observations. For a quantitative match, an appropriate input value of bubble number density seems to be demanded, which is usually lacking due to the complexities and difficulties of the bubble nuclei spectrum measurement in the test facilities.

6.3.3 2D NACA0018-45 ($AoA = 6.5^\circ$)

The third test geometry is the NACA0018-45 hydrofoil at 6.5° angle of attack. The adopted mesh topology is an O-H multiblock one with 309 edges on the foil, which is the same as the mesh used to do the simulation for the non-cavitating condition (see section 5.4.2). The unsteady dynamics is then investigated for a specific cavitation regime with a cavitation number of $\sigma = 0.72$, which falls in the bandwidth of the cavitation numbers in the experimental study on the same geometry by van den Hout (Van den Hout, 2008; Van Terwisga, 2009a). The time step size is selected as 1×10^{-5} s by using the equation (6-1) with a courant number around 0.75.

A velocity-inlet condition is applied on the upstream flow with a vapor fraction equal to zero. On the outlet boundary, a pressure-outlet boundary condition is used. The detailed initial and boundary conditions and the flow properties (taken at a temperature of $23^\circ C$) are listed in Table 6-15.

Table 6-15: Boundary conditions and flow properties for a NACA0018-45 hydrofoil ($AoA = 6.5^\circ$)

Boundary Conditions	NACA0018-45 ($AoA = 6.5^\circ$)	
Velocity Inlet (m/s)	V=24.2	
Pressure Outlet(kPa)	213.115	
Turbulent Intensity (%)	1	
Turbulent Viscosity Ratio	10	
Foil	No-slip Wall	
Tunnel Walls (Top & Bottom)	Slip Wall	
Flow Properties (T=23°C)	Vapor	Liquid
Density (kg/m ³)	0.021	997.5
Dynamic Viscosity(kg/ms)	9.81E-06	0.00093
Vapor Pressure (kPa)	2.811	

The simulation is carried out by using the pressure-based transient solver, and a fully coupled solver is selected to solve the pressure and momentum equations. The pressure is discretized using the PRESTO! scheme, and the convection terms in the momentum equations are discretized by the QUICK scheme which is also used for the turbulence equations and vapor volume fraction equation (ANSYS, 2009). The temporal discretization uses the first-order implicit scheme.

Results by Standard SST $k - \omega$ Turbulence Model

In line with the previous test cases, the residuals of each equation and the volume integral of the mass transfer rate are checked first, and it is found that 40 iterations are sufficient to reach convergence for each time step, as shown in Figure 6-45. With the standard

SST k – ω turbulence model, unsteady dynamics can be observed for the current cavitation number of $\sigma = 0.72$ with a natural frequency of $f \approx 54Hz$, see Figure 6-46.

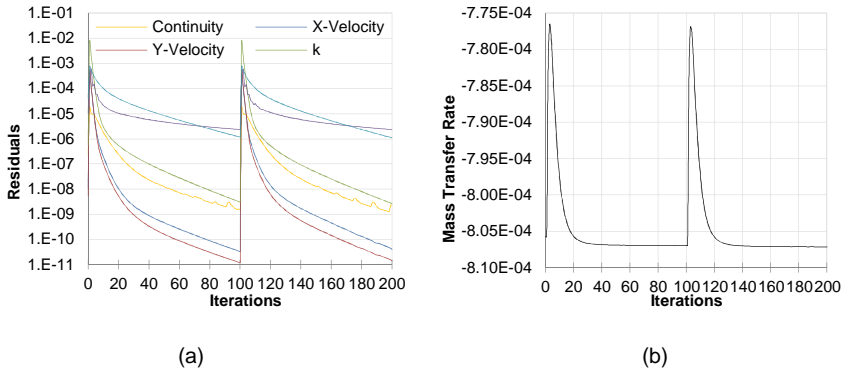


Figure 6-45: The time histories of (a) the residuals and (b) mass transfer rate during two successive time steps with $\Delta t = 1 \times 10^{-5}$ for a NACA0018-45 hydrofoil at 6.5° angle of attack at $\sigma = 0.72$

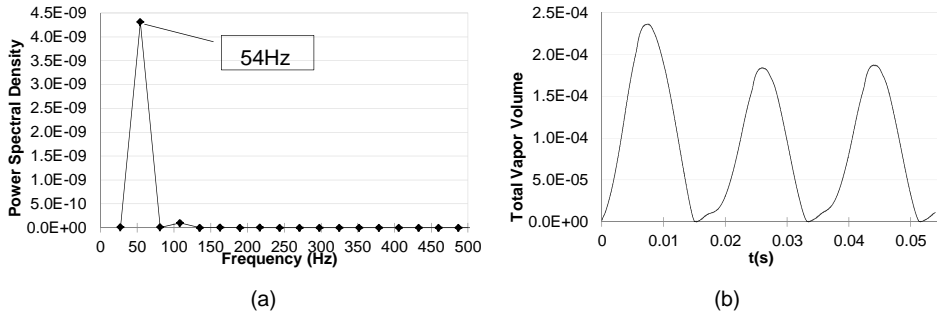


Figure 6-46: (a) The frequency obtained based on the FFT analysis of the time history of (b) the total vapor volume predicted by the standard *SST k – ω* turbulence model for a NACA0018-45 hydrofoil at 6.5° angle of attack at $\sigma = 0.72$

Twelve instants representing the typical unsteady phenomena during one cycle with the standard *SST k – ω* turbulence model are shown in Figure 6-47. The shedding cycle under the current conditions can be described as follows:

- A sheet cavity grows from the leading edge of the hydrofoil on the suction side, and another sheet cavity simultaneously develops from around 66.5% chord length on the pressure side (Figure 6-47-①);
- The sheet cavity on the suction side continues growing. However, the cavity on the pressure side will cease growing when it comes in the vicinity of the trailing edge and then decreases and totally disappears (Figure 6-47-②③);
- The sheet cavity on the suction side will grow into a length which almost covers the whole foil but with a complex vapor fraction distribution inside the cavity. A vapor structure is found developing from the trailing edge on the suction side, and

the upstream sheet cavity will retreat towards the leading edge when this trailing edge cavity grows bigger (Figure 6-47-④⑤);

- A supercavity will be formed together with another newly developed cavity on the pressure side (see Figure 6-48), and a vapor structure will be shed from the pressure side part, and travels and collapses downstream of the trailing edge (Figure 6-47-⑥⑦);
- A second shedding occurs on the suction side, causing a second blend of the cavities on both sides, and vapor structures are then shed off from this newly developed supercavity (Figure 6-47-⑧⑨);
- The cavities on both sides decrease until they disappear (Figure 6-47-⑩⑪), and then develop again to begin a new cycle (Figure 6-47-⑫).

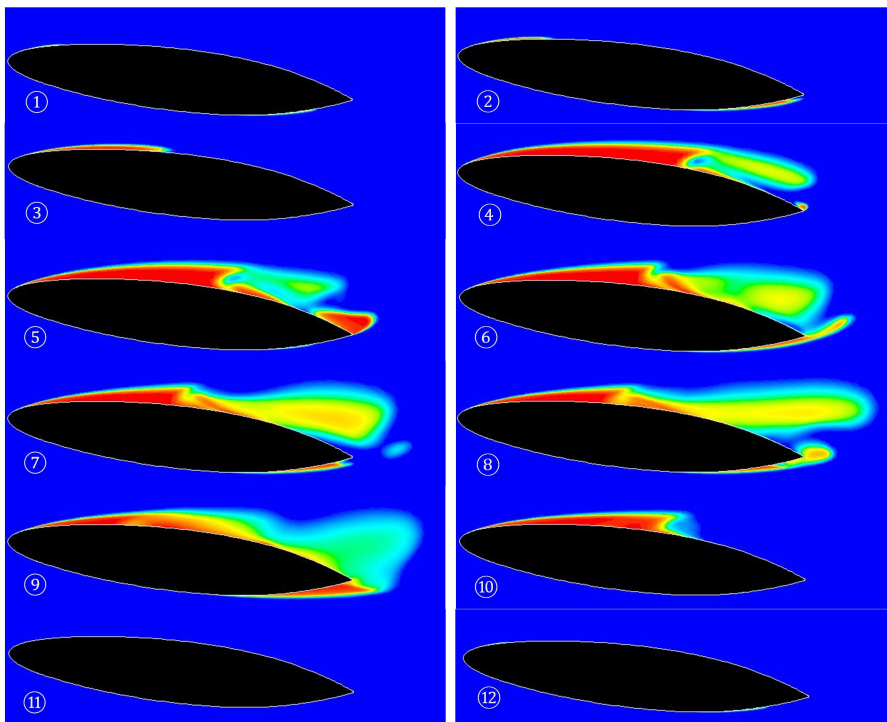


Figure 6-47: Contours of the vapor volume fraction during one cycle over a NACA0018-45 hydrofoil at 6.5° angle of attack with the standard *SST* $k - \omega$ turbulence model at $\sigma = 0.72$ (Red color indicates pure vapor, whereas blue color indicates pure liquid) (Flow from left to right)

$\alpha=0.01$



Figure 6-48: Contour of vapor fraction with iso-value of 0.01 at the instant ⑥ in Figure 6-47

The most prominent difference between the cavitation phenomena observed on the NACA0018-45 hydrofoil and NACA0015 hydrofoil with either 6° or 8° angle of attack is that cavities can be observed not only on the suction side but also on the pressure side. The irregular shape of the interface between the vapor and liquid after the mid-chord is supposedly caused by the strong interaction between the cavities on the suction side and the cavities developed from the pressure side. It is confirmed that more intense cavity dynamics are observed due to the steeper pressure gradient as compared to the NACA0015 hydrofoil.

The time histories of the total vapor volume and the lift and drag coefficient during the selected cycle are illustrated in Figure 6-49, and the twelve instants corresponding to the instants in Figure 6-47 are specified on the three plots respectively. Clear sudden peaks can be observed at the instants where the volume of cavities generated on the pressure side decrease to zero, such as the instants ③, ⑩, and ⑪.

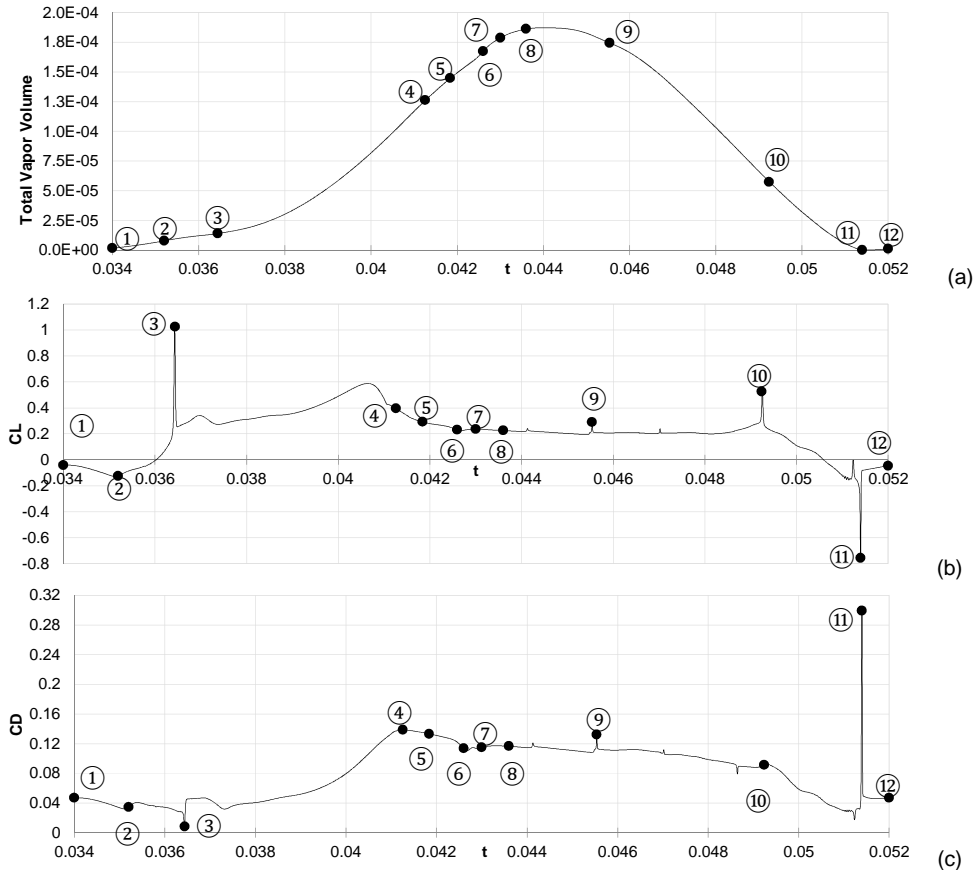


Figure 6-49: Time histories of the (a) total vapor volume; (b) lift; and (c) drag coefficients within a selected shedding cycle corresponding to the instants in Figure 6-47

Results by Modified *SST k – ω* Turbulence Model

The characteristic cavities generated on the pressure side can also be captured when the modified *SST k – ω* turbulence model is used but with a more intense and complex interaction with the vapor structures developed on the suction side. A main frequency of $f \approx 50.5\text{Hz}$ is then obtained from an FFT analysis of the time history of the total vapor volume over ten cycles that already eliminate the start-up effect, see Figure 6-50.

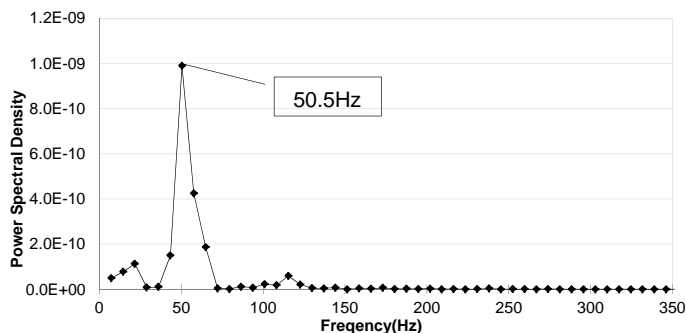


Figure 6-50: The frequency obtained based on the FFT analysis of the time history of the total vapor volume predicted by the modified *SST k – ω* turbulence model over a NACA0018-45 hydrofoil at 6.5° angle of attack at $\sigma = 0.72$

The essential features during one cycle are illustrated in Figure 6-51. It can be observed that the pressure side cavitation indeed affects the suction side flow at the trailing edge. The collapses mostly occur downstream of the trailing edge, and the whole cycle can be characterized as follows:

- On the suction side, a new sheet cavity develops from the leading edge of the hydrofoil and will be merged into the vapor structures that formed at a position of approximately 20% chord length (indicated by the black arrow at instant ①). The vapor structures that formed during the previous cycle continue to travel downstream. On the pressure side, small cavity bubbles are formed and move towards the trailing edge (Figure 6-51-①②);
- The cloudy structures behind the trailing edge completely collapse, and the main sheet cavity on the suction side is growing until it has reached an extent of approximately 90% chord length of the hydrofoil. It is then forced to retreat towards the leading edge driven by the growing vapor structures around the trailing edge (Figure 6-51-③④);
- On the suction side, a vapor structure forms in the closure region of the main sheet cavity where the vertical liquid flow gains enough vortex strength. This vapor

structure affects the cavities on both sides, causing a retreating sheet cavity on the suction side, whereas complex phenomena including shedding and collapse occur in the tail part of the cavity on the pressure side(Figure 6-51-⑤⑥);

- The newly developed cavities on the pressure side will push the cloudy cavity at the trailing edge on the suction side, to merge into the upstream main sheet cavity, and subsequently cut the large-scale sheet cavity into two parts (Figure 6-51-⑦):
- On the suction side, the upstream part of the main sheet cavity will shed off vapor structures several times which will be merged into the downstream cloudy cavities (Figure 6-51-⑧⑨);
- The main sheet cavity decreases and disappears eventually. The remaining small vapor structures travel towards the trailing edge and tend to merge into larger-scale ones. A new sheet cavity develops from the leading edge on the suction side and a new cycle starts (Figure 6-51-⑩⑪⑫).

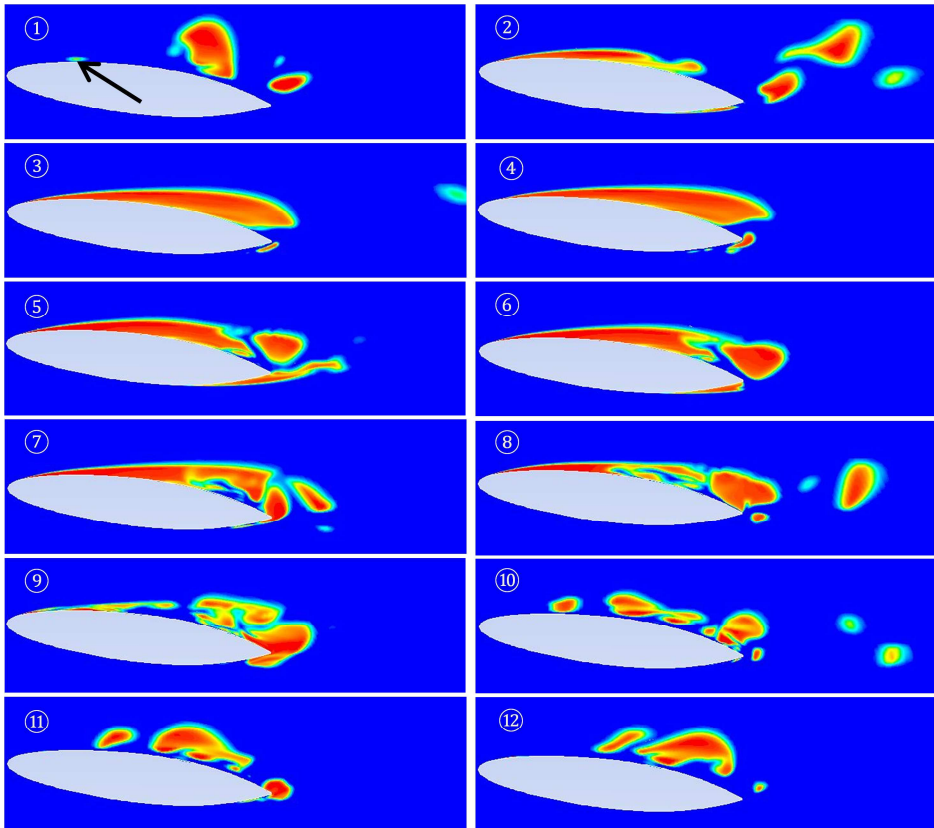


Figure 6-51: Contours of the vapor volume fraction during one cycle for a NACA0018-45 hydrofoil at 6.5° angle of attack with the modified $SST\ k-\omega$ turbulence model at $\sigma = 0.72$ (Red color indicates pure vapor, whereas blue color indicates pure liquid) (Flow from left to right)

In Figure 6-52, the time histories of the total vapor volume, and lift and drag coefficients are plotted with twelve characteristic points indicated, corresponding to the instants illustrated in Figure 6-51.

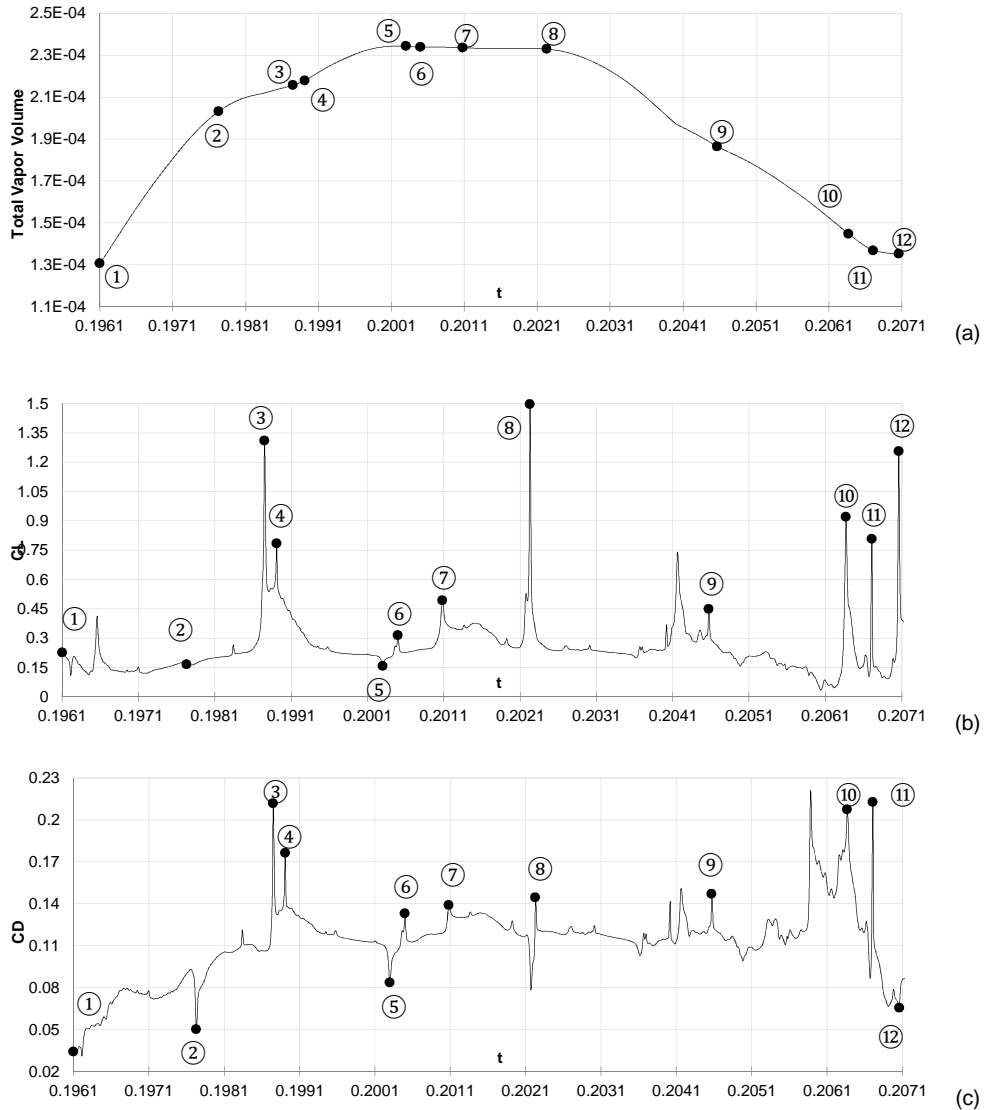


Figure 6-52: Time histories of the (a) total vapor volume; (b) lift; and (c) drag coefficients within a specific shedding cycle in accordance with the instants in Figure 6-51

There are more peaks occurring compared with the same time trace from the uncorrected turbulence model, corresponding to the more intense and complex interaction between the cavities on both sides, see Figure 6-47 and Figure 6-51. It can be observed that when the

modified *SST* $k - \omega$ turbulence model is adopted, the cavities on the suction side have a higher averaged vapor volume fraction, especially at the trailing region. Furthermore, a higher value of the maximum total vapor volume is obtained when the modified *SST* $k - \omega$ turbulence model is used. It is suggested that the stronger interaction predicted by the modified *SST* $k - \omega$ turbulence model is largely induced by a larger volume of cavities with higher averaged vapor volume fraction.

Comparison with Experimental Results

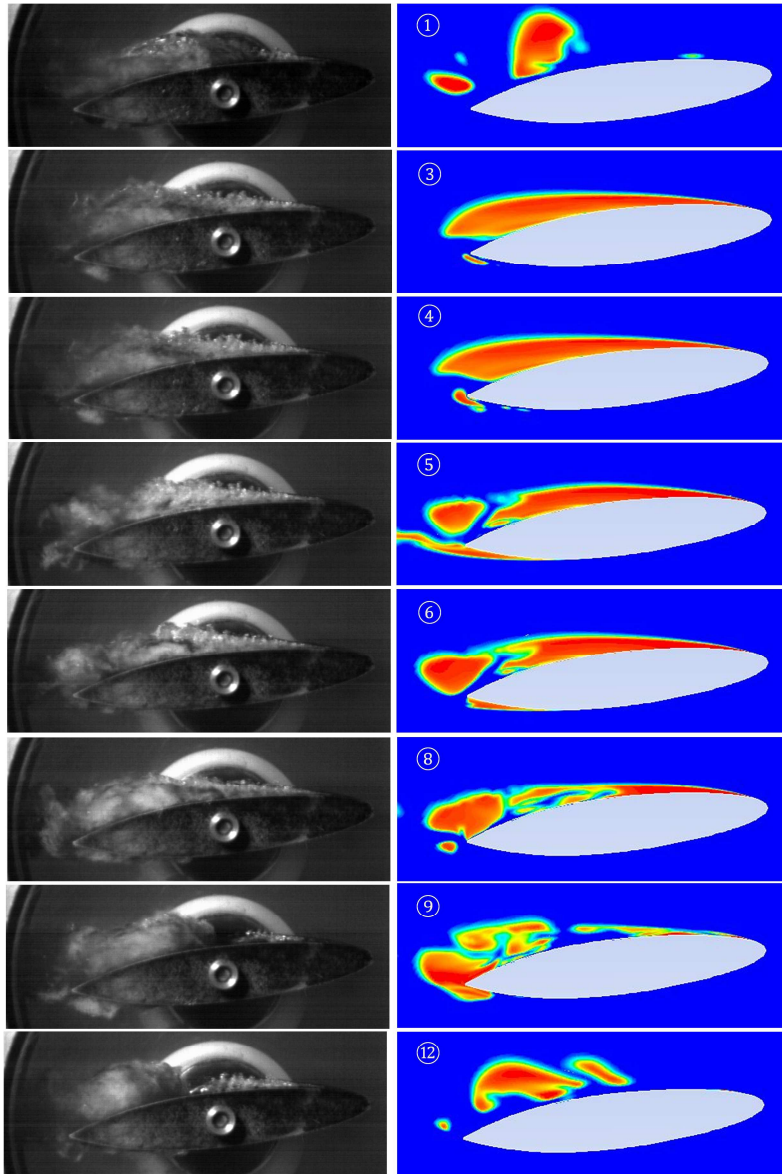
Detailed observations on a NACA0018-45 hydrofoil are carried out in the MARIN High Speed Cavitation Tunnel for a range of cavitation numbers at a tunnel velocity of approximately 24 m/s. The examined test foil has a chord length of 60 mm and a span width of 40 mm. It is rotated over an angle of 6.5° at the mid-chord. The selection of experimental results which are compared to the simulation results are listed in Table 6-16.

Table 6-16: Test conditions for the examined experimental data

	003-04
AoA (deg)	6.5
T(°C)	23
V(m/s)	17.71
σ_v	0.72
Re	150E+06

In Figure 6-53, eight characteristic frames from the high-speed camera are compared with the captured instants during a cycle by the RANS method implemented in FLUENT (as shown in Figure 6-51). It is found that also the dynamics occurring on the pressure side have been captured by the high-speed camera, and pits from the cavitation erosion damage can be observed on both sides under the current test conditions.

From the side view images, the extent and volume of the cavities on both sides predicted by the RANS method implemented in FLUENT show a good match to the experimental observations. It can be observed that the upper interface of the cavity on the suction side can extend over a distance longer than the foil, and a relatively smaller extent is observed for the lower interface when the collapse occurs downstream of the trailing edge. Similar phenomena are captured by FLUENT, and the extent of the cavity on the suction side qualitatively matches the experimental observations, as shown in the instant ③ and ④ in Figure 6-53. Furthermore, the characteristic intensive interactions between the cavities on both sides are observed around the trailing edge of the hydrofoil, which is similar to the simulation results, as shown at the instants ⑤ and ⑨ in Figure 6-53.



Experimental Observations

Numerical Simulations

Figure 6-53: Characteristic frames during one cycle recorded by a high-speed camera corresponding to the eight instants in time from Figure 6-51 (Left: photos recorded by the high-speed camera, Right: images from simulation results) (Flow from right to left)

Conclusions

From the study on the unsteady cavitating flow over a NACA0018-45 hydrofoil at 6.5° angle of attack, the following conclusions can be drawn:

- More intense cavity dynamics and clear pressure side cavities can be observed due to the steeper pressure gradient toward the Trailing Edge of the hydrofoil as compared to the NACA0015 hydrofoil.
- Stronger interactions between the vapor structures at both sides can be observed when Reboud's correction is applied on the eddy viscosity in the region with a higher vapor fraction.

6.4 CONCLUSIONS

In this chapter, the capability of the multiphase RANS method implemented in FLUENT to capture steady cavitating phenomena is assessed for the 2D NACA0015 hydrofoil at 6° angle of attack. For the capability to capture unsteady cavitating phenomena, the investigations are conducted on a 2D NACA0015 hydrofoil at 6° and 8° angle of attack and a 2D NACA0018-45 hydrofoil at 6.5° angle of attack. The 2D cases are primarily used for testing of input and control parameters, such as the influence of the grid density, the turbulence models and the numerical interpolation schemes. The results show that the computational model and the current set-up could capture many of the features seen in the experiments, such as the break-up of the main sheet cavity, the formation of the cloudy cavity and the periodic shedding.

The following conclusions are drawn from the study on the steady cavitating flow over the 2D NACA0015 hydrofoil at 6° angle of attack:

- The order of the temporal discretization scheme does not play a primary role on the integral quantities, such as lift and drag.
- The integral forces and the turbulent kinetic energy are grid independent when using the current grid resolution, where the maximum y^+ value on the foil surfaces is smaller than 1.0. However, more resolution of the cavity structures at the closure of the main cavity can be obtained with the finer grid.

The following conclusions are drawn from the study on the unsteady cavitating flow over the hydrofoils that are tested in this chapter:

- A realistic dynamic shedding of the sheet cavitation is only obtained after attenuating the eddy viscosity in the region with higher vapor volume fraction in the multiphase RANS method implemented in FLUENT. It appears that the reduction of the eddy viscosity plays an essential role in the unsteady dynamics calculated with FLUENT.

- The time step size that is adopted in the transient solver can be estimated from the time for the flow travelling over a characteristic spatial length (See equation (6-1)).
- It should be noted that for the unsteady simulations, the number of iterations per time step should be carefully selected in order to avoid a lack of numerical convergence, which may result in a significant influence on the prediction of the shedding frequency. It is suggested that convergence is reached when the mass transfer rate does not change anymore with the number of iterations during each time step.
- The basic unsteady phenomena are grid independent for the currently used topology and resolution ($y^+ < 1$), which is in an O-H topology with appropriate grid density around the nose and tail of the foil.
- The sudden peaks in both lift and drag are attributed to the unsteady cavitation phenomena, such as the cavity sheddings and collapses.
- The source strength involved in the cavitation model is assumed to be proportional to the bubble number density. Therefore, it is important to be aware of the influence of the bubble number density on the cavitation phenomena predicted by the RANS method implemented in FLUENT.

Chapter 7: RESULTS ON

3D CAVITATING FLOW

7.1 OVERVIEW

This chapter will further examine the capability of the RANS method implemented in FLUENT to predict the three dimensional characteristics of the unsteady cavitating dynamics by conducting simulations in a 3D domain.

The investigation will be conducted on two hydrofoils, the NACA0015 hydrofoil at an angle of attack of 8° and the NACA0018-45 hydrofoil at an angle of attack of 6.5° . The numerical results will be compared with the observations made in the MARIN High Speed Cavitation Tunnel for both hydrofoils. The test conditions that led to obvious impact on the hydrofoil surface are selected. According to currently available experimental data, a regime characterized by $\sigma = 2.01$ is examined for a NACA0015 hydrofoil at 8° angle of attack, whereas a regime characterized by $\sigma = 0.72$ is examined for a NACA0018-45 hydrofoil at 6.5° angle of attack.

7.2 EXPERIMENTAL SET-UP

A series of observations and simultaneous acoustic emission measurements have been conducted for NACA0015 and NACA0018-45 hydrofoils separately in MARIN's High Speed Cavitation Tunnel (Wageningen, The Netherlands). To study the erosiveness of the unsteady cavitating flow, paint erosion tests are conducted in addition to acoustic measurements and high speed video recording.

The aim of these three test methods has been described by Van Rijsbergen and Boorsma (2011) as follows:

- A paint erosion test to localize the most aggressive impacts.
- High speed video observations to record the cavity behavior associated with implosions and rebounds.
- Acoustic emission data to indicate the aggressiveness of the implosion and the

distance to the foil.

The MARIN high speed cavitation tunnel is approximately 2 meters long and has a rectangular test section with 80 mm high by 40mm wide. The two tested NACA hydrofoils are with the same chord length of 60mm . Pictures of the tunnel and test section are shown in Figure 7-1 , as illustrated in the report by Boorsma (2010).

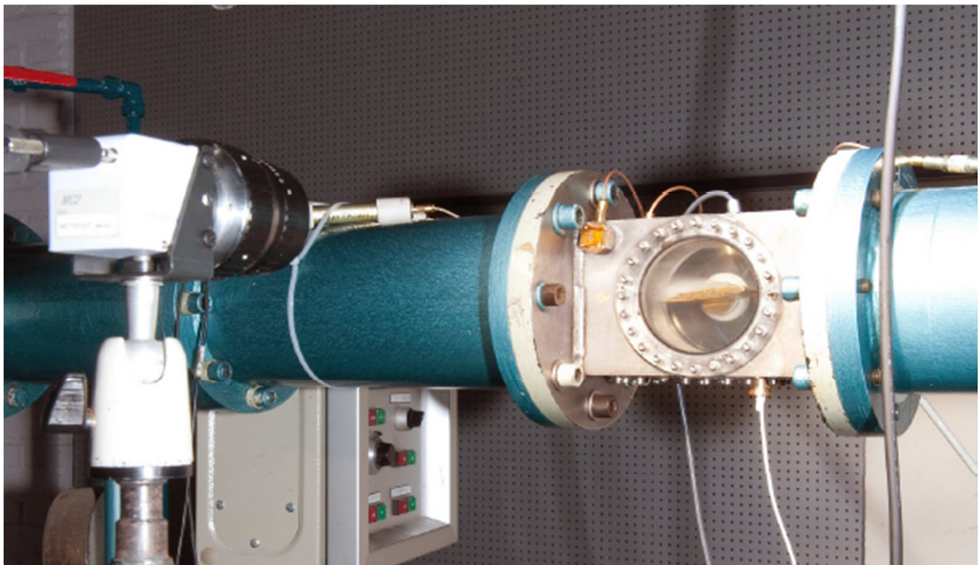


Figure 7-1: Cavitation tunnel and test section

7.3 3D NACA0015 ($AoA = 8^\circ$)

7.3.1 Case Description

In this section, the three-dimensional characteristics of the unsteady cavitating flow over a NACA0015 hydrofoil at an angle of attack of 8° will be studied. The calculations are conducted on a 3D mesh which is obtained by extruding a 2D mesh in the span-wise direction. This original 2D mesh has the same topology as the 2D test case, as described in section 5.3.1. With respect to the expected symmetry characteristic in the span-wise direction, the computational domain is only extended to the mid-span where a symmetry boundary condition is applied. A close-up of the mesh around the hydrofoil with a width of 20mm , i.e. half of the width of the MARIN High Speed Cavitation Tunnel, is shown in Figure 7-2.

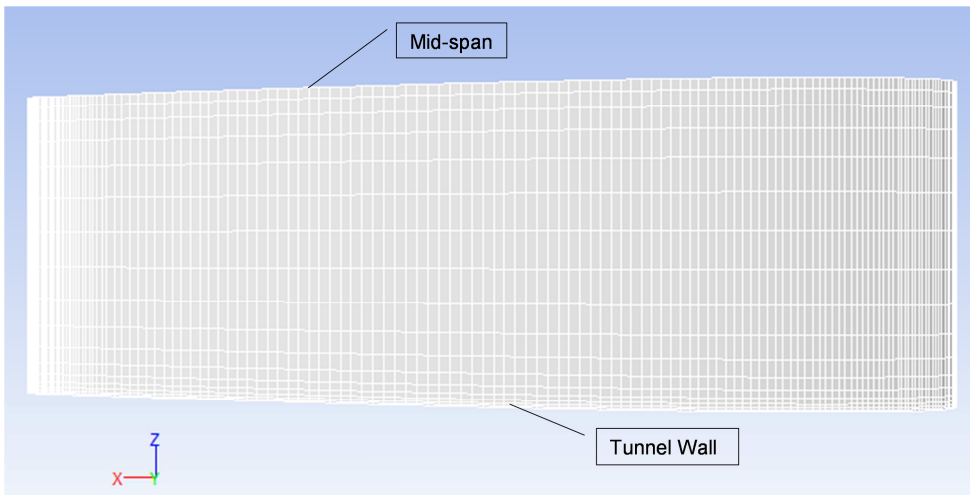


Figure 7-2: Close-up of the mesh for a NACA0015 hydrofoil at 8° angle of attack (3D representation)

A time step size of $\Delta t = 2e-05\text{s}$ is used based on the time scale estimation equation (6-1) with a Courant number around 0.75. A velocity-inlet condition is applied in the upstream inlet plane with an initial vapor fraction equal to zero. A pressure-outlet boundary condition is used at the outlet plane. The specified pressure at the outlet can be derived from the cavitation number to be investigated. On the tunnel walls, a no-slip wall condition is applied. The physical properties of the two-phases, liquid and vapor, are taken at a temperature of 16.3°C . The detailed initial and boundary conditions and the flow

properties are listed in Table 7-1.

Table 7-1: Boundary conditions and flow properties for a NACA0015 hydrofoil ($AoA=8^\circ$)

Boundary Conditions		NACA0015 ($AoA=8^\circ$)	
Velocity Inlet (m/s)	V=17.3		
Pressure Outlet (kPa)	800 ($\sigma=5.34$); 302.295 ($\sigma=2.01$)		
Turbulent Intensity (%)	1		
Turbulent Viscosity Ratio	10		
Foil	No-slip Wall		
Mid-span	Symmetry		
Tunnel Walls	No-slip Wall		
Flow Properties ($T=16.3^\circ\text{C}$)		Vapor	Liquid
Density (kg/m ³)	0.01389	998.85	
Dynamic Viscosity(kg/ms)	9.63E-06	0.0011	
Vapor Pressure (kPa)	1854		

The simulations of the cavitating flow are carried out by using the pressure-based transient solver, and a fully coupled solver is selected to solve the pressure and momentum equations. The pressure is discretized using the PRESTO! scheme, and the convection terms of the momentum equations are discretized by the QUICK scheme, and the same is done for the terms in turbulence equations and vapor volume fraction equation (ANSYS, 2009). The temporal discretization used the first-order implicit scheme.

The experiments to be compared with the numerical simulations are performed by MARIN in cooperation with Lloyd's Register (Van Rijsbergen and Boorsma, 2011). The selected test case is measured in Run No. 26, and the test conditions are listed in Table 7-2. They closely resemble the conditions in the unsteady simulation by FLUENT.

Table 7-2: Test conditions for Run No. 26

	Run No. 26
AoA (deg)	8
V(m/s)	17.3
σ	2.01
Re	9.50E+05

7.3.2 Wetted Flow Results

Before discussing the results for the unsteady cavitating flow, we study the solution for the wetted flow to assess the grid feasibility with a cavitation number of $\sigma = 5.34$. If the computational domain is set with slip sidewalls, the pressure distribution on the hydrofoil is almost unchanged in the span-wise direction. However, the minimum pressure over the hydrofoil will be increased due to the decreased velocity when the effect of no-slip

sidewalls is taken into effect. The minimum static pressure and the pressure distribution will be a bit different from the tunnel wall to the mid-span, as shown in Figure 7-3.

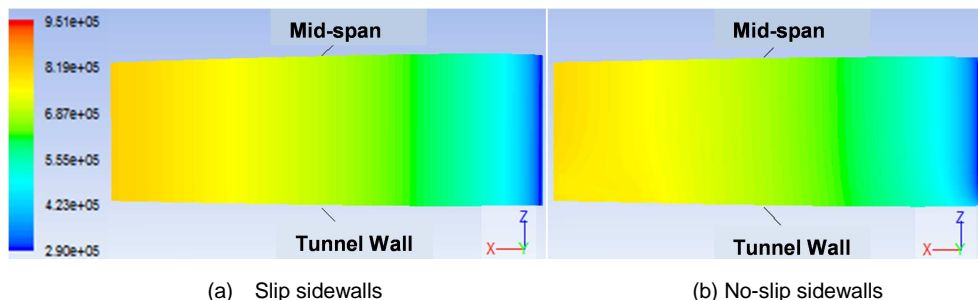


Figure 7-3: The distribution of the static pressure (in Pa) over a NACA0015 hydrofoil at 8° angle of attack (a) without, and (b) with sidewalls (Flow from right to left)

The minimum pressure coefficient for the case with slip sidewalls reaches a value of $C_{p_{\min}} \approx -3.44$, identical to what was obtained in 2D computational domain. When the no-slip sidewalls are applied, the minimum pressure reaches whereas $C_{p_{\min}} \approx -3.3$ at the mid-span, and $C_{p_{\min}} \approx -2.6$ at the tunnel wall. These values are compared with the experimentally observed result and the simulation result by Hoekstra with FreSCo in Table 7-3 (Van Rijsbergen and Boorsma, 2011).

Table 7-3: Comparison of the minimum pressure coefficients

Cases	Cpmin	
	Tunnel Wall	Mid-span
Experimental Result	-3.5	
FreSCo (Hoekstra)	-3.3	
RANS (Slip sidewalls)	-3.44	
RANS (No-Slip sidewalls)	-2.6	-3.3

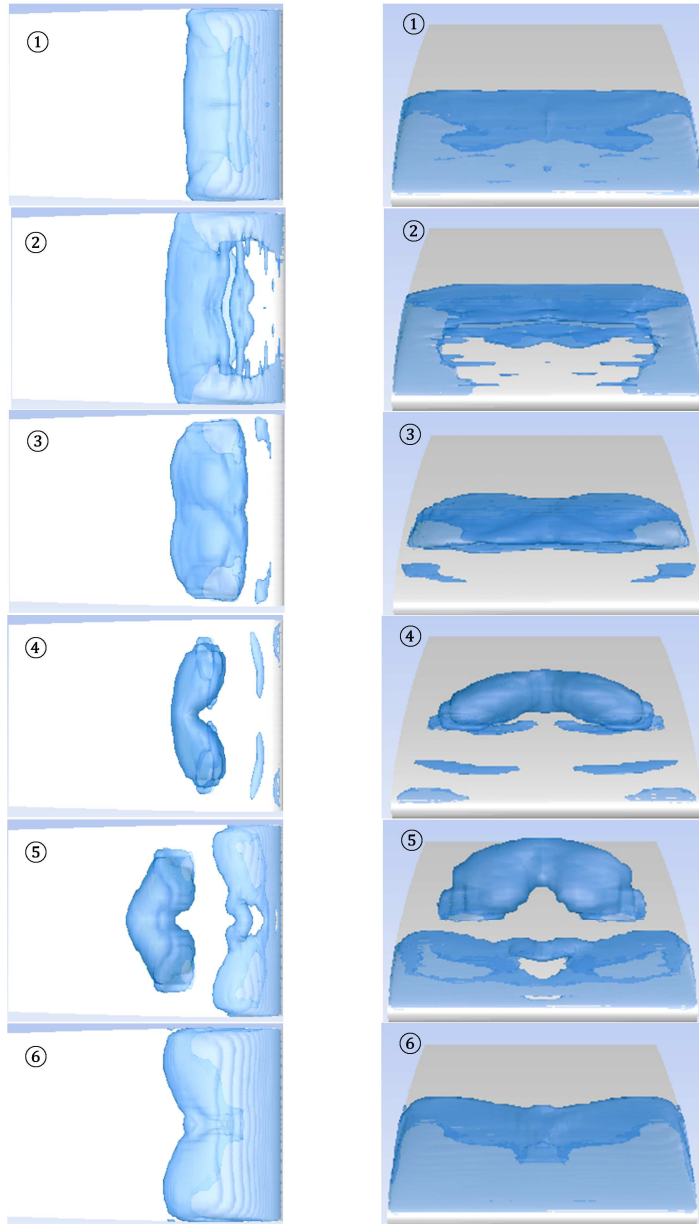
It is concluded by Van Rijsbergen and Boorsma (2011) that the differences between the numerical results and the experimental data may be due to the uncertainties of the experiment, such as application of a leading edge roughness, definition of inception and transducer uncertainties.

7.3.3 Results and Discussion on Cavitating Flow

Shedding Process

The RANS results basically reproduce the features of the shedding process observed in the cavitation tunnel at the selected condition: $\sigma = 2.01$ and $U = 17.3m / s$ at 8° angle of attack, such as the detachment of cloudy cavities from the sheet cavity and the deformation and collapse of the cloudy cavities.

The typical images obtained by visualizing the iso-surface of the instantaneous vapor volume fraction of $\alpha = 0.1$ in top view and downstream view are separately shown in Figure 7-4, representing a typical shedding cycle.



(a) Top view (Flow from right to left)

(b) Downstream view

Figure 7-4: Sequences of iso-surface plots of the instantaneous vapor volume fraction of $\alpha = 0.1$ during one typical shedding cycle in (a) top view; and (b) downstream view for a NACA0015 hydrofoil (3D representation) at 8° angle of attack at $\sigma = 2.01$ with the modified *SST* $k - \omega$ turbulence model

The observed unsteady phenomena can be characterized as follows:

- The leading edge sheet cavity is growing together with the collapse of the cloudy cavity formed from the last pinch-off (Figure 7-4- ①);
- Re-entrant flow moves upstream towards to the leading edge until it breaks up the main sheet cavity. The upstream part of the sheet cavity partially disappears from the mid-span and this causes increasing lift and drag at the same time instant (Figure 7-4- ②);
- The downstream part of the sheet cavity starts to roll up from the foil surface and forms a cloudy cavity in a cylindrical shape, slightly thicker at the mid-span and thinner at the sides of the hydrofoil (Figure 7-4- ③);
- The remaining upstream part of the main sheet cavity prolongs in span-wise location, and is subsequently merged into the new sheet cavity that develops from the leading edge again. The cloudy cavity downstream gradually transforms into a horse-shoe shape (Figure 7-4-④⑤);
- Finally, the cloud cavity collapses downstream and the leading edge sheet cavity extends along the chord length, initiating a new cycle (Figure 7-4- ⑥).

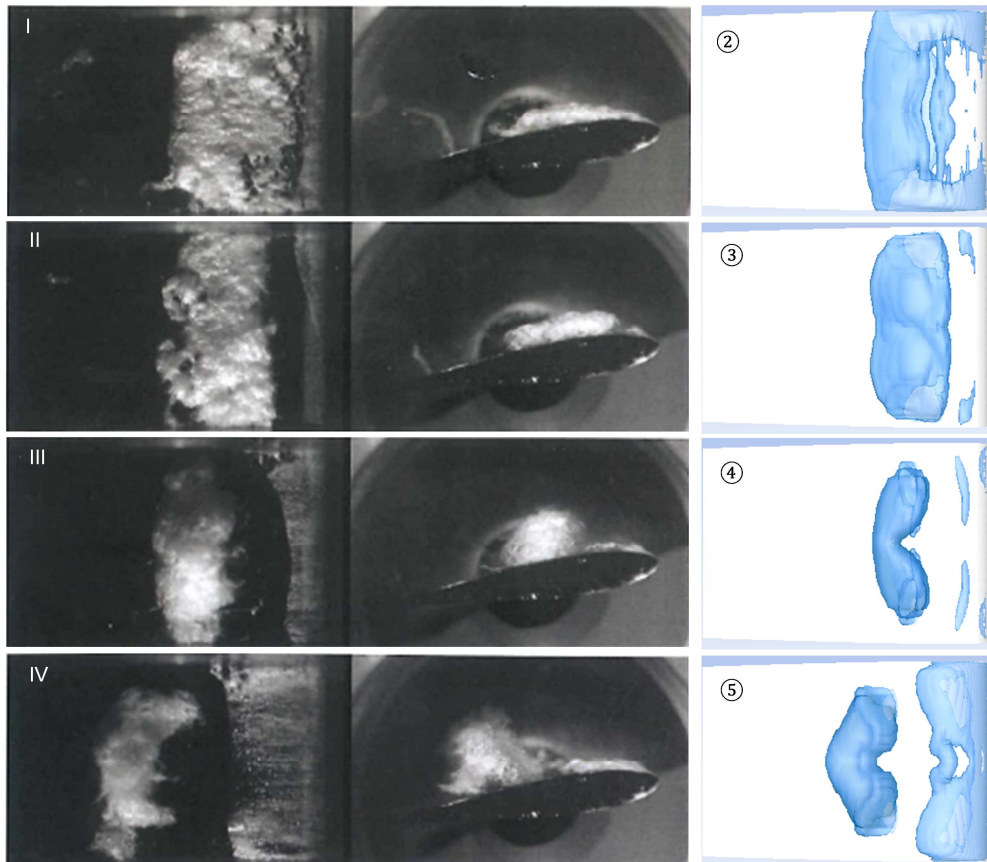
When comparing the numerical simulation results and the experimental observations, it is found that the individual main sheet cavity after the collapse of the cloudy cavities (Figure 7-4-⑥) has not been observed in the experiments. The synchronization of the collapse of the cloudy cavities and the development and break-up of the leading edge sheet cavity is a bit different but qualitatively shows a good match, as shown in Figure 7-5. The cavity structures and their approximate positions seem to be predicted properly.

It can be observed that the characteristic unsteady phenomena predicted by the RANS method implemented in FLUENT are qualitatively compared with the experimental observations, such as the break-up of the sheet cavity by the re-entrant flow, and the formation and collapse of the cloudy cavities. A detailed investigation on the re-entrant flow and collapses of the cloudy cavities in the horse-shoe shape will be done in detail in the following sections.

Total Vapor Volume

The time history of the volume integral of the vapor volume fraction shows a high-frequency fluctuation ($f \approx 216Hz$) with an unsteady amplitude characterized by a very low frequency ($f \approx 36Hz$). It is qualitatively similar as to what has been observed in the 2D computational domain. The two characteristic frequencies are from a FFT spectral

analysis based on the time history of the total vapor volume over twelve cycles with low frequency.



(a) Experimental Observations

(b) Numerical Simulations

Figure 7-5: Comparison between several typical instants obtained by (a) experimental observations; and (b) numerical simulations (iso-surface plots of the instantaneous vapor volume fraction of $\alpha = 0.1$) for the flow over a NACA0015 hydrofoil (3D representation) at 8° angle of attack at $\sigma = 2.01$ with the modified *SST* $k - \omega$ turbulence model (Flow from right to left)

A frequency of $188Hz$ is obtained from the observations by the high-speed camera (Van Rijsbergen and Boorsma, 2011), where an averaged period of about 80 frames at 15 kHz represents a typical cycle. The conditions and properties of the test facility may be the reason for this discrepancy, such as the uncertainties which have already been referred to in the comparison of the wetted flow results, and also the bubble nuclei number distribution in the cavitation tunnel, which has been demonstrated to affect cavitation inception, limited cavitation and even fully developed cavitation (Liu et al., 1993).

Lift and Drag

The relationship between the unsteady shedding and the integral forces on the hydrofoils has been discussed previously in the analysis of the results on the 2D cavitating flow. The study will be further pursued for the results in the 3D cavitating flow, therefore the time histories of the total vapor volume, and lift and drag coefficients during a typical shedding cycle are illustrated in Figure 7-6. Six instants are indicated corresponding to the sequence shown in Figure 7-4.

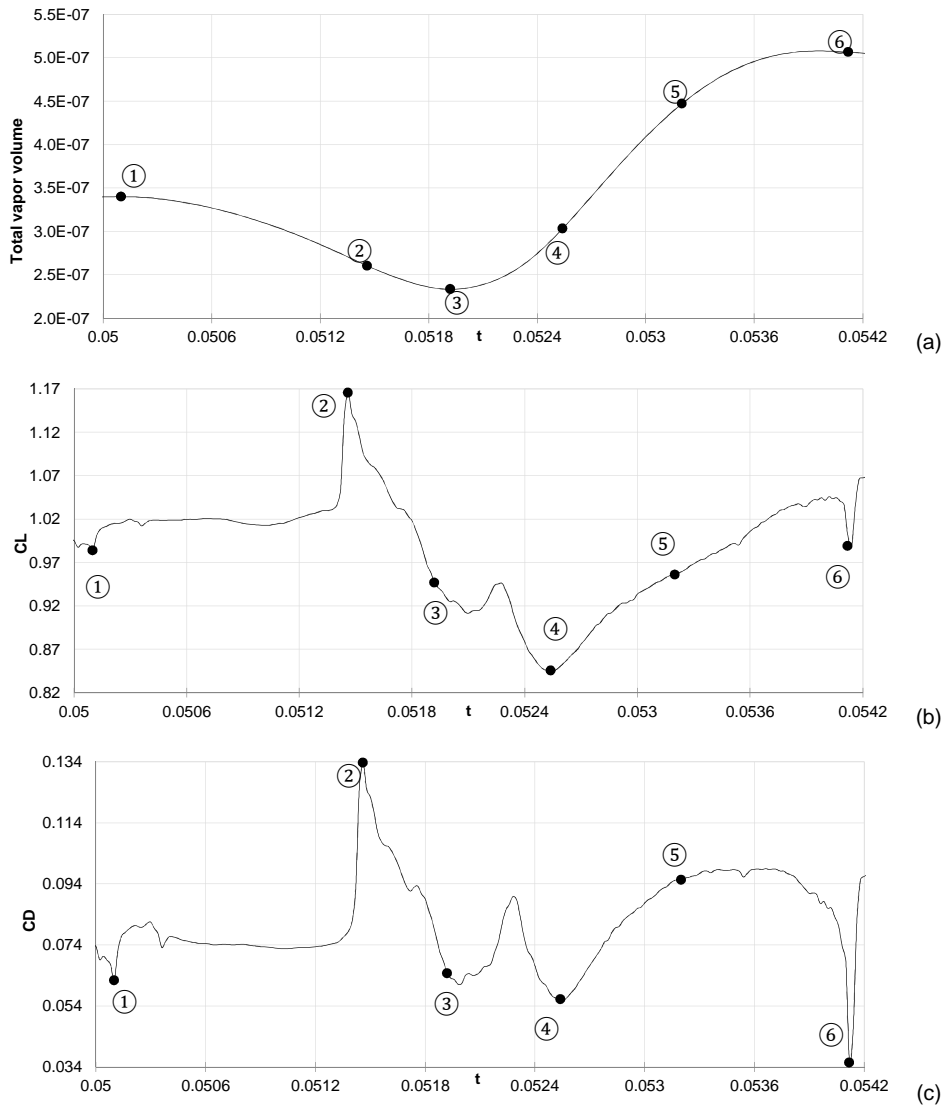


Figure 7-6: Time histories of the (a)total vapor volume; (b) lift; and (c) drag coefficients within a specific shedding cycle in accordance with the time instants in Figure 7-4

The collapses at instant ① and ⑥ correspond to the two drops in both lift and drag. The increase in both lift and drag at instant ② corresponds to partially disappearing leading edge sheet cavity due to the break-up effect of the re-entrant flow. Similar conclusions as for the 2D case can be drawn based on the analysis of the results for the 3D computational domain: the sudden leap of the lift and drag on the hydrofoil is always related to intense unsteady dynamics, such as the shedding off due to the re-entrant flow and the collapses of the cloudy cavities.

Re-entrant Flow

The re-entrant flow which travels in upstream direction underneath the leading edge cavity is the main cause of the break-up of the sheet cavity and the detachment of the cloudy cavities. This has been confirmed by experimental observations on a three dimensional Delft Twist Foil by Foeth (2008). He also presented a sketch of the re-entrant pattern, as shown in Figure 7-7 (a). Foeth (2008) stated that the re-entrant flow could be in various directions. Besides the traditional re-entrant flow which is mainly directed upstream, another re-entrant jet (termed as side-entrant jet by Foeth) which is generated from the sides has a span-wise velocity component directed into the cavity and may have a small up- or down- stream component. This side re-entrant jet is termed as a side-entrant jet to emphasize the three-dimensionality of the flow and its possible directions are sketched in Figure 7-7 (b).

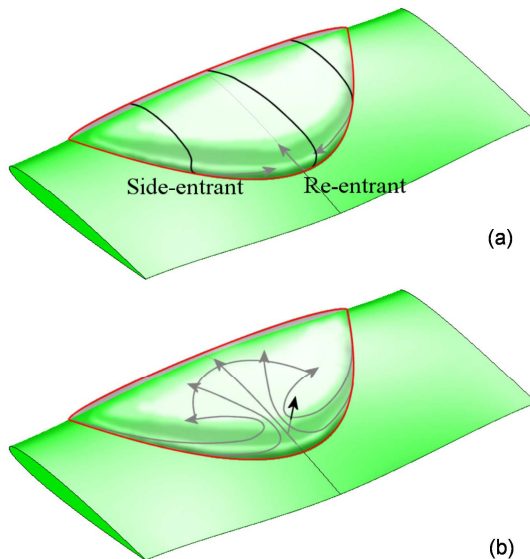


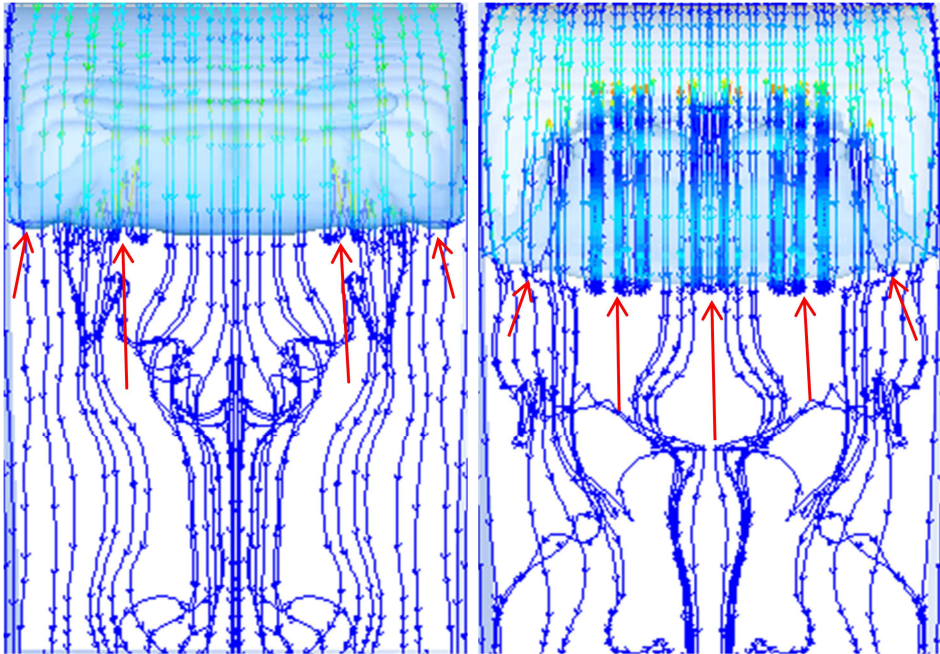
Figure 7-7: (a) Streamlines over the cavity directed inward; (b) Estimate of the direction of re-entrant flow travelling in the lobes causing a second pinch-off (Foeth, 2008)

Boorsma (2010) also observed that the re-entrant jet starts from the wall, moving both upstream and towards the mid-span. He explained that the most likely reason lies in an effect of the wall boundary layer of the tunnel walls, which also may be the reason for the crescent shaped cavity (horse-shoe shaped cavity). This can be explained in the following way: the momentum of the re-entrant jet depends on the pressure gradient in the cavity closure region, and the direction of the re-entrant jet is normal to the cavity closure line; due to the effect of the boundary layer near sidewalls, the end of sheet cavity will bow at the sidewalls and re-entrant jets will be generated starting from the sidewalls heading to the mid-span, resulting in the side-entrant jet referred to by Foeth (2008).

In order to study the behavior of the re-entrant flow in the current unsteady cavitating flow, a number of instants have been selected during the period when the re-entrant flow travels upstream and cuts off the main sheet cavity, i.e. the interval between instant ① and ② in Figure 7-4. The sequences that show the re-entrant flow traveling upstream and reaching the upper liquid/vapor interface are illustrated in Figure 7-8, showing the pathlines over the surface of the cavity colored by the vapor volume fraction. It also shows the pattern of the iso-surface of the instantaneous vapor volume fraction of $\alpha = 0.1$.

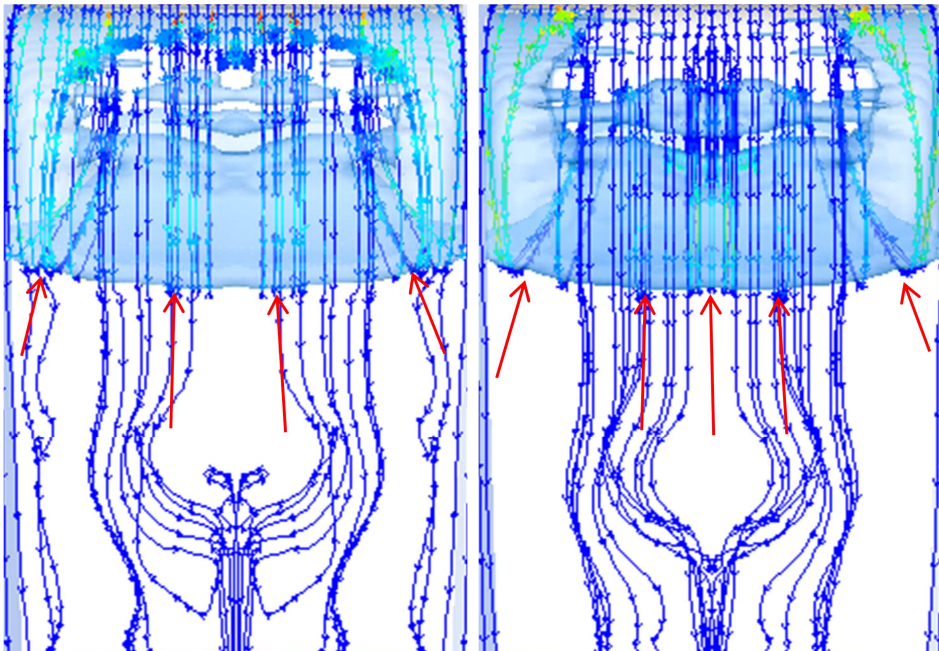
It has been observed by Van Rijsbergen and Boorsma (2011) that the re-entrant jet flow introduces gaps in the sheet cavity and moves upstream until the leading edge is reached, causing a detachment of cloudy cavities from the main sheet. By looking into the details obtained by the numerical simulations, a similar behavior has been observed. It can be characterized as follows:

- At the instant ① in the Figure 7-8, isolated re-entrant jets are formed in the closure region of the sheet cavity, indicated by the red arrows. These isolated re-entrant jets travel underneath the sheet cavity towards the leading edge in both upstream and span-wise direction.
- Subsequently, the re-entrant jets gain more momentum and finally touch the upper interface of the liquid and vapor. Several pieces of vapor structures are formed due to the break-up of the leading edge cavity by the re-entrant and the side-entrant flow, indicated by the red arrows (instant ①-1 and ①-2 in Figure 7-8).
- At the instant ② in the Figure 7-8, the leading edge cavity partially disappears and the remaining structures are further affected by the side-entrant flow originating from the sides of the cavity, also indicated by the red arrows.
- Finally, the sheet cavity will be fully broken up and sheds off a cloudy cavity resembling the shape of a cylinder, as shown at instant ③ in Figure 7-4.



(a) Instant ① (Flow from top to bottom)

(b) Instant ① -1 (Flow from top to bottom)



(c) Instant ① -2 (Flow from top to bottom)

(d) Instant ② (Flow from top to bottom)

Figure 7-8: Re-entrant flow over NACA0015 hydrofoil (3D representation) at 8° angle of attack at $\sigma = 2.01$ with the modified *SST* $k - \omega$ turbulence model

It should be noted that the re-entrant and side-entrant jets are not observed everywhere in the closure region. These phenomena have also been observed in a flow over a Delft Twist foil with a very clear resolution (Foeth, 2004), indicated by red arrows in Figure 7-9.

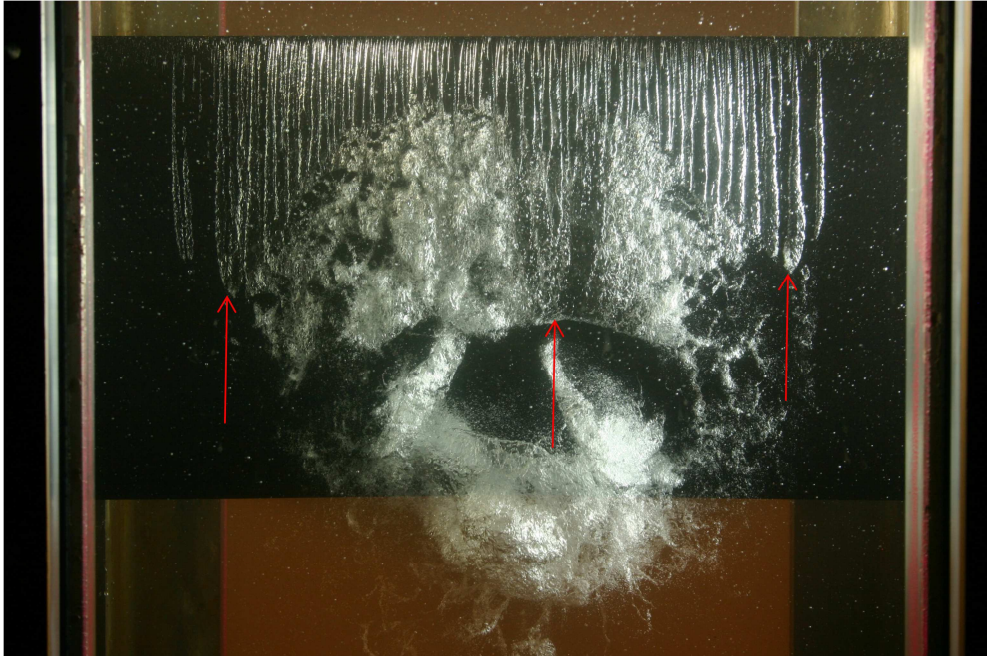


Figure 7-9: Sheet cavity with local re-entrant jets (Flow from top to bottom) (Foeth, 2004)

Horse-Shoe Vortex

A typical horse-shoe vapor structure has been observed during the experiments as well as in the numerical simulations. It is considered to be at least one driving mechanism for cavitation erosion (Kawanami et al., 2002).

Saito et al. (2007) simulated a three-dimensional unsteady cavitating flow around a NACA0015 hydrofoil at 8° angle of attack that was fixed between the sidewalls, and explained that the sidewall effect is an important factor in causing the generation of the horse-shoe shaped cloudy cavity, which is also noticed by Boorsma (2010).

The transformation process to the horse-shoe shaped cloudy cavity has also been presented by Saito et al. (2007) in a schematic diagram as shown in Figure 7-10 and is summarized here as follows:

- The leading edge sheet cavity is formed with bowed surface at the end of the sheet cavity region due to the sidewalls (Figure 7-10-a);

- The re-entrant jet moves towards to the mid-span with a velocity in a direction that is normal to the maximum adverse pressure gradient along the end of the sheet cavity and causes the break-up of the sheet cavity in the mid-span region near the leading edge (Figure 7-10-b);
- The cavity that is shed from the sheet cavity rolls up to form a horse-shoe shaped cloudy cavity (Figure 7-10-c).

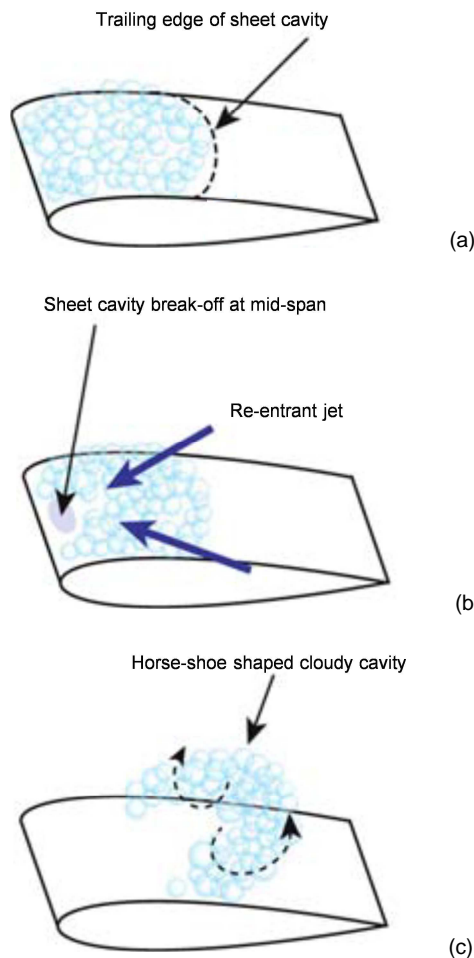


Figure 7-10: Schematic diagram of the transformation process to the horse-shoe cloudy cavity for the cavitating flow over the hydrofoil with sidewalls (Saito et al., 2007): (a) Growth of sheet cavity; (b) Break-off of sheet cavity; and (c) Formation of cloudy cavity

Pereira et al. (1998) reconstruct the horse-shoe vortex by observing the shed cavity structures from different viewing angles, thus allowing for a 3D reconstruction of the vapor

structures, as shown in Figure 7-11.

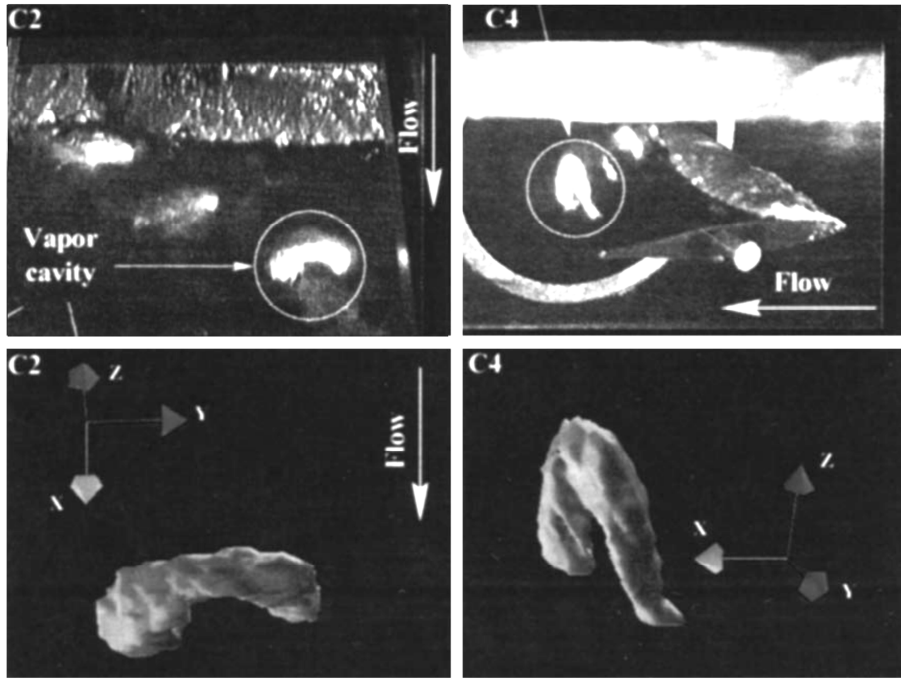
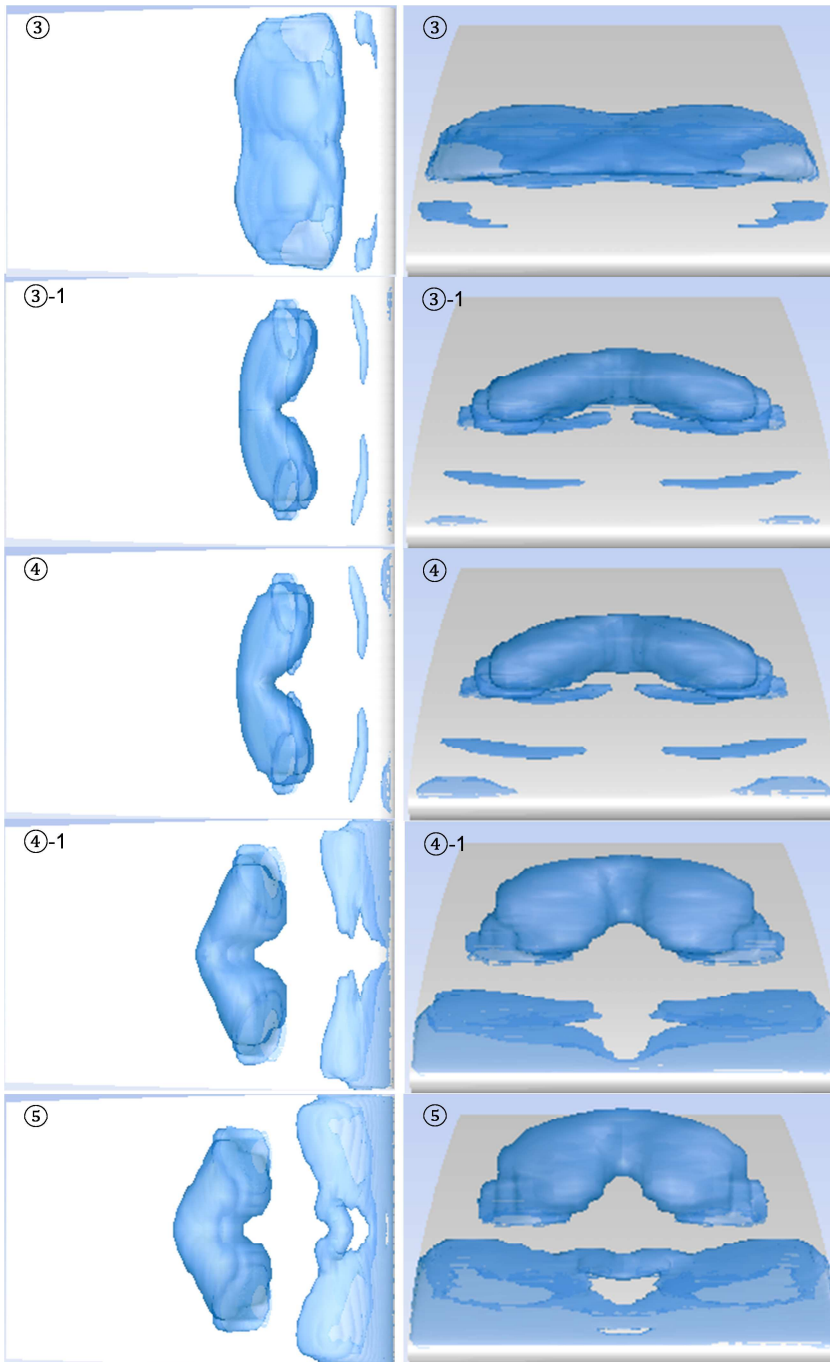


Figure 7-11: Reconstruction of the horse-shoe shaped vortex structure (Pereira et al., 1998)

The generation mechanism of the horse-shoe shaped cloudy cavity is confirmed by the numerical results predicted by the current RANS method. In Figure 7-12, sequences of instantaneous iso-surfaces of the vapor volume fraction of $\alpha=0.1$ between the instant ③ and ⑤ in Figure 7-4 are plotted in both top view and downstream view. The development of the shed cavity from a cylindrical shape into a horse-shoe shape can be clearly observed and described as follows:

- The shed cavity at first rolls up in a cylindrical shape that is thicker in the middle and thinner at the sides (instant ③);
- The center of this cylindrical cloudy cavity is then lifted up, however its sides keep attached to the hydrofoil surface (instant ③-1 & ④);
- The center of the cloudy cavity becomes thicker and thicker, and this “head” of the cloudy cavity will be dragged further downstream than the “legs” that are attached to the surface (instant ④-1);
- The “head” is lifted even higher and dragged even downstream, and the “legs” move towards the mid-span (instant ⑤). The cylindrical cloudy cavity then finally develops into a horse-shoe shape or U-shape structure.



(a) Top view (Flow from right to left)

(b) Downstream view

Figure 7-12: Formation of the horse-shape cloudy cavity on a NACA0015 hydrofoil (3D representation) at 8° angle of attack at $\sigma = 2.01$ with the modified *SST* $k - \omega$ turbulence model: (a) Top view; and (b) Downstream view; of the iso-surface plots of the instantaneous vapor volume fraction of $\alpha = 0.1$

Collapse Process

Kawanami et al. (2002) focused on the inner structure of the horse-shoe shaped cloudy cavity, shed from the sheet cavity which they observed with the aid of a high-speed video camera and still photographs. Three stages of a typical horse-shoe cloudy cavity from break-off to violent collapse are sketched in Figure 7-13, and can be described as follows:

- The horse-shoe cavity consists of one cavitating vortex surrounded by many microbubbles (Figure 7-13-A);
- Furthermore, the bubbles contained in the cavity seem to get attracted toward the foil surface possibly by vortex stretching of the legs in the viscous boundary layer over the foil, and the horse-shoe cavity is thereby split at the head (Figure 7-13-B);
- Then the remaining two legs of the horse-shoe cavity collapse toward the foil surface, potentially causing local cavitation erosion (Figure 7-13-C).

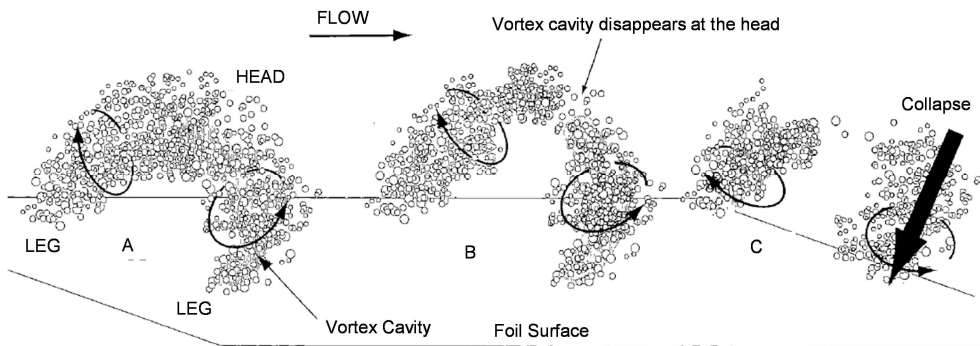
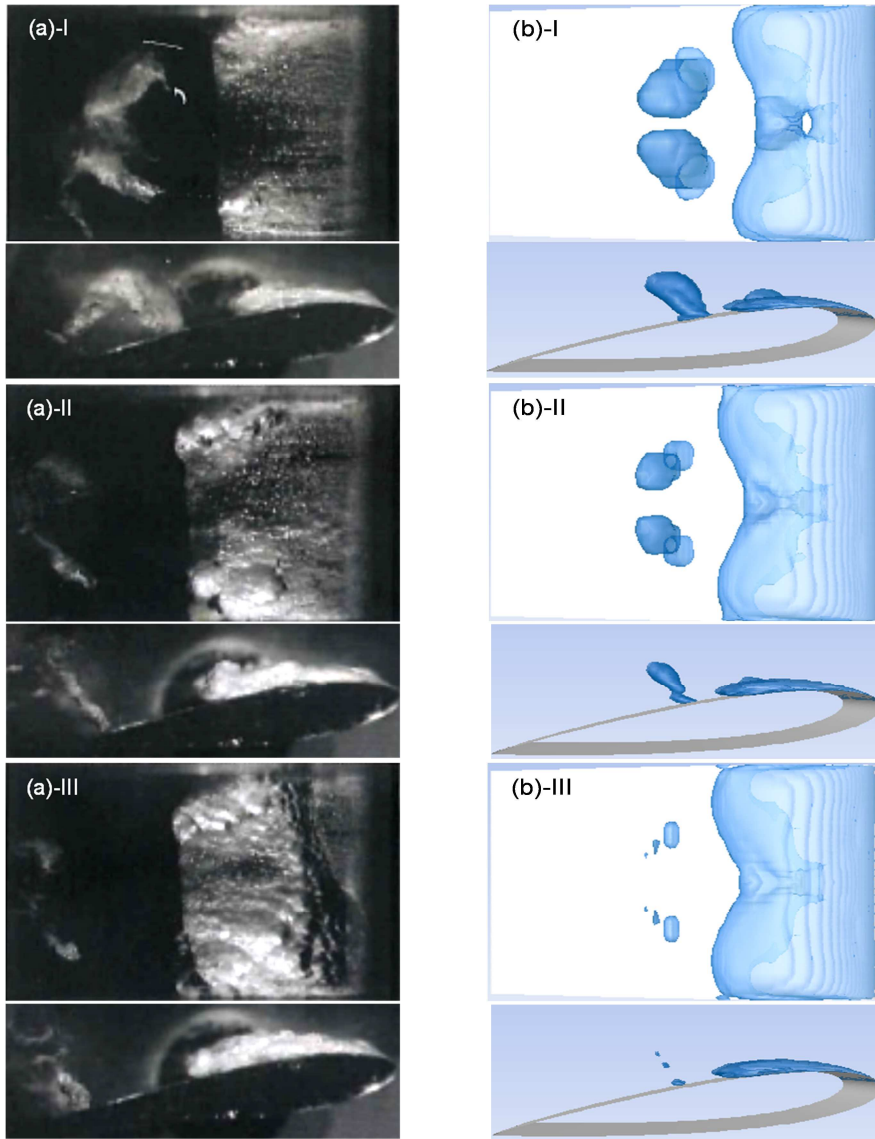


Figure 7-13: Schematic diagram of the transformation process of a horse-shoe cloudy cavity from break-off to violent collapse (Kawanami et al., 2002)

It is also observed by Van Rijsbergen and Boorsma (2011) that the middle part of the cloud implodes and leaves two separate vortices on both sides of the foil. A comparison of the numerical results and the experimental observations by Van Rijsbergen and Boorsma (2011) is shown in Figure 7-14. It can be observed that the basic features of the collapse process have been captured by the current RANS method, such as the collapse of the horse-shoe cloudy cavity into two vortex structures on both sides and the shrinking and collapse of the remaining part toward the foil surface. However, Van Rijsbergen and Boorsma (2011) observed that the downstream attachment of the two legs of the horse-shoe shaped cloudy cavity was located further afterward than in the numerical prediction. Furthermore, the vortices stay most of the time intact rather than that they disappear completely at the end of the collapse, which is the situation simulated by FLUENT.



(a) Experimental Observations

(b) Numerical Simulations

Figure 7-14: Comparison of three typical instants during the collapse of the horse-shoe cloudy cavity between the (a) Experimental observations by Van Rijsbergen and Boorsma (2011); and (b) Numerical results predicted by FLUENT using the current approach (Flow from right to left)

Though there is a discrepancy in the quantity and extent of the vapor structures, the observed collapse behavior qualitatively matches the experimental observations. The large-scale unsteady dynamics are successfully captured, and the sketched collapse process of the horse-shoe cloudy cavity that was observed by Kawanami is reconfirmed

experimentally and numerically. It should be noted here that also some of the small scale structures have been observed to give rise to implosions on the foil surface in the experiments (Van Rijsbergen and Boorsma, 2011). This would challenge the assessment of the risk of cavitation erosion by a RANS method, which is thought to be insufficient to capture small scale structures. The limits of RANS method in this respect will be further investigated in the next chapter.

7.4 3D NACA0018-45 ($AoA = 6.5^\circ$)

7.4.1 Case Description

The second test case is the NACA0018-45 hydrofoil set at 6.5° angle of attack. The computational domain could be halved with respect to the span-wise symmetry. The 2D mesh (see section 5.4.2) is thereby extended by only 20mm (half width of the hydrofoil span) in the span-wise direction to generate a 3D mesh with identical grid topology in chord-wise direction. A close-up of the mesh around the hydrofoil is shown in Figure 7-15.

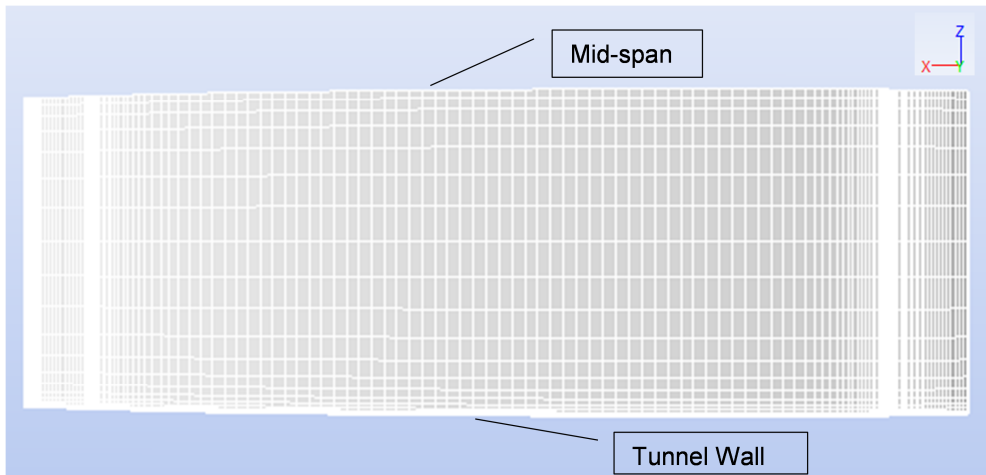


Figure 7-15: Close-up of the mesh for a NACA0018-45 hydrofoil at 6.5° angle of attack (3D representation)

The time step size is selected by using the equation (6-1), giving a value of $1 \times 10^{-5} \text{ s}$. A velocity-inlet condition is applied in the upstream inlet plane with the vapor fraction equaling zero. A pressure-outlet boundary condition is used in the outlet plane. The physical properties of the two phases, liquid and vapor, are taken at a temperature of 23°C . The detailed initial and boundary conditions and the flow properties are listed in Table 7-4.

Table 7-4: Boundary conditions and flow properties for a NACA0018-45 hydrofoil ($AoA=6.5^\circ$)

Boundary Conditions	NACA0018-45 ($AoA=6.5^\circ$)	
Velocity Inlet (m/s)	V=24.2	
Pressure Outlet(kPa)	1000 ($\sigma=3.41$); 213.115 ($\sigma=0.72$)	
Turbulent Intensity (%)	1	
Turbulent Viscosity Ratio	10	
Foil	No-slip Wall	
Mid-span	Symmetry	
Tunnel Walls	No-slip Wall	
Flow Properties ($T=23^\circ\text{C}$)	Vapor	Liquid
Density (kg/m ³)	0.021	997.5
Dynamic Viscosity(kg/ms)	9.81E-06	0.00093
Vapor Pressure (kPa)	2.811	

The simulation is carried out by using a pressure-based transient solver, and a fully coupled solver is selected to solve the pressure and the momentum equations. The pressure is discretized using the PRESTO! scheme, and the convection terms in the momentum equations are discretized by the QUICK scheme which is also used for the terms in turbulence equations and vapor volume fraction equation (ANSYS, 2009). The temporal discretization uses the first-order implicit scheme.

A range of cavitation numbers at a tunnel velocity of approximately 24 m/s over a NACA0018-45 hydrofoil has been performed in the MARIN High Speed Cavitation Tunnel (Van Terwisga, 2009a). The test conditions for the selected case to be compared with the numerical results on the unsteady cavitating flow are listed in Table 7-5.

Table 7-5: Test conditions for the examined experimental data

	003-04
AoA (deg)	6.5
T(°C)	23
V(m/s)	17.71
σ	0.72
Re	150E+06

7.4.2 Wetted Flow Results

The wetted flow is assessed on the NACA0018-45 hydrofoil with a cavitation regime determined by a cavitation number of $\sigma = 3.41$. The boundary conditions at the tunnel walls affect the results on the NACA0018-45 hydrofoil in a similar way as they do for the NACA0015 hydrofoil. The pressure distribution will be different from the wall to the mid-span if the effect of sidewalls is taken into account, as shown in Figure 7-16. The minimum pressure coefficient reaches a value of $C_{p_{\min}} \approx -1.67$ at the mid-span position,

whereas $C_{p_{\min}} \approx -1.18$ at the wall.

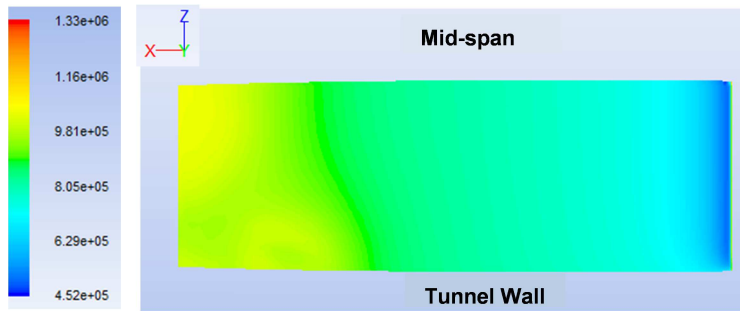


Figure 7-16: The static pressure distribution over a NACA0018-45 hydrofoil at 6.5° angle of attack with no-slip condition at the sidewalls

7.4.3 Results and Discussion on Cavitating Flow

The simulation results to be compared with the experimental observations are obtained with the modified $SST k - \omega$ turbulence model, with Reboud's correction in the region of higher vapor volume fractions. An input bubble number density in the Schnerr-Sauer cavitation model of the default value of $n_b = 1e + 13$ is used.

Total Vapor Volume

The total vapor volume shows a regular harmonic variation at a frequency of $f \approx 59.5\text{Hz}$, which is a bit higher than the 50.5 Hz observed in the 2D computational domain, as shown in Figure 7-17.

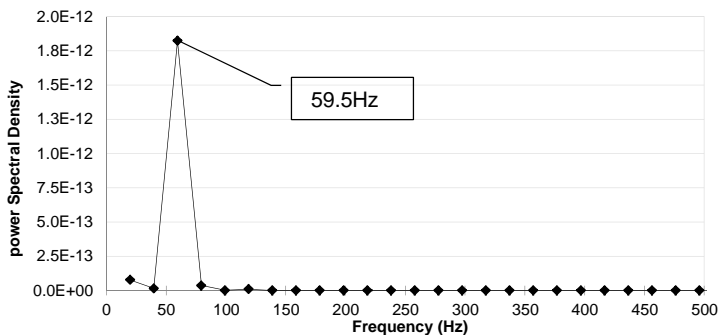


Figure 7-17: The shedding frequency obtained from an FFT analysis of the time history of the total vapor volume predicted by the modified $SST k - \omega$ turbulence model over a NACA0018-45 hydrofoil at 6.5° angle of attack at $\sigma = 0.72$ in a 3D computational domain

Unsteady Dynamics

Compared to the 2D computational domain, much more intensive and complex unsteady dynamics are observed over the NACA0018-45 hydrofoil at 6.5° angle of attack in 3D.

The unsteady dynamics occur on the suction side as well as on the pressure side, similar to what is observed in the 2D computational domain. The collapses mostly occur around the trailing edge or even downstream of the foil, suggesting that high impacts are likely to occur in the trailing edge region.

The basic phenomena during one shedding cycle can be characterized by the following twenty-one instantaneous plots of the iso-surface of $\alpha = 0.1$. Top view pictures are shown in Figure 7-18, and side view pictures corresponding to the twenty-one instants in Figure 7-18 are illustrated in Figure 7-19 in order to get a clearer view of the cavity dynamics on both sides of the hydrofoil. From the top view pictures, the dynamics during a cycle can be described as follows:

- On the suction side, the sheet cavity that develops from the leading edge of the hydrofoil continues to grow and develops a thin hollow space around the mid-span from approximately 40% chord length to 70% chord length; On the pressure side, small vapor structures are formed and move towards the trailing edge (Figure 7-18-①);
- The small vapor structures on the pressure side collapse when they arrive at the trailing edge. The sheet cavity on the suction side continues to grow until it has reached an extent of approximately 90% of the chord length of the hydrofoil; however the upper liquid/vapor interface will keep on growing, forming a triangular shape at the closure of the main sheet cavity (Figure 7-18-②);
- The upper liquid/vapor interface becomes unsteady. Two cloudy vapor structures form in the thin hollow space around the mid-span (indicated by black arrows), traveling further downstream with a growing size (Figure 7-18-③);
- When the cloudy vapor structures travel further downstream, they will be shed from the main sheet cavity and collapse behind the trailing edge. The first collapse can be observed at instant ④, whereas the second collapse at instant ⑥. It is noted that the shedding and collapse of the second cloudy vapor structure that formed from the upper liquid/vapor interface is influenced by the behavior of vapor structures developed at the pressure side;
- Another cloudy vapor structure is shed from the main sheet cavity around the trailing edge due to the interaction between the vapor structures developed from both sides (Figure 7-18-⑦);
- After the collapses of the separated cloudy vapor structures, the main sheet cavity on the suction side will extend beyond the trailing edge of the foil. The upper liquid/vapor interface develops in a very irregular way. Many large scale vapor

structures form and travel downstream along the sheet cavity. These structures tend to roll up and shed from the main sheet cavity (Figure 7-18-(8)(9));

- On the suction side, the sheet cavity sheds a cloudy structure, which will eventually collapse into two vapor structures somewhere behind the trailing edge thereby affected by the shed and collapse occurring on the pressure side near the trailing edge. Several cavities are generated and merged into each other at the mid-span where a hollow space appears without any vapor (Figure 7-18-(10)(11)(12));
- The vapor structures behind the trailing edge collapse completely at a far distance from foil surface, approximately 29% of the chord length downstream of the trailing edge of the foil. On the suction side, a cloudy structure that forms in the region without vapor grows larger and is then connected to the aft part of the sheet cavity by two “legs” (indicated by the black arrows in Figure 7-18-(13)(14)), which will be clearer seen from the side view pictures as shown in Figure 7-19-(13)(14). On the pressure side, two thin vapor structures collapse in the vicinity of the foil surface at the instant (14) shown in Figure 7-18.
- Three main structures are observed on the suction side: the front part is in a type of sheet cavity, which will then be split into two vapor structures with a crescent hollow between them; whereas another cloudy structure shed from the main sheet cavity is observed around the trailing edge. It is observed that the side configurations of the aft cloudy structure cavity will be attached to the foil surface, eventually leading the transformation into a horse-shoe shape (Figure 7-18-(15));
- The leading edge sheet cavity retreats towards the leading edge, and is broken up by the re-entrant and the side-entrant flow. The central vapor structures will be transformed into a crescent shape and grow again. The aft horse-shoe shaped cloudy cavity travels further downstream and lifts up from the suction side, then collapses around the trailing edge (Figure 7-18-(16)(17));
- The remaining vapor structure downstream of the trailing edge shrinks and collapses into two tiny vapor structures. The two tiny vapor structures will rebound and collapse again at a far distance from the foil surface, approximately 23% of the chord length downstream of the trailing edge, seen at the instant (18). The two cloudy cavities generated from the collapse of the center part vapor structures subsequently collapse together with the collapse of cavities at the pressure side at instant (19). A W-shaped cavity is cut off from the front part of sheet cavity and a new sheet cavity is growing from the leading edge (Figure 7-18-(18)(19));
- On the suction side, the W-shape cavity travels further downstream and collapses

at approximately one third of the chord length, causing a sudden drop in lift and drag at instant (20). Some sheddings and collapses occur on the pressure side, causing fluctuations with small magnitude in lift and drag (Figure 7-18-(20));

- The main leading edge sheet cavity is growing with several hollows around the mid-span, and a new cycle starts (Figure 7-18-(21)).

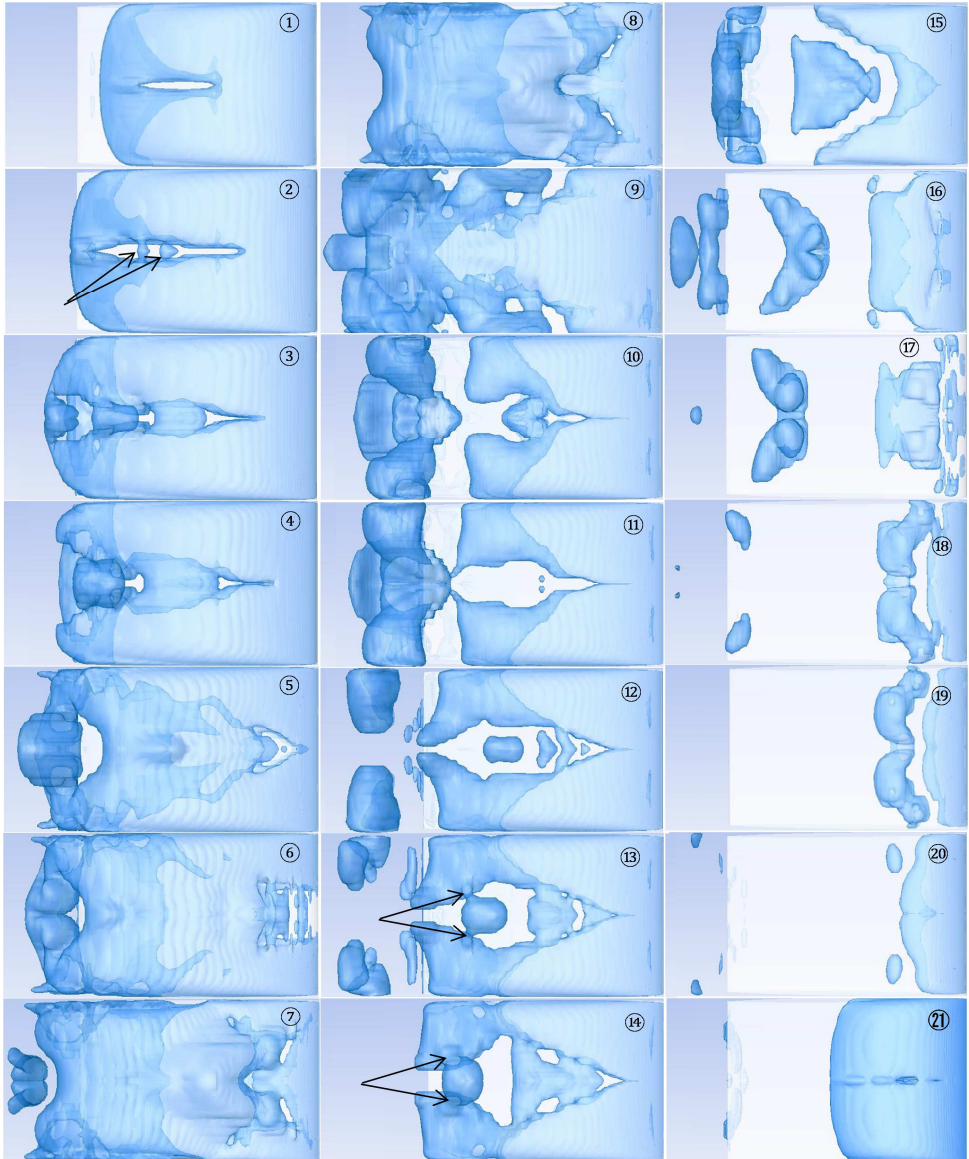


Figure 7-18: Sequences of iso-surface plots of instantaneous vapor volume fraction of $\alpha = 0.1$ during one typical shedding cycle in top view (Flow from right to left) on the NACA0018-45 hydrofoil (3D representation) at 6.5° angle of attack at $\sigma = 2.01$ with the modified *SST* $k - \omega$ turbulence model

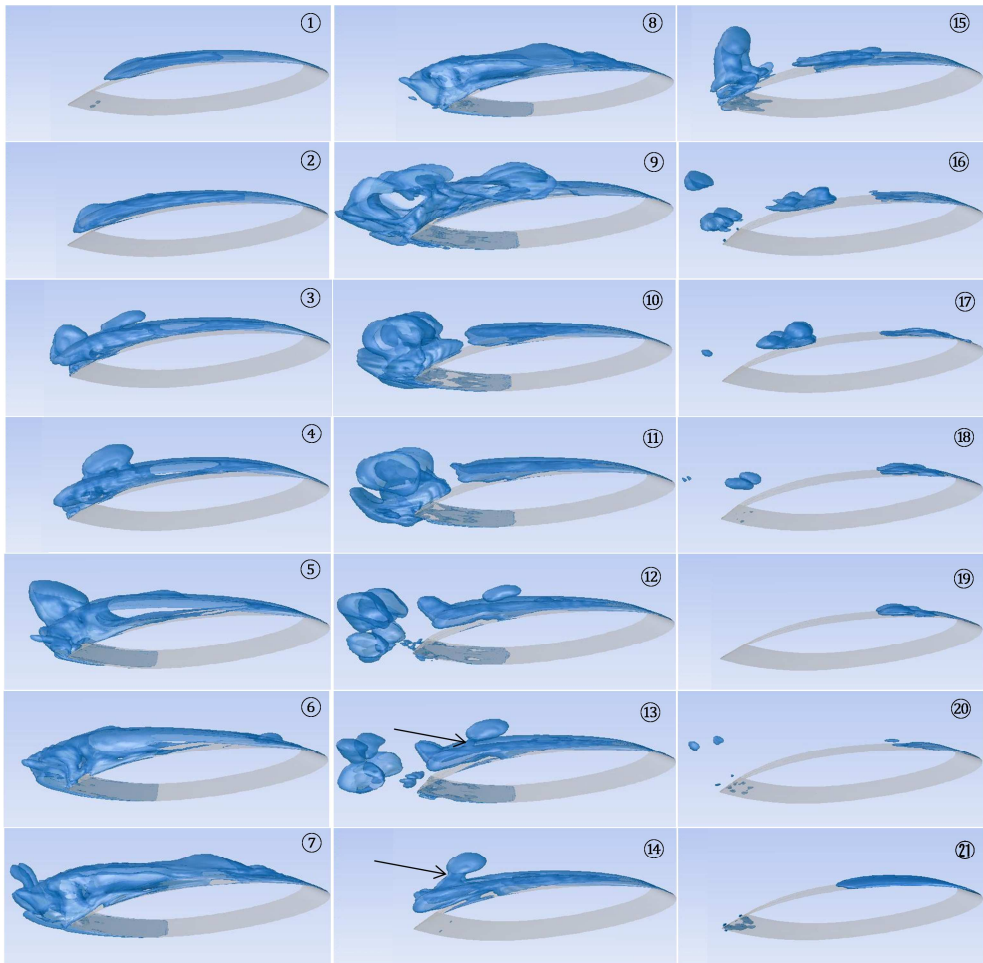


Figure 7-19: Sequences of iso-surface plots of instantaneous vapor volume fraction of $\alpha=0.1$ during one typical shedding cycle in side view (Flow from right to left) on the NACA0018-45 hydrofoil (3D representation) at 6.5° angle of attack at $\sigma=2.01$ with the modified *SST* $k-\omega$ turbulence model

From the side view pictures, it can be observed that the vapor structures that are shed from the pressure side will be merged into the large scale vapor structures that are shed from the suction side (Figure 7-19- ⑨⑩⑪). When the blended cavities travel a bit further away from the trailing edge, new sheddings that developed from the pressure side will move and collapse downstream themselves (Figure 7-19-⑫⑬⑭). Apart from the sheet cavity, individual bubble cavities can also be observed on the pressure side now and then, such as the structures near the trailing edge shown in Figure 7-19-①⑱⑳. Some of them travel with the main flow, and it is supposed that they do not affect the flow domain significantly.

Nevertheless, some of them collapse very close to the lower foil surface, possibly causing a local high impact on the pressure side of the hydrofoil.

Lift and Drag

In Figure 7-20, the time histories of the total vapor volume, and lift and drag coefficients are plotted with twenty-one characteristic points indicated, corresponding to the instants illustrated in Figure 7-18.

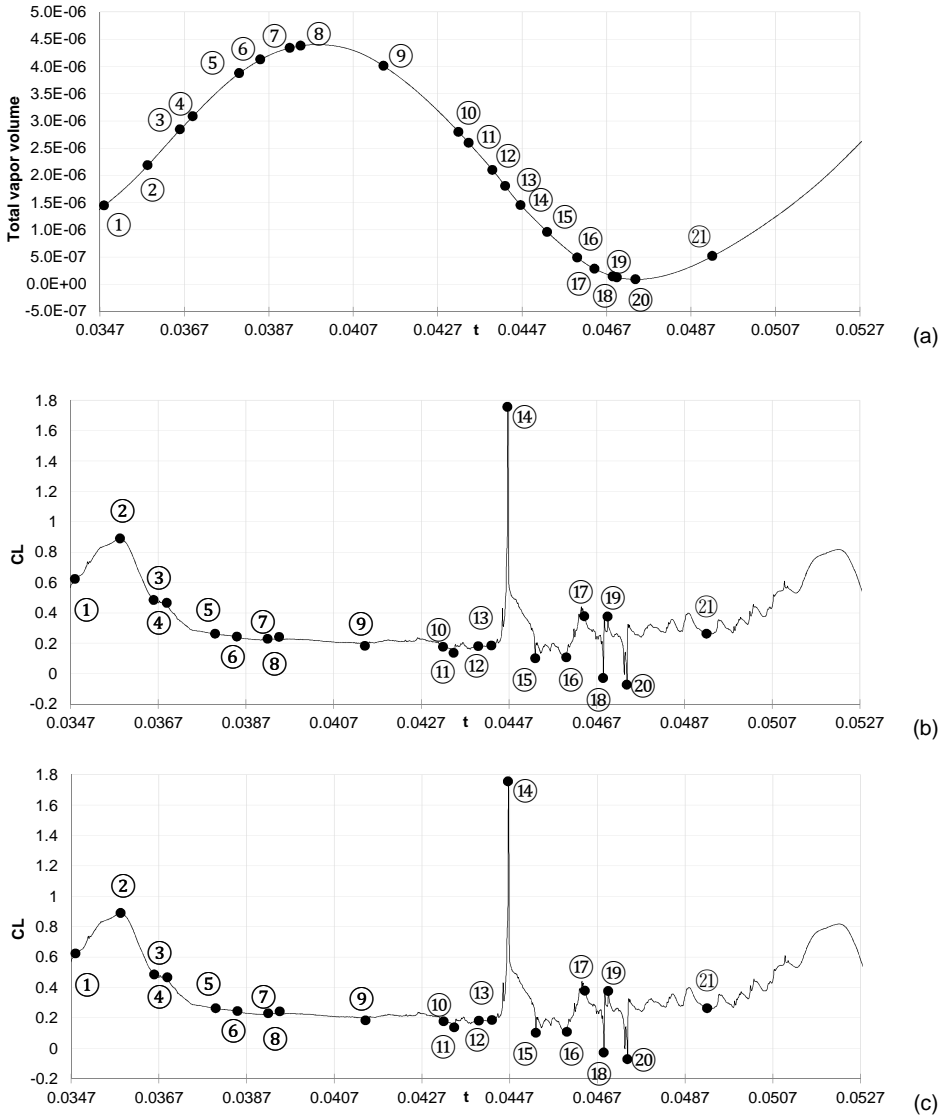
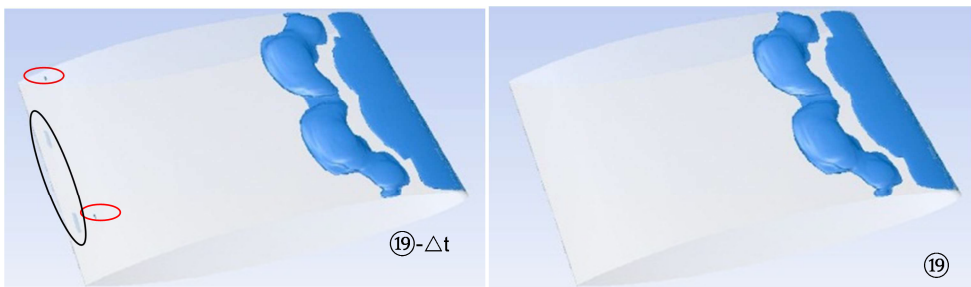


Figure 7-20: Time histories of the (a) total vapor volume; (b) lift; and (c) drag coefficients within a specific shedding cycle in accordance with the instants in Figure 7-18

It can be observed that the highest peak in the lift coefficient occurs at the instant (14), at which the collapse of two small cavities is observed on the pressure side. A very short period before the instant (14), the cloudy cavities behind the trailing edge are observed to collapse completely downstream of the trailing edge. However, it does not trigger a significant peak in lift and drag due to the far distance from the collapse center to the foil surface.

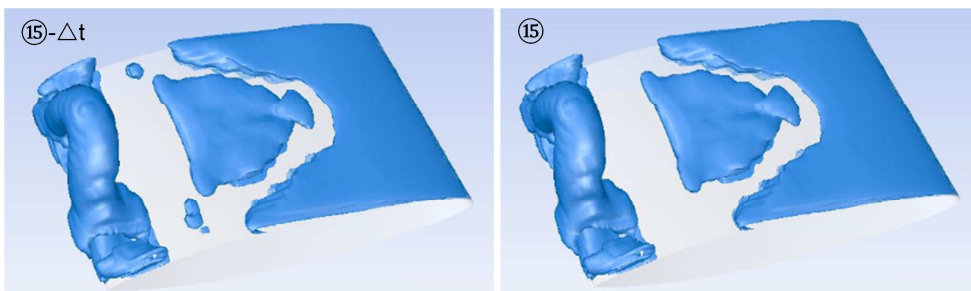
The largest peak in the drag coefficient occurs at the instant (19), at which collapses can be observed both on the suction side (indicated by the red circles) and pressure side (indicated by the black circle), as shown in Figure 7-21. It can be observed that the collapses on both sides are very close to the foil surface. The small peaks in the drag coefficients observed between instant (14) and (19) can also be related to collapse behavior mostly occurring on the suction side, such as the collapse process at the instant (15) shown in Figure 7-22.



(a) The moment before instant (19)

(b) instant (19)

Figure 7-21: Two successive iso-surface plots of instantaneous vapor volume fraction of $\alpha = 0.1$ on the NACA0018-45 hydrofoil (3D representation) at 6.5° angle of attack at $\sigma = 2.01$ with the modified *SST* $k - \omega$ turbulence model



(a) The moment before instant (15)

(b) instant (15)

Figure 7-22: Two successive iso-surface plots of instantaneous vapor volume fraction of $\alpha = 0.1$ on the NACA0018-45 hydrofoil (3D representation) at 6.5° angle of attack at $\sigma = 2.01$ with the modified *SST* $k - \omega$ turbulence model

The interaction between the vapor structures generated from both sides at the trailing edge without collapse dynamics do not trigger any significant peaks in both lift and drag (from instant ⑤ to ⑪). The small fluctuations in the lift and drag after the instant ⑳ seem to be largely caused by the behavior of the bubble cavities on the pressure side.

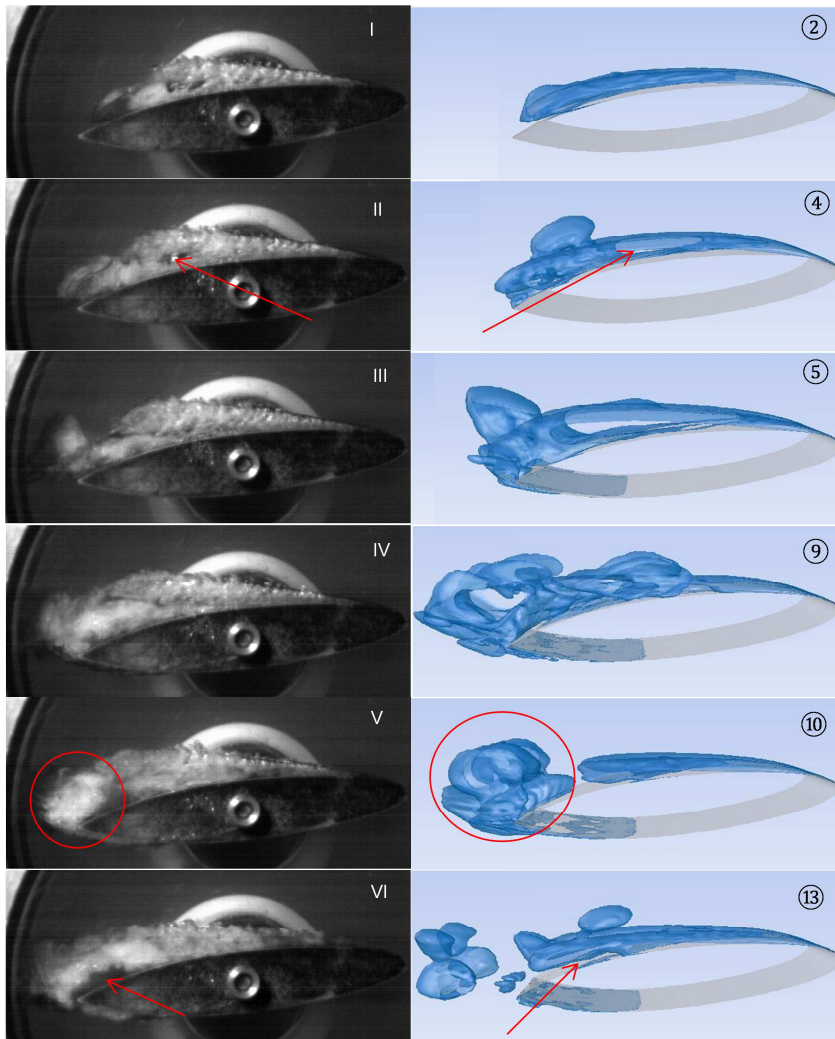
Comparison with Experimental Results

There was only one high-speed camera used to record the dynamics over the hydrofoil, therefore only the side view pictures can be compared. The comparison between the numerical results and experimental observations is categorized into two parts:

- One is the intensive interaction between the vapor structures that are developed on both sides at the trailing edge (Figure 7-23);
- The other is the formation and collapse of the cloudy cavity (Figure 7-24).

From the comparison between the experimental observations and the numerical predictions shown in Figure 7-23, it can be observed that:

- The extent of the experimental and the computed macrostructures at the first three instants are in good agreement.
- The interaction between the vapor structures generated at both sides is very intense for both the experimental observations as well as the numerical results.
- An obvious hollow space is also captured in this experiment, as indicated by the red arrow at instant (a)-II and (b)-④ in Figure 7-23.
- The shape of the closure region of the main sheet cavity is similar in both the experiment and the computation, indicated by the red arrows at the final instant shown in Figure 7-23. However, the RANS method implemented in FLUENT predicts a somewhat longer extension of the vapor structures behind the trailing edge, as shown at instant (a)-IV in Figure 7-23.
- Due to the longer extension, the downstream structures, indicated by the red circle at instant (b)-⑩ in Figure 7-23, tend to be shed further off the trailing edge and collapse further downstream in the numerical results, approximately 29% of the chord length of the hydrofoil. On the contrary, in the experimental observations, the sheddings at the trailing edge region seem to be restrained by the forward part of the main sheet cavity. Thereby no obvious shed and collapse has been recorded behind the trailing edge during the first part of the experimental observations.
- A good resemblance occurs with similar structures, indicated by the red circle at instant (a)-V in Figure 7-23.



(a) Experimental Observations

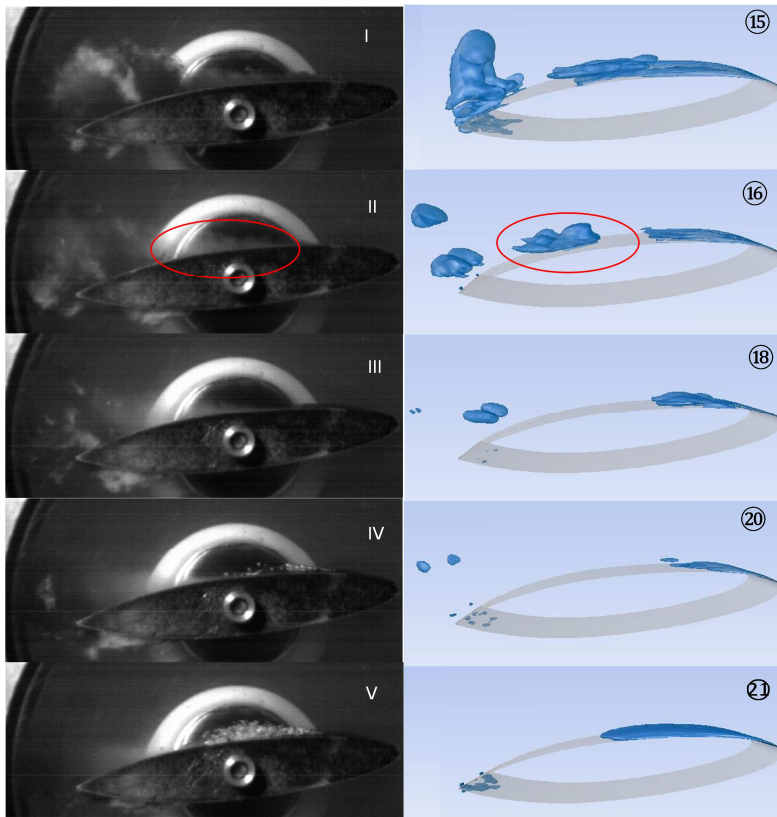
(b) Numerical Simulations

Figure 7-23: Comparison of six typical instants showing the strong interaction at the trailing edge: (a) Experimental observations by Van Terwisga (2009); and (b) Numerical results predicted by RANS method implemented in FLUENT using the current approach (Flow from right to left)

The formation and collapse of the cloudy cavity captured by the high-speed camera and predicted by the RANS method implemented in FLUENT are compared in Figure 7-24. It is hard to judge the shape of the cloudy cavity only from the side views. However, the image (a)-I shows a similar configuration as the image obtained from the simulation of a NACA0015 hydrofoil, which corresponds to a horse-shoe shaped cloudy cavity from the top view images, as shown in Figure 7-14. It is suggested that the cloudy cavity observed in the experiment has a similar shape as a horse-shoe. From the comparison, it can be

observed that:

- The collapse of the horse-shoe shaped cavity is observed to occur at the trailing edge region or even further downstream for the RANS method implemented in FLUENT. However, the collapses are observed to occur at approximately 79% chord length of the foil from the experimental results.
- Some vapor structures are found that are located between the forward part of the sheet cavity and the horse-shoe shaped cloudy cavity, which are also captured by the RANS method implemented in FLUENT. These phenomena are indicated by red circles at instant (a)-II and (b)- 16).
- The overall volume of the cavities observed on the pressure side are predicted a bit smaller than for the experimental observations, while a longer extent of vapor structures is predicted on the suction side.



(a) Experimental Observations

(b) Numerical Simulations

Figure 7-24: Comparison of six typical instants showing the formation and collapse of the cloudy cavity: (a) Experimental observations by Van Terwisga (2009); and (b) Numerical results predicted by RANS method implemented in FLUENT using the current approach (Flow from right to left)

Though only side views are available for the comparison between the numerical results and the experimental observations, it still shows that the large-scale structures and typical unsteady cavitation dynamics from the experiments are in fair agreement with the results from the RANS method implemented in FLUENT using the current approach.

7.5 DISCUSSION OF THE DISCREPANCIES

The locations of the collapses of the large-scale cavity structures predicted by the RANS method implemented in FLUENT are different from what is observed in the experiments, which might well affect the assessment of the risk of cavitation erosion. Possible reasons for these discrepancies will be discussed in this section.

7.5.1 Bubble Number Density

It is hypothesized that the quantitative discrepancies between the numerical results and the experimental observations may result from the bubble number density which is given as input in the Schnerr-Sauer model cavitation model, used in the current approach.

Although the nuclei density spectrum in the test facility used by Boorsma (2010) has not been measured, this spectrum is likely to be different from the default input bubble number density ($n_b = 1e+13$) in FLUENT. A sensitivity study of the bubble number density has been conducted on the NACA0015 hydrofoil at 8° angle of attack. It is observed that a larger bubble number density n_b than the default value did not produce any significant effect on the extent and volume of the vapor structures. However, a smaller bubble number density did indeed predict different extents and volumes of the cavities. It is consequently concluded that a difference between the bubble number density in the cavitation model and the density from the experiments has an influence on the predicted extent and volume of the cavities.

7.5.2 Location of the Reference Pressure

The cavitation number in the numerical simulations is determined with the outlet pressure as the reference pressure. In the experimental measurements, the pressure at an upstream position of the hydrofoil is adopted as the reference pressure to calculate the cavitation number. This difference in the position of the reference pressure results in a discrepancy of the cavitation number between the numerical simulation and the experiment. It is well-known that the general characteristics of the cavitation dynamics are for a large part

determined by cavitation number.

In the experiments for the NACA0015 at 8° angle of attack, the pressure tap was located at the bottom sidewall, and 72mm (1.2 chord length) upstream of the foil rotation center. The pressure used to calculate the cavitation number in the experiments was corrected with 40mm water column to get the pressure at the center of the test facility. In the wetted flow simulations on the same geometry at the same location as in the experiments, a bit higher pressure is observed than the reference pressure at the outlet plane. The non-dimensional value of this difference is around $\Delta\sigma \approx 0.024$. That is to say, the cavitation numbers in the current simulations is somewhat underestimated in the numerical simulations. Therefore, the cavitating phenomena calculated by FLUENT actually correspond to a bit higher cavitation number than what is observed in the experiments, which may result in a shorter cavity length than in the experimental observations. This correlation between the cavitation number and cavity length could be confirmed through the following cavitation regime map for the NACA0015 hydrofoil (Kjeldsen et al., 2000). The current studied cavitation number falls in the region with patch cavitation, and it can be observed that a higher cavitation number would result in a shorter cavity length by extrapolation of the curves.

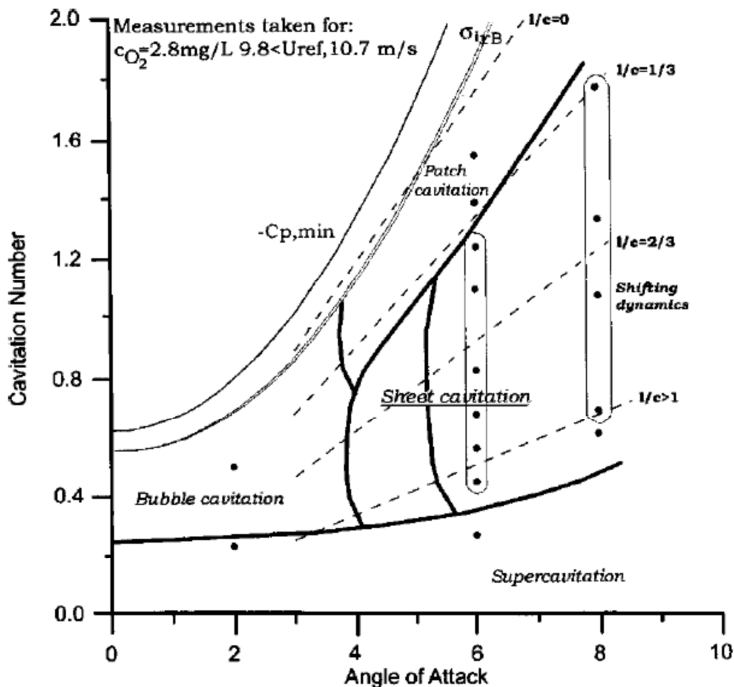


Figure 7-25: Mapping of cavitation regimes for the NACA0015 hydrofoil (Kjeldsen et al., 2000)

It is supposed that the difference of the adopted reference pressure between the numerical simulations and experiments is not so serious so that only some quantitative discrepancies of the extents or volumes of the large-scale structures could be expected without an effect the fundamental characteristics of the unsteady cavitation dynamics.

7.5.3 Wall Boundary Layer

A boundary layer is the flow region adjacent to a solid surface where the viscous effect is dominant. A moving fluid in direct contact with the solid walls is supposed to stick to the surface due to the viscous effect (no-slip boundary condition). However, when it moves away from the solid walls, this zero velocity will not abruptly change to the main flow velocity. It is supposed that the fluid velocity will asymptotically reach the main flow velocity, and the typical laminar boundary layer over a flat plate can be sketched as follows, see Figure 7-26.

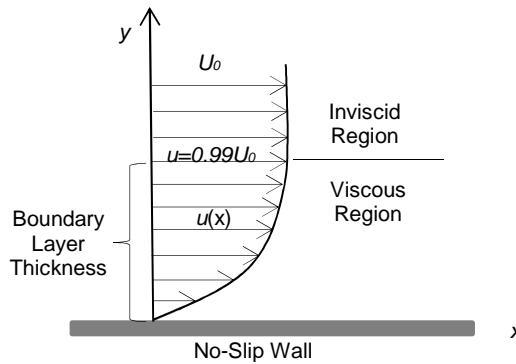


Figure 7-26: Laminar boundary layer velocity profile

The boundary layer thickness can normally be estimated as follows:

$$\delta = \frac{5x}{\sqrt{\text{Re}_x}}; \quad \text{Re}_x = \frac{\rho U_\infty x}{\mu} \quad (7-1)$$

where U_∞ is the main flow velocity, ρ and μ are the liquid density and dynamic viscosity.

In the current study, the velocity at the inlet is assumed to be a constant profile, which is different from the practical condition in the experiments. In addition to the effect of the wall on the mean velocity field, the presence of walls significantly affects the near-wall flow patterns in case of turbulent flows. “The near-wall modeling significantly impacts the fidelity of numerical solutions, inasmuch as walls are the main source of mean vorticity and

turbulence.” Normally, the near-wall region can be divided into three subregions depending on the non-dimensional wall distance y^+ ($y^+ = \rho u_\tau y / \mu$), as shown in Figure 7-27 (referred to Figure 4-2). The near-wall region is handled by the turbulence models in the current study, where the viscous sublayer is resolved.

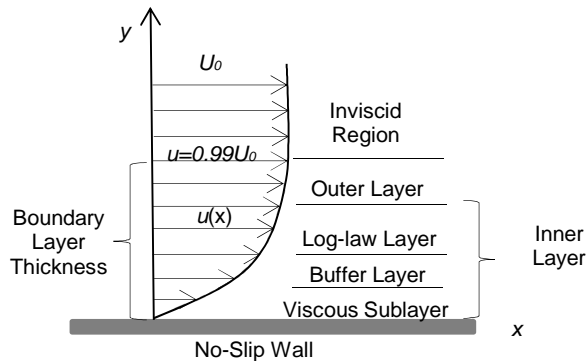


Figure 7-27: Subdivisions of the turbulent boundary layer

From the numerical simulations, the re-entrant jet can be observed not only to move in upstream direction, but also to move towards the mid-span due to the effect of the wall boundary layer. Moreover, the shape of the cloudy cavities shed from the main sheet cavity will develop into different configurations for different boundary conditions for the sidewalls: a horse-shoe shaped cavity with sidewalls (non-slip), whereas a cylindrical cloudy cavity without sidewalls (cyclic) (Saito et al., 2007). Therefore, the different wall boundary layer between the numerical assumptions and the realistic situation in the experiments could well affect the observed cavitation phenomena, possibly resulting in the observed discrepancies in the location of the cavitating structures.

7.5.4 Reliability of Reboud’s Correction

The discrepancies may also be attributed to the application of the Reboud’s correction on the turbulence model. According to the current investigation, the Reboud’s correction is a necessity to obtain unsteady cavitating results from the RANS method implemented in FLUENT, but the reliability of this correction is still an open question.

Bensow (2011) investigated the unsteady cavitation phenomena on a Delft Twist11 foil by DES, LES, and RANS, the latter both with and without Reboud’s correction. The artificial decrease of the turbulent viscosity in the Reboud’s correction has been evaluated by

comparing the effective viscosity μ_{Eff} ($\mu_{Eff} = \mu + \mu_t$, where μ and μ_t are respectively the molecular and turbulent viscosity) on a Delft Twist11 foil, analyzed by DES, and RANS, the latter without and with Reboud's correction (Bensow, 2011). It is surprisingly found that the contours of the effective viscosity μ_{Eff} predicted by a RANS method without correction are quite similar to the results found with DES except for a very high level of μ_{Eff} around the trailing edge of the cavity. However, the RANS method with correction predicted a distribution of the effective viscosity completely different from the results found with DES and RANS without correction, as shown in Figure 7-28.

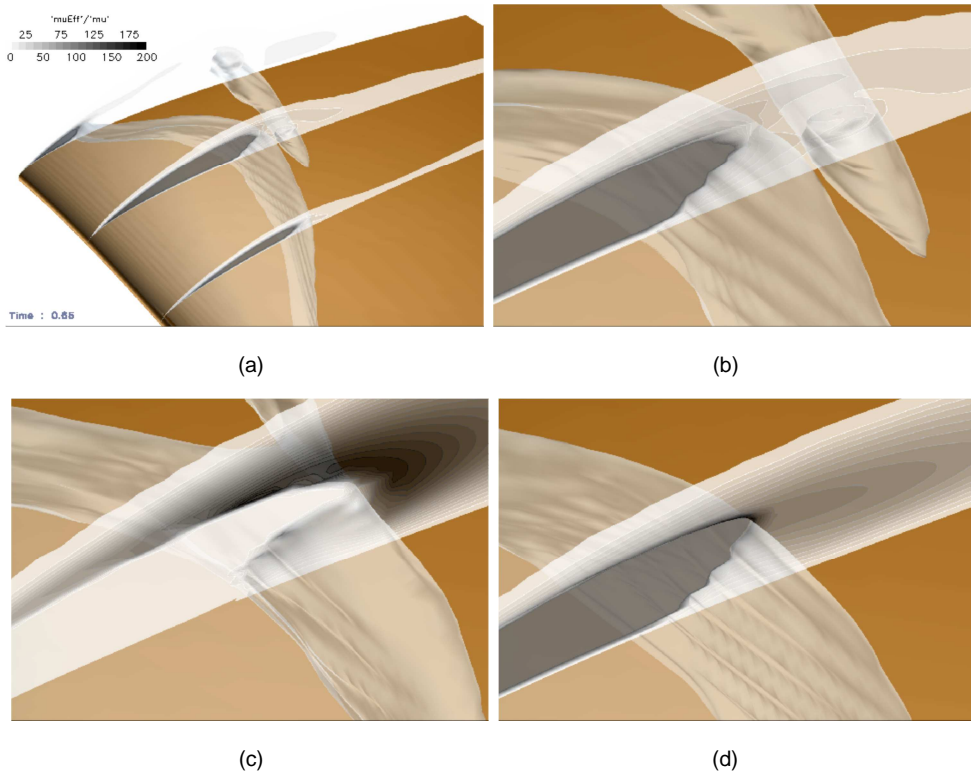


Figure 7-28: Comparison of total viscosity, μ_{Eff} / μ for (a) DES in global view, and (b) DES, (c) RANS with correction, and (d) RANS without correction in a close-up view of the central region of frame (a). (Bensow, 2011)

The RANS method without correction shows a more or less stable behavior of the cavitation. The RANS method with correction gives the expected shedding behavior, however with a distribution of the effective viscosity almost inversely to the one for LES and DES. It is indicated that the inherent mechanisms to generate the unsteady shedding dynamics for the Reboud's correction in RANS method implemented in FLUENT could not be validated from other numerical methodologies, such as LES and DES.

7.5.5 Time Scale

As is generally known, in an unsteady RANS method, part of the turbulent fluctuations are modeled, and part of them are resolved. As stated previously in section 6.2.2, the turbulent fluctuations are composed of a wide range of scales. The condition for an appropriate averaging is that the time scale of the resolved turbulent fluctuations should be much larger than the modeled turbulent ones. The estimate of the time scale for the turbulent eddies is related to scale separation.

It is found that the time step sizes adopted in the current numerical simulations are very close to the estimated Kolmogorov time scale (refer to equation (6-3)), which represents the smallest turbulent time scale. Therefore, it is very likely to cause an unpredictable interference between the resolved turbulent fluctuations and the modeled ones. The possible over-averaging of the turbulent fluctuations may cause an underestimation of the unsteadiness of the cavitating flow, finally resulting in the discrepancies between the numerical results and the experimental observations.

7.6 CONCLUSIONS

The following conclusions can be drawn from the investigations of the three dimensional cavitating flow over a NACA0015 hydrofoil at 8° angle of attack and a NACA0018-45 hydrofoil at 6.5° angle of attack:

- Due to the effect of the vertical side wall boundary layer, the re-entrant jet can be observed not only to move in upstream direction, but also to move towards the mid-span. It is believed that this wall effect is an important reason for the horse-shoe shaped cloudy cavity to develop.
- The re-entrant flow which travels upstream and towards mid-span underneath the leading edge cavity is the main cause of the break-up of the sheet cavity and the detachment of the cloudy cavities. This confirms earlier experimental observations by Foeth (2008) on the cavity over a twisted hydrofoil.
- The large-scale structures and typical unsteady cavity dynamics are qualitatively well captured by the RANS method implemented in FLUENT using the current approach, such as the formation and collapse of the horse-shoe shaped cloudy cavity.
- Possible reasons for the observed discrepancies (particularly in the location of the large-scale cavity structures) could be caused by the following factors: The bubble

number density input in the cavitation model, the differences in the location of the reference pressure in the computations and the experiments, the assumed velocity profile in the wall boundary layer at the inlet of the computational domain, the reliability of Reboud's correction of the turbulence model and the possible interference between the cavity time scale and the turbulent time scale. Of all these factors mentioned, deviations in the tunnel wall boundary layer and Reboud's correction at the liquid/vapor interface are thought to be the more important effects.

Chapter 8: ASSESSMENT OF RISK OF CAVITATION EROSION

8.1 OVERVIEW

This chapter seeks the best possible criteria for an evaluation of the risk of cavitation erosion that is imposed on a NACA0015 hydrofoil and a NACA0018-45 hydrofoil. A review of literature on existing cavitation erosion models has been presented in Chapter 3. It demonstrates that the full and detailed mechanisms producing cavitation erosion are still subject to debate, and the same holds even more for the quantitative assessment of the risk or even the rate of cavitation erosion either experimentally or numerically. Despite the fact that serious attempts to derive criteria for such assessments based on experiments have been derived in a more formal way (Bark et al., 2004), it is still open to subjective judgment whether a certain type of cavitation is erosive or not. Van Rijsbergen and Boorsma (2011) also argue that no specific type of cavitation development could be associated with the highest impacts and the collapse of the shed sheet. They showed that also far smaller structures than the primary cloudy cavity can give rise to high impacts.

With the hypotheses made in Chapter 2, all calculations over the different hydrofoils at different angles of attack are all supposed to focus only on modeling of the large-scale cavity dynamics thereby deliberately ignoring microscale details, such as the inner structures and their interactions during the collapse of the shed cloudy cavity. Though the RANS method is thought to be less reliable for modeling implosions than LES or DES models which can capture small scale structures in space and time, it is still of interest to assess the possibility to use only the large-scale dynamics by a RANS method to make an assessment of the risk of cavitation erosion given the relatively limited computational efforts involved.

In this chapter, the transient impulsive pressure pulses that may be related to the impact loads on the solid surface are examined at first. The high values of the pressure peaks may be an indicator of the aggressiveness of the cavitating flow over the hydrofoils. Then, analyses of the variation in time of the local field over the hydrofoil will be conducted to

find the correlation between the risk of cavitation erosion and local unsteady phenomena. The effectiveness of the formulas predicting instantaneous local cavitation aggressiveness proposed by Nohmi et al. (2008) is subsequently evaluated. The feasibility of a quantitative assessment of the risk of erosion by applying a post-processing model to the RANS results will be addressed subsequently. This model is supposed to look into the microscale details during the collapse, like the bubble cloud collapse model proposed by Wang and Brennen (1999). A new erosion intensity function is finally proposed and is evaluated on both foils.

8.2 EXPERIMENTAL RESULTS

Paint erosion tests have been conducted on the NACA0015 hydrofoil at 8° angle of attack and NACA0018-45 hydrofoil at 6.5° angle of attack, respectively. Paint removal experiments are used to give an estimation of the erosiveness of the cavitating flow.

8.2.1 NACA0015 Hydrofoil (Van Rijsbergen and Boorsma, 2011)

For the NACA0015 hydrofoil (Van Rijsbergen and Boorsma, 2011), the erosion result that is recorded after re-application of the paint and two observation runs (No. 26 and 27) is shown in Figure 8-1.



Figure 8-1: Paint test result after re-application of paint and run No.26 and 27 ($\sigma = 2.01$, $U = 17.3m/s$) on a NACA0015 hydrofoil at 8° angle of attack (30 – 60 minutes)

The test conditions of No.26 and 27 are essentially similar to each other but differ only slightly in Reynolds number, as listed in Table 8-1. The total exposure time of the foil to the aggressive cavitation is not accurately recorded, but it is estimated to be between 30 minutes to 60 minutes.

Table 8-1: Test conditions for Run No.26 and 27

	Run No. 26	Run No. 27	S02M10
AoA (deg)	8	8	8
V(m/s)	17.3	17.3	17.71
σ_v	2.01	2.01	2.2
Re	9.50E+05	9.80E+05	9.70E+05

Boorsma (2010) has, in addition to High Speed Video observations, made an analysis of the acoustic emission data recorded on the NACA0015 hydrofoil at 8° angle of attack but under different test condition “S02M10”, as listed in Table 8-1. According to the measurements for case “S02M10”, the high impacts can be mainly attributed to two types of events: The collapse of the substructures that separated from the main sheet cavity, and the collapse of the primary cloudy cavity directly shed from the main sheet cavity.

The Collapse of the Substructures

Boorsma (2010) observed that large acoustic emission impacts are associated with the collapse of small substructures that were generated by turbulent flow patterns originating from the break-up of the sheet cavitation, instead of the disintegration of the primary structure shed from the sheet cavity (see the structures circled by the red dashed line shown in Figure 8-2).

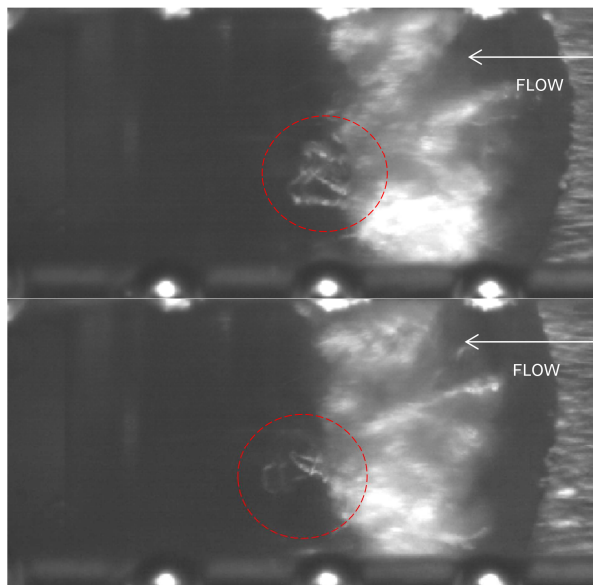


Figure 8-2: Substructures (red circled area) that might cause an erosive impact over a NACA0015 hydrofoil at 8° angle of attack at $\sigma = 2.2$, observed by Boorsma (2010)

Similar structures also have been observed by Van Rijsbergen and Boorsma (2011) under the test condition Run No.26, marked by the red dashed circle in Figure 8-3 and Figure 8-4-(a). It is suggested that the erosion observed around and before the mid-chord is caused by the collapse of these types of substructures of the large shed vortical (cloudy) cavity structure, as shown in Figure 8-4.

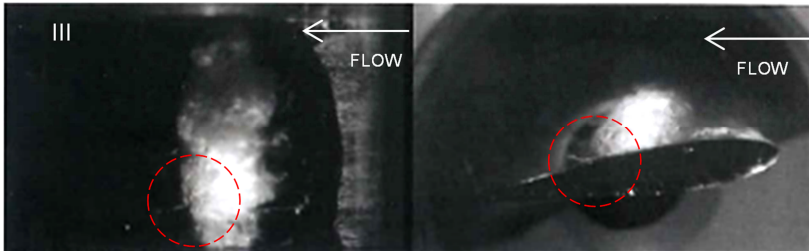


Figure 8-3: Substructures possibly related to high impact on a NACA0015 hydrofoil at 8° angle of attack under $\sigma = 2.01$, observed by Van Rijsbergen and Boorsma (2011)

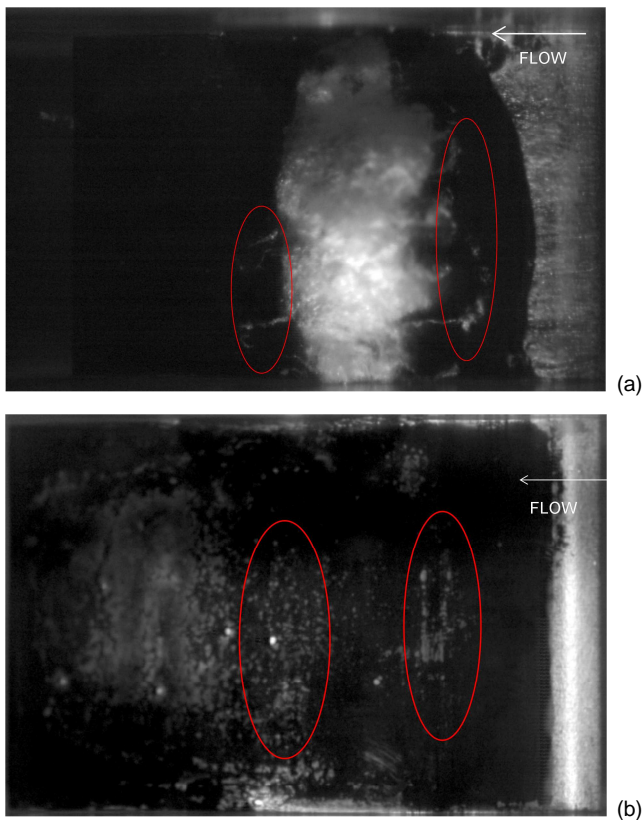


Figure 8-4: Possible relation between (a) the substructures observed by high-speed camera, and (b) damage area observed on a NACA0015 hydrofoil at 8° angle of attack under $\sigma = 2.01$ (Van Rijsbergen and Boorsma, 2011)

It is discussed by Van Rijsbergen and Boorsma (2011) that the measured high impact possibilities are not only attributed to the collapse of specific types of vapor structures, and both the collapse of the shed sheet and the collapse of far smaller structures appear to give rise to high impacts. The strongly turbulent multiphase flow could impose intense pressure changes on the substructures that are generated from the break-up of the cavitation, which in turn might cause aggressive collapse. Because these substructures are very small, they are difficult to discern and evaluate.

The Collapse of the Primary Cloudy Cavity

From the observations by Boorsma (2010), the collapse of the horse-shoe shaped cloudy cavity near the trailing edge was also seen to cause high impact, as shown in Figure 8-5 (Boorsma, 2010).

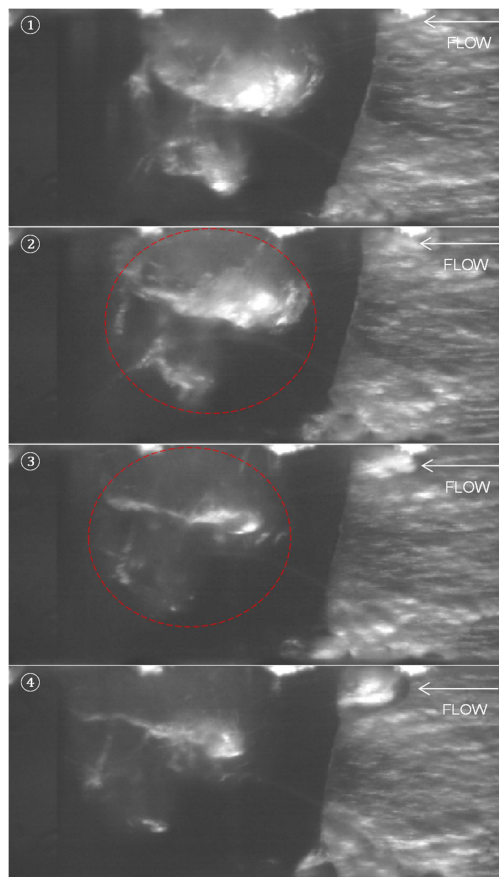


Figure 8-5: High-speed video observations showing the collapse of the horse-shoe shaped cloudy cavity that is associated with high impacts on the NACA0015 hydrofoil at 8° angle of attack at $\sigma = 2.2$ (Boorsma, 2010)

An impulsive impact is measured when a collapse is observed in the red circled area between frame ② and ③. The frequent collapses of similar primary horse-shoe shaped cloudy cavities to even smaller volumes however not automatically led to high impacts on the foil. This is to a large extent attributable to the different collapse rate of the cloudy structures, which is also noted by Van Rijsbergen and Boorsma (2011): “at times cavitation disintegrates and dissolves in the flow slowly without giving rise to impacts on the metal surface. At other times, seemingly similar structures, collapse rapidly causing a high impact load.” So the collapse speed also plays a role in the generation of high impacts. Nevertheless, this collapse behavior gives a clue to explain the larger eroded area on the second half of the foil, which can be attributed to the rapid collapse of the horse-shoe shaped cloudy vortical cavity in the vicinity of the foil surface, as shown in Figure 8-6.

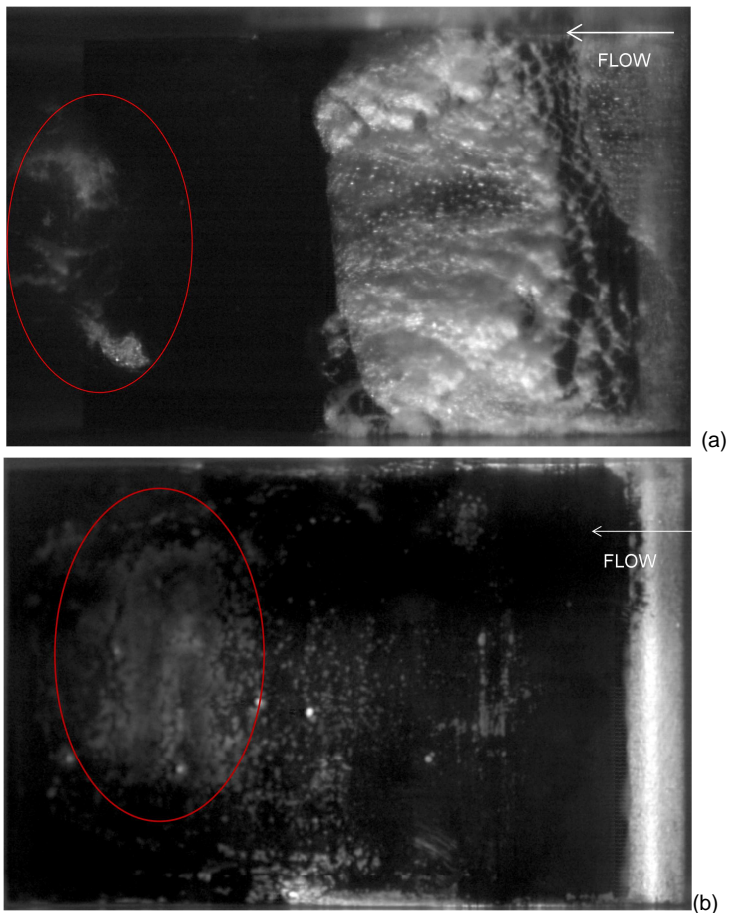


Figure 8-6: Possible relation between (a) the collapse of the horse-shoe shaped cloudy cavity that is observed by high-speed camera, and (b) damage area observed on a NACA0015 hydrofoil at 8° angle of attack under $\sigma = 2.01$ (Van Rijsbergen and Boorsma, 2011)

8.2.2 NACA0018-45 Hydrofoil (Van Terwisga, 2009a)

For the NACA0018-45 hydrofoil (Van Terwisga, 2009a), the eroded area is located on the second half of the foil surface and the trailing edge, as indicated by the red circles in Figure 8-7. Though only side view images from the high-speed camera are available, it can be concluded that the erosion can be attributed to the intense unsteady phenomena, which are mainly associated with the collapse of the horse-shoe shaped cloudy cavity and the collapse of cloudy cavities near the trailing edge.

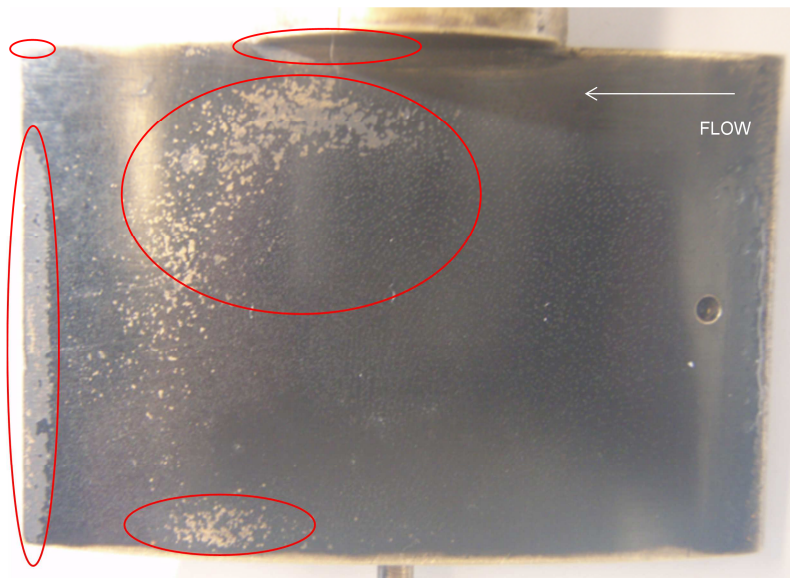


Figure 8-7: Paint test result on a NACA0018-45 hydrofoil at 6.5° angle of attack after 45 minutes ($\sigma = 2.01$, $U = 17.3 \text{ m/s}$)

8.3 RATIONALE BEHIND THE EVALUATIONS

From an energy consideration, it is suggested that the process of focusing of potential energy in a macro cavity may lead to high values of the impact loads, which are supposed to be related to the impulsive pressure pulses produced during the break-up and collapse process.

The potential energy E_{pot} of the macro cavity at the start of the collapse can be written as (see also Bark et al., 2004):

$$E_{pot} = V_v(p - p_v) \quad (8-1)$$

where V_v is the total vapor volume of the macro cavity, and p and p_v are the surrounding pressure and the vapor pressure.

But since it is not the energy that determines the erosion intensity, but rather the energy per unit time that is converted from potential energy into acoustic energy, it is the potential power that forms the basis of cavitation aggressiveness (see Van Terwisga et al., 2009b).

The potential power P_{pot} can then be written as follows:

$$P_{pot} = \frac{\partial E_{pot}}{\partial t} = \frac{\partial V_v}{\partial t} (p - p_v) + V_v \frac{\partial p}{\partial t} \quad (8-2)$$

The above equation (8-2) suggests that the instantaneous pressure p and its time derivative $\partial p / \partial t$, and the total vapor volume V_v and its time derivative $\partial V_v / \partial t$ could determine the erosive risk factors.

However, Boorsma (2010) argued that the volume variation of the shed cavity does not contribute to the flow aggressiveness in the stationary NACA0015 tests, but that instead it is the local pressure field that controls cavitation impact levels.

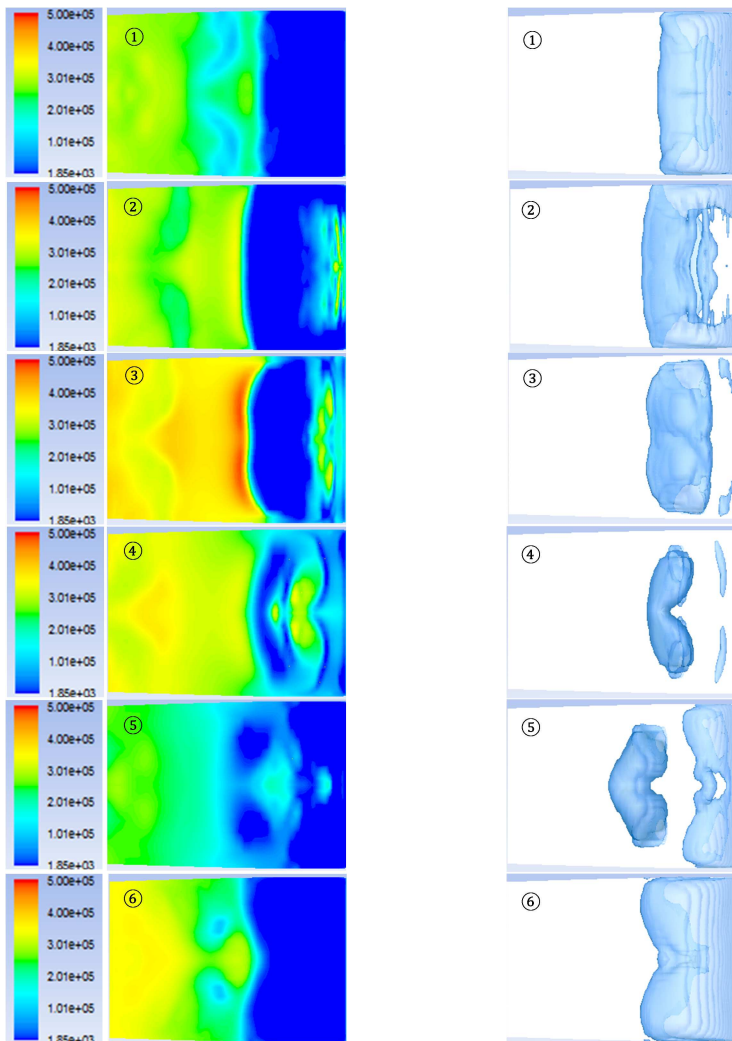
To qualitatively assess the risk of cavitation erosion, the evaluations in this section are mainly focusing on the local field which could be taken as the final consequence of the global unsteady dynamics on the foil surface, such as the local pressure p and its variation in time $\partial p / \partial t$. Since the rate of the vapor generation and destruction can be related to the vapor volume fraction α , the local variation of vapor volume fraction $\partial \alpha / \partial t$ is also evaluated.

8.4 NUMERICAL RESULTS - NACA0015 HYDROFOIL

The analyses will be conducted on the NACA0015 hydrofoil at 8° angle of attack in the first instance. The instantaneous pressure, the variation in time of the local flow field, and several time-averaged aggressiveness indices proposed by Nohmi et al. (2008) will be evaluated one by one.

8.4.1 Instantaneous Pressure

The most direct indicator of the location possibly loaded with high impacts is the place where the maximum instantaneous static pressure could be observed over a period of time. It is often used to show the regions that are most likely to be damaged. In Figure 8-8, the contours of the instantaneous static pressure at the surface of the hydrofoil are displayed together with the instants representing the characteristic dynamics during a shedding cycle, taken from the images shown in Figure 7-4.



(a) Instantaneous static pressure (b) Typical shedding cycle (Figure 7-4)

Figure 8-8: (a) Contours of the instantaneous static pressure (in Pa) distribution on the suction side of a NACA0015 hydrofoil at 8° angle of attack (3D representation) corresponding to (b) the six instants representing a typical shedding cycle shown in Figure 7-4 (Flow from right to left)

A clear correlation is present between the locus of damage on the foil surface (obtained from the paint tests) and the position of the highest instantaneous pressure:

- The high impacts caused by the collapse of the substructures of the shed cavity in the cylindrically shaped cloudy cavity can be observed at the instant (a)-③ in Figure 8-8, where high pressure values are observed at the closure of the shed cylindrically shaped cloudy cavity when it has a minimum total vapor volume.
- The high impacts caused by the collapse of the horse-shoe shaped cloudy cavity can be associated with the instant (a)-⑥ in Figure 8-8, where high pressure values are observed behind the collapse center, viz. the yellow colored area.

It can be observed that the highest instantaneous pressure among the six specific instants in Figure 7-4 is at the closure of the shed cylindrical cavity, and not in the area associated with the collapse of the horse-shoe cloudy cavity. So it seems that the break-up of the sheet cavity could be associated with a higher erosion risk than the collapse of the shed cloudy cavities, based on the analysis of the current numerical results by the RANS method implemented in FLUENT. The collapse of the small vapor structures near the leading edge of the hydrofoil, which is generated from the break-up of the sheet cavity, could also give rise to a high pressure impact near the leading edge (instant ② in Figure 8-8).

Though the capture of the dynamics of small-scale structures is not reliable with a RANS method, the area that is potentially exposed to high impacts produced by both the collapse of the shed horse-shoe cloudy cavity and the far smaller substructures around the cylindrical cavity have been successfully identified through an analysis of the instantaneous pressure predicted by the RANS method implemented in FLUENT. The difference between the localized impacts by the instantaneous pressure and the paint erosion test is mainly ascribed to the difference in the cavity extent as predicted by the RANS method implemented in FLUENT and as observed from experiments. However, the possible high impacts generated near the leading edge of the hydrofoil, see instant ② in Figure 8-8 is still lacking an explanation.

8.4.2 Variation of Local Field

The instantaneous pressure distribution corresponding to the typical instants during a shedding cycle has already been investigated in the previous section. However, the experimental observations indicate that the collapse speed is more important for the erosive potential than the actual size of the cavity (Van Rijsbergen and Boorsma, 2011). If we take the local events on the foil surface as a result of the complex unsteady cavitating dynamics,

the risk of cavitation erosion can be assessed by the analysis of the local pressure field or local vapor production/destruction, as discussed in section 8.3. Therefore, the variation in time of the pressure and the vapor volume fraction on the hydrofoil will be studied in the following. In section 7.3.3, a typical period is selected to show the features of the shedding process, and six instants showing the characteristic unsteady cavitation phenomena are respectively illustrated in a top view and a downstream view in Figure 7-4. In the current section, the rate of pressure rise ($\partial p / \partial t$) and the rate of vapor generation/destruction ($-\partial \alpha / \partial t$) over the hydrofoil at the intervals between the six specific instants will be examined to link the RANS results to the risk of cavitation erosion.

Rate of Pressure Rise

Contours of the time derivative of the instantaneous local pressure ($\partial p / \partial t$) are compared here with the plots of the instantaneous vapor volume fraction of $\alpha = 0.1$ at the relevant time points in the following figures. The red color indicates the highest rate of pressure rise ($\partial p / \partial t$), whereas the blue color indicates a zero value of pressure rise.

It should be noted that the partial differential is estimated by using the first-order backward difference method:

$$\left. \frac{\partial p}{\partial t} \right|_{t+\Delta t} = \frac{p|_{t+\Delta t} - p|_t}{\Delta t} \quad (8-3)$$

Two adjacent instants in time will therefore be involved for each maximum value of $\partial p / \partial t$ and will be analyzed to explore the correlation between the high variation in time of the pressure and the unsteady phenomena.

An evaluation of the five intervals is made as follows:

- Interval between instant ① and ②: The maximum value of $\partial p / \partial t$ is around $1.50e+10$ and occurs when the remaining leading edge sheet cavity begins to collapse and disappears from the leading edge, as shown in Figure 8-9. It is noted that there is no damage observed near the leading edge of the hydrofoil in the paint test, see Figure 8-1.
- Interval between instant ② and ③: The maximum value of $\partial p / \partial t$ is around $1.21e+10$ and occurs in the vicinity of sidewalls where the cavity disappears, as shown in Figure 8-10. High values are also observed surrounding the cylindrical cavity especially in the closure region. This is qualitatively in accordance with the high impacts observed in the paint erosion tests.

- Intervals between instant ③ and ④: The maximum value of $\partial p / \partial t$ is around $7.71e + 09$, which is about an order lower than the highest value of $\partial p / \partial t$ in the previous two intervals. Moreover, no big changes are observed from the plots of the instantaneous vapor volume fraction with iso-value of $\alpha = 0.1$.
- Intervals between instant ④ and ⑤: There is no big difference between the horse-shoe cloudy cavities at the two time points, but a high value of $\partial p / \partial t$ (around $1.80e + 09$) can be observed at the center of the area where the horse-shoe cloudy cavity attaches to the hydrofoil, as shown in Figure 8-12.
- Intervals between instant ⑤ and ⑥: Relatively high values of $\partial p / \partial t$ can be observed at the center where the horse-shoe cloudy cavity eventually collapses. The value of the maximum pressure time derivative is however one order smaller than $\partial p / \partial t$ in the first time interval, causing a broad response downstream of the horse-shoe, qualitatively in accordance with the paint results.

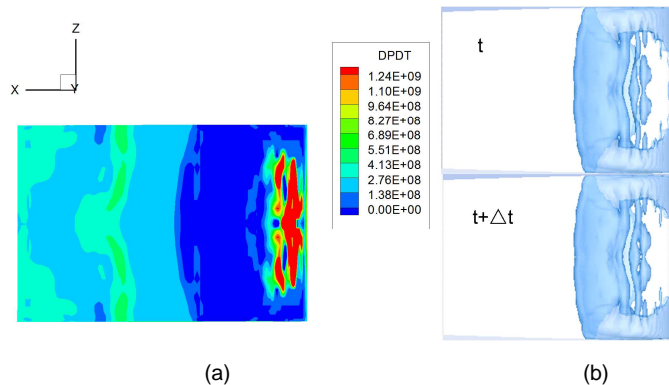


Figure 8-9: (a) Contour of $\partial p / \partial t$ at the moment when its maximum value is observed (between instant ① and ② in Figure 7-4); and (b) plots of the vapor volume fraction with an iso-value of $\alpha = 0.1$ at the relevant time points (Flow from right to left)

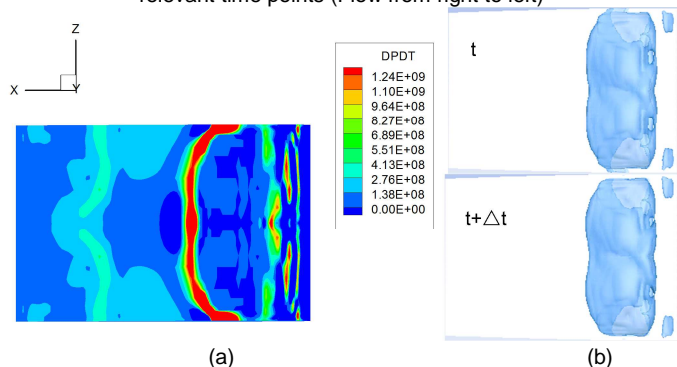


Figure 8-10: (a) Contour of $\partial p / \partial t$ at the moment when its maximum value is observed (between instant ② and ③ in Figure 7-4); and (b) plots of the vapor volume fraction with an iso-value of $\alpha = 0.1$ at the relevant time points (Flow from right to left)

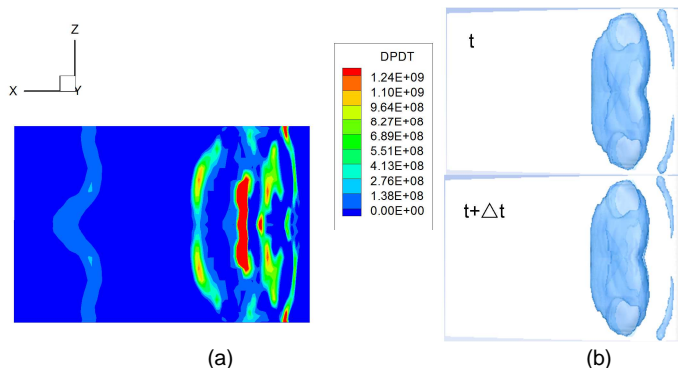


Figure 8-11: (a) Contour of $\partial p / \partial t$ at the moment when its maximum value is observed (between instant ③ and ④ in Figure 7-4); and (b) plots of the vapor volume fraction with an iso-value of $\alpha = 0.1$ at the relevant time points (Flow from right to left)

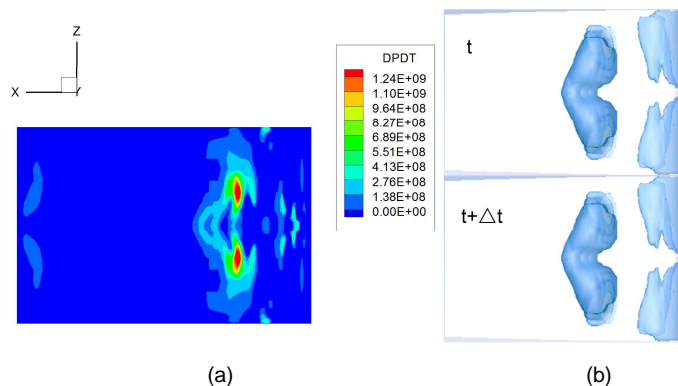


Figure 8-12: (a) Contour of $\partial p / \partial t$ at the moment when its maximum value is observed (between instant ④ and ⑤ in Figure 7-4); and (b) plots of the vapor volume fraction with an iso-value of $\alpha = 0.1$ at the relevant time points (Flow from right to left)

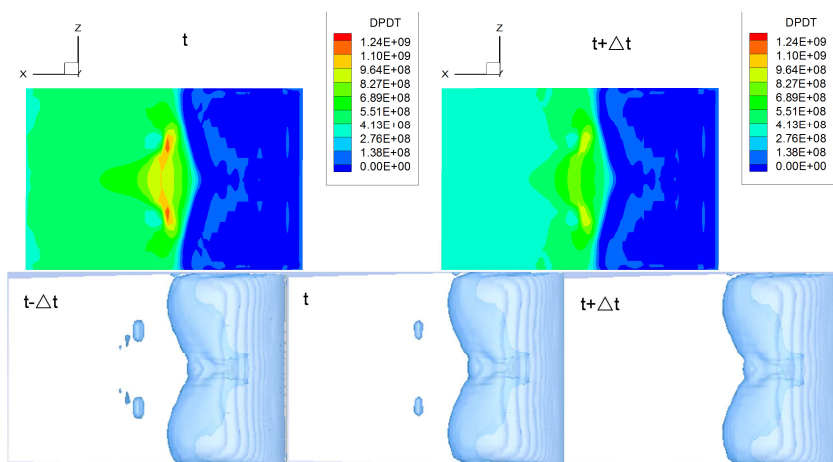


Figure 8-13: Up: Contours of $\partial p / \partial t$ at the moment when collapse occurs (between instant ⑤ and ⑥ in Figure 7-4); Low: Plots of the vapor volume fraction with an iso-value of $\alpha = 0.1$ at the relevant time points (Flow from right to left)

The damaged region that is associated with high impacts that can be related to the collapse of the substructures of the sheet cavity and the horse-shoe shaped cloudy cavity has been successfully indicated by large values of the time derivative of pressure. The location of high impacts that are related to the collapse of the substructures around the large-scale sheet cavity predicted by $\partial p / \partial t$ is similar to what is observed for the instantaneous pressure p .

However, the $\partial p / \partial t$ criterion indicates a more specific region than the instantaneous pressure p when it comes to the collapse of the horse-shoe shaped cloudy cavity. It is also noted that the highest value of $\partial p / \partial t$ during the collapse of the horse-shoe cavity is observed one time step before the final collapse. Moreover, the erosion at the location close to the sidewalls (recorded by the paint tests) that was not predicted by the instantaneous pressure is successfully captured from an analysis of $\partial p / \partial t$. The time derivative of pressure ($\partial p / \partial t$) seems to give a better correlation with the damaged regions than the instantaneous pressure p .

Rate of Vapor Production/Destruction

The variation of the local vapor volume fraction α on the hydrofoil is analyzed in this section. It is the vapor destruction that is related to the erosive cavitation phenomena rather than the vapor production, therefore the examined criterion is $-\partial \alpha / \partial t$. A positive value of $-\partial \alpha / \partial t$ thus represents vapor destruction, whereas a negative value represents vapor production.

An evaluation of the five intervals is made as follows:

- Interval between instant ① and ②: The maximum value of $-\partial \alpha / \partial t$ is around $4.42e+04$ and occurs at the leading edge of the hydrofoil where the remaining sheet cavity disappears, as shown in Figure 8-14.
- Interval between instant ② and ③: The maximum value of $-\partial \alpha / \partial t$ is around $3.40e+04$ and is observed at the same location loading as the maximum $\partial p / \partial t$, as shown in Figure 8-15.
- Intervals between instant ③ and ④: The maximum value of $-\partial \alpha / \partial t$ is around $2.22e+04$, and the maximum $\partial p / \partial t$ is also observed at the same time. It is suggested that the lift of the large-scale vapor structure from the hydrofoil surface results a high rate of vapor destruction $-\partial \alpha / \partial t$. However, these details cannot be clearly observed from the top view of the iso-plots of volume fraction, as shown in Figure 8-16.
- Intervals between instant ④ and ⑤: The maximum value of $-\partial \alpha / \partial t$ is also

observed at the area where the horse-shoe cloudy cavity is attached to the hydrofoil. In addition, a high rate of vapor production is observed near the leading edge and the sidewalls at the first quarter of chord length, as shown in Figure 8-17.

- Intervals between instant ⑤ and ⑥: The vapor production at the front half of the chord length is dominant during this period, and the highest $-\partial\alpha/\partial t$ is observed at the sidewalls in a very tiny area, indicated by the red circle in Figure 8-18. Vapor destruction can be observed in the area where the horse-shoe cloudy cavity is attached to the foil surface, but with a smaller value. It is also found that the rate of local vapor destruction when the final collapse occurs is one order smaller than the vapor destruction rate in the first time interval.

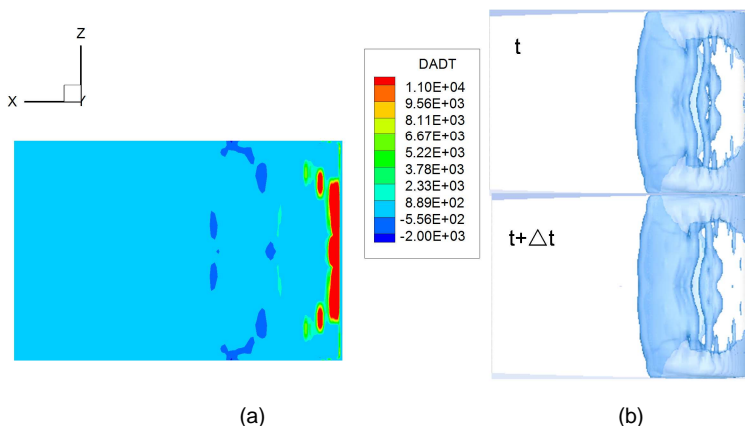


Figure 8-14: (a) Contour of $-\partial\alpha/\partial t$ at the moment when its maximum value is observed (between instant ① and ② in Figure 7-4); and (b) plots of the vapor volume fraction with an iso-value of $\alpha = 0.1$ at the relevant time points (Flow from right to left)

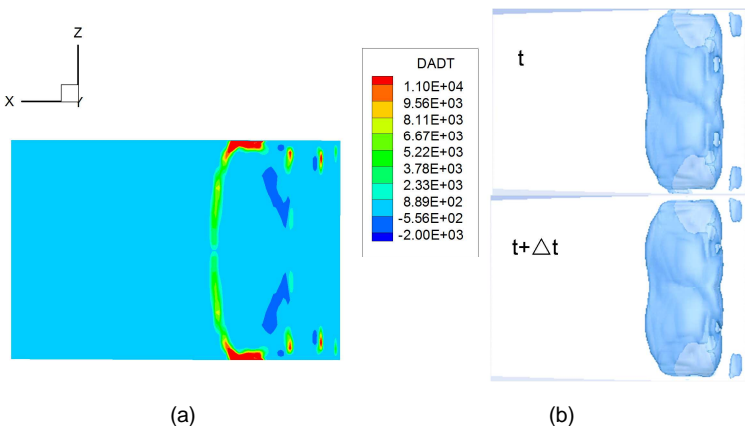


Figure 8-15: (a) Contour of $-\partial\alpha/\partial t$ at the moment when its maximum value is observed (between instant ② and ③ in Figure 7-4); and (b) plots of the vapor volume fraction with an iso-value of $\alpha = 0.1$ at the relevant time points (Flow from right to left)

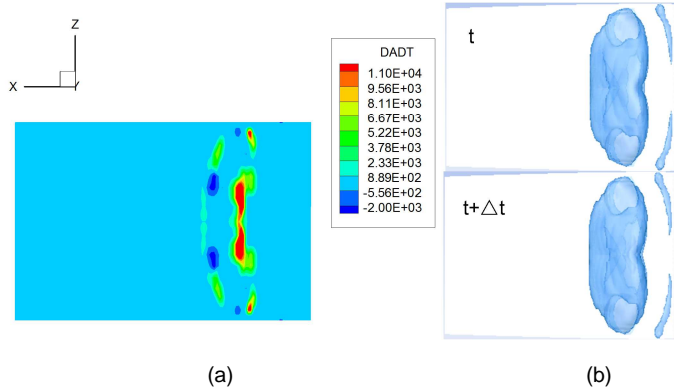


Figure 8-16: (a) Contour of $-\partial\alpha/\partial t$ at the moment when its maximum value is observed (between instant ③ and ④ in Figure 7-4); and (b) Plots of the vapor volume fraction with an iso-value of $\alpha = 0.1$ at the relevant time points (Flow from right to left)

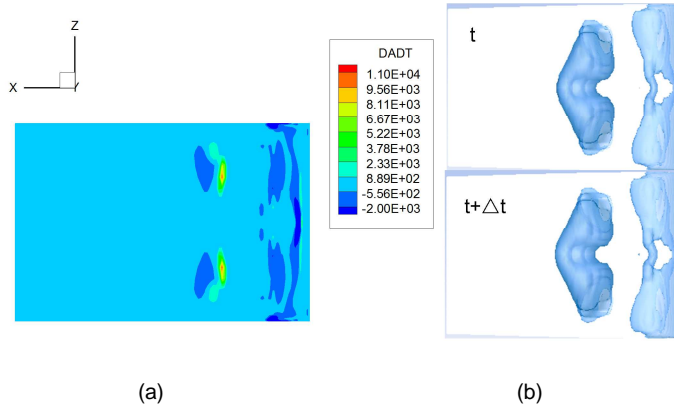


Figure 8-17: (a) Contour of $-\partial\alpha/\partial t$ at the moment when its maximum value is observed (between instant ④ and ⑤ in Figure 7-4); and (b) plots of the vapor volume fraction with an iso-value of $\alpha = 0.1$ at the relevant time points (Flow from right to left)

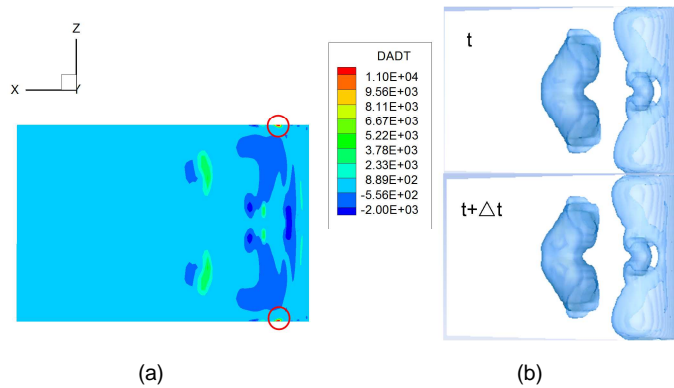


Figure 8-18: (a) Contour of $-\partial\alpha/\partial t$ at the moment when its maximum value is observed (between instant ⑤ and ⑥ in Figure 7-4); and (b) plots of the vapor volume fraction with an iso-value of $\alpha = 0.1$ at the relevant time points (Flow from right to left)

Though the contours of $-\partial\alpha/\partial t$ clearly show the location with higher rate of vapor production/destruction, it appears a less reliable indicator of the regions with erosion damage from the experiments. This worse correlation may be caused because it is the collapse of vapor structures in the vicinity of the foil giving rise to high impacts, rather than the local vapor destruction on the foil surface.

Conclusions

The possible damaged region that is associated with the collapse of the horse-shoe shaped cloudy cavity, which is indicated by $\partial p/\partial t$, has not been observed by the evaluation of $-\partial\alpha/\partial t$. The rate of pressure rise ($\partial p/\partial t$) seems a better criterion than the rate of vapor destruction ($-\partial\alpha/\partial t$) for the assessment of the locations that are potentially exposed to a high erosion risk.

The rate of local pressure rise ($\partial p/\partial t$) and the rate of vapor destruction ($-\partial\alpha/\partial t$) appear qualitatively correlated. Similarly as for the pressure derivative criterion, the rationale for the vapor destruction criterion can be derived from the relation for potential power (equation (8-2)). However, sometimes high impacts can be triggered by the collapses occurring adjacent to the surface but without any significant change of the local vapor volume fraction at the surface. This can explain that a low $-\partial\alpha/\partial t$ but high $\partial p/\partial t$ are obtained around the collapse center of the horse-shoe shaped cloudy cavity, as shown in Figure 8-19.

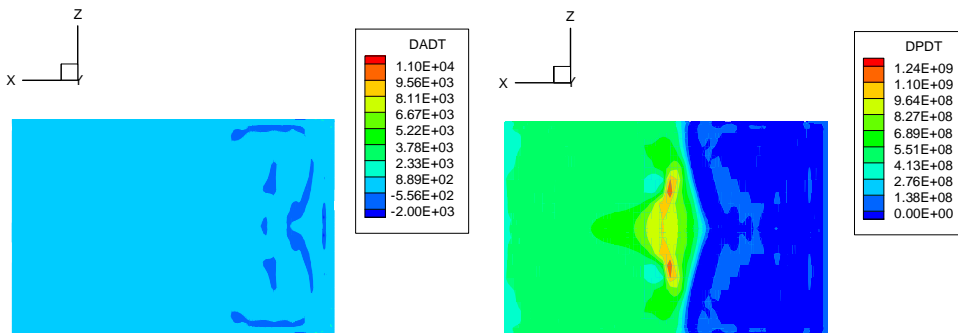


Figure 8-19: Contours of (a) $-\partial\alpha/\partial t$; and (b) $\partial p/\partial t$; at the same instant when maximum $\partial p/\partial t$ is observed during the collapse of the horse-shoe shape cloudy cavity (Flow from right to left)

8.4.3 Time-Averaged Aggressiveness Indices (Nohmi et al., 2008)

In section 3.7, four formulas of the time-averaged aggressiveness indices that possibly indicate the local cavitation erosion rate have been already introduced in the following form (Nohmi et al., 2008):

$$\begin{aligned}
 Index_1 &= \frac{1}{T_c} \int_0^{T_c} \alpha \max\left[\frac{\partial p}{\partial t}, 0\right] dt \\
 Index_2 &= \frac{1}{T_c} \int_0^{T_c} \alpha \max[(p - p_v), 0] dt \\
 Index_3 &= \frac{1}{T_c} \int_0^{T_c} \max\left[-\frac{\partial \alpha}{\partial t}, 0\right] \max[(p - p_v), 0] dt \\
 Index_4 &= \frac{1}{T_c} \int_0^{T_c} \max\left[-\frac{\partial \alpha}{\partial t}, 0\right] dt
 \end{aligned} \tag{8-4}$$

where:

- α is the instantaneous local vapor volume fraction
- p is the instantaneous local pressure
- p_v is the vapor pressure
- T_c is the period of the examined time cycle of the unsteady dynamic shedding

Based on the hypotheses made by Nohmi et al. (2008), the necessary conditions that possibly contribute to the risk of cavitation erosion can be summarized as:

$$\alpha > 0; \frac{\partial p}{\partial t} > 0; p > p_v; \frac{\partial \alpha}{\partial t} < 0 \tag{8-5}$$

The above conditions would assure that only the events potentially generating impacts on the foil surface will be accumulated during the shedding period. These indices are thought to be related to the intensity of the cavitation erosion and are based on an analysis of the global flow phenomena.

Nohmi et al. (2008) estimated the four indices on a 2D hydrofoil. It is reported that all indices showed a broad peak all over the averaged sheet cavity region, and the peak at the fore part was higher than at the aft part. Particular, the $Index_1$ and $Index_3$ showed the highest peak at the leading edge of the sheet cavity, which is supposed to be attributable to the steep pressure change in time.

The temporal partial derivative is estimated by using a first-order backward difference method and the integral in time is estimated by using the rectangle rule. Taking the instantaneous pressure as an example, its first-order temporal partial derivative at instant $t + \Delta t$ can be calculated by the relationship:

$$\left. \frac{\partial p}{\partial t} \right|_{t+\Delta t} = \frac{p|_{t+\Delta t} - p|_t}{\Delta t} \tag{8-6}$$

and its integral during the time interval $[0, T_c]$ can be written as:

$$\int_0^{T_c} p dt = \sum_0^{T_c} (p_{t+\Delta t} \Delta t) \tag{8-7}$$

where Δt is the time step size.

The components in the integrands of the four formulas are calculated during a typical shedding cycle, corresponding to the selected cycle in section 7.3.3 (see Figure 7-4). The contours of the four aggressiveness indices are plotted in Figure 8-20, and the red color indicates high impact load whereas the blue color stands for the low impact load.

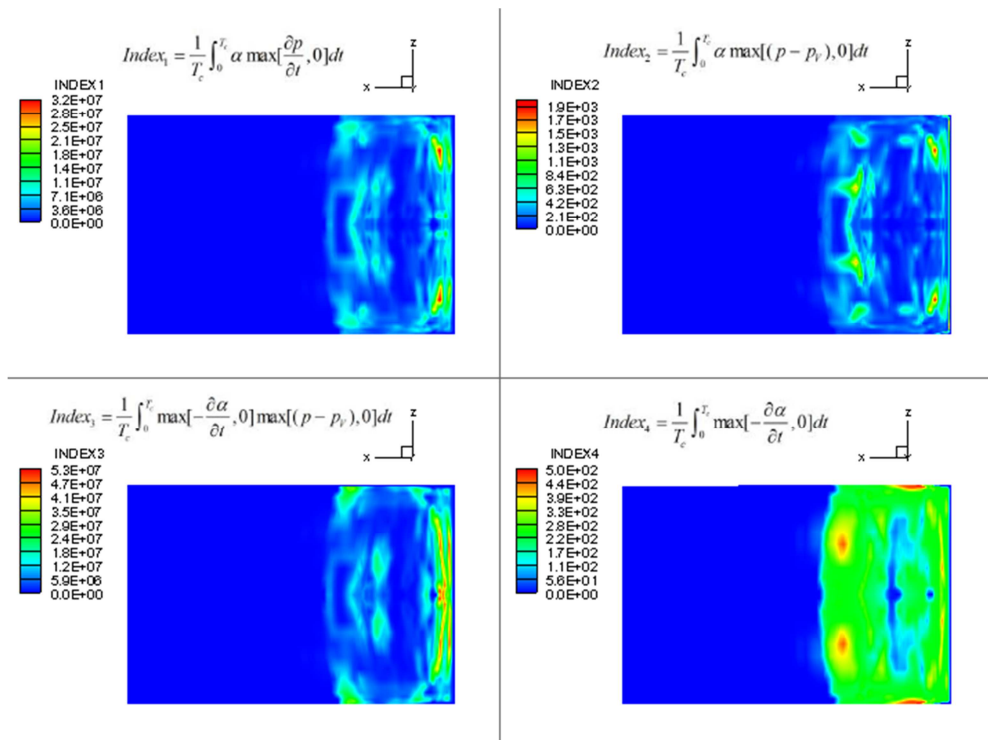


Figure 8-20: Contours of the four aggressiveness indices in equation (8-4) during a typical shedding cycle referred to the cyclic images shown in Figure 7-4 (Flow from right to left)

It can be observed that the aggressiveness indices $Index_1$, $Index_2$ and $Index_3$ show some resemblances in the predicted regions with high erosion risk. All of them are found in the region surrounding the cloudy cavity that sheds from the sheet cavity before it develops into the horse-shoe shape, and also around the leading edge. However, $Index_4$ predicts an unrealistically large region with high aggressiveness possibilities occupying the fore part of the foil. The comparison between the aggressiveness indices ($Index_2$ and $Index_3$) and the

iso-plot of the vapor volume fraction with a value of $\alpha = 0.1$ at the instant ④ (see Figure 7-4) is shown in Figure 8-21.

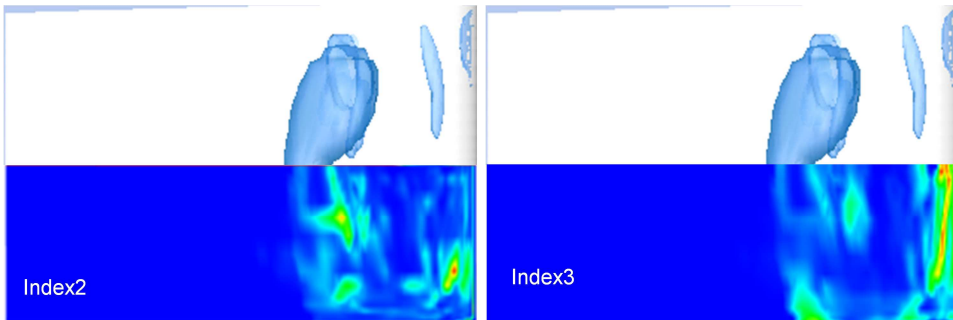


Figure 8-21: Comparison between the aggressiveness indices ($Index_2$ and $Index_3$) and the iso-plot of the vapor volume fraction with a value of $\alpha = 0.1$ at the instant ④ (See Figure 7-4, flow from right to left)

It is also observed that all of the four indices are not capable of predicting the high impacts residence at the location where the horse-shoe shaped cloudy cavity collapse. According to the numerical results predicted by the RANS method implemented in FLUENT, the collapse of the horse-shoe shaped cloudy cavity occurs around the mid-span at approximately 50% chord length. This is validated by the evaluations on the variation of local pressure ($\partial p / \partial t$), as shown in Figure 8-13. However, the regions with high erosion risk shown by the analyses of the four indices are mainly distributed over the front 39% chord length. This discrepancy can be seen in Figure 8-22, showing the comparison between the aggressiveness indices ($Index_2$ and $Index_3$) and the rate of pressure rise ($\partial p / \partial t$) at the end of the collapse of the horse-shoe shaped cloudy cavity.

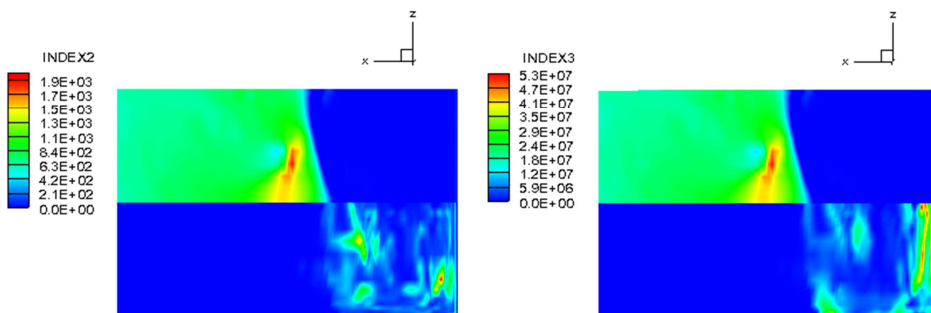


Figure 8-22: The comparison between the aggressiveness indices ($Index_2$ and $Index_3$) and the rate of pressure rise ($\partial p / \partial t$) at the end of the collapse of the horse-shoe shaped cloudy cavity (Flow from right to left)

A possible reason for this incapability is that the high rate of pressure rise ($\partial p / \partial t$) due to the collapse of the horse-shoe shaped cloudy cavity has been compensated by the small or even zero value of the local vapor volume fraction α or the change of vapor volume fraction ($-\partial\alpha / \partial t$), as shown in Figure 8-19.

High values of $Index_1$ and $Index_3$ are observed in the vicinity of the tunnel sidewalls (span-wise direction), which is qualitatively in accordance with the evaluations of $\partial p / \partial t$ and $-\partial\alpha / \partial t$, as well as the measurements with paint tests. However, obvious high impacts are found near the leading edge where sheet cavitation disappears, see instant ② and ③ in Figure 8-8.

Though some of the possible locations where cavitation erosion is likely to occur can be predicted by the four indices in equation (8-4), it lacks the support of a physical background and cannot be correlated with the experimental measurements under the current approach. For these reasons, these time-averaged formulas that are composed of vapor volume fraction, pressure and their temporal differential values seem somewhat unreliable to make an assessment of the risk of cavitation erosion.

8.4.4 Discussion and Conclusions

Schmidt et al. (2007) studied the maximum instantaneous static pressure with high resolution (time-steps in the order of 10^{-8} to 10^{-7} seconds) to get a better understanding of cavitation erosion. Their results are obtained with a compressible Riemann Solver, solving compressible Euler equations.

Two kinds of collapse were found to correspond to the high static pressure found during the shedding cycle: A “crescent-shaped” vapor cloud leading to peak pressure in Point B, and “leading-edge” structures leading to a high pressure region near Point A, as shown in Figure 2-11.

The unsteady behavior that may be related to these two points can be characterized as follows:

- Point A: This location is supposed to be related to the collapse of the leading-edge structures. An identical location is found in our results between the disappearing leading edge cavity and the shed primary cloudy cavity, as shown in Figure 8-23-(b).
- Point B: This location is supposed to be related to the collapse of the horse-shoe

shaped cloudy cavity, as shown in Figure 8-23-(a).

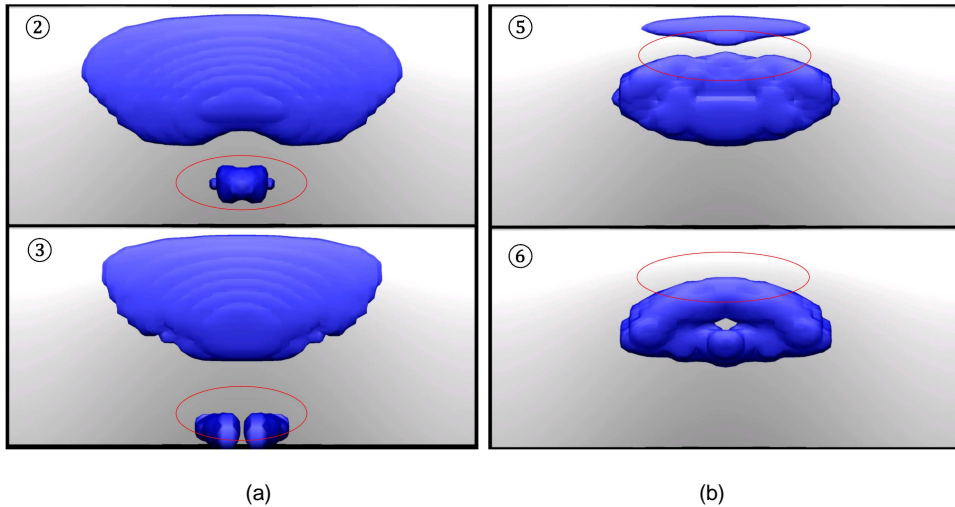


Figure 8-23: Iso-plots of a vapor volume fraction with value of $\alpha=0.1$ during a shedding cycle (Schmidt et al., 2007) (Flow from top to bottom)

Though the results are obtained from an analysis of the cavitating flow over a 3D twisted hydrofoil, which is built based on a NACA0015 profile with a varying angle of attack in the span-wise direction, the correlation between the regions exposed to the highest impacts and the collapse behaviors are qualitatively matching with what is observed in the results from the RANS method implemented in FLUENT. The results from this latter code are with a lower resolution in time ($\Delta t = 2e - 05s$) and do not include compressibility effects.

The fourth index in equation (8-4) proposed by Nohmi et al. (2008) cannot be correlated with the damaged areas from the experimental observations. The other three indices are capable of capturing the potentially high impacts generated by the shed cylinder shaped cavity, but miss the important information that could be related to the collapse of the horse-shoe shaped cloudy cavity. However, the regions with an increased erosion risk that were predicted from the rate of the pressure rise $\partial p / \partial t$ correlate well with the damage resulting from the paint experiments. It seems that the maximum $\partial p / \partial t$ is the best choice, among all examined evaluation methods in this section, to make an assessment of the regions that are likely exposed to highly erosive impacts according to the current research on the NACA0015 hydrofoil at 8° angle of attack. This will be further evaluated on another foil in the next section: a NACA018-45 hydrofoil at 6.5° angle of attack.

8.5 NUMERICAL RESULTS - NACA0018-45 HYDROFOIL

This section presents the cavitation erosion analysis of the numerical results on the NACA0018-45 hydrofoil at 6.5° angle of attack. The evaluation is based on instantaneous pressure, variation in time of the local flow field, and the four time-averaged aggressiveness indices proposed by Nohmi et al. (2008).

8.5.1 Instantaneous Pressure

Figure 8-24 shows the contours of the instantaneous static pressure over the hydrofoil to investigate whether there is a correlation between high impacts and instants in time representing the corresponding dynamics during a shedding cycle. These dynamics have been discussed through the images shown in Figure 7-19. It should be noted that the high impacts are not only observed on the suction side but also on the pressure side. Although the paint tests are only conducted on the suction side, the intense dynamics around the trailing edge of the hydrofoil are likely to also cause damage at the pressure side near the trailing edge of the hydrofoil in a similar way as to what is observed at the suction side.

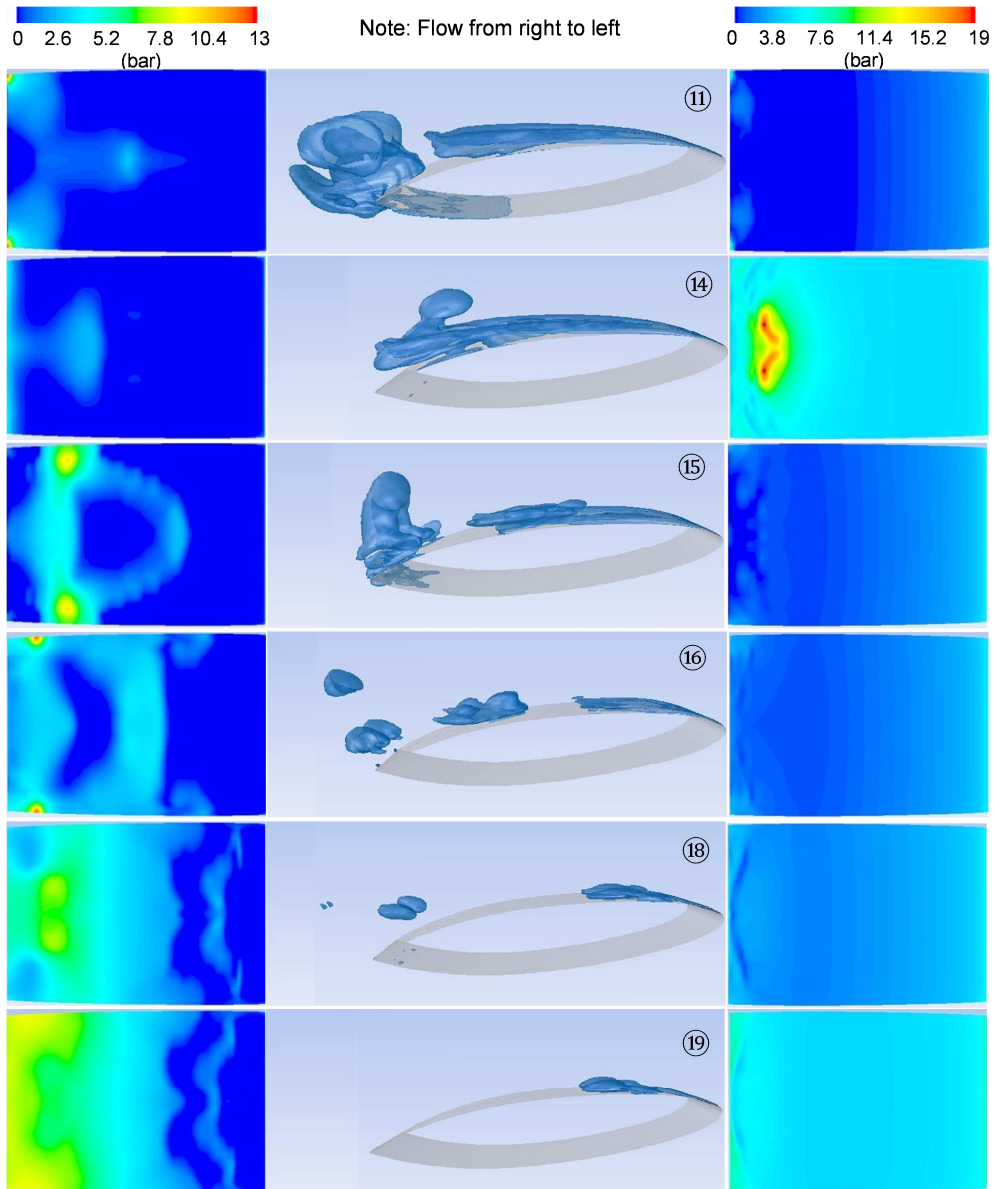
Suction Side

The damage located around the trailing edge of the hydrofoil (observed from the paint tests) is believed to be caused by the intense interaction between the vapor structures generated from both sides of the foil. The comparable high static pressure that could be related to the intensive interaction is observed at the corners of the foil trailing edge with a value of 13 bars, as shown in Figure 8-24-(a)-(11).

The trailing edge damage may also be caused by the further downstream collapse of the small vapor structures, caused by the disintegration of the cavities generated during the collapse of the horse-shoe shaped cloudy cavity. These remaining structures collapse in the vicinity of the trailing edge, resulting in maximum instantaneous pressure values of 8 bars and 9 bars respectively, as shown in Figure 8-24-(a)-(18)&(19).

A crescent-shaped damage area is found from the paint tests, located slightly upstream from the trailing edge of the hydrofoil, which is ascribed to the collapse of the horse-shoe shaped cloudy vapor structure shed from the main sheet cavity. Corresponding high instantaneous pressures are observed in Figure 8-24-(a)-(15)(16)&(18), which could be related to the development and collapse of the primary horse-shoe shaped cloudy cavity ((a)-(15), with a

peak value of 9 bars), or the collapses of the vapor structures separated from the primary cloudy cavity ((a)-⑮, with a value of 12 bars; and (a)-⑰, with a peak value of 9 bars).



(a) Suction side (b) Side view (instants shown in Figure 7-19) (c) Pressure side
 Figure 8-24: Contours of instantaneous pressure (in bar) distribution on (a) suction side and (c) pressure side; and (b) the corresponding side view images showing the characteristic dynamics at the same instant for the flow over a NACA0018-45 hydrofoil at 6.5° angle of attack (3D representation)

From the numerical results, high impacts are also observed in the forward half part of the foil on the suction side, which is not observed in the paint tests. These high impacts are associated with the collapses of two vapor structures in the vicinity of the foil surface at time instant ⑳ (see to images in Figure 7-18 & 7-19), as shown in Figure 8-25. However, the collapses observed at the instant ⑳ are not as repeatable as the intense trailing edge interaction between the vapor structures generated from both sides and the collapses of the horse-shoe shaped cloudy cavity. This phenomenon cannot be always captured by the RANS method implemented in FLUENT during different shedding cycles. Thus the erosion risk may not be always high because the high impacts at this location are occasional.

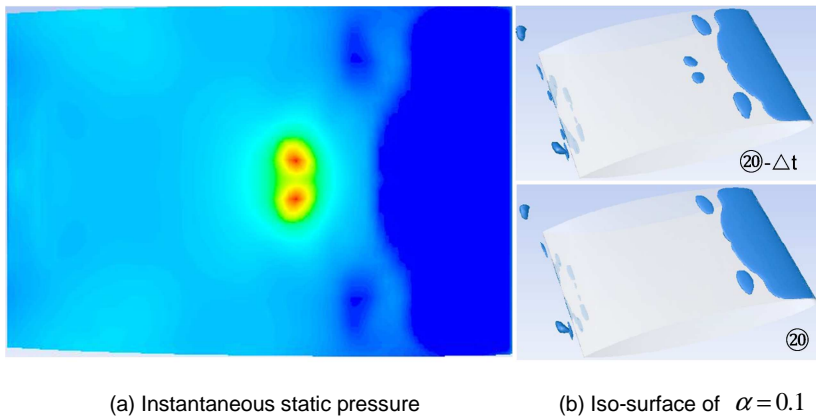


Figure 8-25: High impacts observed at the instant ⑳ (referred to images in Figure 7-18 & 7-19): (a) the contours of the instantaneous static pressure at instant (flow from right to left); (b) iso-surface plots of vapor volume fraction of $\alpha = 0.1$ during one typical shedding cycle

Pressure Side

On the pressure side, the highest instantaneous static pressure is observed when the vapor structures at the pressure side collapse into a very tiny volume, with a peak value of around 19 bars, as shown in Figure 8-24-(b)-⑭.

In Figure 8-24-(b)-⑪, a high static pressure in the order of 10 bars can also be observed at similar locations as what is observed on the suction side (around the corners of the trailing edge), which is supposed to be caused by the intensive interaction between the vapor structures generated from both sides.

The collapses of the small vapor structures on the suction side (between instant ⑱ and ⑲) also generated relatively high pressures at the trailing edge of the pressure side with a value of 8 bars.

Conclusions

The correlation between the high impacts and their possible causes has been successfully demonstrated in the analyses of the high instantaneous static pressure. The regions that are potentially exposed to high erosion risks are identified by the static pressure and show a good match with the paint results.

8.5.2 Variation of Local Field

The two time derivatives of the local pressure and vapor volume fraction respectively are evaluated in this subsection. In section 7.4.3, twenty-one instants are selected to represent the characteristic unsteady phenomena over the NACA0018-45 hydrofoil at 6.5° angle of attack during a typical shedding cycle. In the current section, the two time derivatives of the local pressure ($\partial p / \partial t$) and vapor volume fraction ($-\partial \alpha / \partial t$) at the intervals between the twenty-one time instants will be examined in search for a correlation between the numerical based criteria and the damaged regions shown in paint tests.

Rate of Pressure Rise

Contours of the time derivative of the local pressure are compared here with the contour plots of the iso-surfaces with a vapor volume fraction of $\alpha = 0.1$ at the relevant moments in the following figures. The analyses are made on the 20 intervals for a shedding cycle illustrated in section 7.4.3.

A selection of typical intervals which show a high rate of pressure rise is evaluated as follows:

- Interval between instant ⑩ and ⑪: The maximum value of $\partial p / \partial t$ is around $1.08e+11$. A high rate of pressure rise is observed at the corners of the trailing edge on both the suction side and pressure side. It can be related to the collapse of small vapor structures at the corners of the trailing edge, as indicated by the red circled region from the iso-surface plots in Figure 8-26.
- Interval between instant ⑫ and ⑬: The maximum value of $\partial p / \partial t$ is around $4.92e+10$ which is found to be located at the pressure side. It may be caused by the collapse of the vapor structures near the trailing edge, as indicated by the red circled region from the iso-surface plots in Figure 8-27.
- Interval between instant ⑬ and ⑭: The highest $\partial p / \partial t$ during the examined shedding cycle is observed on the pressure side at the instant ⑭ with a value of $1.74e+11$. This high rate of pressure rise may be related to the collapse of the vapor structures circled by red lines on the pressure side, as shown in Figure 8-28.

- Interval between instant ⑭ and ⑮: The maximum value of $\partial p / \partial t$ is around $8.77e+10$. This high rate of pressure rise, occurring at the instant ⑮, is largely caused by the collapse of the vapor structures on the suction side, as shown in Figure 8-29.
- Interval between instant ⑮ and ⑯: The maximum value of $\partial p / \partial t$ is around $8.94e+10$. It could be related to the collapses of the two small vapor structures close to the tunnel walls at the instant ⑯, as shown in Figure 8-30. It should be noted that these two vapor structures are separated from the attached parts of the horse-shoe shaped cloudy cavity, and the separation process can be seen from the downstream images as shown in Figure 8-31.
- Interval between instant ⑱ and ⑲: The maximum value of $\partial p / \partial t$ is around $2.81e+10$ and is observed at the instant ⑲, as shown in Figure 8-32. On the suction side, the collapses of the two very tiny vapor structures (indicated by the red circles) not only give rise to a relatively high rate of pressure rise around the collapse centers, but also generate relatively high rates of pressure rise on the aft half of the hydrofoil. On the pressure side, the collapses of the vapor structures (indicated by the black circle) also generate relatively high $\partial p / \partial t$ around their collapse center, and a broad response has been also observed on the aft half of the hydrofoil on the pressure side.

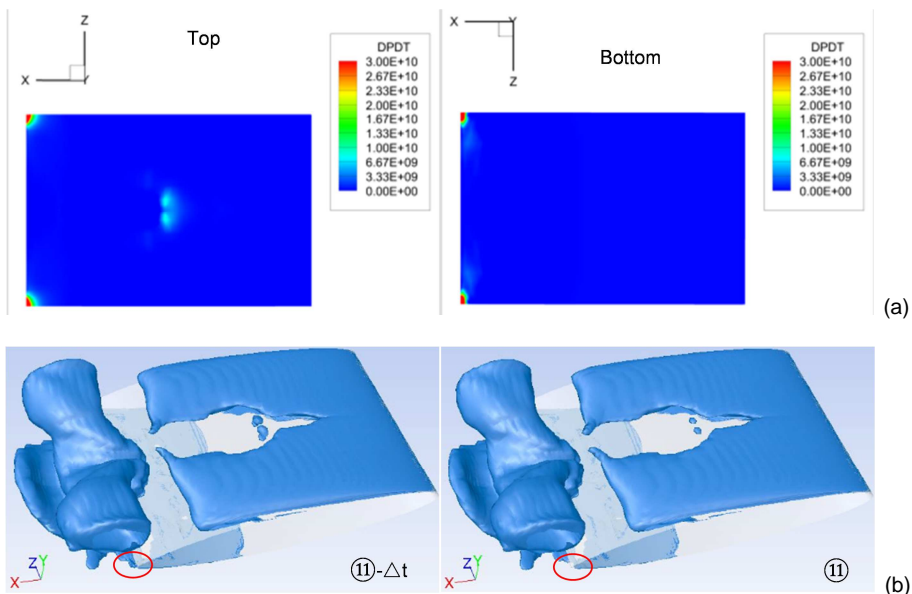
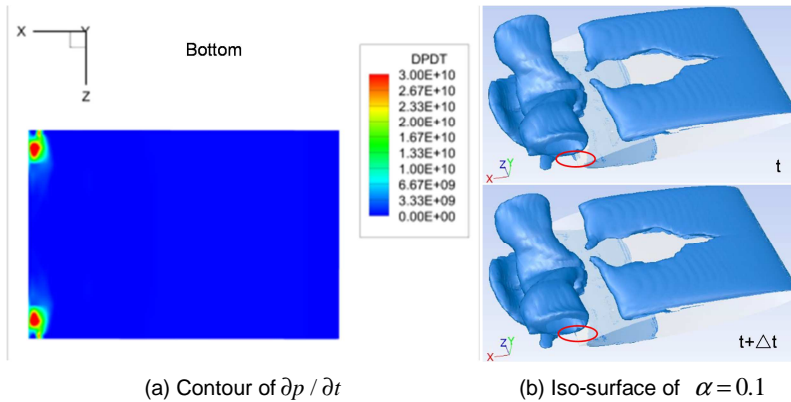
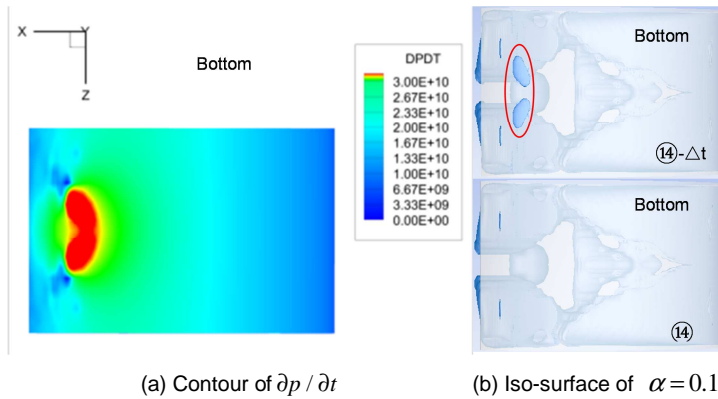


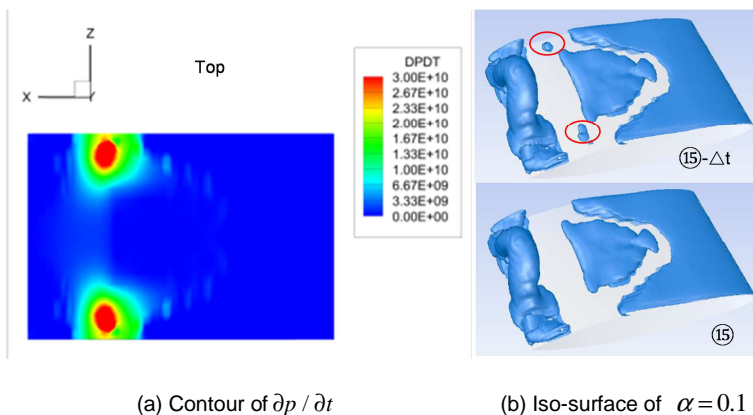
Figure 8-26: (a) Top view and bottom view (flow from right to left) of the contour of $\partial p / \partial t$ at the moment when its maximum value is observed (between instant ⑩ and ⑪ in Figure 7-18); and (b) plots of the vapor volume fraction with an iso-value of $\alpha = 0.1$ at the relevant time points



(a) Contour of $\partial p / \partial t$ (b) Iso-surface of $\alpha = 0.1$
 Figure 8-27: (a) Bottom view (flow from right to left) of the contour of $\partial p / \partial t$ at the moment when its maximum value is observed (between instant ⑫ and ⑬ in Figure 7-18); and (b) plots of the vapor volume fraction with an iso-value of $\alpha = 0.1$ at the relevant time points



(a) Contour of $\partial p / \partial t$ (b) Iso-surface of $\alpha = 0.1$
 Figure 8-28: (a) Bottom view (flow from right to left) of the contour of $\partial p / \partial t$ at the moment when its maximum value is observed (between instant ⑬ and ⑭ in Figure 7-18); and (b) plots of the vapor volume fraction with an iso-value of $\alpha = 0.1$ at the relevant time points (in bottom view)



(a) Contour of $\partial p / \partial t$ (b) Iso-surface of $\alpha = 0.1$
 Figure 8-29: (a) Top view (flow from right to left) of the contour of $\partial p / \partial t$ at the moment when its maximum value is observed (between instant ⑭ and ⑮ in Figure 7-18); and (b) plots of the vapor volume fraction with an iso-value of $\alpha = 0.1$ at the relevant time points

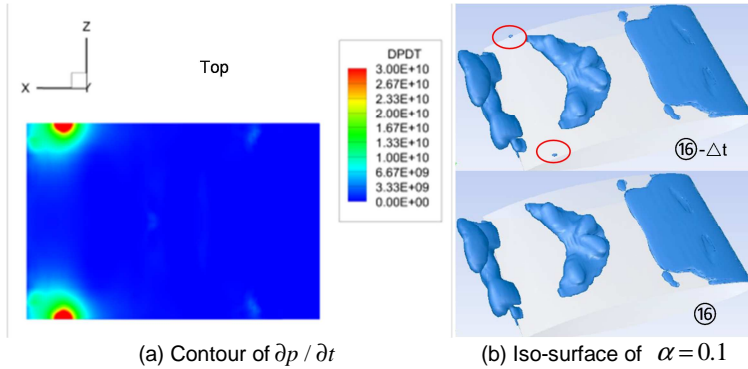


Figure 8-30: (a) Top view (flow from right to left) of the contour of $\partial p / \partial t$ at the moment when its maximum value is observed (between instant (15) and (16) in Figure 7-18); and (b) plots of the vapor volume fraction with an iso-value of $\alpha = 0.1$ at the relevant time points

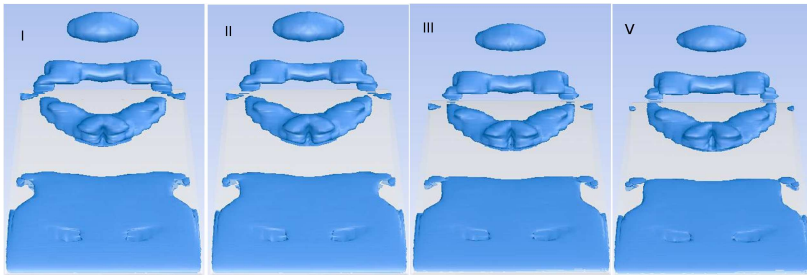


Figure 8-31: Contours of the iso-surface plots of the vapor volume fraction with value of $\alpha = 0.1$, which showing the separation process of the small vapor structures from the horse-shoe shaped cloudy cavity and their collapses in the vicinity of the tunnel walls and foil surface (downstream view)

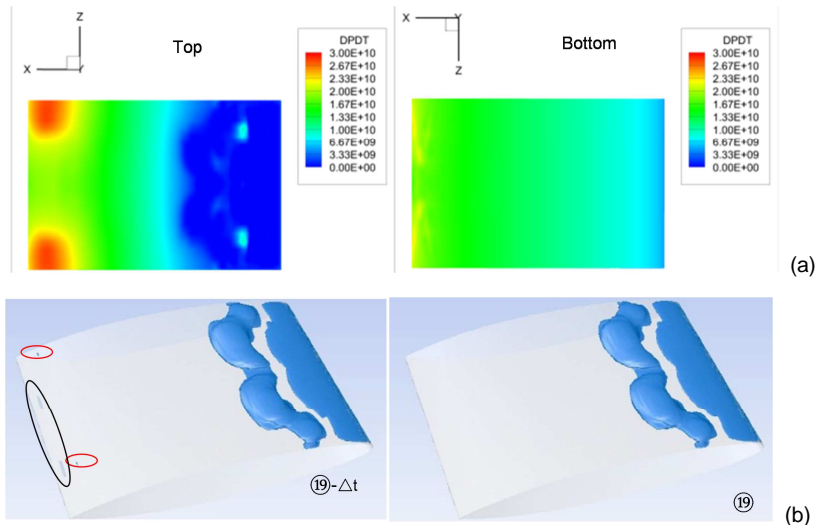


Figure 8-32: (a) Top view and bottom view (flow from right to left) of the contour of $\partial p / \partial t$ at the moment when its maximum value is observed (between instant (18) and (19) in Figure 7-18); and (b) plots of the vapor volume fraction with an iso-value of $\alpha = 0.1$ at the relevant time points

The results on the pressure side show that the damage most likely occurs around the mid-span at 80% chord length of the hydrofoil, as shown in Figure 8-28. From the numerical results, the trailing edge of both pressure side and suction side is exposed to high risk of cavitation erosion, especially the two corners. This is qualitatively in accordance with the observations from paint tests, except for the fact that a larger span-wise extent of the damage is observed from the paint tests.

The damage near the tunnels walls (from the paint tests measurements) are successfully predicted by the evaluation of $\partial p / \partial t$, as shown in Figure 8-29. However, the crescent shaped damage area which is supposed to be caused by the collapse of the horse-shoe shaped cloudy cavity is not clearly shown by the analyses of the $\partial p / \partial t$ criterion. It seems that the larger distance of the collapses from the foil surface, as predicted by the RANS method implemented in FLUENT (see Figure 7-24), than that as observed in experiments weakens the aggressiveness risk of cavitation erosion. Only the collapse of the vapor structures that were separated from the horse-shoe shaped cloudy cavity are likely to contribute the high impacts on the foil surface, as shown in Figure 8-30.

Rate of Vapor Production/Destruction

The evaluation of the rate of vapor production/destruction is conducted on the twenty intervals in the same way as the previous investigation of the rate of pressure rise. It is found that rarely high values of $-\partial\alpha / \partial t$ are observed on the suction side. One of the possible reasons for this finding is the long extent of the sheet cavity that developed from the leading edge (see instant ① to ⑩ in Figure 7-18). The second reason is that the collapses observed at the end of a shedding cycle also do not always produce high values of $-\partial\alpha / \partial t$ on the foil because they are found not to occur just on the hydrofoil but a bit further away from the foil surface (referring to instant ⑯ to ⑳ in Figure 7-19).

The instants with high values of $-\partial\alpha / \partial t$ are illustrated in the following:

- Interval between instant ⑩ and ⑪: The maximum value of $-\partial\alpha / \partial t$ is around $7.32e+04$. A high rate of vapor production $-\partial\alpha / \partial t$ is observed at the corners of the trailing edge of the hydrofoil, but only on the pressure side. This is qualitatively in accordance with the evaluation on the rate of pressure rise $\partial p / \partial t$ at the same moment, indicating that the high value of $\partial p / \partial t$ that is observed on both sides is mainly related to the collapse of small vapor structures at the corners of the trailing edge on pressure side, as shown in Figure 8-33.
- Interval between instant ⑬ and ⑭: The maximum value of $-\partial\alpha / \partial t$ is around

$6.87e+04$ and is found to locate at the pressure side. The regions with high erosion risk are found to correspond to the collapse centers of the vapor structures in the red circle on the pressure side, as shown in Figure 8-34.

- Interval between instant ⑭ and ⑮: The maximum value of $-\partial\alpha/\partial t$ is around $4.70e+04$. The location with a maximum rate of vapor destruction are similar to what is observed in the analyses of $\partial p/\partial t$, corresponding to the collapse of the vapor structures in the red circles on the suction side, as shown in Figure 8-35.
- Interval between instant ⑯ and ⑰: Relative high values of $-\partial\alpha/\partial t$ in the order of $5e+04$ are also observed during this interval. However, the regions with high erosion risk are found to be located around the leading edge due to the break-up of the new developed sheet cavity. These locations were identified neither from an evaluation with $\partial p/\partial t$ criterion nor from the damage observed in the paint tests.

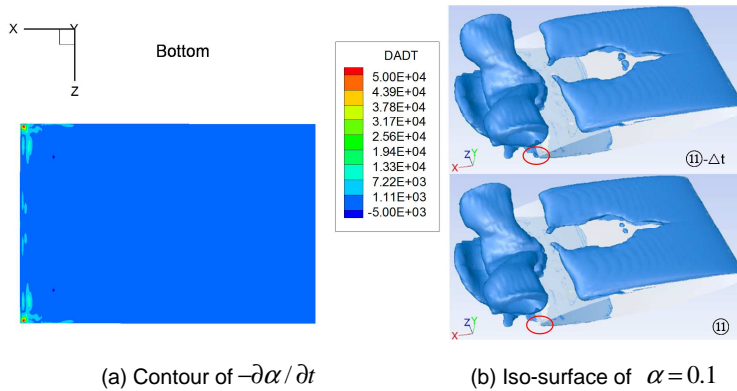


Figure 8-33: (a) Bottom view (flow from right to left) of the contour of $-\partial\alpha/\partial t$ at the moment when its maximum value is observed (between instant ⑩ and ⑪ in Figure 7-18); and (b) plots of the vapor volume fraction with an iso-value of $\alpha=0.1$ at the relevant time points

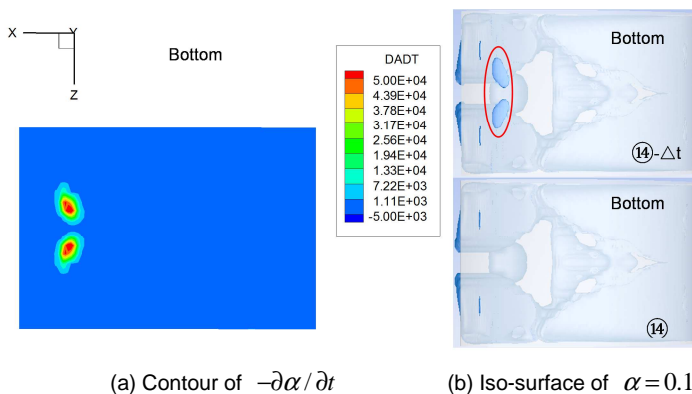


Figure 8-34: (a) Bottom view of the contour of $-\partial\alpha/\partial t$ at the moment when its maximum value is observed (between instant ⑬ and ⑭ in Figure 7-18); and (b) plots of the vapor volume fraction with an iso-value of $\alpha=0.1$ at the relevant time points (in bottom view) (flow from right to left)

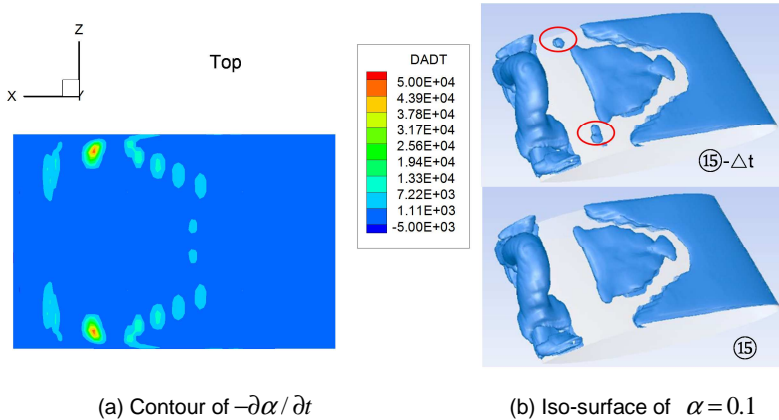


Figure 8-35: (a) Top view (flow from right to left) of the contour of $-\partial\alpha/\partial t$ at the moment when its maximum value is observed (between instant ⑭ and ⑮ in Figure 7-18); and (b) plots of the vapor volume fraction with an iso-value of $\alpha=0.1$ at the relevant time points

Conclusions

Similar conclusions as drawn from the previous evaluations of both time derivatives on the NACA0015 hydrofoil can be demonstrated here: The rate of vapor destruction ($-\partial\alpha/\partial t$) is somewhat correlated to the rate of pressure rise ($\partial p/\partial t$), and the rate of pressure rise ($\partial p/\partial t$) seems do a better job than the rate of vapor destruction ($-\partial\alpha/\partial t$) for the assessment of the locations that are potentially exposed to a high erosion risk. Furthermore, the evaluation of $-\partial\alpha/\partial t$ becomes more unreliable when the unsteady dynamics occurs around the trailing edge or even further downstream, because there will be no significant change of the local vapor volume fraction in cells on the foil surface.

8.5.3 Time-Averaged Aggressiveness Indices (Nohmi et al., 2008)

The four criteria proposed by Nohmi et al. (2008) (see equation (8-4)) will be evaluated on the NACA0018-45 hydrofoil in the following. The contours of the four aggressiveness indices on the suction side are plotted in Figure 8-36. The four aggressiveness indices are capable of predicting the high erosion risk located around the trailing edge of the hydrofoil, which is possibly caused by the intense interaction between the vapor structures generated at both the suction side and the pressure side.

It is observed that there are some resemblances between the results of $Index_1$ and $Index_3$. Both of them are found to locate a damage area at regions near the sidewalls, which is qualitatively in accordance with the observations from the paint tests. However, the predicted scattered high erosion risk on the suction side by these two indices cannot be correlated to the damage area observed from the paint tests. The red spots (as indicated by

white arrows in $Index_3$) located at approximately 75% chord length could be possibly related to the collapses of the vapor structures that are shed from the central sheet cavity on the suction side, as shown in Figure 7-22. The other two aggressiveness indices $Index_2$ and $Index_4$ show a high erosion risk over a very large extent on the suction side, which is in major disagreement with the observations from paint tests. It can also be observed that none of the four aggressiveness indices is capable of predicting the crescent-shaped damage that is observed from the paint tests.

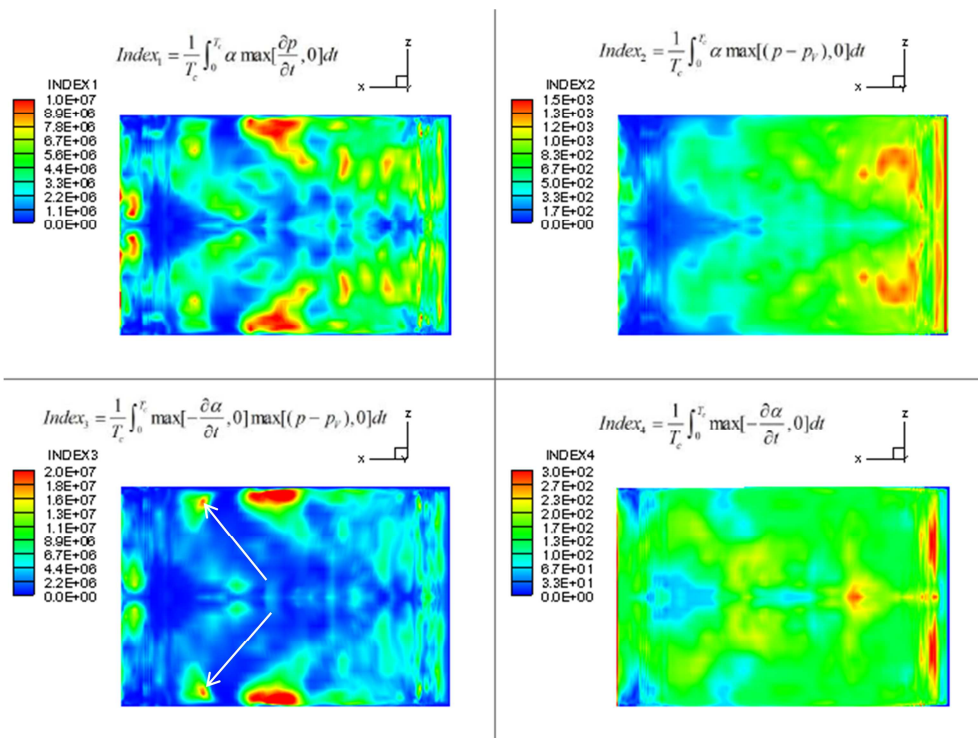


Figure 8-36: Contours of the four aggressiveness indices in equation during a typical shedding cycle referred to the cyclic images shown in Figure 7-17& Figure 7-18 (Flow from right to left)

8.5.4 Conclusions

The four aggressiveness indices proposed by Nohmi et al. (2008) could predict the region with a high erosion risk around the trailing edge of the hydrofoil, which is possibly caused by the intense interaction between the vapor structures generated at both the suction side and the pressure side. The indices $Index_1$ and $Index_3$ could also predict regions of high erosion risk located near the sidewalls, which is qualitatively in accordance with the observations from the paint tests. None of the four aggressiveness indices is however capable of predicting the crescent-shaped damage that is observed from the paint tests.

Neither of the scattered damage predicted by $Index_1$ and $Index_3$ nor the very large extent of damage on the suction side as predicted by $Index_2$ and $Index_4$ can be correlated with the experimental result.

The crescent-shaped damage is also not clearly identified by an evaluation of variation in time of the local pressure and vapor volume fraction. From the experimental results, the crescent shaped damage area could be related to the collapse of the primary horse-shoe shaped vapor structures in the vicinity of the foil surface. However, the collapse center of the horse-shoe shaped cavity is predicted further downstream and not close to the foil surface by the RANS method implemented in FLUENT. Therefore, the collapse of the primary horse-shoe shaped cavity has not been able to generate a higher value of $\partial p / \partial t$ than the collapses of the vapor structures that separated from the horse-shoe shaped cloudy cavity and which collapsed in the area close to the sidewalls, as shown in Figure 8-30. However, part of the regions with a high erosion risk that was indicated by the $\partial p / \partial t$ criterion can be correlated with the damage area from the paint tests.

The deficiency of the evaluation method $\partial p / \partial t$ could be partially ascribed to the discrepancies between the numerical results and experimental observations for the cavitating phenomena, which indeed imposes limitations on the assessment of the cavitation erosion. Furthermore, it is noted that some of the relatively high values of $\partial p / \partial t$ may also possibly have the potential to accumulate loads by implosions on the foil surface. It is hypothesized that a cumulative effect of these sufficiently high values could give a more reasonable assessment than the instantaneous peak of $\partial p / \partial t$. This will be discussed in section 8.7 in more detail.

8.6 BUBBLE COLLAPSE MODEL

As stated in Chapter 3, the bubble collapse model proposed by Wang and Brennen (1999) is supposed to solve the details of the collapsing bubbles and to allow for a quantitative assessment of the impulsive pressure released by the collapse of the cloudy cavity. However, several critical issues need to be addressed:

- The appropriate initial condition and corresponding parameters, which should provide a quasi-equivalent bubble cloud in an approximately spherical shape.
- The appropriate pressure perturbation and the corresponding period, which should reflect the circumstance as predicted by the RANS method as close as possible.
- The sensitivity of the model results for errors in the input variables.

According to a sensitivity study carried out by Van Loo (2011), the results from the spherical collapse model strongly depend on the cloud interaction parameter β , which is defined as:

$$\beta = \alpha_0(1 - \alpha_0) \frac{A_0^2}{R_0^2} \quad (8-8)$$

where:

- α_0 is the initial vapor volume fraction
- A_0 is the initial radius of the bubble cloud
- R_0 is the initial bubble radius

The initial bubble radius R_0 is a non-dimensional parameter and is defined as $R_0 = R_0^* / R_0^* \equiv 1$. However, the unsettled variables A_0 and R_0 could result in a scatter of values of three orders of the magnitude for the bubble interaction parameter β , resulting in a remarkably different collapse behavior and a different aggressiveness risk. It is also suggested by Van Loo (2011) that the collapse behavior of the spherical bubble cloud will be significantly influenced by the operation time of the pressure perturbation rather than its development pattern. It is then concluded that the selection of the initial parameters at the start-up point and the choice of operation time of the pressure perturbation make the reliability of this assessment very unpredictable.

Furthermore, according to the numerical results and the experimental observations on either NACA0015 hydrofoil or NACA0018-45 hydrofoil, a horse-shoe shaped rather than a spherical cloudy cavity is associated with a high erosion risk. The collapse process discussed by Kawanami et al. (2002), which is successfully reconfirmed by the RANS method with the current approach, differs significantly from the spherical symmetry system in the model by Wang and Brennen (1999). For an improved implementation, the bubble collapse model by Wang and Brennen needs to be reformulated to be capable of calculating non-spherical collapse (Colonius et al., 1998).

8.7 A NEW EROSION INTENSITY FUNCTION

An erosion intensity function is proposed here based on the following assumptions:

- The rapid increase of the local static pressure corresponding to high values of $\partial p / \partial t$, shows a good correlation with the damaged areas and is associated with a high erosion risk. This $\partial p / \partial t$ criterion has been evaluated in the sections 8.4 and 8.5.

- It can be argued that erosion damage is not only dependent on one maximum value, but that it is a cumulative loading effect on the material, as already suggested by Hammitt (1979). For this reason, it seems better if we take the accumulated rate of pressure rise ($\partial p / \partial t$) for those higher than a critical threshold value. This cumulative erosion intensity would then not only point toward the locations that are suffering from isolated peaks.
- The above mentioned threshold for $\partial p / \partial t$ for the contributions to cumulative erosion intensity function depends on the material properties.

Therefore, the following erosion intensity function is proposed:

$$I_{Erosion} = \frac{1}{N} \sum I_i \quad \text{and} \quad I_i = \begin{cases} \frac{\partial p}{\partial t}; & \frac{\partial p}{\partial t} \geq \text{Threshold} \\ 0; & \frac{\partial p}{\partial t} < \text{Threshold} \end{cases} \quad (8-9)$$

where the subscript i refers to each individual time instant, determined by the selected time step size. N is the number of the events with a value of $\partial p / \partial t$ higher than a certain threshold level.

By letting the threshold level go to zero, the erosion risk indicated by the erosion intensity $I_{Erosion}$ (equation (8-9)) can be observed all over the suction side, which could not be correlated to the experimentally observe damage areas from the paint tests. On the other hand, when the threshold level is chosen too high, the results estimated from the equation (8-9) also can also not be correlated to the observations from the paint test due to the absence of some of the important events related to high erosion risk. Due to a lack of the knowledge on the metallurgic properties of the foil material, a series of thresholds are applied to the equation (8-9) for the evaluation of erosion intensity on the two geometries respectively.

8.7.1 Results on NACA0015 Hydrofoil

A minimum level of the threshold level is found to be $1e+08$ in order to avoid a situation in which a high erosion risk is indicated over the complete suction side. It is also found that when the threshold level becomes higher than a value in the order of $4e+09$, the damage caused by the collapse of the horse-shoe shaped vapor structures will be omitted. The results from the erosion intensity function $I_{Erosion}$ with eight different threshold levels, from $2e+08$ to $4e+09$, that are evaluated on the NACA0015 hydrofoil are shown in Figure 8-37.

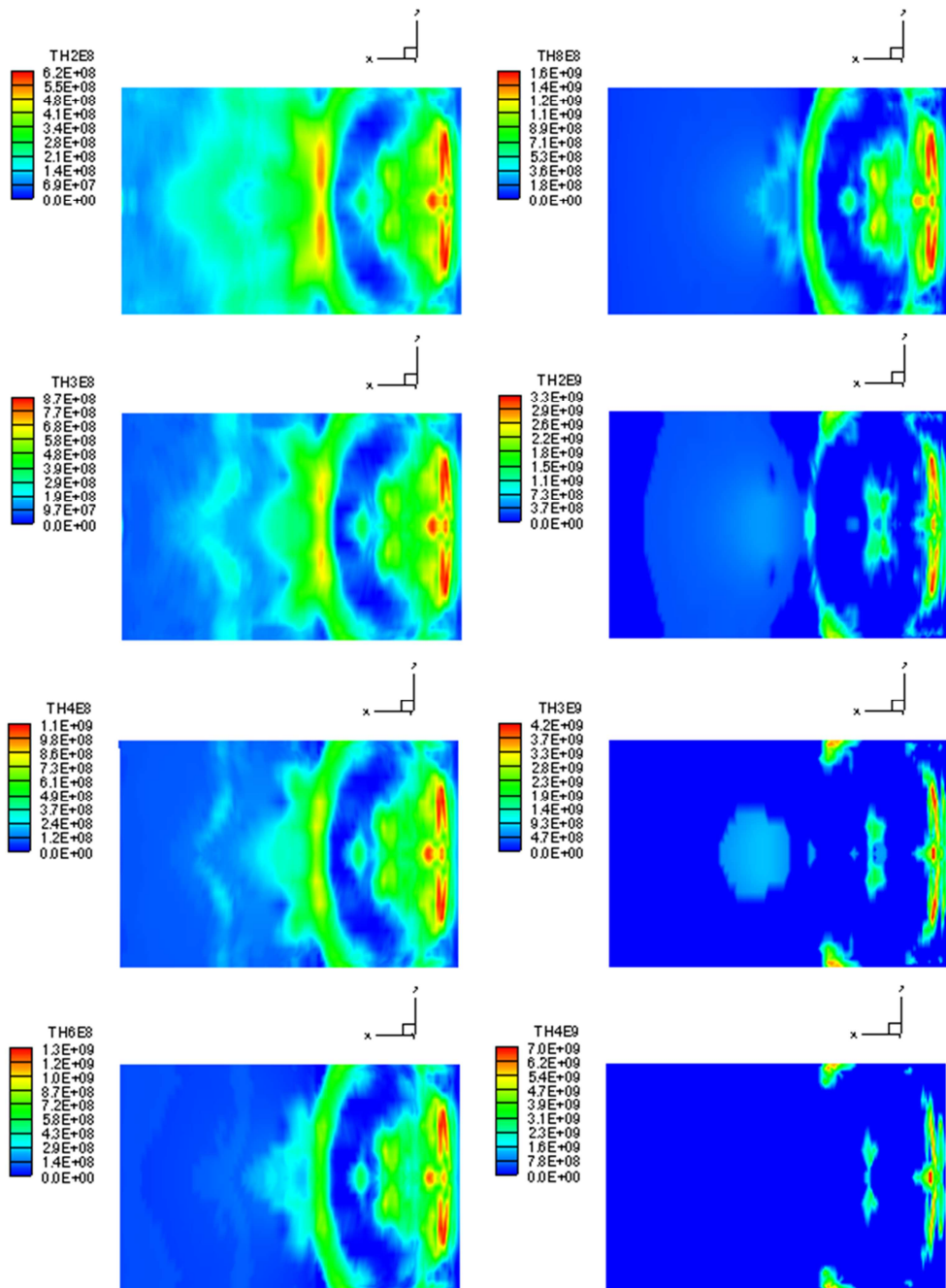
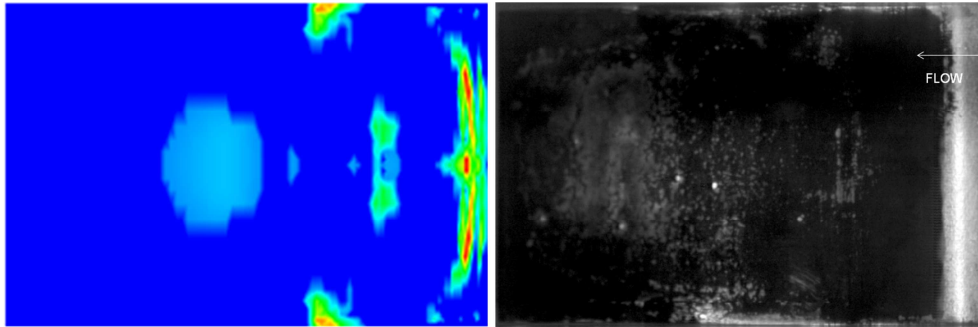


Figure 8-37: Erosion intensity estimated by equation (8-9) with eight different threshold levels, where the name above the threshold scale represents the applied threshold level, e.g. TH2E8 represents a value of $2e+08$ (Foil: NACA0015, $AoA=8^\circ$; flow from right to left)

Compared with the experimental results, the erosion intensity calculated with a threshold level of $3e+09$ seems to best correlate to the damage areas from the paint test, as shown in Figure 8-38.



(a) Results from the current study

(b) Results from paint tests

Figure 8-38: The comparison between (a) the high erosion risk predicted by equation (8-9) with a threshold value of $3e+09$ and (b) the damage area observed from paint tests (Foil: NACA0015, $AoA=8^\circ$; flow from right to left)

The discrepancies between the numerical results and the experimental results can be evaluated on two aspects:

- Discrepancies in the chord-wise direction: This can be ascribed to the discrepancies in the locations of the collapses of the shed cloudy cavity and the far smaller structures in the chord-wise direction between the numerical results and the experimental observations, which have been discussed in section 7.5.
- Discrepancies at the leading edge of the hydrofoil: No damage is found at the leading edge in the paint tests. However, the collapses of the vapor structures at the leading edge indeed cause a very high rate of pressure rise $\partial p / \partial t$ in the order of $1.5e+10$, which is one order higher than the high value of $\partial p / \partial t$ observed at the instant of the collapse of the horse-shoe shaped vapor cavity.

8.7.2 Results on NACA0018-45 Hydrofoil

For the NACA0018-45 hydrofoil, the minimum threshold level to exclude the situation that the erosion risk is distributed over the complete suction side is $7e+08$, a bit higher than the corresponding minimum level for the NACA0015 hydrofoil. It can be observed that the erosion risk on the trailing edge of the hydrofoil is smeared out with an increasing threshold level and will disappear when the threshold level reaches $2e+10$. The results of the erosion intensity $I_{Erosion}$ with six different threshold levels, from $2e+08$ to $4e+09$, that are evaluated on the NACA0018-45 hydrofoil are shown in Figure 8-39.

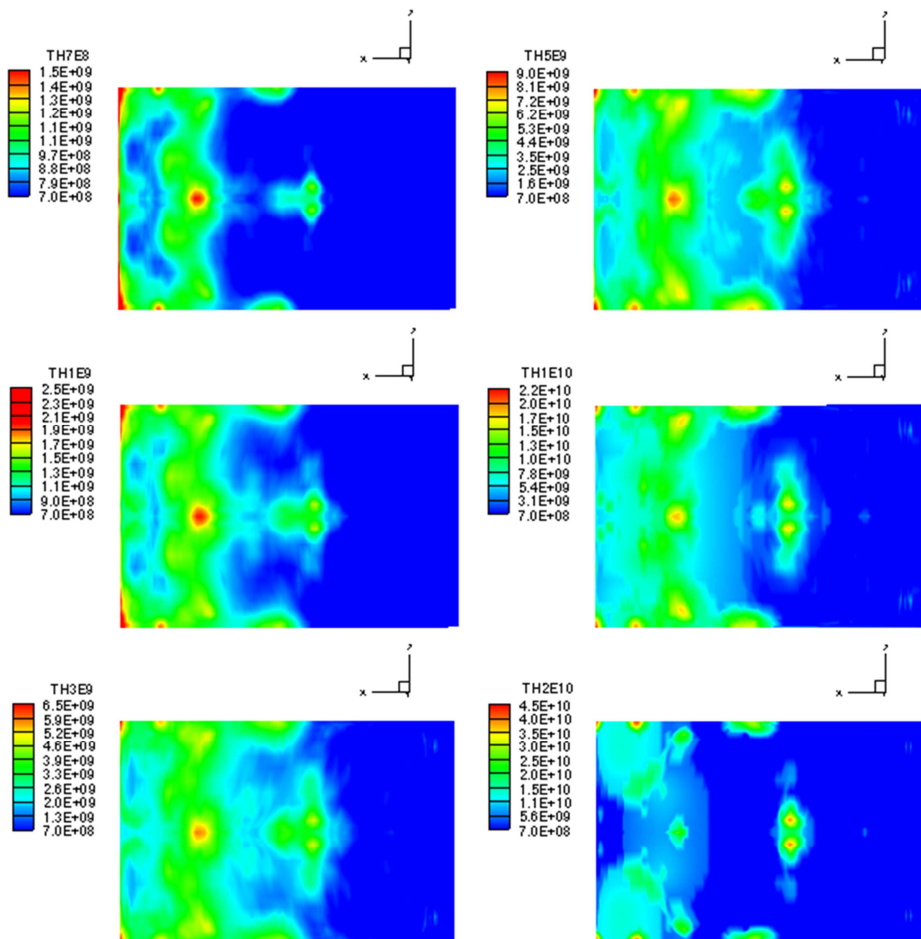


Figure 8-39: Erosion intensity estimated by equation (8-9) with eight different threshold levels, where the name above the threshold scale represents the applied threshold level, e.g. TH7E8 represents a value of $7e+08$ (Foil: NACA0018-45, AoA=6.5° ; flow from right to left)



(a) Results from the current study

(b) Results from paint tests

Figure 8-40: The comparison between (a) the high erosion risk predicted by equation (8-9) with a threshold value of $7e+08$ and (b) the damage area observed from paint tests (Foil: NACA0018-45, AoA=6.5° ; flow from right to left)

From the comparison with the experimental results, it is found that the best choice for the threshold level seems the smallest one of $7e+08$: Very high erosion risk is observed over the trailing edge of the hydrofoil in span-wise direction, and a relatively high erosion risk is located from approximately 70% C to 86% of the chord length. This is well correlated with the damage area from the paint tests, as shown in Figure 8-40.

However, the high erosion risk that is located around 45% of the chord length is not observed from the paint tests. The phenomenon related to this high erosion risk cannot always be captured by the RANS method implemented in FLUENT for each shedding cycle (discussed in section 8.5, see Figure 8-25), and therefore this location could not always be observed as a high risk erosion area from an analysis by the erosion intensity function. It is thus concluded that the threshold level with a value of $7e+08$ shows the best correlation between the high erosion risk estimated by equation (8-9) and the damage area observed from the paint tests.

8.7.3 Conclusions

It can be concluded that the erosion intensity function based on the normalized highest rate of pressure rise as defined by equation (8-9) provides a better criterion to assess the cavitation erosion risk than either the instantaneous static pressure p or the time derivative of local pressure $\partial p / \partial t$. An appropriate threshold level for the initial accumulation is critical for the final results, which is supposed to be only dependent on the material properties.

8.8 CONCLUSIONS

In this chapter, an evaluation of the erosion risk on a NACA0015 hydrofoil and a NACA0018-45 hydrofoil is conducted by using the following methods: instantaneous static pressure, variation in time of the local pressure and the local vapor volume fraction, and the four aggressiveness indices proposed by Nohmi et al. (2008).

It can be observed that there are discrepancies between the predicted regions with high erosion risk for these evaluation methods and the damaged area measured in the paint tests. However, the correlation between the regions exposed to a high erosion risk and the corresponding unsteady dynamics by experimental observations is found to be qualitatively similar as to what is observed for some of the evaluation methods, such as the instantaneous static pressure p and the variation in time of the local pressure $\partial p / \partial t$.

The model proposed by Wang and Brennen (1999) that is investigated here as a possible postprocessor to the RANS results, seems to have a lack of reliability due to the assumption of a spherically symmetric collapse and the great dependence on the initial parameters and the reaction time of the pressure perturbation. Further efforts are needed for a quantitative assessment of the risk of cavitation erosion with this Wang & Brennen model.

The proposed new erosion intensity function (equation (8-9)) is capable of indicating a high erosion risk with a good correlation with the damage area observed from the paint tests. The evaluation of this function on more shedding cycles is recommended for further investigation.

Chapter 9: CONCLUSIONS AND

RECOMMENDATIONS

In the following, the most important conclusions of the current research will be given first, after which the more detailed conclusions will be discussed chapter by chapter. Recommendations for further studies will be given in Section 9.2.

9.1 CONCLUSIONS

The most important conclusions for the current study can be summarized as:

- The large-scale structures and the typical unsteady cavitation dynamics from the experiments are in fair agreement with the results from the RANS method implemented in FLUENT using the current approach. However, the location of some of the primary vapor structures deviates from the experimental observations. Possible reasons for this discrepancy are discussed in section 7.5.
- As to the assessment of the cavitation erosion risk, a good correlation is found between the regions with high erosion risk evaluated by the new proposed erosion intensity function (equation (8-9)) and the observed damage area from paint tests.

In chapter 5, the capability of the RANS method implemented in FLUENT to predict the wetted flow (non-cavitating flow) is studied for three cases: A NACA0015 hydrofoil at 6° and 8° angle of attack and a NACA0018-45 hydrofoil at 6.5° angle of attack.

The following conclusions could be drawn from the obtained results in this chapter:

- Among the two-equation turbulence models, *SST* $k - \omega$ turbulence model is the preferred one in terms of the computational effort required and accuracy attained.
- The pressure distributions along the foil and the integral flow characteristics are grid independent under the condition that a sufficiently fine mesh is obtained along the foil even for the coarse grid. A maximum value for the non-dimensional cell height y^+ along the hydrofoil surface smaller than 1.0 indicates a fine enough mesh near the hydrofoil surface.
- The size of the computational domain in the direction normal to the main flow will significantly affect the flow characteristics, and a bounded domain will give a

delayed flow separation.

In chapter 6, the capability of the RANS method implemented in FLUENT to predict a steady cavitating flow and an unsteady cavitating flow over the hydrofoils is studied in a 2D computational domain.

The following conclusions could be drawn from the study on the steady cavitating flow over the 2D NACA0015 hydrofoil at 6° angle of attack:

- The order of the temporal discretization scheme does not play a primary role on the integral quantities.
- The integral forces and the turbulent kinetic energy are grid independent when using the current grid resolution, where the maximum y^+ value on the foil surfaces is smaller than 1.0. However, more resolution of the cavity structures at the closure of the main cavity can be obtained with the finer grid.

From the investigation of the unsteady cavitating flow over the hydrofoils, it can be observed that the RANS method implemented in FLUENT with the current set-up is capable of capturing important unsteady dynamics observed in the experiments, such as the break-up of the main sheet cavity, the formation of the cloudy cavity and the periodic shedding. Several conclusions can be drawn from the investigations of the NACA0015 hydrofoil and the NACA0018-45 hydrofoil:

- A realistic dynamic shedding of the sheet cavitation is only obtained after attenuating the eddy viscosity in the region with higher vapor volume fraction in the multiphase RANS method implemented in FLUENT. It appears that the reduction of the eddy viscosity plays an essential role in the unsteady dynamics calculated with FLUENT.
- The time step size that is adopted in the transient solver can be estimated from the time for the flow travelling over a characteristic spatial length (See equation (6-1)).
- It should be noted that for the unsteady simulations, the number of iterations per time step should be carefully selected in order to avoid a lack of numerical convergence, which may result in a significant influence on the prediction of the shedding frequency. It is suggested that convergence is reached when the mass transfer rate does not change anymore with the number of iterations during each time step.
- The basic unsteady phenomena are grid independent for the currently used

topology and resolution ($y^+ < 1$), which is in an O-H topology with appropriate grid density around the nose and tail of the foil.

- The sudden peaks in both lift and drag are attributed to the unsteady cavitation phenomena, such as the cavity sheddings and collapses.
- The source strength involved in the cavitation model is assumed to be proportional to the bubble number density. Therefore, it is important to be aware of the influence of the bubble number density on the cavitation phenomena predicted by the RANS method implemented in FLUENT.

In chapter 7, the capability of the RANS method implemented in FLUENT to predict the unsteady cavitating flow over the hydrofoils is studied in a 3D computational domain. It can be observed that the large-scale structures and typical unsteady cavitation dynamics from the experiments are in fair agreement with the results from the RANS method using the current approach. However, the location of the collapses of these large-scale structures predicted by the RANS method show some discrepancies with the experiments.

The following conclusions can be drawn from an analysis of the simulation results and a comparison with the experimental observations:

- Due to the effect of the vertical side wall boundary layer, the re-entrant jet can be observed not only to move in upstream direction, but also to move towards the mid-span. It is believed that this wall effect is an important reason for the horse-shoe shaped cloudy cavity to develop.
- The re-entrant flow which travels upstream and towards mid-span underneath the sheet cavity is the main cause of the break-up of the sheet cavity and the detachment of the cloudy cavities. This confirms earlier experimental observations by Foeth (2008) on the cavity over a twisted hydrofoil.
- Possible reasons for the discrepancies in the location of some of the main cavity structures could be related to the following aspects: The bubble number density input in the cavitation model, differences in the location of the reference pressure in the computations and the experiments, the assumed wall boundary layer velocity profile at the inlet, the reliability of Reboud's correction of the turbulence model and the possible interference between the cavity time scales and the turbulent time scales.

In chapter 8, an evaluation of the erosion risk on the hydrofoils is made by using the different damage functions that could be derived from the relation in the potential power

function (see equation (8-2)). The functions investigated are based on: instantaneous static pressure p , variation of the local pressure in time $\partial p / \partial t$, variation of the local vapor volume fraction in time $-\partial \alpha / \partial t$, and the aggressiveness indices proposed by Nohmi et al. (2008). The feasibility of using the bubble collapse model proposed by Wang and Brennen (1999) as a post-processor of the RANS results is also examined. A new erosion intensity function is finally proposed and is found to be the most promising evaluation method for the erosion risk.

The following conclusions are drawn:

- The correlation between the regions exposed to a high erosion risk and the corresponding unsteady dynamics by experimental observations is found to be qualitatively similar as to what is observed for some of the evaluation methods, such as the instantaneous static pressure p and the time derivative of the local pressure $\partial p / \partial t$.
- The erosion intensity function shown in equation (8-9), is based on the mean value of those values of the time derivative of the local pressure $\partial p / \partial t$ that exceed a certain threshold. This function gives the best correspondence between the locations with the highest erosion risk from the computations and the damage areas obtained from the experiments.
- The current post-processing model proposed by Wang and Brennen (1999) seems less reliable due to the simplification imposed by the assumption of the symmetrical and spherical collapse and the uncertainty in the initial conditions, as well as in the pressure perturbation period.

9.2 RECOMMENDATIONS

For a more accurate prediction of cavitation phenomena in the flow over hydrofoils from a RANS method, the following recommendations are given:

- The bubble number density should be as close as possible to the condition in the test facility.
- The outlet pressure in the outlet plane should be measured at the same location as used in the experiments.
- To use the same inlet velocity profile as measured in the experiments, and this holds especially for the vertical side wall boundary layer in 3D computations.
- To find a time step size to give a better balance between the numerical stability and resolution of physics in view of possible interference between the cavity time

scales and the turbulent time scales.

For an evaluation of the risk of cavitation erosion, it is found that the classical idea to assess the cavitation erosion risk by calculating the energy emitted by the large scale cavity events could be converted into an analysis of the cavitation dynamics in a local cell. It is recommended that:

- LES and DES may be used to give a better resolution of the local events, which potentially enhance the reliability of the evaluations.
- The proposed erosion intensity function, based on accumulated peak pressures exceeding a certain threshold, is demanded for further validation on more shedding cycles.

Appendix A: A BRIEF INTRODUCTION OF TURBULENCE MODELS IN FLUENT

A.1 OVERVIEW

Appendix A provides a brief introduction of two classes of available two-equation turbulence models in FLUENT (ANSYS 12.0), which have been listed in Table 4-1, namely:

- $k - \varepsilon$ Models: standard $k - \varepsilon$ model, *RNG* $k - \varepsilon$ model, Realizable $k - \varepsilon$ model
- $k - \omega$ Models: standard $k - \omega$ model and *SST* $k - \omega$ model.

In the RANS method, the field variables can be written in the mean plus fluctuation decomposition, such as:

$$u = \bar{u} + u'; p = \bar{p} + p'; \tau_{ij} = \bar{\tau}_{ij} + \tau'_{ij}; S_{ij} = \bar{S}_{ij} + S'_{ij} \quad (\text{A-1})$$

where:

- $u(x, t)$ represents the velocity vector field
- $p(x, t)$ represents the pressure vector field
- τ_{ij} is the viscous stress tensor, and can be written as $\tau_{ij} = 2\mu S_{ij} - \frac{2}{3}\mu\delta_{ij}\frac{\partial u_k}{\partial x_k}$, where

μ is the dynamic viscosity, and δ_{ij} denotes the Kronecker symbol ($\delta_{ij} = 1$ if $i = j$

and $\delta_{ij} = 0$ otherwise)

- $S_{ij} = \frac{1}{2}\left(\frac{\partial u_i}{\partial x_j} + \frac{\partial u_j}{\partial x_i}\right)$ is the strain-rate tensor

The fluctuating parts satisfy:

$$\bar{u}' = 0; \bar{p}' = 0; \bar{\tau}'_{ij} = 0; \bar{S}'_{ij} = 0 \quad (\text{A-2})$$

Before going to the introduction of the turbulence models, several important variables are introduced at first:

- Turbulent kinetic energy k :

$$k = \frac{1}{2} \overline{u'_i u'_i} \quad (\text{A-3})$$

- Dissipate rate of the turbulent kinetic energy, i.e. ε :

$$\varepsilon = 2\nu \overline{S'_{ij} S'_{ij}} \quad (\text{A-4})$$

$$S'_{ij} = \frac{1}{2} \left(\frac{\partial u'_i}{\partial x_j} + \frac{\partial u'_j}{\partial x_i} \right) \quad (\text{A-5})$$

where S'_{ij} represents the fluctuating component of the strain-rate tensor, $\nu = \mu / \rho$ is the kinematic viscosity, μ is the dynamic viscosity and ρ is the liquid density.

- Specific dissipation rate of the turbulent kinetic energy, i.e. ω :

$$\omega = \frac{\varepsilon}{k} \quad (\text{A-6})$$

A.2 $k - \varepsilon$ MODELS

This section will introduce three turbulence models that are based on transport equations for the turbulence kinetic energy k and its dissipation rate ε : The transport equation for the turbulent kinetic energy k was derived from the exact equations, while the transport equation for its dissipation rate ε was obtained using physical reasoning and bears little resemblance to its mathematically exact counterpart. The modeling of turbulent viscosity μ_t , the transport equations for k and ε model constants will be introduced for each model.

A.2.1 Transport Equation for Turbulent Kinetic Energy k

The general transport equation for the turbulent kinetic energy k without taking the buoyancy effects and compressibility into account can be derived as follows:

- Subtraction of the Navier-Stokes equations and RANS equations,
- Multiplication of the resulting equations by the corresponding fluctuating velocity components, i.e. u'_i ,
- Addition of all the results and finally very substantial rearrangement.

The Navier-Stokes equations can be written as (referred to equation (4-4)):

$$\frac{\partial}{\partial t}(\rho u_i) + \frac{\partial}{\partial x_j}(\rho u_i u_j) = -\frac{\partial p}{\partial x_i} + \frac{\partial \tau_{ij}}{\partial x_j} \quad (\text{A-7})$$

The Reynolds-Averaged Navier-Stokes equations can be written as (see equations (4-10) and (4-11)):

$$\frac{\partial}{\partial t}(\overline{\rho u_i}) + \frac{\partial}{\partial x_j}(\overline{\rho u_i u_j}) = -\frac{\partial \overline{p}}{\partial x_i} + \frac{\partial \overline{\tau}_{ij}}{\partial x_j} - \frac{\partial}{\partial x_j}(\overline{\rho u'_i u'_j}) \quad (\text{A-8})$$

where:

- $u(x, t)$ represents the velocity vector field
- ρ is the liquid density
- $p(x, t)$ is the pressure field
- $\overline{\tau}_{ij} = 2\mu\overline{S}_{ij} - \frac{2}{3}\delta_{ij}\frac{\partial \overline{u}_k}{\partial x_k}$ is the mean viscous stress tensor, and $\overline{S}_{ij} = \frac{1}{2}\left(\frac{\partial \overline{u}_i}{\partial x_j} + \frac{\partial \overline{u}_j}{\partial x_i}\right)$ is

the mean strain-rate tensor(referred to equation (4-12))

Subtracting the equation (A-7) and (A-8) one obtains:

$$\frac{\partial(\rho u'_i)}{\partial t} + \frac{\partial}{\partial x_j}(\overline{\rho u_j u'_i} + \overline{\rho u_i u'_j} + \rho u'_i u'_j) = -\frac{\partial p'}{\partial x_i} + \frac{\partial \tau'_{ij}}{\partial x_j} + \frac{\partial}{\partial x_j}(\overline{\rho u'_i u'_j}) \quad (\text{A-9})$$

$$\tau'_{ij} = 2\mu S'_{ij} - \frac{2}{3}\delta_{ij}\frac{\partial u'_k}{\partial x_k} \quad (\text{A-10})$$

Multiplying (A-9) with u_i and averaging the resulting equations yields:

$$\begin{aligned} \frac{\partial(\overline{\rho u'_i})}{\partial t} u'_i + \frac{\partial(\overline{\rho u_j u'_i})}{\partial x_j} u'_i &= \frac{\partial \overline{p'}}{\partial x_i} u'_i + \frac{\partial \overline{\tau'_{ij}}}{\partial x_j} u'_i + \frac{\partial(\overline{\rho u_i u'_j})}{\partial x_j} u'_i + \frac{\partial(\overline{\rho u'_i u'_j})}{\partial x_j} u'_i \end{aligned} \quad (\text{A-11})$$

(I) (II) (III) (IV) (V) (VI)

By using the definition of turbulent kinetic energy (equation (A-3)), terms (I) + (II) can be written as:

$$(I) + (II) = \frac{\partial}{\partial t}(\rho k) + \frac{\partial}{\partial x_j}(\rho k \bar{u}_j) \quad (A-12)$$

Term (III) is usually rearranged in the following way:

$$\frac{\partial \overline{p' u'_i}}{\partial x_i} = -\frac{\partial}{\partial x_i}(\overline{p' u'_i}) + p' \frac{\partial u_i}{\partial x_i} \quad (A-13)$$

where the first term at the right hand of equation (A-13) is in the divergence form, normally referred to as pressure diffusion term, and the second term at the right hand of equation (A-13) is normally referred to as pressure strain-rate term, and can be eliminated when the incompressibility condition is used.

Term (IV) can be similarly written as:

$$\frac{\partial \overline{\tau'_{ij} u'_i}}{\partial x_j} = \frac{\partial}{\partial x_j}(\overline{\tau'_{ij} u'_i}) - \overline{\tau'_{ij}} \frac{\partial u'_i}{\partial x_j} \quad (A-14)$$

If we substitute equation (A-10) and apply the incompressibility condition, equation (A-14) can be written as:

$$\frac{\partial \overline{\tau'_{ij} u'_i}}{\partial x_j} = \frac{\partial}{\partial x_j}(2\mu \overline{S'_{ij} u'_i}) - 2\mu \overline{S'_{ij}} \frac{\partial u'_i}{\partial x_j} \quad (A-15)$$

where the first term at the right hand of equation (A-15) is also in the divergence form, and the second term is normally referred to as “dissipation of Reynolds stress by the turbulence viscous stresses” (CFD Online).

The second term at the right hand of equation (A-15) can be treated in the following way:

$$-2\mu \overline{S'_{ij}} \frac{\partial u'_i}{\partial x_j} = -2\mu \overline{S'_{ij} (S'_{ij} + \Omega'_{ij})} = -2\mu \overline{S'_{ij} S'_{ij}} = -\rho \epsilon \quad (A-16)$$

$$S'_{ij} = \frac{1}{2} \left(\frac{\partial u'_i}{\partial x_j} + \frac{\partial u'_j}{\partial x_i} \right); \Omega'_{ij} = \frac{1}{2} \left(\frac{\partial u'_i}{\partial x_j} - \frac{\partial u'_j}{\partial x_i} \right) \quad (A-17)$$

where Ω'_{ij} represents the fluctuating components of rotation-rate tensor, and the product of the symmetric tensor S'_{ij} and the anti-symmetric tensor Ω'_{ij} results in a value of zero.

Applying the derivation rules and the incompressibility condition, term (V) can be written as:

$$\overline{\frac{\partial(\rho \bar{u}_i u'_j)}{\partial x_j} u'_i} = \overline{\frac{\partial(\rho u'_j)}{\partial x_j} u'_i} \bar{u}_i - \overline{\rho u'_i u'_j} \frac{\partial \bar{u}_i}{\partial x_j} = -\overline{\rho u'_i u'_j} \frac{\partial \bar{u}_i}{\partial x_j} \quad (\text{A-18})$$

Term (VI) can be similarly written as:

$$\overline{\frac{\partial(\rho u'_i u'_j)}{\partial x_j} u'_i} = -\frac{1}{2} \frac{\partial}{\partial x_j} (\overline{\rho u'_i u'_j u'_i}) \quad (\text{A-19})$$

which is also a divergence form.

Rearranging the resulting terms yields the following equation, i.e. the basic form of the transportation equation of turbulence kinetic energy k :

$$\begin{aligned} \frac{\partial}{\partial t}(\rho k) + \frac{\partial}{\partial x_j}(\rho k \bar{u}_j) &= \frac{\partial}{\partial x_j}(-\overline{p' u'_j} - \frac{1}{2} \overline{\rho u'_i u'_i u'_j} + 2\overline{\mu S'_{ij} u'_j}) - \overline{\rho u'_i u'_j} \frac{\partial \bar{u}_i}{\partial x_j} - \rho \varepsilon \\ \text{(I)} \quad \quad \quad \text{(II)} \quad \quad \quad \text{(III)} \quad \quad \quad \text{(IV)} \quad \quad \quad \text{(V)} \quad \quad \quad \text{(VI)} \quad \quad \quad \text{(VII)} \end{aligned} \quad (\text{A-20})$$

and the terms can be expressed in words as:

- (I) the rate of change of turbulent kinetic energy k
- (II) transport of k by convection
- (III) transport of k by pressure
- (IV) transport of k by Reynolds stresses
- (V) transport of k by viscous stresses
- (VI) rate of production of k
- (VII) rate of dissipation of k

A.2.2 Standard $k - \varepsilon$ Model (Launder and Spalding, 1972)

Transport Equations

The turbulence kinetic energy k and its dissipation rate ε are obtained from the following transport equations:

$$\frac{\partial}{\partial t}(\rho k) + \frac{\partial}{\partial x_j}(\rho k \bar{u}_j) = \frac{\partial}{\partial x_j}[(\mu + \frac{\mu_t}{\sigma_k}) \frac{\partial k}{\partial x_j}] + G_k + G_b - \rho \varepsilon - Y_M + S_k \quad (\text{A-21})$$

$$\frac{\partial}{\partial t}(\rho\varepsilon) + \frac{\partial}{\partial x_j}(\rho\varepsilon u_j) = \frac{\partial}{\partial x_j} \left[\left(\mu + \frac{\mu_t}{\sigma_\varepsilon} \right) \frac{\partial \varepsilon}{\partial x_j} \right] + C_{1\varepsilon} \frac{\varepsilon}{k} (G_k + C_{3\varepsilon} G_b) - C_{2\varepsilon} \rho \frac{\varepsilon^2}{k} + S_\varepsilon \quad (\text{A-22})$$

where:

- $G_k = -\rho \overline{u'_i u'_j} \frac{\partial \bar{u}_i}{\partial x_j}$ represents the generation of k due to the mean velocity gradients
- G_b represents the generation of k due to buoyancy
- Y_M represents the contribution of the fluctuating dilatation in compressible turbulence to the overall dissipation rate
- σ_k and σ_ε are the turbulent Prandtl numbers for k and ε respectively
- S_k and S_ε are the source terms for k and ε respectively
- $C_{1\varepsilon}, C_{2\varepsilon}$ are constants, $C_{3\varepsilon}$ is not specified, and could be calculated by:

$$C_{3\varepsilon} = \tanh \left| \frac{v}{u} \right| \quad (\text{A-23})$$

where v is the component of the flow velocity parallel to the gravitational vector, and u is the component of the flow velocity perpendicular to the gravitational vector.

The first term at the right hand of equation (A-21) could be related to the divergence terms (III), (IV) and (V) in equation (A-20), representing the transport of turbulent kinetic energy k by pressure, Reynolds stresses and viscous stresses. Likewise for the first term at the right hand of equation (A-22), representing the transport of ε by pressure, Reynolds stresses and viscous stresses.

Modeling the Turbulent Viscosity

The turbulent viscosity μ_t is modeled as:

$$\mu_t = \rho C_\mu k^2 / \varepsilon \quad (\text{A-24})$$

where C_μ is a constant.

Model Constants

$$C_{1\varepsilon} = 1.44; C_{2\varepsilon} = 1.92; C_\mu = 0.09; \sigma_k = 1.0; \sigma_\varepsilon = 1.3$$

A.2.3 RNG $k - \varepsilon$ Model (Yakhot, V. and Orszag, S.A., 1986)

The RNG $k - \varepsilon$ model is derived from the application of a Renormalized Group (RNG) Method to the instantaneous Navier-Stokes equations. It has the following features:

- It has an additional term in the transport equation for ε that significantly improves the accuracy for rapidly strained flows.
- It includes the effect of swirl on turbulence that enhances the accuracy for swirling flows.
- It provides an analytical formula for turbulent Prandtl numbers rather than constant values specified in the standard $k - \varepsilon$ model.
- It provides an analytical differential formula for effective viscosity that also accounts for low-Reynolds-number effects, while the standard $k - \varepsilon$ model only accounts for high-Reynolds-number effects.

Transport Equations

The transport equations in RNG $k - \varepsilon$ model have a similar form to the transport equations in the standard $k - \varepsilon$ model:

$$\frac{\partial}{\partial t}(\rho k) + \frac{\partial}{\partial x_j}(\rho k \bar{u}_j) = \frac{\partial}{\partial x_j}(\alpha_k \mu_{eff} \frac{\partial k}{\partial x_j}) + G_k + G_b - \rho \varepsilon - Y_M + S_k \quad (A-25)$$

$$\frac{\partial}{\partial t}(\rho \varepsilon) + \frac{\partial}{\partial x_j}(\rho \varepsilon \bar{u}_j) = \frac{\partial}{\partial x_j}(\alpha_\varepsilon \mu_{eff} \frac{\partial \varepsilon}{\partial x_j}) + C_{1\varepsilon} \frac{\varepsilon}{k} (G_k + C_{3\varepsilon} G_b) - C_{2\varepsilon} \rho \frac{\varepsilon^2}{k} - R_\varepsilon + S_\varepsilon \quad (A-26)$$

where α_k and α_ε are the inverse effective Prandtl numbers for k and ε , and can be computed using the following formula:

$$\left| \frac{\alpha - 1.3929}{\alpha_0 - 1.3929} \right|^{0.6321} \left| \frac{\alpha + 2.3929}{\alpha_0 + 2.3929} \right|^{0.3679} = \frac{\mu_{mol}}{\mu_{eff}} \quad (A-27)$$

where μ_{mol} is the molecular viscosity. $C_{3\varepsilon}$ is calculated in the same way as in the standard $k - \varepsilon$ model, referred to equation (A-23). The main differences are the first term at the right hand of both equations, and an additional term R_ε in transport equation for ε .

Modeling the Effective Turbulent Viscosity

The effective turbulent viscosity μ_{eff} is modeled through a differential equation resulted from the scale elimination procedure in Renormalization Group (RNG) Method:

$$d\left(\frac{\rho^2 k}{\sqrt{\varepsilon\mu}}\right) = 1.72 \frac{\hat{v}}{\sqrt{\hat{v}^3 - 1 + C_v}} d\hat{v} \quad (\text{A-28})$$

where $\hat{v} = \mu_{\text{eff}} / \mu$ and $C_v \approx 100$.

Term R_ε in transport equation for ε

$$R_\varepsilon = \frac{C_\mu \eta^3 (1 - \eta / \eta_0)}{1 + \beta \eta^3} \rho \frac{\varepsilon^2}{k} \quad (\text{A-29})$$

where $\eta = \sqrt{2\bar{S}_{ij}\bar{S}_{ij}k} / \varepsilon$, $\eta_0 = 4.38$ and $\beta = 0.012$.

Model Constants

$$C_\mu = 0.0845; C_{1\varepsilon} = 1.42; C_{2\varepsilon} = 1.68$$

A.2.4 Realizable $k - \varepsilon$ Model (Shih et al., 1995)

The term ‘‘Realizable’’ means that the model satisfies certain mathematical constraints on the normal stresses, consistent with the physical of turbulent flows. It has the following features:

- It has the same turbulent kinetic energy equation as the standard $k - \varepsilon$ model.
- It provides a new formula for the turbulent viscosity, involving a variable C_μ originally proposed by Reynolds.
- It provides a new transport equation for the dissipation rate ε , which is derived from an exact equation for the transport of the mean-square vorticity fluctuation instead of the mathematically resembled equation as the equation for k used in $k - \varepsilon$ model and *RNG* $k - \varepsilon$ model.

Transport Equations

The transport equations for k and ω in Realizable $k - \varepsilon$ model are as follows:

$$\frac{\partial}{\partial t}(\rho k) + \frac{\partial}{\partial x_j}(\rho k \bar{u}_j) = \frac{\partial}{\partial x_j}[(\mu + \frac{\mu_t}{\sigma_k}) \frac{\partial k}{\partial x_j}] + G_k + G_b - \rho\varepsilon - Y_M + S_k \quad (\text{A-30})$$

$$\begin{aligned} \frac{\partial}{\partial t}(\rho\varepsilon) + \frac{\partial}{\partial x_j}(\rho\varepsilon \bar{u}_j) &= \frac{\partial}{\partial x_j}[(\mu + \frac{\mu_t}{\sigma_\varepsilon}) \frac{\partial \varepsilon}{\partial x_j}] + \rho C_1 \sqrt{2\bar{S}_{ij}\bar{S}_{ij}} \varepsilon - \rho C_2 \frac{\varepsilon^2}{k + \sqrt{\nu\varepsilon}} \\ &+ C_{1\varepsilon} \frac{\varepsilon}{k} C_{3\varepsilon} G_b + S_\varepsilon \end{aligned} \quad (\text{A-31})$$

where $C_1 = \max[0.43, \eta / (\eta + 5)]$, and η is same as the definition in the *RNG* $k - \varepsilon$ model. $C_{3\varepsilon}$ is calculated in the same way as in the standard $k - \varepsilon$ model, referred to equation (A-23).

Modeling the Turbulent Viscosity

The turbulent viscosity μ_t is modeled in the same way as to the standard $k - \varepsilon$ model:

$$\mu_t = \rho C_\mu k^2 / \varepsilon \quad (\text{A-32})$$

but with a different value of C_μ , which is calculated from:

$$C_\mu = \frac{1}{A_0 + A_s k U^* / \varepsilon} \quad (\text{A-33})$$

$$U^* \equiv \sqrt{\overline{S_{ij}} \overline{S_{ij}} + \overline{\Omega_{ij}} \overline{\Omega_{ij}}}$$

$$A_0 = 4.04; A_s = \sqrt{6} \cos \phi; \phi = \frac{1}{3} \cos^{-1}(\sqrt{6}W)$$

and:

$$W = \frac{\overline{S_{ij}} \overline{S_{ji}} \overline{S_{ki}}}{\sqrt{\overline{S_{ij}} \overline{S_{ij}}}} \quad (\text{A-34})$$

which is a function of the mean strain and rotation rates, the angular velocity of the system rotation and the turbulence fields (i.e. k and ε).

Model Constants

$$C_2 = 1.9; C_{1\varepsilon} = 1.44; \sigma_k = 1.0; \sigma_\varepsilon = 1.2$$

A.3 $k - \omega$ MODELS

This section will introduce two turbulence models that based on transport equations for the turbulence kinetic energy k and a specific dissipation rate ω , which is defined as $\omega = \varepsilon / k$.

A.3.1 Standard $k - \omega$ Model (Wilcox, 1998)

Transport Equations

The transport equations for k and ω in the standard $k - \omega$ model are as follows:

$$\frac{\partial}{\partial t}(\rho k) + \frac{\partial}{\partial x_j}(\rho k \bar{u}_j) = \frac{\partial}{\partial x_j}[(\mu + \frac{\mu_t}{\sigma_k}) \frac{\partial k}{\partial x_j}] + G_k - Y_k + S_k \quad (\text{A-35})$$

$$\frac{\partial}{\partial t}(\rho \omega) + \frac{\partial}{\partial x_j}(\rho \omega \bar{u}_j) = \frac{\partial}{\partial x_j}[(\mu + \frac{\mu_t}{\sigma_\omega}) \frac{\partial \omega}{\partial x_j}] + G_\omega - Y_\omega + S_\omega \quad (\text{A-36})$$

where:

- σ_k and σ_ω are the turbulent Prandtl numbers for k and ω
- G_k and G_ω represent the production of k and ω due to mean velocity gradients
- Y_k and Y_ω represent the dissipation of k and ω due to turbulence
- S_k and S_ω are the source terms for k and ω

Modeling the Turbulent Viscosity

The turbulent viscosity μ_t is computed in the following way:

$$\mu_t = \alpha^* \frac{\rho k}{\omega} \quad (\text{A-37})$$

$$\alpha^* = \alpha_\infty^* \left(\frac{\alpha_0^* + \text{Re}_t / R_k}{1 + \text{Re}_t / R_k} \right) \quad (\text{A-38})$$

and:
$$\text{Re}_t = \frac{\rho k}{\mu \omega}; R_k = 6; \alpha_0^* = \frac{\beta_i}{3}; \beta_i = 0.072 \quad (\text{A-39})$$

Modeling the Production Terms G_k and G_ω

The term G_k is same as to the definition in the standard $k - \varepsilon$ model:

$$G_k = -\rho \overline{u'_i u'_j} \frac{\partial \bar{u}_i}{\partial x_j} \quad (\text{A-40})$$

The term G_ω is correlated to the term G_k and is given by:

$$G_\omega = \alpha \frac{\omega}{k} G_k \quad (\text{A-41})$$

$$\alpha = \frac{\alpha_\infty}{\alpha^*} \left(\frac{\alpha_0 + \text{Re}_t / R_\omega}{1 + \text{Re}_t / R_\omega} \right) \quad (\text{A-42})$$

and $R_\omega = 2.95$, other items are given by equation (A-39).

Modeling the Dissipation Terms Y_k and Y_ω

The dissipation terms for k and ω can be given by:

$$Y_k = \rho \beta^* f_\beta k \omega; \quad Y_\omega = \rho \beta f_\beta \omega^2 \quad (\text{A-43})$$

where the details for each variable involved in the equation (A-43) can be found in the help files for FLUENT (ANSYS, 2009).

Model Constants

$$\alpha_\infty^* = 1; \alpha_\infty = 0.52; \alpha = \frac{1}{9}; \beta_i = 0.072$$

$$R_k = 6; R_\omega = 2.95; \sigma_k = 2.0; \sigma_\omega = 2.0$$

A.3.2 SST $k - \omega$ Model (Menter, 1994)

The SST $k - \omega$ turbulence model was proposed by Menter (1994), and is a blending between the standard $k - \omega$ model in the near-wall region and the standard $k - \varepsilon$ model in the far field. It has the following features:

- It has an advantage in terms of performance over both the standard $k - \omega$ model and standard $k - \varepsilon$ model, ensuring an appropriate behavior in both the near-wall and far-field regions.
- It includes an additional cross-diffusion term in the ω equation.
- It modifies the definition of the turbulent viscosity to account for the transport of the principal turbulent shear stress, and this is also the original of the name of the model, which is shear-stress transport (SST) $k - \omega$ model.

Transport Equations

The transport equations for the turbulent kinetic energy k and its specific dissipation rate ω are as follows:

$$\frac{\partial}{\partial t}(\rho k) + \frac{\partial}{\partial x_j}(\rho k \bar{u}_j) = \frac{\partial}{\partial x_j} \left[\left(\mu + \frac{\mu_t}{\sigma_k} \right) \frac{\partial k}{\partial x_j} \right] + \tilde{G}_k - Y_k + S_k \quad (\text{A-44})$$

$$\frac{\partial}{\partial t}(\rho \omega) + \frac{\partial}{\partial x_j}(\rho \omega \bar{u}_j) = \frac{\partial}{\partial x_j} \left[\left(\mu + \frac{\mu_t}{\sigma_\omega} \right) \frac{\partial \omega}{\partial x_j} \right] + G_\omega - Y_\omega + D_\omega + S_\omega \quad (\text{A-45})$$

where:

- σ_k and σ_ω are the turbulent Prandtl numbers for k and ω

- G_k and G_ω represent the generation of k and ω
- Y_k and Y_ω represent the dissipation of k and ω due to turbulence
- S_k and S_ω are the source terms for k and ω
- D_ω represents the cross-diffusion term due to the transformation of the standard $k - \varepsilon$ model into equations based on k and ω

Turbulent Prandtl Numbers

The turbulent Prandtl numbers for k and ω are given by:

$$\sigma_k = \frac{1}{F_1 / \sigma_{k,1} + (1 - F_1) / \sigma_{k,2}}; \quad \sigma_\omega = \frac{1}{F_1 / \sigma_{\omega,1} + (1 - F_1) / \sigma_{\omega,2}} \quad (A-46)$$

$$F_1 = \tanh(\Phi_1^4)$$

and:

$$\Phi_1 = \min \left[\max \left(\frac{\sqrt{k}}{0.09\omega y}, \frac{500\mu}{\rho y^2 \omega} \right), \frac{4\rho k}{\sigma_{\omega,2} D_\omega^+ y^2} \right] \quad (A-47)$$

$$D_\omega^+ = \max \left[2\rho \frac{1}{\sigma_{\omega,2} \omega} \frac{\partial k}{\partial x_j} \frac{\partial \omega}{\partial x_j}, 10^{-10} \right]$$

where y is the distance to the next surface and D_ω^+ is the positive portion of the cross-diffusion term D_ω .

Modeling Turbulent Viscosity

The ‘‘SST’’ stands for shear-stress transport because of the definition of the turbulent viscosity μ_t which is modified to account for the transport of the turbulent shear-stress. The turbulent viscosity μ_t is defined as (FLUENT Theory Guide, 2009):

$$\mu_t = \frac{\rho k}{\omega} \frac{1}{\max \left[\frac{1}{\alpha^*}, \frac{\sqrt{2S_{ij}S_{ij}} F_2}{a_1 \omega} \right]} \quad (A-48)$$

$$F_2 = \tanh(\Phi_2^4)$$

$$\Phi_2 = \max \left[\frac{2\sqrt{k}}{0.09\omega y}, \frac{500\mu}{\rho y^2 \omega} \right] \quad (A-49)$$

where α^* is same as given in equation (A-38), and F_2 is a function that is one for boundary-layer flows and zero for free shear layers and is meant to obtain improved results for the adverse pressure gradient boundary layer.

Modeling the Production Terms \tilde{G}_k and G_ω

The production terms \tilde{G}_k and G_ω are defined as:

$$\tilde{G}_k = \min(G_k, 10\rho\beta^*k\omega) \quad (\text{A-50})$$

$$G_\omega = \frac{\alpha}{\mu_t} \rho G_k \quad (\text{A-51})$$

where G_k , β^* and α are defined in the same way as in the standard $k - \omega$ model. However, α_∞ is given by $\alpha_\infty = F_1\alpha_{\infty,1} + (1 - F_1)\alpha_{\infty,2}$ instead of a constant value.

Modeling the Dissipation Terms Y_k and Y_ω

The dissipation terms for k and ω can be given by:

$$Y_k = \rho\beta^*k\omega; \quad Y_\omega = \rho\beta\omega^2 \quad (\text{A-52})$$

where β^* and β are defined in the same way as in the standard $k - \omega$ model. However, β_i is given by $\beta_i = F_1\beta_{i,1} + (1 - F_1)\beta_{i,2}$ instead of a constant value.

Cross-diffusion Term D_ω

The cross-diffusion term D_ω is defined as:

$$D_\omega = 2(1 - F_1)\rho \frac{1}{\sigma_{\omega,2}\omega} \frac{\partial k}{\partial x_j} \frac{\partial \omega}{\partial x_j} \quad (\text{A-53})$$

Model Constants

$$\begin{aligned} \sigma_{k,1} &= 1.176; \sigma_{k,2} = 1.0; \sigma_{\omega,1} = 2.0; \sigma_{\omega,2} = 1.168 \\ a_1 &= 0.31; \beta_i^1 = 0.075; \beta_i^2 = 0.0828 \end{aligned}$$

Appendix B: A BRIEF INTRODUCTION OF CURRENT CAVITATION MODELS

B.1 OVERVIEW

In this appendix, cavitation models that are currently used to numerically simulate the cavitating flows are briefly introduced in two main categories (referred to section 4.4):

- The Interface-tracking Approach: This is based on the free surface flow hypothesis. The cavity region is assumed to have a constant pressure equal to the vapor pressure of the corresponding liquid at the cavity interface. The computations are performed only for the liquid phase, and the cavity shape is iterated until the vapor pressure is achieved at the cavity boundary (Bouziad, 2006; Koop, 2008; Frikha et al., 2008).
- The Multiphase-flow Approach: This is based on the concept of phase averaging. The cavitating flow can be taken as a homogenous mixture of liquid and vapor (sometimes non-condensable gas is considered as the third phase). The mass and momentum transfer between the two phases can be modeled by two methods, the barotropic state law or the void fraction transport equation model (Frikha et al., 2008; Morgut et al., 2011).

This appendix will put the emphasis on the introduction of the latter approach, which is normally adopted for more general viscous flow solution methods, such as the RANS equation solvers.

B.2 THE INTERFACE-TRACKING APPROACH

This approach has been widely adopted for inviscid flow solution methods, such as potential flow boundary element methods (BEM), and Euler equation solvers (Arazgaldi et al., 2009; Bouziad, 2006). Three main methods for the interface-tracking approach will be briefly introduced in the following (Lind, 2010; Chen and Hagen, 2010):

- The Front Tracking Method: This method specifies a series of marker points at the interface, and the topology of this interface will be kept during the simulation. The

sharp change in variables, such as the densities, across the interface is smoothed as information is passed on to the fixed grid.

- The Level Set Method: This method defines the interface by a zero set of iso-surface of a scalar field ϕ , and it can be given as:

$$\phi = \begin{cases} > 0; & \text{in phase 1} \\ = 0; & \text{at the interface} \\ < 0; & \text{in phase 2} \end{cases} \quad (\text{B-1})$$

- The Volume of Fluid Method: This method is “one of the best established interface volume tracking methods currently in use” (Chen and Hagen, 2010). A volume fraction variable f is defined as the integral of the marker function χ in the controlled volume, which can then be updated by the advection equation to determine the phase in each grid cell. This fraction variable can be given as:

$$f = \frac{1}{V} \int \chi(\vec{x}, t) dV = \begin{cases} = 0; & \text{cell is filled with phase 1} \\ \in [0, 1]; & \text{interface goes cross this cell} \\ = 1; & \text{cell is filled with phase 2} \end{cases} \quad (\text{B-2})$$

B.3 THE MULTIPHASE-FLOW APPROACH

This approach has been widely used in the numerical simulation of cavitation phenomena, and it is often combined with the RANS equation solvers. The cavitating flow is treated as a homogenous mixture of liquid and vapor, sometimes non-condensable gas is considered as the third phase, and the relative motion between the phases is neglected. Very large and steep density variation is observed when the liquid phase vaporization into vapor phase.

The key issue in this approach is how to define the density of the mixture flow, which can be often categorized into two main methods:

- The barotropic state law method: In this method, the density variations in the mixture flow are related to the pressure following the barotropic law, where the density is kept constant in the liquid and vapor, and a barotropic relation is used in the transitional region.
- The void fraction transport equation method: This method models the phase change by the transport equation of a void fraction with various source terms modeling the mass transfer between the phases.

The Barotropic State Law Method

By assuming the cavitating process to be isothermal, the density of the mixture flow is defined as a function of pressure $\rho_m = f(p)$, and a common description of this relationship is shown in Figure B-1.

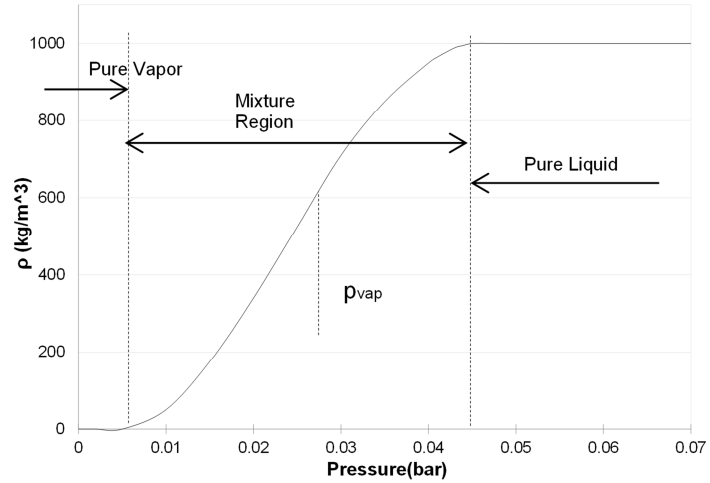


Figure B-1: The barotropic state law $\rho(p); T = 24^\circ\text{C}$

The densities in the pure vapor and liquid regions are supposed to be constant, and the two phases are jointed smoothly by a sinusoidal curve (Delannoy and Kueny, 1998) or by a polynomial curve (Song and He, 1998), and it can also be drawn by an isenthalpic approach (Salvatore et al., 2001).

The Sinusoidal model proposed by Delannoy and Kueny (1998) is characterized by its maximum slope $1/a_{\min}^2$. The density variation can be assumed as:

$$\rho_m = \rho_v + \frac{1}{a_{\min}^2} \frac{2}{\pi} (p_l - p_v) \sin\left(\frac{\pi}{2} \frac{p_m - p_v}{p_l - p_v}\right) \quad (\text{B-3})$$

where a_{\min} is the minimum speed of sound in the mixture ρ is the density, p is the pressure, and the subscripts of m, l and v represent mixture, liquid and vapor respectively. The sin function will then result in a slope relation as:

$$\frac{\partial \rho}{\partial p} = \frac{1}{a_{\min}^2} \cos\left(\frac{\pi}{2} \frac{p_m - p_v}{p_l - p_v}\right) \quad (\text{B-4})$$

The Void Fraction Transport Equation Method

This method introduces a concept of void fraction α , and the density of the mixture flow can be calculated by:

$$\rho_m = \alpha\rho_v + (1 - \alpha)\rho_l \quad (\text{B-5})$$

where ρ_v , ρ_l are the vapor and liquid density respectively, and α is the vapor volume fraction.

The general void fraction transport equation can be written as:

$$\frac{\partial}{\partial t}(\rho_v\alpha) + \frac{\partial}{\partial x_j}(\rho_v\alpha u_{v,j}) = S_e - S_c \quad (\text{B-6})$$

where,

- ρ_v is the vapor density
- α is the vapor volume fraction
- u_v means the vapor phase velocity
- S_e and S_c represent the mass transfer source terms due to the evaporation (growth) and condensation (collapse) of the vapor bubbles

The different models by this method are characterized by the different forms of the source terms that represent the evaporation and condensation processes. Three cavitation models based on the void fraction transport equation method are available in FLUENT (ANSYS 12.0): the Singhal et al. model, the Zwart-Gerber-Belamri Model and the Schnerr and Sauer Model. All of them are modeled based on the Rayleigh-Plesset equation:

$$R_B \frac{D^2 R_B}{Dt^2} + \frac{3}{2} \left(\frac{DR_B}{Dt} \right)^2 = \frac{p_B - p}{\rho_l} - \frac{4\nu_l}{R_B} \frac{DR_B}{Dt} - \frac{2\gamma}{\rho_l R_B} \quad (\text{B-7})$$

where,

- R_B represents the bubble radius
- ρ_l and ν_l are the density and kinematic viscosity of the liquid
- γ is the liquid surface tension
- p_B and p represent the bubble surface pressure and local far-field pressure

An overview of the three models based on the Rayleigh-Plesset equation and also other four models with different forms of source terms as a function of pressure is given in Table B-1

(Bouziad, 2006;Frikha et al., 2008; ANSYS, 2009;Morgut et al., 2011).

Table B-1: An overview of the current cavitation models

Models	Source Terms (S_e :evaporation; S_c :condensation)	Constants & Denotations
Singhal et al. Model	$S_e = F_{vap} \frac{\max(1.0, \sqrt{k})(1 - f_v - f_g)}{\gamma} \rho_v \rho_l \sqrt{\frac{2}{3} \frac{p_v - p}{\rho_l}}, \quad p_v \geq p$ $S_c = F_{cond} \frac{\max(1.0, \sqrt{k}) f_v}{\gamma} \rho_v \rho_l \sqrt{\frac{2}{3} \frac{p_v - p}{\rho_l}}, \quad p_v \leq p$	γ : surface tension k : turbulent kinetic energy f_v :vapor mass fraction f_g :non-condensable gases $p_v = p_{sat} + 0.39k / 2$ $F_{vap} = 0.02; F_{cond} = 0.01$
Schnerr and Sauer Model	$S_e = \frac{\rho_v \rho_l}{\rho_m} \frac{3\alpha(1-\alpha)}{R_B} \sqrt{\frac{2}{3} \frac{p_v - p}{\rho_l}}, \quad p_v \geq p$ $S_c = \frac{\rho_v \rho_l}{\rho_m} \frac{3\alpha(1-\alpha)}{R_B} \sqrt{\frac{2}{3} \frac{p - p_v}{\rho_l}}, \quad p_v \leq p$	$\alpha = \frac{\frac{4}{3} n_b \pi R_B^3}{1 + n_b \frac{4}{3} \pi R_B^3}$ is the vapor volume fraction n_b : bubble number density
Zwart-Gerber-Belamri Model	$S_e = F_{vap} \frac{3\alpha_{nuc}(1-\alpha)\rho_v}{R_B} \sqrt{\frac{2}{3} \frac{p_v - p}{\rho_l}}, \quad p_v \geq p$ $S_c = F_{cond} \frac{3\alpha\rho_v}{R_B} \sqrt{\frac{2}{3} \frac{p - p_v}{\rho_l}}, \quad p_v \leq p$	R_B :bubble radius= $10^{-6} m$ α_{nuc} :nucleation site volume fraction= 5×10^{-4} $F_{vap} = 50; F_{cond} = 0.001$
Merkle et al. Model	$S_e = \frac{F_{vap}}{t_\infty} \frac{\min(0, p - p_v)}{\frac{1}{2} \rho_l U_{ref}^2} (1-\alpha)\rho_l, \quad p_v \geq p$ $S_c = \frac{F_{cond}}{t_\infty} \frac{\max(0, p - p_v)}{\frac{1}{2} \rho_l U_{ref}^2} \alpha, \quad p_v \leq p$	$t_\infty = l / U_{ref}$ is the characteristic time, where l is the characteristic length and U_{ref} is the flow velocity F_{vap}, F_{cond} are empirical factors and are adjusted for different cases
Kunz Model	$S_e = \frac{F_{vap}}{t_\infty} \frac{\min(0, p - p_v)}{\frac{1}{2} \rho_l U_{ref}^2} (1-\alpha)\rho_v, \quad p_v \geq p$ $S_c = \frac{F_{cond}}{t_\infty} \rho_v (1-\alpha)^2 \alpha, \quad p_v \leq p$	F_{vap}, F_{cond} are empirical factors and are adjusted for different cases
Dauby et al. Model	$S_e = F_{vap} \min(0, p - p_v) \alpha, \quad p_v \geq p$ $S_c = F_{cond} \max(0, p - p_v) (1-\alpha), \quad p_v \leq p$	F_{vap}, F_{cond} are empirical factors and are adjusted for different cases
Saito et al. Model (2003)	$S_e = F_{vap} A \alpha (1-\alpha) \frac{\rho_l}{\rho_v} \frac{p_v - p}{\sqrt{2\pi R_B T_s}}, \quad p_v \geq p$ $S_c = F_{cond} A \alpha (1-\alpha) \frac{p_v - p}{\sqrt{2\pi R_B T_s}}, \quad p_v \leq p$	T_s : saturation temperature $A = F_a \alpha (1-\alpha)$ denotes the interfacial area concentration in the mixture, where $F_a F_{vap} = F_{vap} F_{cond} = 0.1$

BIBLIOGRAPHY

- Abdel-Maksoud, M. (2011). "Proceedings of workshop on cavitation and propeller performance." The 2nd International Symposium on Marine Propulsors, Hamburg, Germany.
- Anderson, J. D. (1995). Computational fluid dynamics: The basics with applications, McGraw-HILL, Inc.
- Anonymous contributor. (2008). "2D foil test case: summary." VIRTUE WP4 Workshop, Contribution from Chalmers University.
- ANSYS, Inc. (2009). FLUENT Theory Guide (Release 12.0).
- ANSYS, Inc. Proprietary. (2009). Introductory Fluent Training (Lecture10):Transient Flow Modeling.
- Arazgaldi, R., Hajilouy, A. and Farhanieh, B. (2009). "Experimental and numerical investigation of marine propeller cavitation." Scientia Iranica Transaction B: Mechanical Engineering, 16: 525-533.
- Bark, G., Berchiche, N. and Grekula, M. (2004a). Application of principles for observation and analysis of eroding cavitation-The EROCAV observation handbook, Edition 3.1.
- Bark, G., Friesch, J., Kuiper, G., and Ligtelijn, J.T. (2004b). "Cavitation erosion on ship propellers and rudders." 9th Symposium on Practical Design of Ships and Other Floating Structures, Luebeck-Travemuende, Germany.
- Bark, G., Grekula, M., Bensow, R.R., and Berchiche, N. (2009). "On some physics to consider in numerical simulation of erosive cavitation." Proceedings of the 7th International Symposium on Cavitation, Ann Arbor, Michigan, USA.
- Bensow, R.E. (2011). "Simulation of the unsteady cavitation on the DelftTwist11 foil using RANS, DES and LES." 2nd International Symposium on Marine Propulsors, Hamburg, Germany.
- Billet, M.L., Weir, D.S. (1975). "The effect of gas diffusion on the flow coefficient for a

ventilated cavity." ASME Journal of Fluids Engineering, 97: 501-506.

Boorsma, A. (2010). "Cavitation tests on a NACA0015 aerofoil – Quantification of cavitation impacts from high speed video and AE signals." CRS EROSION II Working Group.

Boorsma, A., Whitworth, S. (2011). "Understanding details of cavitation." 2nd International Symposium on Marine Propulsors, SMP2011, Hamburg, Germany.

Brennen, C.E. (1969). "The dynamic balances of dissolved air and heat in natural cavity flows." Journal of Fluid Mechanics, 37(1): 115-127.

Bouziad, Y.A. (2006). Physical modeling of leading edge cavitation: Computational methodologies and application to hydraulic machinery, PhD Thesis, University of Paris, France.

Challier, G., Fortes-Patella, R., and Reboud, J.L. (2000). "Interaction between pressure waves and spherical cavitation bubbles: discussion about cavitation erosion mechanism." Proceedings of the 2000 ASME Fluids Engineering Summer Conference, Boston, Massachusetts.

CFD Online. (www.cfd-online.com). "Introduction to turbulence/Reynolds averaged equations."

Colonius, T., Brennen, C.E. and d'Auria, F. (1998). "Computation of shock waves in cavitating flows." Proceedings of FED98, 3rd International Symposium on Numerical Methods for Multiphase Flow, Washington, DC, USA.

Coutier-Delgosha, O., Reboud, J.L. and Delannoy, Y. (2003a). "Numerical simulation of the unsteady behaviour of cavitating flows." International Journal for Numerical Methods in Fluids, 42: 527-548.

Coutier-Delgosha, O., Fortes-Patella, R., and Reboud, J.L. (2003b). "Evaluation of the turbulence model influence on the numerical simulation of unsteady cavitation." Transactions of the ASME, 125: 38-45.

De Lange, D.F., De Bruin, G.J. (1998). "Sheet cavitation and cloud cavitation, re-entrant jet and three-dimensionality." Applied Scientific Research, 58: 91-114.

Delannoy, Y., Kueny, J.L. (1998). "Two-phase approach in unsteady cavitation modeling." ASME Cavitation and Multiphase Flow Forum (98), Grenoble, France.

Dular, M., Bachert, R., Širok, B. and Stoffel, B. (2005). "Transient simulation, visualization

and PIV-LIF measurements of the cavitation on different hydrofoil configurations." Journal of Mechanical Engineering, 51(1): 13-27.

Dular, M, Sirok, B. and Stoffel, B. (2006). "Experimental and numerical modelling of cavitation erosion." 6th International Symposium on Cavitation, Wageningen.

Ferziger, J. H., Peric, M. (2002). Computational methods for fluid dynamics, Springer-Verlag.

Foeth, E.J. (2008). The structure of three-dimensional sheet cavitation, PhD Thesis, Delft University of Technology.

Foeth, J.P., Van Terwisga, T.J.C. and Van Doorne, C. (2008). "On the collapse structure of an attached cavity on a three dimensional hydrofoil." Journal of Fluids Engineering, 130 (7).

Fortes-Patella, R., Reboud, J.L. (1998). "A new approach to evaluate the cavitation erosion power." Journal of Fluids Engineering-Transactions of the ASME, 120.

Fortes-Patella, R., Challier, G., Reboud, J.L., and Archer, A. (2001). "Cavitation erosion mechanism: numerical simulation of the interaction between pressure waves and solid boundaries." Proceedings of CAV2001 Symposium, Pasadena.

Fortes-Patella, R., Reboud, J.L. and Briancon-Marjollet, L. (2004). "A phenomenological and numerical model for scaling the flow aggressiveness in cavitation erosion." EROCAV Workshop, Val de Reuil.

Franc, J.P., Michel, J.M. (2004). Fundamentals of cavitation, Kluwer Academic Publishers.

Franc, J.P. (2006). "Physics and control of cavitation." Education notes RTO-EN-AVT-143 in 'Design and Analysis of High Speed Pumps', Paper 2: 2-2 - 2-36

Friesch, J. (2006). "Rudder erosion damages caused by cavitation." Proceedings of 6th International Symposium on Cavitation, Wageningen, the Netherlands.

Frikha, S., Coutier-Delgosha, O. and Astolfi, J.A. (2008). "Influence of the cavitation model on the simulation of cloud cavitation on 2D foil section." International Journal of Rotating Machinery, 2008: 12.

Fujikawa, S., Akamatsu, T. (1980). "Effects of non-equilibrium condensation of vapor on the pressure wave produced by the collapse of a bubble in a liquid." Journal of Fluids Engineering, 97(3): 481-512.

Hammitt, F.G. (1963). "Observations on cavitation damage in a flowing system." Journal of

Basic Engineering, 85 (3): 347-356.

Hammit, F.G. (1979). "Cavitation erosion state of art and predicting capability." Applied Mechanics Review, ASME.

Hasuike, N., Yamasaki, S. and Ando, J. (2009). "Numerical study on cavitation erosion risk of marine propellers operating in wake flow." Proceedings of the 7th International Symposium on Cavitation, Ann Arbor, Michigan, USA.

Hoekstra, M., Vaz, G. (2008). "FreSCo exercises for NACA0015 foil." VIRTUE WP4 Workshop, Contribution from MARIN.

Hoekstra, M., Vaz, G. (2009). "The partial cavity on a 2D foil revisited." Proceedings of the 7th International Symposium on Cavitation, Ann Arbor, Michigan, USA.

Hoekstra, M., Van Terwisga, T.J.C. and Foeth, E.J. (2011). "smp'11 Workshop – Case 1: DelftFoil." 2nd International Symposium on Marine Propulsors, Hamburg, Germany.

ITTC-Quality Manual (1999). "CFD General-Uncertainties analysis in CFD uncertainty assessment methodology." Proceedings of 22nd International Towing Tank Conference.

ITTC. (2002). "CFD General-Uncertainties analysis in CFD: Verification and validation methodology and procedures." Proceedings of 23rd International Towing Tank Conference.

ITTC. (2005). "The specialist committee on cavitation erosion on propellers and appendages on high powered/high speed ships." Proceedings of the 24th International Towing Tank Conference, Volume III, UK.

ITTC. (2008). "Specialist committee on cavitation." Proceedings of 25th International Towing Tank Conference.

Kato, H., Konno, A., Maeda, M., and Yamaguchi, H. (1996). "Possibility of quantitative prediction of cavitation erosion without model test." Journal of Fluids Engineering, 118: 582-588.

Kawanami, Y., Kato, H., Yamaguchi, H., Maeda, M. and Nakasumi, S. (2002). "Inner structure of cloud cavity on a foil section." JSME International Journal, 45 (3): 655-661.

Kawamura, T., Sakoda, M. (2003). "Comparison of bubble and sheet cavitation models for simulation of cavitating flow over a hydrofoil." Proceedings of 25th International Towing Tank Conference, Osaka, Japan.

Kjeldsen, M., Arndt, R.E.A., and Effertz, M. (2000). "Spectral characteristic of sheet/cloud cavitation." Journal of Fluids Engineering, 122: 481-487.

- Koop, A.H. (2008). Numerical simulation of unsteady three-dimensional sheet Cavitation, PhD Thesis, University of Twente, Enschede, the Netherlands.
- Kuiper, G. (2001). "New developments around sheet and tip vortex cavitation on ship's propeller." Proceedings of the 4th International Symposium on Cavitation, CAV2001, Pasadena, California, USA.
- Lauder, B.E., Spalding, D.B. (1972). Lectures in Mathematical Models of Turbulence. Academic Press, London, England.
- Lecoffre, Y. (1999). Cavitation - Bubble trackers. Translation of La Cavitation traqueurs de bulles from French by Dr. M.M. Oberai. A.A.Balkema Publishers.
- Li, D. Q., Grekula, M. and Lindell, P. (2009). "A modified SST $k - \omega$ turbulence model to predict the steady and unsteady sheet cavitation on 2D and 3D hydrofoils." Proceedings of the 7th International Symposium on Cavitation, Ann Arbor, Michigan, USA.
- Li, Z. R., Van Terwisga, T.J.C. (2011). "On the capability of multiphase RANS codes to predict cavitation erosion." Proceedings of the 2nd International Symposium on Marine Propulsors, SMP2011, Hamburg, Germany.
- Liu, D.C., Hong, F.W., Zhao, F. and Zhang, Z.R. "The CFD analysis of propeller sheet cavitation." Proceedings of the 8th International Conferences on Hydrodynamics, Nantes, France.
- Liu, Z.H., Sato, K. and Brennen, C.E. (1993). "Cavitation nuclei population dynamics in a water tunnel." Cavitation and Multiphase Flow, ASME 1993, 153: 119-125.
- Menter, F. R. (1994). "Two-equation eddy-viscosity turbulence models for engineering applications." AIAA Journal, 32(8): 1598-1605.
- Morgut, M., Nobile, E. and Biluš, I. (2011). "Comparison of mass transfer models for the numerical prediction of sheet cavitation around a hydrofoil." International Journal of Multiphase Flow, 37: 620-626.
- Nohmi, M., Iga, Y., and Ikohagi, T. (2008). "Numerical prediction method of cavitation erosion." Proceedings of FEDSM2008, Jacksonville, Florida USA.
- Obar, R. (1994). "The severe cavitation erosion." Proceedings of 2nd International Symposium on Cavitation, Tokyo, Japan.
- Oprea, I. (2009a). "Wärtsilä CFD results: 2D NACA0015 foil." VIRTUE WP4 Workshop, Contribution from Wärtsilä.

Oprea, I., Bulten, B. (2009b). "RANS simulation of a 3D sheet-vortex cavitation." Proceedings of the 7th International Symposium on Cavitation, Ann Arbor, Michigan, USA.

Pereira, F., Avellan, F. and Dupont, Ph. (1998). "Prediction of cavitation erosion: An energy approach." Journal of Fluids Engineering, 120: 719-727.

Reboud, J. L., Stutz, B. and Coutier-Delgosha, O. (1998). "Two phase flow structure of cavitation: experiment and modeling of unsteady effects." Proceedings of the 3rd International Symposium on Cavitation, Grenoble, France.

Reisman, G.E., Wang, Y.C. and Brennen, C.E. (1998). "Observations of shock waves in cloud cavitation." Journal of Fluid Mechanics, 355: 255-283.

Saito, Y., Nakamori, I. and Ikohagi, T. (2003). "Numerical analysis of unsteady vaporous cavitating flow around a hydrofoil." 5th International Symposium on Cavitation, Osaka, Japan.

Saito, Y., Takami, R., Nakanori, I. and Ikohagi, T. (2007). "Numerical analysis of unsteady behavior of cloud cavitation around a NACA0015 foil." Computational Mechanics, 40: 85-96.

Salvatore, V., Pascarella, C. and d' Agostino, L. (2001). "Numerical evaluation of cavitating flows using different two-phase models." ICMF2001, New Orleans, Louisiana USA.

Sampson, R. (2010). "Resistance & Propulsion (I)." Lecture Notes, School of Marine Science and Technology, Newcastle University.

Sauer, J. (2000). Instationär kavitierende strömungen – Ein neues modell, basierend auf front capturing (VoF) und blasendynamik, PhD Thesis, Karlsruhe University.

Schmidt, S.J., Sezal, I.H., Schnerr, G.H. and Thalhamer, M. (2007). "Shock waves as driving mechanism for cavitation erosion." Proceedings of the 8th International Symposium on Experimental and Computational Aerothermodynamics of Internal Flows, Lyon, France.

Schnerr, G.H., Schmidt, S.J., Sezal, I.H., and Thalhamer, M. (2006). "Shock and wave dynamics of compressible liquid flows with special emphasis on unsteady load on hydrofoils and cavitation in injection nozzles." Proceedings of 6th International Symposium on Cavitation, Wageningen, the Netherlands.

Shih, T.H., Liou, W.W., Shabbir, A., Yang, Z. and Zhu, J. (1995). "A new $k-\varepsilon$ eddy-viscosity model for high Reynolds number turbulent flows – Model development and validation." Computers Fluids. 24 (3):227-238.

- Song, C., He, G. (1998). "Numerical simulation of cavitating flow by single-phase flow approach." 3rd International Symposium on Cavitation, Grenoble, France.
- Sorguven, E., Schnerr, G.H. (2003). "Modified $k-\omega$ model for simulation of cavitating flows." Proceedings in Applied Mathematics and Mechanics, 2(1): 386-387.
- Stern, F. Wilson, R.V., Coleman, H.W. and Paterson, E.G. (1999). "Verification and Validation of CFD simulations." IIHR Report No. 407, The University of Iowa, Iowa City IA 52242.
- Stern, F. (2007). "Quantitative V(verification) & V(validation) of CFD solutions and certification of CFD codes." Computational Uncertainty in Military Vehicle Design (Meeting Proceedings RTO-MP-AVT-147), 21:1-21:22.
- Syamlal, M. et al. (2006). Report on workshop on multiphase flow research. Morgantown, West Virginia, USA.
- Tukker, J., Kuiper, G. (2004). "High-speed video observations and erosive cavitation." PRADS 2004, Luebeck-Travemuende, 941-948.
- Van der Hout, A. (2008). "An experimental study on cavitation erosion on a 2D hydrofoil." Experimental Report, Contribution from TUDelft.
- Van Loo, S. (2011). Numerical study on the collapsing behavior of a cavitating cloud of bubbles. MSc Thesis, Faculty of Engineering Technology, Department of Engineering Fluid Dynamics, University of Twente.
- Van Rijsbergen, M., Boorsma, A. (2011). "High speed video observations and acoustic impact measurements on a NACA0015 foil." CRS EROSION II Working Group.
- Van Terwisga, T.J.C. (2009a). "Criteria for assessment of cavitation erosion risk." CRS EROSION II Working Group.
- Van Terwisga, T.J.C., Fitzsimmons, P.A., Li, Z.R. and Foeth, E.J. (2009b). "Cavitation Erosion – A critical review of physical mechanisms and erosion risk models." Proceedings of the 7th International Symposium on Cavitation, Ann Arbor, Michigan, USA.
- Versteeg, H. K., Malalasekera, W. (2007). An introduction to computational fluid dynamics: The finite volume method, Bell & Bain Limited, Glasgow.
- Wang, Y.C., Brennen, C.E. (1999). "Numerical computation of shock waves in a spherical cloud of cavitation bubbles." Journal of Fluids Engineering, 121(4): 872-880.
- Waniewski, T.A., Hunter, C. and Brennen, C.E. (2001). "Bubble measurement downstream

of hydraulic jumps." International Journal of Multiphase Flow, 27(7): 1271-1284.

Wilcox, D.C. (1998). Turbulence modeling for CFD. DCW Industries, Inc., La Canada, California.

Yakhot, V., Orszag, S.A. (1986). "Renormalization Group analysis of turbulence: I. Basic theory." Journal of Scientific Computing, 1(1): 1-51.

Yakushiji, R., Yamaguchi, H., Kawamura, T., Maeda, M. and Sakota, M. (2001). "Investigation for unsteady cavitation and re-entrant jet on a foil section: Approach by experiments and CFD." Journal of the Society of Naval Architects of Japan, No.190: 61-74.

Young, F.R. (1989). Cavitation, McGRAW-HILL Book Company.

Zima, P. Sedlář, M. and Müller, M. (2009). "Modeling collapse aggressiveness of cavitation bubbles in hydro machinery." Proceedings of the 7th International Symposium on Cavitation, Ann Arbor, Michigan, USA.

LIST OF FIGURES

Figure 2-1: Schematic of the phase change from liquid to vapor	8
Figure 2-2: Typical visualization of travelling bubble cavitation	9
Figure 2-3: Typical visualization of a leading edge sheet cavity	10
Figure 2-4: Typical visualization of tip and hub vortex cavitation on a propeller	10
Figure 2-5: Typical visualization of the shed of a cloud cavitation	11
Figure 2-6: Energy spectra and their relation to cavitation erosion	12
Figure 2-7: Local pulse structures in the cavitation on the NACA0021 foil	15
Figure 2-8: The cloudy structures that is shed from the leading edge over a twisted foil....	16
Figure 2-9: Visualization of the breaking up tip vortex cavitation.....	17
Figure 2-10: Visualization of the development of the propeller tip vortex	18
Figure 2-11: Maximum static pressure for the flow over a 3D twist foil.....	19
Figure 3-1: Scheme of the physical scenario based on an energy balance.....	24
Figure 3-2: Cavitation erosion model by Dular et al.	27
Figure 3-3: Generation and collapse of cloud cavity	30
Figure 3-4: Bubble layer, effective layer, and reference trajectory.....	31
Figure 3-5: Schematic of a spherical bubble cloud.....	33
Figure 4-1: Averaging for a statistically steady flow and a transient flow.....	43
Figure 4-2: Velocity distribution near a solid wall.....	46
Figure 4-3: Modification of the density function in the turbulent viscosity ($n = 10$).....	48
Figure 5-1: Geometry of the NACA0015 hydrofoil with a unit chord length	60
Figure 5-2: Computational domain: NACA0015, AoA= 6°	60
Figure 5-3: The coarse grid: NACA0015, AoA= 6°	61
Figure 5-4: The pressure distribution for the coarse grid: NACA0015, AoA= 6°	63
Figure 5-5: Contours of the turbulent viscosity by different turbulence models	64
Figure 5-6: The histogram of normalized lift and drag coefficient.....	65
Figure 5-7: Pressure distribution: : NACA0015, AoA= 6°	66

Figure 5-8: Comparisons between the lift, drag and the minimum pressure coefficients	68
Figure 5-9: Computational domain: NACA0015, AoA= 8°	69
Figure 5-10: Enlarged view of the O-grid: NACA0015, AoA= 8°	69
Figure 5-11: Pressure distributions on two grids	71
Figure 5-12: Contours of the x-velocity predicted on two grids.....	71
Figure 5-13: Geometry of three foils with unit chord length.....	73
Figure 5-14: Enlarged view of the O-grid:NACA0018-45, AoA= 6.5°	74
Figure 5-15: Pressure distribution:NACA0018-45 hydrofoil, AoA= 6.5°	75
Figure 5-16: Comparison of contours of x-velocity: NACA0015 and NACA0018-45	75
Figure 5-17: Pressure distribution: NACA0018-45, AoA= 6.5°	76
Figure 6-1: The time history of lift, drag coefficients and the total volume of vapor: NACA0015, AoA= 6° , $\sigma = 1.6$, $\Delta t = 5 \times 10^{-4} s$	83
Figure 6-2: The convergence histories of the residuals and the mass transfer rate during two successive time steps: NACA0015, AoA= 6° , $\sigma = 1.6$ with different time step size.....	84
Figure 6-3: The distributions of pressure coefficients and vapor volume fraction for different time step size: NACA0015, AoA= 6° , $\sigma = 1.6$	86
Figure 6-4: The contours of the vapor volume fraction and the vectors of the velocity for different time step sizes: NACA0015, AoA= 6° , $\sigma = 1.6$	87
Figure 6-5: The time histories of the residuals and mass transfer rate during two successive time steps with second-order implicit temporal discretization scheme for the coarse grid: NACA0015, AoA= 6° , $\sigma = 1.6$, $\Delta t = 2 \times 10^{-4} s$	89
Figure 6-6: The distributions of pressure coefficients and vapor volume fraction on different orders of temporal discretization scheme:NACA0015, AoA= 6° , $\sigma = 1.6$	90
Figure 6-7: Time histories of the residuals and mass transfer rate during two successive time steps for the medium grid: NACA0015, AoA= 6° , $\sigma = 1.6$	91
Figure 6-8: Time histories of the residuals and mass transfer rate during two successive time steps for the fine grid: NACA0015, AoA= 6° , $\sigma = 1.6$	91
Figure 6-9: The distribution of pressure coefficient and vapor volume fraction for three grids: NACA0015 hydrofoil, AoA= 6° , $\sigma = 1.6$, $\Delta t = 2 \times 10^{-4} s$	92
Figure 6-10: Contours of vapor volume fraction for different grids:NACA0015, AoA= 6° , $\sigma = 1.6$, $\Delta t = 2 \times 10^{-4} s$	93
Figure 6-11: Contours of turbulent kinetic energy for different grids: NACA0015, AoA= 6° , $\sigma = 1.6$, $\Delta t = 2 \times 10^{-4} s$	93
Figure 6-12: The break-off cycle: Schematic view and High Speed Video observations	95

Figure 6-13: The time histories of residuals and mass transfer rate during two successive time steps with different time step sizes on coarse grid: NACA0015, AoA= 6° , $\sigma = 1.0$	98
Figure 6-14: Time histories of the total vapor volume for different I_N with $\Delta t = 5 \times 10^{-4} s$	98
Figure 6-15: Spectral analysis of the total vapor volume shown in Figure 6-14	99
Figure 6-16: Time histories of the total vapor volume for different I_N with $\Delta t = 2 \times 10^{-4} s$	99
Figure 6-17: The spectral analysis of the total vapor volume shown in Figure 6-16	99
Figure 6-18: Time histories of the total vapor volume: $\Delta t = 5 \times 10^{-4} s$ and $\Delta t = 2 \times 10^{-4} s$	100
Figure 6-19: Contours of vapor fraction during one cycle on coarse grid: NACA0015, AoA= 6° , $\sigma = 1.0$, standard SST $k - \omega$ model	101
Figure 6-20: Shedding frequencies based on FFT analysis of the integrated vapor volume by Li et al. (2009) and current approach with $\Delta t = 5 \times 10^{-4} s$	103
Figure 6-21: Shedding frequencies based on FFT analysis of the integrated vapor volume and lift coefficient for $\Delta t = 2 \times 10^{-4} s$ with different I_N	104
Figure 6-22: Time history of the integrated vapor volume by $\Delta t = 2 \times 10^{-4} s$ with $I_N = 50$...	104
Figure 6-23: Contours of the vapor volume fraction during one typical cycle on coarse grid: NACA0015, AoA= 6° , modified SST $k - \omega$ model	106
Figure 6-24: Time histories of the total vapor volume, lift and drag coefficients within a selected shedding cycle	107
Figure 6-25: The time histories of the residuals and mass transfer rate during two successive time steps on fine grid: NACA0015, AoA= 6° , $\sigma = 1.0$, $\Delta t = 2 \times 10^{-4} s$	108
Figure 6-26: Time histories of the integrated vapor volume and lift coefficient	109
Figure 6-27: The time history of the total vapor volume by coarse grid and fine grid	109
Figure 6-28: Contours of the vapor volume fraction during one typical cycle on fine grid: NACA0015 , AoA= 6° , modified SST $k - \omega$ model	110
Figure 6-29: Time histories of the total vapor volume, lift and drag coefficients within a selected shedding cycle in accordance with the instants in Figure 6-28	111
Figure 6-30: Contours of stream function and vapor volume fraction: NACA0015, standard SST $k - \omega$ turbulence model	113
Figure 6-31: Velocity vectors in the color of vapor volume fraction showing the overlap between the separation bubbles and the cavity	114
Figure 6-32: Comparison of the turbulent viscosity distribution for the SST $k - \omega$ turbulence model with and without Reboud's correction	115
Figure 6-33: Typical sequences of the velocity vectors colored by the vapor fraction at the tail of the sheet cavity during instant ③ to ⑤ in Figure 6-28	117
Figure 6-34: Sequences of the velocity vectors colored by the vapor fraction corresponding to the period from instants ⑥ to ⑨ in Figure 6-28	118

Figure 6-35: The time histories of residuals and mass transfer rate during two successive time steps: $\Delta t = 2.5 \times 10^{-5} s$, NACA0015, $AoA = 8^\circ$, $\sigma = 2.2$ 120

Figure 6-36: The pressure distribution and vapor fraction distribution: NACA0015, $AoA = 8^\circ$, standard *SST k- ω* turbulence model, $\sigma = 2.2$ 121

Figure 6-37: Time history of total vapor volume: NACA0015, $AoA = 8^\circ$, modified *SST k- ω* turbulence model, $\sigma = 2.2$ 121

Figure 6-38: Shedding frequencies based on FFT analysis of the time history of the total vapor volume: NACA0015, $AoA = 8^\circ$, modified *SST k- ω* turbulence model, $\sigma = 2.2$ 121

Figure 6-39: Two shedding cycles corresponding to the oscillations with minimum and maximum magnitude of the total vapor volume amplitude: NACA0015, $AoA = 8^\circ$, modified *SST k- ω* turbulence model, $\sigma = 2.2$ 122

Figure 6-40: Time histories of the lift and drag coefficients within a specific shedding cycle in accordance with the instants in Figure 6-39 123

Figure 6-41: Characteristic frames during a cycle recorded by high-speed camera in top view and side view respectively, compared with the contours of vapor volume fraction corresponding to the six instants in Figure 6-39 124

Figure 6-42: Comparison of measured bubble spectra and theoretical values 125

Figure 6-43: Comparison of the side views of the images recorded by the high speed camera and the contours of vapor volume fraction predicted by $n_b = 1e+13$ and $n_b = 1e+08$ corresponding to the instants shown in Figure 6-41 127

Figure 6-44: Time histories of the lift and drag coefficients within a specific shedding cycle, predicted by bubble number density of $n_b = 1e+08$ 128

Figure 6-45: The time histories of residuals and mass transfer rate during two successive time steps: $\Delta t = 1 \times 10^{-5}$, NACA0018-45, $AoA = 6.5^\circ$, $\sigma = 0.72$ 130

Figure 6-46: The frequency obtained based on the FFT analysis of the total vapor volume: NACA0018-45, $AoA = 6.5^\circ$, $\sigma = 0.72$, standard *SST k- ω* turbulence model 130

Figure 6-47: Contours of the vapor volume fraction during one cycle: NACA0018-45, $AoA = 6.5^\circ$, standard *SST k- ω* turbulence model, $\sigma = 0.72$ 131

Figure 6-48: Contour of vapor fraction with $\alpha = 0.01$ at the instant ⑥ in Figure 6-47 131

Figure 6-49: Time histories of the total vapor volume, lift and drag coefficients within a selected shedding cycle in accordance with the instants in Figure 6-47 132

Figure 6-50: The frequency obtained based on the FFT analysis of the total vapor volume: NACA0018-45, $AoA = 6.5^\circ$, $\sigma = 0.72$, modified *SST k- ω* turbulence model 133

Figure 6-51: Contours of the vapor volume fraction during one cycle over a NACA0018-45 hydrofoil at $AoA = 6.5^\circ$ with the modified *SST k- ω* turbulence model at $\sigma = 0.72$ 134

Figure 6-52: Time histories of the total vapor volume, lift and drag coefficients within a

specific shedding cycle in accordance with the instants in Figure 6-51	135
Figure 6-53: Characteristic frames during one cycle corresponding to the eight instants from Figure 6-51.....	137
Figure 7-1: Cavitation tunnel and test section	142
Figure 7-2: Close-up of the mesh: NACA0015, AoA= 8°	143
Figure 7-3: The distribution of the static pressure (in Pa) without and with sidewalls: NACA0015, AoA= 8°	145
Figure 7-4: Sequences of instantaneous vapor volume fraction of $\alpha = 0.1$ during one typical shedding cycle: NACA0015, AoA= 8° , $\sigma = 2.01$, modified <i>SST k - ω</i> turbulence model	146
Figure 7-5: Comparison between experimental observations and numerical simulations: NACA0015, AoA= 8° , $\sigma = 2.01$, modified <i>SST k - ω</i> turbulence model.....	148
Figure 7-6: Time histories of the total vapor volume, lift and drag coefficients within a specific shedding cycle in accordance with the time instants in Figure 7-4	149
Figure 7-7: Streamlines over the cavity directed inward and estimate of the direction of re-entrant flow focusing in the lobes causing a second pinch-off.....	150
Figure 7-8: Re-entrant flow: NACA0015, AoA= 8° , $\sigma = 2.01$, modified <i>SST k - ω</i> turbulence model	152
Figure 7-9: Sheet cavity with local re-entrant jets	153
Figure 7-10: Schematic diagram of the transformation process to the horse-shoe cloudy cavity for the cavitating flow over the hydrofoil with sidewalls.....	154
Figure 7-11: Reconstruction of the horse-shoe shaped vortex structure	155
Figure 7-12: Formation of the horse-shape cloudy cavity: NACA0015, AoA= 8° , $\sigma = 2.01$, modified <i>SST k - ω</i> turbulence model	156
Figure 7-13: Schematic diagram of the transformation process of a horse-shoe cloudy cavity from break-off to violent collapse.....	157
Figure 7-14: Comparison of three typical instants during the collapse of the horse-shoe cloudy cavity.....	158
Figure 7-15: Close-up of the mesh: NACA0018-45, AoA= 6.5°	159
Figure 7-16: The static pressure distribution with no-slip condition at the sidewalls: NACA0018-45, AoA= 6.5°	161
Figure 7-17: The shedding frequency obtained from an FFT analysis of the total vapor volume: modified <i>SST k - ω</i> turbulence model, NACA0018-45, AoA= 6.5° , $\sigma = 0.72$	161
Figure 7-18: Sequences of iso-surface plots of instantaneous vapor volume fraction of $\alpha = 0.1$ during one typical shedding cycle in top view: NACA0018-45, AoA= 6.5° , $\sigma = 2.01$, modified <i>SST k - ω</i> turbulence model	164

Figure 7-19: Sequences of iso-surface plots of instantaneous vapor volume fraction of $\alpha = 0.1$ during one typical shedding cycle in side view: NACA0018-45, $AoA = 6.5^\circ$, $\sigma = 2.01$, modified SST $k - \omega$ turbulence model 165

Figure 7-20: Time histories of the total vapor volume, lift and drag coefficients within a specific shedding cycle in accordance with the instants in Figure 7-18 166

Figure 7-21: Two successive iso-surface plots of instantaneous vapor volume fraction of $\alpha = 0.1$: NACA0018-45, $AoA = 6.5^\circ$, $\sigma = 2.01$, modified SST $k - \omega$ turbulence model 167

Figure 7-22: Two successive iso-surface plots of instantaneous vapor volume fraction of $\alpha = 0.1$: NACA0018-45, $AoA = 6.5^\circ$, $\sigma = 2.01$, modified SST $k - \omega$ turbulence model 167

Figure 7-23: Comparison of six typical instants showing the strong interaction at the trailing edge between experimental observations and numerical results 169

Figure 7-24: Comparison of six typical instants showing the formation and collapse of the cloudy cavity between experimental observations and numerical results 170

Figure 7-25: Mapping of cavitation regimes for the NACA0015 hydrofoil 172

Figure 7-26: Laminar boundary layer velocity profile 173

Figure 7-27: Subdivisions of the turbulent boundary layer 174

Figure 7-28: Comparison of total viscosity 175

Figure 8-1: Paint test result after re-application of paint and run No.26 and 27: NACA0015, $AoA = 8^\circ$, $\sigma = 2.01$, $U = 17.3m/s$ 180

Figure 8-2: Cavitating structures that might cause an erosive impact observed by Boorsma (2010): NACA0015, $AoA = 8^\circ$, $\sigma = 2.2$ 181

Figure 8-3: Sub-structures possibly related to high impact observed by Van Rijsbergen and Boorsma (2011): NACA0015, $AoA = 8^\circ$, $\sigma = 2.01$ 182

Figure 8-4: Possible relation between the sub-structures observed by high-speed camera and erosion result: NACA0015, $AoA = 8^\circ$, $\sigma = 2.01$ 182

Figure 8-5: Observations representing the collapse of the horse-shoe shaped cloudy cavity that is associated with high impacts: NACA0015, $AoA = 8^\circ$, $\sigma = 2.2$ 183

Figure 8-6: The images that possibly give rise to impacts on the foil surface 184

Figure 8-7: Paint test result: NACA0018-45, $AoA = 6.5^\circ$, $\sigma = 2.01$, $U = 17.3m/s$ 185

Figure 8-8: Contours of the instantaneous static pressure distribution corresponding to the six instants shown in Figure 7-4: NACA0015, $AoA = 8^\circ$ 187

Figure 8-9: Contour of $\partial p / \partial t$ at the moment when its maximum value is observed (between instant ① and ② in Figure 7-4) and plots of vapor fraction with $\alpha = 0.1$ 190

Figure 8-10: Contour of $\partial p / \partial t$ at the moment when its maximum value is observed (between instant ② and ③ in Figure 7-4) and plots of vapor fraction with $\alpha = 0.1$ 190

Figure 8-11: Contour of $\partial p / \partial t$ at the moment when its maximum value is observed (between instant③and④in Figure 7-4) and plots of vapor fraction with $\alpha = 0.1$	191
Figure 8-12: Contour of $\partial p / \partial t$ at the moment when its maximum value is observed (between instant④and⑤in Figure 7-4) and plots of vapor fraction with $\alpha = 0.1$	191
Figure 8-13: Contours of $\partial p / \partial t$ at the moment when collapse occurs (between instant⑤and⑥in Figure 7-4) and plots of the vapor volume fraction with $\alpha = 0.1$	191
Figure 8-14: Contour of $-\partial \alpha / \partial t$ at the moment when its maximum value is observed (between instant①and②in Figure 7-4) and plots of vapor fraction with $\alpha = 0.1$	193
Figure 8-15: Contour of $-\partial \alpha / \partial t$ at the moment when its maximum value is observed (between instant②and③in Figure 7-4) and plots of vapor fraction with $\alpha = 0.1$	193
Figure 8-16: Contour of $-\partial \alpha / \partial t$ at the moment when its maximum value is observed (between instant③and④in Figure 7-4) and plots of vapor fraction with $\alpha = 0.1$	194
Figure 8-17: Contour of $-\partial \alpha / \partial t$ at the moment when its maximum value is observed (between instant④and⑤in Figure 7-4) and plots of vapor fraction with $\alpha = 0.1$	194
Figure 8-18: Contour of $-\partial \alpha / \partial t$ at the moment when its maximum value is observed (between instant⑤and⑥in Figure 7-4) and plots of vapor fraction with $\alpha = 0.1$	194
Figure 8-19: Contours of $-\partial \alpha / \partial t$ and $\partial p / \partial t$ at the same instant when maximum $\partial p / \partial t$ is observed during the collapse of the horse-shoe shape cloudy cavity	195
Figure 8-20: Contours of the four aggressiveness indices in equation (8-4) during a typical shedding cycle referred to the cyclic images shown in Figure 7-4	197
Figure 8-21: Comparison between the aggressiveness indices ($Index_2$ and $Index_3$) and the iso-plot of the vapor volume fraction with $\alpha = 0.1$ at the instant④	198
Figure 8-22: The comparison between the aggressiveness indices and the rate of pressure rise at the end of the collapse of the horse-shoe shaped cloudy cavity	198
Figure 8-23: Iso-plots of vapor volume fraction with $\alpha = 0.1$ during a shedding cycle	200
Figure 8-24: Contours of instantaneous pressure distribution on suction side and pressure side, and the corresponding side view images: NACA0018-45, AoA= 6.5°	202
Figure 8-25: High impacts observed at the instant ⑳ (see images in Figure 7-18 & 7-19)	203
Figure 8-26: Contour of $\partial p / \partial t$ at the moment when its maximum value is observed (between instant⑩and⑪in Figure 7-18) and plots of vapor fraction with $\alpha = 0.1$	205
Figure 8-27: Contour of $\partial p / \partial t$ at the moment when its maximum value is observed (between instant⑫and⑬in Figure 7-18) and plots of vapor fraction with $\alpha = 0.1$	206
Figure 8-28: Contour of $\partial p / \partial t$ at the moment when its maximum value is observed (between instant⑬and⑭in Figure 7-18) and plots of vapor fraction with $\alpha = 0.1$	206
Figure 8-29: Contour of $\partial p / \partial t$ at the moment when its maximum value is observed	

(between instant⑭and⑮in Figure 7-18) and plots of vapor fraction with $\alpha = 0.1$ 206

Figure 8-30: Contour of $\partial p / \partial t$ at the moment when its maximum value is observed (between instant⑮and⑯in Figure 7-18) and plots of vapor fraction with $\alpha = 0.1$ 207

Figure 8-31: Contours of the iso-surface plots of the vapor volume fraction with $\alpha = 0.1$ showing the disintegrations and collapses 207

Figure 8-32: Contour of $\partial p / \partial t$ at the moment when its maximum value is observed (between instant⑰and⑱in Figure 7-18) and plots of vapor fraction with $\alpha = 0.1$ 207

Figure 8-33: Contour of $-\partial \alpha / \partial t$ at the moment when its maximum value is observed (between instant⑩and⑪in Figure 7-18) and plots of vapor fraction with $\alpha = 0.1$ 209

Figure 8-34: Contour of $-\partial \alpha / \partial t$ at the moment when its maximum value is observed (between instant⑬and⑭in Figure 7-18) and plots of vapor fraction with $\alpha = 0.1$ 209

Figure 8-35: Contour of $-\partial \alpha / \partial t$ at the moment when its maximum value is observed (between instant⑭and⑮in Figure 7-18) and plots of vapor fraction with $\alpha = 0.1$ 210

Figure 8-36: Contours of the four aggressiveness indices in equation during a typical shedding cycle referred to the cyclic images shown in Figure 7-17& Figure 7-18 211

Figure 8-37: Erosion intensity estimated by equation (8-9) with eight different threshold levels: NACA0015, AoA=8° 215

Figure 8-38: The comparison between the high erosion risk predicted by equation (8-9) and the damage area observed from paint tests: NACA0015, AoA=8° 216

Figure 8-39: Erosion intensity estimated by equation (8-9) with eight different threshold levels: NACA0018-45, AoA=6.5° 217

Figure 8-40: The comparison between the high erosion risk predicted by equation (8-9) and the damage area observed from paint tests: NACA0018-45, AoA=6.5° 217

Figure B-1: The barotropic state law $\rho(p); T = 24^{\circ}C$ 243

LIST OF TABLES

Table 2-1: Review of impact loadings for different cavity phenomena	14
Table 4-1: Available two-equation turbulence models in FLUENT (ANSYS 12.0)	45
Table 5-1: Grid Features of a NACA0015 hydrofoil at 6° angle of attack	61
Table 5-2: Boundary conditions and flow properties:NACA0015, AoA= 6°	62
Table 5-3: The chosen solver and discretization schemes: NACA0015, AoA= 6°	62
Table 5-4: Flow characteristics comparison by different grids	66
Table 5-5: Participants and their adopted methods in the VIRTUE WP4 Workshop	67
Table 5-6: Difference between the results by FLUENT and the reported mean values from VIRTUE WP4 Workshop	68
Table 5-7: Characteristics of the grids: NACA0015, AoA= 8°	70
Table 5-8: Boundary conditions and flow properties:NACA0015, AoA= 8°	70
Table 5-9: The chosen solver and discretization schemes:NACA0015, AoA= 8°	70
Table 5-10: Flow characteristics and error estimation: NACA0015, AoA= 8°	72
Table 5-11: Boundary conditions and flow properties: NACA0018-45, AoA= 6.5°	74
Table 5-12: The chosen solver and discretization schemes: NACA0018-45, AoA= 6.5°	75
Table 5-13: Flow characteristics predicted by XFOIL and FLEUNT:NACA0018-45.....	77
Table 6-1: Matrix of the tested cases related to the investigation of steady cavitating phenomena.....	79
Table 6-2: Matrix of the tested cases related to the investigation of unsteady cavitating phenomena.....	80
Table 6-3: Boundary conditions and flow properties: NACA0015, AoA= 6°	81
Table 6-4: Properties of the selected time step size	83
Table 6-5: Flow characteristics comparison with different time step size	86
Table 6-6: Flow characteristics comparison with different temporal discretization schemes	89
Table 6-7: Properties of the grids related to the time step size	90

Table 6-8: Flow characteristics comparison with different grid densities.....	91
Table 6-9: Boundary conditions and flow properties: NACA0015, AoA= 6°	97
Table 6-10: Relative deviations between the sufficiently converged value and the value obtained from the default 20 iterations	100
Table 6-11: Summary of the numerically obtained frequencies.....	103
Table 6-12: Boundary conditions and flow properties: NACA0015, AoA=8°	120
Table 6-13: Test conditions for S02M10.....	124
Table 6-14: Comparison of results by different input of bubble number density.....	126
Table 6-15: Boundary conditions and flow properties: NACA0018-45, AoA= 6.5°	129
Table 6-16: Test conditions for the examined experimental data.....	136
Table 7-1: Boundary conditions and flow properties: NACA0015, AoA= 8°	144
Table 7-2: Test conditions for Run No. 26.....	144
Table 7-3: Comparison of the minimum pressure coefficients	145
Table 7-4: Boundary conditions and flow properties:NACA0018-45, AoA= 6.5°	160
Table 7-5: Test conditions for the examined experimental data.....	160
Table 8-1: Test conditions for Run No.26 and 27	181
Table B-1: An overview of the current cavitation models	245

NOMENCLATURE

ROMAN

a_p	Center coefficient for a control volume designated cell P	
a_{nb}	Influence coefficients for the neighboring cells of cell P	
A	Radius of bubble cloud	m
A_0	Initial radius of the bubble cloud	m
AoA	Angle of attack	$^\circ$
AoA_0	Zero lift angle	$^\circ$
B	Breadth of the hydrofoil	m
C	Chord Length of the hydrofoil	m
C_D	Drag coefficient	
C_L	Lift coefficient	
C_p	Pressure coefficient	
$C_{p\min}$	Minimum pressure coefficient	
$C_{p\infty}$	Pressure coefficient at infinity	
C_{Qc}	Non-dimensional flow rate	
D	Length scale	m
E_{pot}	Potential energy	kgm^2s^{-2}
E_c	Potential energy in a cavity	kgm^2s^{-2}
E_s	Damage threshold	kgm^2s^{-2}
f	Body force	$kgms^{-2}$

F_s	Factor of safety	
h	Distance between the bubble center and the solid surface	m
h_b	Bubble layer thickness	m
h_e	Effective layer thickness	m
h_r	Reference trajectory	m
I_{pR}	Accumulative collapsing rate on pickup	
I_{LE}	Index related to the leading edge radius	
$I_{Erosion}$	Erosion intensity	$kgm^{-1}s^{-3}$
I_i	i^{th} individual intensity	$kgm^{-1}s^{-3}$
I_N	Iteration numbers per time step	
I_R	Accumulative distribution of cavity bubbles	
k	Turbulence kinetic energy	m^2s^{-2}
n_b	Bubble number density	m^{-4}
N	Number of events	
p	Local mixture pressure	$kgm^{-1}s^{-2}$
p_a	Acoustic pressure in the far field	$kgm^{-1}s^{-2}$
p_h	Impact pressure for a single bubble with a distance of h from the solid surface	$kgm^{-1}s^{-2}$
p_k	Order of accuracy for the k^{th} parameter	
p_{max}	Maximum pressure	$kgm^{-1}s^{-2}$
p_{min}	Minimum pressure	$kgm^{-1}s^{-2}$
p_{ref}	Reference pressure	$kgm^{-1}s^{-2}$
p_{th}	Theoretical order of accuracy for the k^{th} parameter	
p_v	Vapor pressure	$kgm^{-1}s^{-2}$
p_∞	Surrounding pressure	$kgm^{-1}s^{-2}$
p_0	Initial pressure at undisturbed condition	$kgm^{-1}s^{-2}$

Δp	Pressure difference	$kgm^{-1}s^{-2}$
P_{pot}	Instantaneous potential power	kgm^2s^{-3}
P_{wave}	Acoustic power related to pressure wave	kgm^2s^{-3}
P_{pot}^{mat}	Flow aggressiveness potential power	kgm^2s^{-3}
P_{waves}^{mat}	Pressure wave power	kgm^2s^{-3}
Q	Ventilated flow rate	m^3s^{-1}
r	Radial coordinate from the center of the cloud	m
r_{LE}	Leading edge radius	m
$R ; R_B$	Bubble radius	m
R_{min}	Minimum bubble radius	m
R_k	Convergence ratio	
R_0	Initial bubble radius	m
Re	Reynolds number related to R_0 , $Re = \rho_l UR_0 / \mu_E$	
Re_x	Reynolds number related to x , $Re_x = \rho_l U_0 x / \mu_E$	
S	Strain rate magnitude	s^{-1}
S_{km}	m^{th} solution for the k^{th} parameter	
S_e	Evaporation of the vapor bubbles	
S_c	Condensation of the vapor bubbles	
ΔS	Analyzed sample surface	mm^{-2}
S_{ij}	Strain rate tensor	s^{-1}
t	Time	s
t_{max}	Maximum thickness	m
T	Period of time	s
T_c	Period of assessed time cycle	s
Δt	Time step size	s

u	Velocity of the mixture	ms^{-1}
u_τ	Velocity scale	ms^{-1}
U_∞	Velocity of the main flow	ms^{-1}
U_k	Uncertainty for the k^{th} parameter	
U_{ref}	Reference velocity	ms^{-1}
V_v	Vapor volume	m^3
V_d	Volume damage rate	$\mu m^3 mm^{-2} s^{-1}$
We	Weber number, $We = \rho_l U^2 R_0 / S$	
x	Coordinates in the x-direction	m
y^+	Non-dimensional wall distance	
y_{max}^+	Maximum value of the non-dimensional wall distance	

GREEK

α	Vapor volume fraction	
α_0	Initial vapor volume fraction	
β	Cloud interaction parameter	
β^*	Mechanical transfer function	
δ	Boundary layer thickness	m
δ_k	Error for the k^{th} parameter	
δ_{km}^*	Error estimate for the k^{th} parameter and m^{th} solution	
ε	Dissipation rate of turbulent kinetic energy	$m^2 s^{-3}$
ϕ	Arbitrary quantity	
ϕ_P	A generic variable at the center of cell P	
ϕ_{nb}	A generic variable at the neighboring cells of cell P	
γ	Surface tension	$kg s^{-2}$

η	Non-dimensional bubble population per unit liquid volume	
η^*	Collapse efficiency	
η^{**}	Energy transfer efficiency	
κ	Polytropic index for non-condensable gas inside a bubble	
$\mu_E ; \mu_{Eff}$	Effective viscosity	$kgm^{-1}s^{-1}$
μ_m	Mixture viscosity	$kgm^{-1}s^{-1}$
μ_t	Turbulent viscosity	$kgm^{-1}s^{-1}$
ρ_m	Mixture density	kgm^{-3}
ρ_l	Liquid density	kgm^{-3}
ρ_v	Vapor density	kgm^{-3}
σ	Cavitation Number	
τ_p	Pressure time scale	s
τ_η	Kolmogorov time scale	s
τ_ω	Wall shear stress	$kgm^{-1}s^{-2}$
τ_{ij}	Viscous stresses tensor	$kgm^{-1}s^{-2}$
ν_l	Kinematic viscosity of the liquid	m^2s^{-1}
ω	Specific dissipation rate of turbulent kinetic energy	s^{-1}

SYMBOLS

–	Mean component
'	Fluctuating component

ACRONYM

ASME	American Society of Mechanical Engineers
CFD	Computational Fluid Dynamics
CPU	Central Processing Unit
DEM	Discrete Element Method

DES	Direct Numerical Simulation
FEDSM	Fluids Engineering Division Summer Meeting
FFT	Fast Fourier Transform
HSV	High Speed Video
ITTC	International Towing Tank Conference
LES	Large Eddy Simulation
MARIN	Maritime Research Institute Netherlands
PRESTO!	Pressure Staggering Option
QUICK	Quadratic Upwind Interpolation for Convective Kinematics
RANS	Reynolds-Averaged Navier-Stokes
RE	Richardson Extrapolation Technique
RNG	Renormalization Group
RSM	Reynolds Stress Model
R&D	Resistance and Development
SST	Shear-Stress Transport
URANS	Unsteady Reynolds-Averaged Navier-Stokes
VOF	Volume of Fluid
V&V	Verification and Validation

ACKNOWLEDGMENT

After almost five-years study in the section of Ship Hydromechanics and Science at the faculty of Mechanical, Maritime and Materials Engineering (3ME) in Delft University of Technology (TUDelft), my journey of finishing the PhD Thesis is finally completed. This thesis has been successfully accomplished with valuable assistance of many people in various ways. At the end of this period, it is a great pleasure to thank those who made this thesis possible.

The research contained in this thesis was sponsored by the China Scholar Ship Council (CSC) and Delft University of Technology (TUDelft). I want to thank CSC and TUDelft for the financial support and the opportunity for me to pursue a PhD degree. I'm also grateful to my home university, Wuhan University of Technology, for allowing me to pursue my PhD degree abroad.

First and foremost, I offer my sincerest gratitude to my supervisor, Prof. Tom van Terwisga, for his guidance, patience and encouragement. His knowledge and wisdom have inspired me to negotiate the obstacles in the completion of this thesis. I am very grateful for his understanding and kindness to help me to be accustomed to the new academic field and new cultural environment.

I owe my special gratitude to Mathieu Pourquie, who guided me in the CFD field and was always available to provide suggestions and guidance. I will never forget those funny jokes which he made during the discussions that were never boring. I would like to give my special thanks to Prof. Harry Hoeijmakers, who was often present at my PhD progress meetings, for his valuable suggestions and constructive comments. I also would like to give my special thanks to Dr. Daqing Li, with whom I can communicate in Chinese, for his unwearied help and valuable suggestions during the start-up of the study. It was very helpful for me to get a deeper understanding of the CFD issues in Chinese. Along with them, I would like to thank the rest of my thesis committee for their effort to fix their time schedule to review my thesis and also for their comments and suggestions to help improving this thesis.

I am grateful for the reports of the experiments on the NACA0015 hydrofoil provided by the Cooperative Research Ships (CRS), administered by MARIN. Experimental data on the NACA0015 hydrofoil have been made available by the Cavitation Erosion Project of CRS. I am also grateful for the support of MARIN for the regular PhD progress meetings.

My special thanks go to Dr. Martin Hoekstra for the supply of original meshes of NACA0015 hydrofoil, for his inspired and helpful comments and suggestions on my PhD work, and for his kindness to do the presentation instead of me on the 3rd International Cavitation Forum. I also want to thank Iulia Oprea, Johan Bosschers, Erik van Wijngaarden, Sebastiaan van Loo, Martijn van Rijsbergen and Pepijn Pennings for their helpful suggestions during the theoretical and scientific discussions on my work.

It is an honor for me to give special thanks to my colleagues to support me. I thank Prof. Hopman and Prof. Huijsmans for their academic support. I thank Dr. Henk de Koning Gans, who shared the same office room during the last three-years of my PhD study, for his kind concern in my life in the new cultural environment and also for his academic help in the research. I thank Piet de Heer, Marysa Dunant and Ria Nieuwland-Jobse for their reliable secretarial support. I thank the Vulcanus for offering me the summer internship opportunities. I also thank other colleagues in SHS section and SDPO section: Prof. Douwe Stapersma, Hugo Grimmelijs, Xiaoli Jiang, Peter Naaijen, Robert Hekkenberg, Erik Ulijn and Elena Moredo.

I gratefully appreciate Mr. Cees Dirkse, Ms. Franca Post and Mr. Cees Timmers for their kind and warming welcome and support regarding the international student issues. I wish to thank Mrs. Mae Sterk and Mr. Frits Sterk for their kindness and nice invitations. I wish to thank my friends who came here to start the PhD study at the same year, especially the colleagues in the same faculty: Shun Chen, Wei Shi, Wei Zheng, Yan Wei and Yu Ding, for the share of joy and frustrations in life and study.

Last but not the least, I would like to pay high regards to my grandmother, my parents, my sister and other family members for their sincere encouragement and spiritual support throughout this phase of my life. I am indebted to my beloved husband Wei He for his understanding of the long-term study abroad and his inspiration and valuable opinions in my PhD research. I finally want to offer my apologies that I could not individually acknowledge all contributors to this thesis.

CURRICULUM VITAE

Personal Information:

Name	Li Ziru
Birthday	March, 3 th , 1983
Birthplace	XINJI, HEBEI Province, P.R. China
Nationality	Chinese

Education Background:

Sep.1999~July.2003	BS. , Major: Ship and Ocean Engineering; School of Transportation, Wuhan University of Technology, P.R. China
Sep.2003~July.2006	MS. , Major: Design and Manufacture for Ships and Marine Structures; School of Transportation, Wuhan University of Technology, P.R. China
Sep.2006~Sep.2007	PhD. , Major: Design and Manufacture for Ships and Marine Structures; School of Transportation, Wuhan University of Technology, P.R. China
Oct.2007~June.2012	PhD. , Research direction: Assessment of cavitation erosion by RANS method; Section of Ship Hydromechanics and Science, Faculty of Mechanical, Maritime and Materials Engineering, Delft University of Technology, the Netherlands

Publications:

Li, Z. R., Pourquie, M. and Van Terwisga, T.J.C. (2009). "A numerical study of steady and unsteady cavitation on a 2D Hydrofoil." Journal of Hydrodynamics, Shanghai, China.

Li, Z. R., Van Terwisga, T.J.C. (2011). "On the capability of multiphase RANS codes to predict cavitation erosion." Proceedings of the 2nd International Symposium on Marine Propulsors, SMP2011, Hamburg, Germany.

Li, Z. R., Pourquoi, Mathieu, and Van Terwisga, T.J.C. (2011). "On the assessment of cavitation erosion on a hydrofoil using unsteady RANS." WIMRC 3rd International Cavitation Forum 2011, University of Warwick, UK.

Li, Z.R., Van Terwisga, T.J.C. (2012). "On the capability of a RANS method to assess the cavitation erosion risk on a hydrofoil." Proceedings of the 8th International Symposium on Cavitation, CAV2012, Singapore. (In preparation)